Skolkovo Institute of Science and Technology

FLUORESCENT PHOTOCONVERTIBLE POLYMER MICROCAPSULES FOR CELL LABELING AND TRACKING

Doctoral Thesis

by

ZHANNA KOZYREVA

DOCTORAL PROGRAM IN MATERIALS SCIENCE AND ENGINEERING

Supervisor
Professor Gleb Sukhorukov

Moscow - 2024

© Zhanna Kozyreva 2024

I hereby declare that the work presented in this thesis was carried out by myself at Skolkovo Institute of Science and Technology, Moscow, except where due acknowledgement is made, and has not been submitted for any other degree.

Zhanna Kozyreva (Candidate)

Prof. Gleb Sukhorukov (Supervisor)

Abstract

Tracing individual cell pathways in the whole cell population is important for understanding the behaviour, migration, and fate of single cells. Optical labeling of cells is usually performed via a genetic modification to generate photoconvertible proteins. At the same time, genetic alterations are unacceptable for some cell types. For example, the genetic modification of stem cells makes their safety questionable for personal therapy applications and might change their properties and behaviour. Another approach for cell labeling is the use of lipophilic membrane dyes. Nevertheless, long-term tracking is limited in this case because dyes often leak from cells. Moreover, a decrease in the signal intensity is common because of cell division, which leads to dye dilution.

The aim of this thesis is to develop trackable microparticles for bioapplications in cell labeling and tracking, which serve as an alternative to the genetic modification approach and lipophilic dyes. As such, the polymer photoconvertible capsules were prepared by two methods: thermal treatment in polyvinyl alcohol (PVA) gel (which induces the generation of carbon nanodots) and a regular layer-by-layer approach without thermal treatment. In this study, several organic dyes were investigated and tested as potential photoconvertible labels. The capsules were characterized for morphology, fluorescence, photostability, and photoconversion. Thermally treated microcapsules containing RhB were used for cell labeling and tracking experiments on mouse mesenchymal stromal cells, human mesenchymal stromal cells, and myocytes.

We demonstrated that the treatment of capsules in PVA gel with fluorescent dyes increased the yield of capsules from one synthesis by at least 250 times in comparison to the synthesis in water. Thermally treated capsules containing RhB and Rh6G were found to be photostable and exhibited photoconversion properties. We also found that capsules prepared without thermal treatment and containing Cy3.5, Cy5.5, and RITC demonstrated profound photoconversion properties. In cell experiments, it was demonstrated that capsules remained inside the cells for up to four days of tracking, preserving a bright fluorescence signal and allowing tracking of the daughter cells. Such polymer capsules open possibilities for studying cell-cell interactions, fate, and migration patterns while preserving high cell viability and providing intensive fluorescence signals.

Chapters 1 and 2 present an introduction and literature review to obtain a better understanding of the research topic. A literature review covers the production, properties, and applications of polymer microcapsules and carbon nanodots. The mechanism of photoconversion of fluorescent proteins and organic dyes is explained. Cell labeling and tracking approaches are also discussed. In Chapter 3, the materials and methods used in this study are described. Chapter 4 describes the development and characterization of photoconvertible polymer microcapsules using the hydrothermal approach. Chapter 5 covers photoconvertible capsules prepared without thermal treatment using dye-labeled polyallylamine hydrochloride. Chapter 6 is devoted to cell labeling and tracking experiments. The general conclusions and future work are discussed in Chapter 7.

Publications

Publications relevant to the thesis

1. Olga A. Sindeeva, Polina A. Demina, Zhanna V. Kozyreva, Albert R. Muslimov, Olga I. Gusliakova, Valeriia O. Laushkina, Ekaterina A. Mordovina, Daria Tsyupka, Olga S. Epifanovskaya, Anastasiia Yu. Sapach, Irina Yu. Goryacheva, and Gleb B. Sukhorukov. Labeling and tracking of individual human mesenchymal stromal cells using photoconvertible fluorescent microcapsules. International Journal of Molecular Sciences, 24(17):13665, September 2023.

2. Zhanna V. Kozyreva, Polina A. Demina, Anastasiia Yu. Sapach, Daria A. Terentyeva, Olga I. Gusliakova, Anna M. Abramova, Irina Yu. Goryacheva, Daria B. Trushina, Gleb B. Sukhorukov, and Olga A. Sindeeva. Multiple dyes applications for fluorescent convertible polymer capsules as macrophages tracking labels. Heliyon, page e30680, May 2024.

3. Olga A. Sindeeva, Polina A. Demina, Zhanna V. Kozyreva, Daria A. Terentyeva, Olga I. Gusliakova, Albert R. Muslimov, and Gleb B. Sukhorukov. Single mesenchymal stromal cells migration tracking into glioblastoma using photoconvertible nanoengineered vesicles. Nanomaterials, 14(14):1215, July 2024.

4. Polina A. Demina, Olga I. Gusliakova, Zhanna V. Kozyreva, Daria A. Terentyeva, Dmitry A. Gorin, Irina Yu. Goryacheva, Gleb B. Sukhorukov, and Olga A. Sindeeva. Photoconvertible markers for study individual myoblast migration into the macrophage's colony. Optical Materials, 157:116148, September 2024.

5. Zhanna V. Kozyreva, Polina A. Demina, Olga I. Gusliakova, Gleb B. Sukhorukov, and Olga A. Sindeeva. Transferring of cyanine dyes in free and encapsulated

form between cells. Journal of Materials Chemistry B (under review)

Other publications

1. Mikhail N. Zharkov, Ekaterina P. Brodovskaya, Oleg A. Kulikov, Elena V. Gromova, Valentin P. Ageev, Aleksandra V. Atanova, Zhanna V. Kozyreva, Alexander M. Tishin, Alexander P. Pyatakov, Nikolay A. Pyataev, and Gleb B. Sukhorukov. Enhanced cytotoxicity caused by AC magnetic field for polymer microcapsules containing packed magnetic nanoparticles. Colloids and Surfaces B: Biointerfaces, 199:111548, March 2021.

2. A.A. Ivanova, Z.V. Kozyreva, A.Y. Chekalov, P.I. Proshin, A.S. Abdurashitov, A.S. Bello, S. Markovic, G.B. Sukhorukov, and A.N. Cheremisin. Development and characterization of nanostructured surfactant compositions with prolonged action and stimuli-responsible physicochemical properties. Colloids and Surfaces A: Physicochemical and Engineering Aspects, 687:133396, April 2024

Conferences

1. Zhanna V. Kozyreva, Polina A. Demina, Anastasiia Yu. Sapach, Daria A. Terentyeva, Olga I. Gusliakova, Anna M. Abramova, Irina Yu. Goryacheva, Daria B. Trushina, Gleb B. Sukhorukov, and Olga A. Sindeeva. Fluorescence Convertible Polymer Capsules with Various Dyes as Tracking Labels for Macrophages. The 27th Annual Conference Saratov Fall Meeting 2023 XI Symposium on Optics & Biophotonics, Saratov, 25-29 September 2023. Oral report.

2. Zhanna V. Kozyreva, Polina A. Demina, and Olga A. Sindeeva. Photoconvertible capsules with multiple dyes for stem cell tracking. XXXI International Conference of Students, Postgraduate Students, and Young Scientists "Lomonosov", section "Fundamental Materials Science and Nanomaterials", Moscow, 12-26 April 2024. Poster session. (A certificate was received for one of the best reports in the section).

3. Zhanna V. Kozyreva, Polina A. Demina, Daria A. Terentyeva, Gleb B. Sukhorukov, and Olga A. Sindeeva. Photoconvertible polymer capsules for cell labeling and tracking. The first All-Russian Conference on Luminescence LUMOS-2024, Moscow, 23-26 April 2024. Poster session.

4. Zhanna V. Kozyreva, Polina A. Demina, Anastasiia Yu. Sapach, Daria A. Terentyeva, Gleb B. Sukhorukov, and Olga A. Sindeeva. Photoconvertible polymer labels for macrophages tracking. 21st International Conference Laser Optics ICLO 2024, St. Petersburg, 1-5 July 2024. Oral report.

5. Zhanna V. Kozyreva, Olga A. Sindeeva, Polina A. Demina, Daria A. Terentyeva, and Gleb B. Sukhorukov. Tracking single mouse mesenchymal stromal cells

migration into glioblastoma using photoconvertible microparticles. XX International Scientific and Practical Conference “New Polymer Composite Materials”, “Mikitaev Readings”, Elbrus, 4-10 July 2024. Oral report.

6. Zhanna V. Kozyreva, Olga A. Sindeeva, Polina A. Demina, Daria A. Terentyeva, Olga I. Gusliakova, and Gleb B. Sukhorukov. Fluorescent convertible microcapsules as a tool for studying the migration of mouse mesenchymal stromal cells into glioblastoma. XXXVI Symposium "Modern Chemical Physics", Tuapse, 16-26 September 2024. Oral report.

Acknowledgements

Most importantly, I would like to thank my scientific advisor Professor Gleb B. Sukhorukov for making it possible for me to study at Skolkovo Institute of Science and Technology. I am grateful for his guidance, support, and all the resources he provided for my research.

I am also thankful to my MSc supervisor, Dr. Marina Pigaleva (Lomonosov Moscow State University, Physics Department). Without her impact, I would not have been where I am today.

I am very grateful to my colleague, Dr. Olga Sindeeva, for her guidance during this work and for helping with the cell experiments. My colleagues Dr. Polina Demina, Dr. Olga Guslyakova, Daria Terentyeva, and Anastasiia Sapach also greatly helped me at different stages of this research.

I am thankful for being a member of Professor Sukhorukov's group, where we receive enough freedom to express ourselves and learn to be responsible for our research. Many thanks to my friends and family, who encouraged me and believed in me when I needed this support the most.

This work was supported by the Russian Science Foundation (grant number 22-15-00292).

Contents

Abstract **1**

Publications **3**

Conferences **5**

Acknowledgements **7**

Contents **8**

List of Symbols, Abbreviations **14**

List of Figures **18**

List of Tables **24**

Chapter 1. Introduction **25**

1.1 Background 25

1.2 Aim and Objectives 28

Chapter 2. Review of the Literature **30**

2.1 Polymer microcapsules synthesis 30

2.1.1 Multilayer assembly of polymers for film formation 30

2.1.2 Multilayer assembly of polymers on spherical templates for capsule formation 31

2.1.2.1 Charge overcompensation and inversion 32

2.1.2.2 Polyelectrolyte multilayer growth 34

2.1.3 Encapsulation in Layer-by-Layer Capsules 36
2.1.3.1 Pre-loading 37
2.1.3.2 Post-loading 38
2.1.4 Properties of microcapsules 40
2.1.4.1 Cellular internalization of capsules 41
2.1.4.2 Capsule cytotoxicity 43
2.1.5 Biomedical applications of polymer microcapsules 45
2.1.5.1 Drug delivery 45
2.1.5.2 Cell manipulation 46
2.1.5.3 Bioreactors 47
2.1.5.4 Biosensors 48
2.2 Carbon nanodots 49
2.2.1 Carbon nanodots production 50
2.2.2 Carbon nanodots properties 53
2.2.2.1 Optical absorption 53
2.2.2.2 Photoluminescence 54
2.2.2.3 Up-converted photoluminescence 55
2.2.3 Carbon nanodots applications 56
2.2.3.1 Photocatalysis 56
2.2.3.2 Nanosensing applications 58
2.2.3.3 Optoelectronic devices 58
2.2.3.4 Biomedical applications 59
2.3 Photoconversion 60

2.3.1 Photoconversion mechanism in fluorescent proteins 61
2.3.2 Photoconversion mechanism in organic dyes 65
2.3.2.1 Cyanine dyes 65
2.3.2.2 Xanthene dyes 68
2.3.2.3 Acridine dyes 73
2.3.2.4 Other dyes 75
2.4 Cell labeling techniques 76
2.4.1 Fluorescent proteins 76
2.4.2 Organic fluorophores 80

Chapter 3. Materials and Methods 84

3.1 Materials 84
3.2 Methods 85
3.2.1 Capsules synthesis with thermal treatment in PVA gel . . . 85
3.2.1.1 Layer-by-layer polymer application 85
3.2.1.2 Hydrothermal synthesis 86
3.2.1.3 Surface modification 86
3.2.2 Capsules synthesis without thermal treatment 87
3.2.2.1 Preparation of labeled PAH 87
3.2.2.2 Layer-by-layer polymer application 89
3.2.3 Cell studies 89
3.2.3.1 Mouse mesenchymal stem cells (mMSCs) 89
3.2.3.2 Human mesenchymal stromal cells (hMSC) 93
3.2.3.3 Myocytes 94

3.3 Instruments 95
3.3.1 Scanning electron microscopy 95
3.3.2 Focused ion beam scanning electron microscopy (FIB-SEM) 97
3.3.3 Fluorescence microscopy 99
3.3.4 Confocal laser scanning microscopy (CLSM) 101
3.3.4.1 Confocal microscope 101
3.3.4.2 CLSM studies of fluorescent polymer microcapsules 103
3.3.5 Zeta-sizer 105
3.3.6 Plate reader measurements 107
3.3.7 Mass spectrometery 108

Chapter 4. Thermal Treatment in PVA Gel to Facilitate Photoconvertible Capsule Synthesis and Capsules' Characterization 111

4.1 Introduction 111
4.2 High yield production of fluorescent capsules synthesis via PVA gel 113
4.3 Carbon nanodots influence on photoconvertible capsules 122
4.3.1 Capsules containing RhB with and without DS 123
4.3.2 Capsules containing no dye with and without DS 125
4.4 Encapsulation of fluorescent dyes 127
4.5 Fluorescence intensity of capsules containing selected dyes 131
4.6 Study of the photostability of the dyes in the capsules 133
4.7 Photoconversion on capsules with RhB, Rh6G, and PyB 134
4.8 Mass spectrometric study of RhB and Rh6G photoconversion mechanism 138

4.9 Capsules' surface modification 142

4.10 Conclusions 146

Chapter 5. Non-thermal Layer-by-layer Synthesis of Photoconvertible Capsules and their Characterization 148

5.1 Introduction 148

5.2 Non-thermal approach to photoconvertible capsule synthesis 149

5.3 Photoconversion of LbL capsules with Cy3.5 152

5.4 Photoconversion of LbL capsules with Cy5.5 155

5.5 Photoconversion of LbL capsules with Cy7 158

5.6 Photoconversion of LbL capsules with RITC 161

5.7 Photostability of capsules containing Cy3.5 and Cy5.5 163

5.8 Conclusions 165

Chapter 6. Photoconvertible Polymer Capsules For Cell Labeling and Tracking 167

6.1 Introduction 167

6.1.1 Selection of the optimal ratio of capsules per cell for effective and safe labeling of mMSCs and cell mobility 171

6.1.2 Tracking the migration of individual mMSCs labeled using photoconverted microcapsules in 2D и 3D EPNT-5 glioblastoma cells colony 175

6.1.3 Approbation of photoconvertible microcapsules for myoblasts (C2C12) and hMSCs labeling and tracking 180

6.1.3.1 hMSCs 181

6.1.3.2 Myoblasts (C2C12) 184

6.2 Conclusions 186

Chapter 7. General Conclusions and Future Work 190

7.1 General conclusions 190

7.2 Future work 193

Bibliography 194

List of Symbols, Abbreviations

AY – acridine yellow

AO – acridine orange

AF647 – Alexa Fluor 647

ADC – apparent diffusion coefficient

BSA – bovine serum albumin

BODIPY – boron dipyrromethenes

Cy3.5 – cyanine 3.5

Cy5.5 – cyanine 5.5

Cy7 – cyanine 7

CLSM – confocal laser scanning microscopy

CNDs – carbon nanodots

Con A – Concanavalin A

DNA – deoxyribonucleic acid

DI – deionized

DS – dextran sulfate

DAPI – 4'-6-Diamidino-2-phenylindole

DMEM – Dulbecco's modified Eagle's medium

DMSO – dimethyl sulfoxide

DOX – doxorubicin

DACT – dual-activatable cell tracker

EDTA – ethylenediaminetetraacetic acid

FP – fluorescent protein

FBS – fetal bovine serum

FIB-SEM – focused ion beam scanning electron microscopy

FITC – fluorescein isothiocyanate

FACS – fluorescence-activated cell sorting

GFP – green fluorescent protein

GOx – glucose oxidase

GQDs – graphene quantum dots

HA – hyaluronic acid

HRP – horseradish peroxidase

HRTEM – high-resolution transmission electron microscopy

HSPCs – hematopoietic stem/progenitor cells

hMSC – human mesenchymal stromal cells

imLEC – immortalized lymphatic endothelial cell

LbL – layer-by-layer

LAMP1 – lysosomal associated membrane protein

LED – light emitting diodes

LPD – laser power density

MS – mass spectrometry

MTT – tetrazolium salt, 3-(4,5-dimethylthiazol-2-yl)-2,5-diphenyl-2H-tetrazolium bromide

MNPs – magnetic nanoparticles

mMSC – mouse mesenchymal stem cells

NIR – near-infrared

NHS – N-hydroxysuccinimide

PAH – poly(allylamine hydrochloride)

PSS – poly(4-styrene sulfonate)

PAA – poly(acrylic acid)

PDADMAC – poly(diallyldimethylammonium chloride)

PVPON – poly(N-vinylpyrrolidone)

PArg – poly-L-arginine hydrochloride

PMAA – poly(methacrylic acid)

PPEI – poly(propionylethyleneimine-co-ethyleneimine)

PGA – poly(L-glutamic acid)

PLL – poly(L-lysine)

PBD – phosphate-buffered saline

PBFI – potassium-binding benzofuran isophthalate

PL – photoluminescence

PyB – pyronin B

QD – quantum dot

QCE – quantum confinement effect

RhB – rhodamine B

Rh6G – rhodamine 6G

RITC – rhodamine B isothiocyanate

ROI – region of interest

RI – refractive index

SEM – scanning electron microscope

SNARF-1 – seminaphtorhodafluor-1

SBFI – sodium-binding benzofuran isophthalate

TR – thiazine red

TRITC – tetramethylrhodamine

TDDFT – time-dependent density-function theory

TIRF – total internal reflection fluorescence

UV – ultraviolet

US – ultrasound

UCPL – up-converted photoluminescence

List of Figures

Figure 2.1 LbL multilayer deposition on a flat surface by dip-coating technique [28]. . . . 30
Figure 2.2 Chemical molecular formulas of polyelectrolytes PAH (left) and PSS (right) [31]. 31
Figure 2.3 (a-d) Alternating application of polyelectrolytes, (e) dissolution of the inner core, (f) final polymer microcapsule [30]. 32
Figure 2.4 ζ-potential change of particles depending on the polymer layer number. □ PSS/PDADMAC; ■ BSA/PDADMAC; ◯ PSS/PAH; △ DNA/PDADMAC [25]. 33
Figure 2.5 Chemical molecular formula of PDADMAC [35]. 33
Figure 2.6 Schematic representation of linear and non-linear dependence of the adsorbed polymer on the number of bilayers [28]. 35
Figure 2.7 Molecular formulas of (A) PAA [43], (B) PLL [44], and (C) PGA [45]. 35
Figure 2.8 Chemical molecular formulas of PMAA and PVPON [71]. 39
Figure 2.9 Chemical molecular formulas of (A) PArg [90] and (B) DS [91]. 44
Figure 2.10 Schematic illustration of various production options of CNDs [115]. 50
Figure 2.11 Commonly reported CND structures. Black dots – carbon atoms and red dots – nitrogen atoms [129]. 52
Figure 2.12 The absorption (ABS) and luminescence emission spectra of poly(propionyl ethyleneimine-co-ethyleneimine) (PPEI-EI) CNDs in water. The excitation wavelength is increased from 400 nm at the 20 nm step [114]. 53
Figure 2.13 Emission wavelength of different sizes GQDs with different sizes obtained through TDDFT [131]. 55
Figure 2.14 Proposed mechanism of photocatalytic activity of CNDs: (a) electron sink, (b) electron donor [142]. 57
Figure 2.15 Schematic illustration of differences between photoactivatable, photoconvertible, and photoswitchable FP [160]. 60
Figure 2.16 Proposed green-to-red photoconversion mechanism of photoconvertible FPs [163]. 62
Figure 2.17 Proposed important bond rotations in photoconversion of photoconvertible FP. The rotation angles are τ – chromophoric β-methylene bridge, and υ – His62 side chain [163]. 63
Figure 2.18 Cyan-to-green photoconversion of PS-CFP and PS-CFP2 proteins from (O) neutral form to (P) anionic form [167]. 64
Figure 2.19 Redding reaction [167]. 64
Figure 2.20 Mechanism of photoconversion from Cy5 to Cy3 upon red laser irradiation [178]. 66
Figure 2.21 Photoconversion from Cy5.5 to Cy3.5 [178]. 66
Figure 2.22 (a) Fluorescence signals recorded in the Cy7 channel and Cy5 channel over time. (b) Fluorescence imaging under irradiation intensity of 0.1 kW/cm^2 at corresponding time points [181]. 67
Figure 2.23 Proposed photooxidation pathway of RhB under visible light irradiation 68
Figure 2.24 (a) Absorption and (b) fluorescence spectra changes of RhB under irradiation with 405 nm LED [184]. 69

Figure 2.25 Proposed photooxidation pathway of RhB under visible light irradiation [185]. 70
Figure 2.26 Absorbance of Rh6G depending on the irradiation time [189]. 71
Figure 2.27 Chemical structures of Acridine Red, Pyronin Y, and Pyronin B [191]. 71
Figure 2.28 (a) 9-dithianyl-pyronin derivative (1) transformation upon irradiation to (2) and (3) compounds. (b) Absorption spectra measured in methanol of the compound (1) –red line, compound (2) – green line, (3) – blue line [193]. 72
Figure 2.29 (a) HPLC chromatogram of AO solution after 2 h of irradiation with visible light (UV detector). (b) Absorbance spectra of corresponding AO intermediates [199]. 74
Figure 2.30 Identification of the N-de-methylation intermediates of AO [199]. 74
Figure 2.31 Proposed scheme of AY photodegradation [200]. 75
Figure 2.32 Areas of FP application [206]. 77
Figure 2.33 (E) Rectangular cell labeling at the start of embryo culture. (F) Migration of photoconverted cells after 6 h. (G) Red channel. (H) Overlay of the red channel and bright field image. The scale bar is 200 μm [212]. 79
Figure 2.34 Scheme of *in vivo* photoconversion method to track the fate of an individual cell. (A) DiR-labeled cell. (B) Later, the same area was without photoconversion. (C) Photoconversion of the DiR-labeled cell, (D) cell proliferation and migration, and (E) cell differentiation [207]. 81

Figure 3.1 Scheme of RITC conjugation with PAH. 87
Figure 3.2 Scheme of cyanine 3.5 (or Cy5.5, or Cy7) NHS ester conjugation with PAH [226]. 88
Figure 3.3 Image of scanning electron microscope VEGA 3 LM [228]. 96
Figure 3.4 Image of FIB-SEM Tescan Solaris. 97
Figure 3.5 Common FIB-SEM scheme [230]. 98
Figure 3.6 Olympus IX73 inverted microscope. 99
Figure 3.7 Scheme of the light path of a fluorescent microscope [233]. 100
Figure 3.8 Image of CLSM Leica TCS SP8 X. 101
Figure 3.9 CLSM scheme [234]. 102
Figure 3.10 Gwyddion program interface when "Radial profiles" tool is used. 105
Figure 3.11 Image of zeta sizer Malvern Nano. 106
Figure 3.12 Image of plate reader Tecan Infinite 200 PRO. 107
Figure 3.13 Image of Q Exactive Hybrid Quadrupole-Orbitrap mass spectrometer. 109
Figure 3.14 General scheme of the mass spectrometer [237]. 110

Figure 4.1 SEM image of polymer microcapsules after thermal treatment in water (scale bar is 5 μm). 114
Figure 4.2 Scheme of the preparation of the thermally treated microcapsules in 10, 15, and 20 wt% PVA gel with RhB. 116
Figure 4.3 SEM images of capsules (a) before and after thermal treatment in (b) 10, (c) 15 and (d) 20 wt% PVA gel with corresponding histograms of diameters distribution (scale bar is 2 μm). 117

Figure 4.4 FIB-SEM images of capsules before and after cut with ion beam. Capsules prepared in 10 (a,d), 15 (b,e), and 20 (c,f) wt% PVA gel (scale bar is 2 μm). . 118
Figure 4.5 CLSM images of capsules prepared in (a) 10, (b) 15, and (c) 20 wt% PVA gel with RhB before and after photoconversion (scale bar is 5 μm). Λ-scans of capsules prepared in (d) 10, (e) 15, and (f) 20 wt% PVA gel with RhB before and after photoconversion. 120
Figure 4.6 Angularly averaged intensities of capsules (prepared in 10, 15, and 20 wt% PVA) in (a) red and (b) green channels before and after photoconversion. **P<0.001, *P<0.05 121
Figure 4.7 SEM images and corresponding histograms of diameters of capsules after thermal treatment in PVA gel (a) with RhB and DS applied on the capsule surface, (b) with Rh B and no DS, (c) without the dye and with applied DS, (d) without the dye and no DS (scale bar is 2 μm). 122
Figure 4.8 (a) CLSM images of capsules containing RhB without application of DS before and after photoconversion (scale bar is 5 μm). (b) Λ-scans of capsules with RhB with and without DS before and after photoconversion. 123
Figure 4.9 Box plot of capsule intensities before and after photoconversion (containing RhB with and without DS) in (a) red and (b) green channels. 124
Figure 4.10 CLSM images of capsules (containing no dye) (a) with DS and (b) without DS before and after 561 nm laser irradiation (scale bar is 5 μm). (c) Corresponding angular intensities of capsules before and after 561 nm laser irradiation. 126
Figure 4.11 Λ-scans of capsules (containing no dye) (a) with DS and (b) without DS before and after 561 nm laser irradiation. Green lines correspond to the excitation of λ-scan at 488 nm, violet line corresponds to the excitation of λ-scan at 405 nm. 126
Figure 4.12 Scheme of the preparation of the thermally treated microcapsules in PVA gel with the dye. 128
Figure 4.13 SEM images of polymer microcapsules before (a) and after thermal treatment in PVA gel with Rhodamine B (b), Rhodamine 6G (c), Pyronin B (d), Fluorescein (e), Acridine Yellow (f), Acridine Orange (g), and Thiazine Red (h) (scale bar is 2 μm). 128
Figure 4.14 Histograms of polymer microcapsule size distribution before (a) and after thermal treatment in PVA gel. Microcapsules are loaded with Rhodamine B (b), Rhodamine 6G (c), Pyronin B (d), Fluorescein (e), Acridine Yellow (f), Acridine Orange (g), and Thiazine Red (h). 129
Figure 4.15 Graph of the capsule diameters before and after thermal treatment with the dyes RhB, Rh6G, PyB, Fl, AY, AO, and TR with the corresponding CLSM images (scale bar is 2 μm). 129
Figure 4.16 Normalized absorption (a) and fluorescence (b) spectra of the dye solutions. . . 130

Figure 4.17 (a) Angularly averaged fluorescence intensities of the capsules with dyes RhB, Rh6G, and PyB (detection range 580–620/670 nm, red channel) and Fl, AY, AO, and TR (detection range 505–600 nm, green channel). λ-scans of capsules with (b) RhB, (c) Rh6G, and PyB (488 nm excitation). λ-scans of capsules with (d) Fl, AY, AO, and TR (405 nm excitation). Red and green rectangles correspond to the detection ranges 580–620/670 nm and 505–600 nm, respectively. 132
Figure 4.18 Normalized changes in the fluorescence intensity of the dyes before and after the bleaching test. 134
Figure 4.19 CLSM images of thermally treated microcapsules in PVA gel with RhB (a), Rh6G (b), and PyB (c) before and after photoconversion (scale bar is 5 μm). 135
Figure 4.20 Changes in the angularly averaged fluorescence intensity of the capsules before and after laser irradiation in the red and green channels of RhB (a,b), Rh6G (d,e), and PyB (h,i). Capsule emission spectra under 488 nm excitation before and after laser conversion for RhB (c), Rh6G (f), and PyB (j) (green and red rectangles correspond to the 505–540 and 580–620/670 nm detection ranges of the confocal microscope, respectively). 137
Figure 4.21 Mass spectrometry of RhB and Rh6G solutions (a,b), RhB and Rh6G solutions with DS after TT (c,d), and after UV irradiation (e,f). 139
Figure 4.22 Photooxidation pathways of (a) RhB [185] and (b) Rh6G [188]. Fragment ions present in the solutions after UV irradiation are marked with blue ovals. The location of the removed groups is marked with red ovals. 141
Figure 4.23 Normalized fluorescence spectra of the RhB (a) and Rh6G (b) dye solutions after thermal treatment with DS before and after UV irradiation for 10, 20, and 30 minutes. 142
Figure 4.24 Scheme of polymer microcapsules surface modification with PAH and PSS polymers. 143
Figure 4.25 Photoconversion of microcapsules using 561 nm laser depending on the duration of one-pixel irradiation. The laser exposure area is marked with a yellow square (size - 500 $\times$ 500 pixels (20 $\times$ 20 μm)). Excitation – 488 nm, emission: 505 – 540 nm (green channel), 505 – 540 nm (red channel). The scale bar is 2 μm. . 144
Figure 4.26 Changes in fluorescence intensity of capsules without (a) and with an outer layer of PSS (b) and PAH (c) depending on irradiation duration of one pixel in green and red channels. Corresponding λ-scans of capsules (d-f) before and after one-pixel laser irradiation for 0.4 ms. 145

Figure 5.1 Fluorescence intensities of the (a) PAH-Cy3.5, (b) PAH-Cy5.5, and (c) PAH-Cy7 aqueous solutions before and after thermal treatment 150
Figure 5.2 SEM images and histograms of the size distribution of LbL polymer microcapsules with RITC, Cy3.5, Cy5.5, and Cy7. The scale bar is 2 μm. 151
Figure 5.3 Normalized absorbance and fluorescence spectra of Cy3.5 (a) and PAH-Cy3.5 (b). 152

Figure 5.4 (a) CLSM images of microcapsules with encapsulated Cy3.5 before and after photoconversion depending on the duration of one pixel irradiation at 193, 322, and 451 kW/cm^2 LPD. The scale bar is 5 μm. 153
Figure 5.5 λ-scans of capsules with Cy3.5 before and after photoconversion depending on the duration of one pixel irradiation at (b) 193, (c) 322, and (d) 451 kW/cm^2 laser power density. Corresponding changes in intensity over time under irradiation at (d) 193, (e) 322, and (f) 451 kW/cm^2 LPD. 154
Figure 5.6 Normalized absorbance and fluorescence spectra of Cy5.5 (a) and PAH-Cy5.5 (b). 155
Figure 5.7 CLSM images of capsules with Cy5.5 before and after photoconversion depending on the duration of one pixel irradiation at 180, 451, and 721 kW/cm^2 LPD. Scale bar is 5 μm 156
Figure 5.8 λ-scans of capsules with Cy5.5 before and after photoconversion depending on the duration of one pixel irradiation at (b) 180, (c) 451, and (d) 721 kW/cm^2 laser power density. Corresponding changes in intensity over time under irradiation at (d) 180, (e) 451, and (f) 721 kW/cm^2 laser power density. 157
Figure 5.9 Normalized absorbance and fluorescence spectra of Cy7 (a) and PAH-Cy7 (b). 159
Figure 5.10 (a) CLSM images of capsules with Cy7 before and after photoconversion depending on the duration of one pixel irradiation at LPD of 0.7, 1.8, and 4.5 MW/cm^2. The scale bar is 5 μm. (b) Changes in the capsule's fluorescence intensity depending on the duration of one pixel irradiation. Each irradiation time point corresponds to its CLSM image and LPD of 0.7, 1.8, and 4.5 MW/cm^2 159
Figure 5.11 Normalized absorbance and fluorescence spectra of RITC (a) and PAH-RITC (b). 161
Figure 5.12 CLSM images of capsules with PAH-RITC before and after photoconversion depending on the duration of one pixel irradiation at 193, 322, and 451 kW/cm^2 LPD. The scale bar is 5 μm. 162
Figure 5.13 λ-scans of capsules with RITC before and after photoconversion depending on the duration of one pixel irradiation at (b) 193, (c) 322, and (d) 451 kW/cm^2 laser power density. Corresponding changes in intensity over time under irradiation at (d) 193, (e) 322, and (f) 451 kW/cm^2 laser power density. 163
Figure 5.14 Normalized changes in the fluorescence intensity of the Cy3.5 and Cy5.5 dyes before and after the bleaching test. *P $<$ 0.05 164

Figure 6.1 (a) Dependence of the metabolic activity of mMSCs on the number of added microcapsules with various surface modifications. ***P $<$ 0.001. (b) Dependence of the percentage of cells in the population that internalized the microcapsules 24 h after incubation with different concentrations. (c) The influence of the amount of microcapsules on mMSCs cell proliferation at different initial cell densities 24 h after incubation. ***P $<$ 0.001. (d) Fluorescence images of mMSCs (green) 24 h after cultivation with 25 capsules per cell (microcapsules are yellow). The scale bar is 200 μm. 172

Figure 6.2 (a) Fluorescence images of the wound closure for mMSCs (green) at 0, 12, and 24 h after cultivation with different concentrations of photoconvertible microcapsules. The scale bar is 500 μm. (b) Graph of wound closure over time for mMSCs. *P < 0.05. 175

Figure 6.3 Migration of mMSCs (green) into a population of EPNT-5 glioblastoma cells (yellow) at 0, 24, 48, and 72 h. Cell 1 and Cell 2 were additionally labeled with photoconverted (green) PAH-modified microcapsules. Daughter cells shared converted capsules during doubling. Non-converted capsules are red. The white scale bar is 500 μm, and yellow is 50 μm. 177

Figure 6.4 Fluorescence images of mMSCs (green) and the EPNT-5 glioblastoma cell spheroid (yellow) 24 h after placing a mixed cell suspension into the wells of low-adhesion 96-well floater plates SDL3D. Non-converted capsules – red. 179

Figure 6.5 (a) Migration of mMSCs (green) in EPNT-5 glioblastoma cells spheroid (yellow) at 0, 24, and 48 h. Photoconverted capsules are green, and non-converted capsules are red. (b) 3D reconstruction of the EPNT-5 glioblastoma cell spheroid with labeled mMSCs at 0 and 48 h after photoconversion. Scale bar – 20 µm. The scale bar is 20 μm. 180

Figure 6.6 CLSM images of hMSCs with microcapsules at 0 (a) and 7 (b) days after labeling (hMSCs – yellow (Cy7), non-photoconverted microcapsules – blue, photoconverted – red). Green arrows indicate the photoconverted microcapsules. The scale bar is 100 μm. (c) Tracking diagram of six cells over 4 days. The dots circled in black indicate day 0. The remaining dots show the position of the nucleus of the labeled cell every 24 h. The side of each square is 500 μm. Tracks of individual cell movement are marked with different colors. (d) Image of one of the marked cells 1 day after the tracking commenced. The scale bar is 50 μm. 183

Figure 6.7 (a) Fluorescence images of C2C12 cells with internalized capsules and RAW 264.7 cells at 0 h (RAW 264.7 cells are stained with DiD (yellow)). (b-e) Fluorescence images showing the changes in the borders of the cells after 24, 48, 72, and 96 h (the area with RAW 264.7 is green, and area with C2C12 is violet). (f) Tracking diagram of two labeled cells over four days. Day 0 is marked with a circle. (g-h) Fluorescence images of two cells before (blue) and after (red) photoconversion of the capsules. 187

List of Tables

Table 3.1 Parameters for fluorescence spectra detection of the dyes. 108

Table 4.1 Interpretation of the removed groups of fragment ions of Rhodamine B and Rhodamine 6G after thermal treatment and UV irradiation. 140

Table 4.2 Zeta potential of polymer microcapsules. 143

Chapter 1. Introduction

1.1 Background

A wide variety of materials and approaches are available for manipulating cells and influencing their migration, proliferation, and differentiation. For example, scaffolds for tissue engineering can provide guidance and physical support for cell growth and tissue formation [1]. Substrates with varying stiffness are used to study cell differentiation and migration depending on surface stiffness gradients [2]. In addition, optical tweezers are used to trap and move particles, including cells, at the microscopic scale using focused laser beams [3]. Acoustic forces can be used to position cells or particles by creating acoustic traps or standing waves [4]. Magnetic nanoparticles can be internalized by cells and an external magnetic field can be applied to remotely move and position cells [5]. Moreover, fluorescent proteins (FPs) and lipophilic membrane dyes are widely used for cell labeling and tracking [6, 7].

Cell labeling usually involves staining cells with fluorescent dyes or attaching certain markers, such as nanoparticles or genetic tags, to make them visible. Cell tracking is the process of monitoring the behaviour, migration, and fate of labeled cells over time [8, 9]. Both these methods are especially important in the fields of neurobiology [10], immunology [11], transplantology [6], and carcinogenesis [7]. Cells can be tracked in monolayer cultures, tissues, organs, and whole animals to provide information about cellular dynamics and disease mechanisms for therapeutic applications and drug development.

The optical marking of cells has emerged as a powerful tool for cell tracking, offering the potential to label and monitor cells with high precision. This approach primarily relies on the use of genetically modified cells expressing FPs, such as Dreiklang [12], Dronpa [13], IrisFPs [14], and others. The synthesis of FPs in cells is achieved via transfection, which allows for the study of various biological processes *in situ* [15]. Nevertheless, FPs have certain disadvantages. They were reported to be prone to aggregation and formation of tetramers [16] and dimeric complexes [17]. Such aggregates exhibit cytotoxicity because they impair cellular processes by interacting with the cell membranes [18,19]. Moreover, the behaviour and properties of cells may change after genetic modification, which limits the application options of FPs [20].

Another conventional approach to cell labeling involves the use of lipophilic membrane dyes. These dyes spontaneously noncovalently intercalate into the bilayers owing to aliphatic pending chains and, through lateral diffusion, stain the outer cellular membrane [21]. Lipophilic membrane dyes typically exhibit high photostability and brightness. In addition, the staining procedure is quite simple compared to that using FPs. Nevertheless, long-term tracking is limited when using membrane dyes, because they often experience leakage from cells [22]. This leads to staining of nearby non-labeled cells [23], potentially distorting the research results. Moreover, a decrease in the intensity signal is common because of cell division, which leads to dye dilution. In addition, to ensure rapid staining, large concentrations of dye should be used, complicating the separation proto-

cols [21]. These challenges limit the applicability of traditional optical labeling with lipophilic membrane dyes.

A combination of the fluorescent dye and microcapsule can provide a perspective alternative for the discussed cell tracking approaches [24]. Polymer microcapsules are produced using the layer-by-layer (LbL) technique from biocompatible polymers [25]. Oppositely charged polyelectrolytes are applied to a spherical template via electrostatic interactions. The core is then dissolved to obtain a hollow microcapsule. Such capsules have low cytotoxicity, can be easily internalized by diverse cell types, and exhibit prolonged retention within cells [25,26]. These properties make them a desirable option for cell tracking. In the reported study [24], such photoconvertible capsules were produced by hydrothermal treatment in dye aqueous solution. Capsules functioned as microreactors that combined the fluorescent dye rhodamine B (RhB) and carbon nanodots (CNDs) as photocatalyst. Dextran sulfate (DS) was applied to the capsule shell as a source of CNDs. Upon subjecting the polymer capsules to laser radiation, a photocatalytic reaction occurred within the capsule, resulting in alterations to the emission spectra of RhB or photoconversion. Such capsules can be used for cell labeling and tracking by utilizing the described photoconversion phenomenon.

Nevertheless, several challenges persist with this approach. One such challenge is the need to explore additional fluorescent dyes that emit in different spectral ranges, thereby expanding the possibility of cell tracking. The use of distinct colors for convertible capsules is crucial for tracking multiple cell populations within the

same region and for investigating their behaviour and interactions. Furthermore, it is essential to select dyes with non-overlapping spectral ranges for capsules and other dye-based cell staining techniques. Another unresolved issue pertains to the significant loss of capsules during hydrothermal treatment. This occurs primarily because of the melting of the capsules with each other when the synthesis is performed in a dye-aqueous solution. Subsequent filtration to remove fused capsules further exacerbates capsule loss. These issues should be addressed to provide a more efficient labeling technique using polymer microcapsules.

1.2 Aim and Objectives

Aim

Cell tracking plays a crucial role in understanding the behaviour, migration, and fate of individual cells within large populations. Current labeling techniques have certain limitations, as discussed above. The aim of this thesis was to develop material for labeling and tracking cells that is photostable, provides bright fluorescence, and has low cytotoxicity and low effect on cell mobility. This was achieved by utilizing polymer microcapsules as a platform for fluorescent photoconvertible dyes.

Objectives

1. Increase the photoconvertible capsule production yield using polyvinyl alcohol gel as a medium for capsule hydrothermal treatment. Analyze the influence of the additional dextran sulfate in the capsule shell on the capsule fluorescence inten-

sity and morphology. Perform encapsulation of various dyes using hydrothermal treatment. The dyes unclude rhodamine B, rhodamine 6G, pyronin B, fluorescein, acridine yellow, acridine orange, and thiazine red. Evaluate capsule's brightness of fluorescence, photostability, and photoconversion ability with confocal laser scanning microscopy.

2. Develop a non-hydrothermal approach for photoconvertible capsule production using dye-labeled polyallylamine hydrochloride. The dyes include Rhodamine B isothiocyanate, Cyanine 3.5, Cyanine 5.5, and Cyanine 7.

3. Analyze cytotoxicity and uptake of capsules prepared with the hydrothermal approach. Evaluate how polymer microcapsules affect cell mobility. Perform cell labeling and tracking experiments.

Chapter 2. Review of the Literature

2.1 Polymer microcapsules synthesis

Polymer microcapsules are made by layer-by-layer assembly of polymers on the template with subsequent template dissolution to obtain hollow capsules. This review focuses on the synthesis, properties, and applications of polymer microcapsules.

2.1.1 Multilayer assembly of polymers for film formation

The layer-by-layer (LbL) technique for film production was first reported in 1966 [27]. Briefly, LbL assembly of polyelectrolytes on a flat surface was achieved using the dip-coating technique (Figure 2.1) [28]. Polymers are sequentially applied to form films due to electrostatic interactions. There is a washing step between each absorption cycle to remove non-adsorbed polymers and to avoid cross-contamination of the solutions [26, 29].

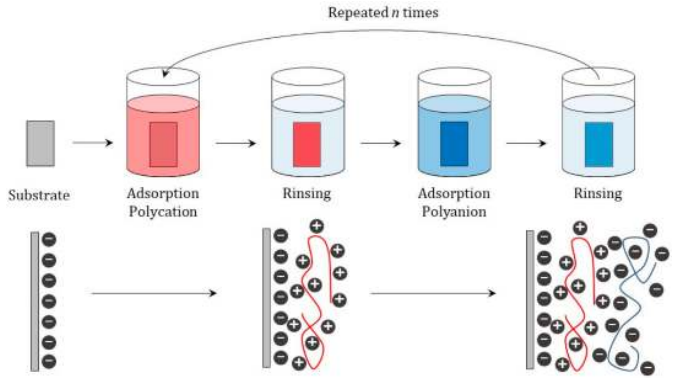

Figure 2.1: LbL multilayer deposition on a flat surface by dip-coating technique [28].

2.1.2 Multilayer assembly of polymers on spherical templates for capsule formation

In 1998, the LbL method for capsule production using micron-sized spherical templates instead of flat surfaces was reported [25, 30]. The synthesis scheme is shown in Figure 2.3 [30]. Here, melamine-formaldehyde particles were used as a template because they decompose at a pH below 1.6. Poly(sodium styrenesulfonate) (PSS) and poly(allylamine hydrochloride) (PAH) were adsorbed on the surface of particles in the layers. The chemical formulas of these polymers are presented in Figure 2.2 [31].

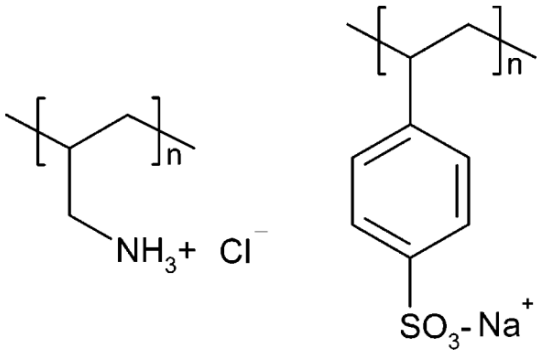

Figure 2.2: Chemical molecular formulas of polyelectrolytes PAH (left) and PSS (right) [31].

After each layer, excess polyelectrolyte was removed via repeated centrifugation and washing. Once sufficient layers were obtained, the inner core was dissolved in HCl solution.

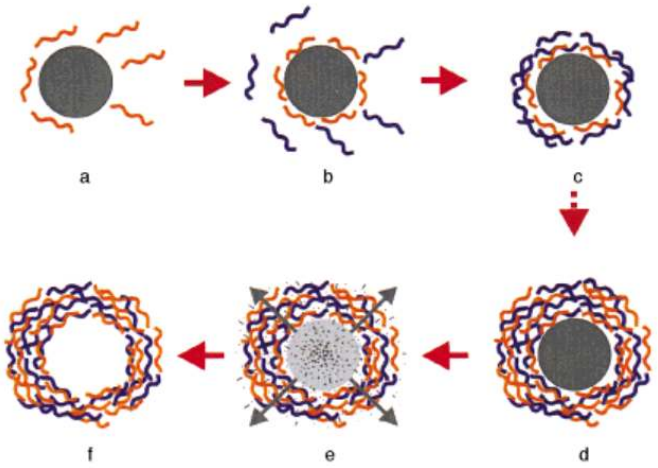

Figure 2.3: (a-d) Alternating application of polyelectrolytes, (e) dissolution of the inner core, (f) final polymer microcapsule [30].

2.1.2.1 Charge overcompensation and inversion

As a simple explanation, this LbL assembly occurs because of electrostatic interactions between oppositely charged polyelectrolytes [32]. Nevertheless, this process is complex and depends on many parameters, including the presence of salt in the solution, pH, ionic strength, and temperature. In addition, both electrostatic and entropic forces contribute to LbL assembly and should be considered [33,34].

Moreover, it was demonstrated that the consecutive adsorption of polyelectrolytes occurs because of charge inversion. This means that after neutralization of the surface charge, adsorption does not stop, and an excessive charge is obtained [25]. Figure 2.4 shows the dependence of ζ-potential of the polystyrene sulfate latex particles after each layer of polyelectrolyte deposition from 0.5 M NaCl.

The polyelectrolyte pairs used were PSS/PDADMAC, DNA/PDADMAC, BSA/PDADMAC,

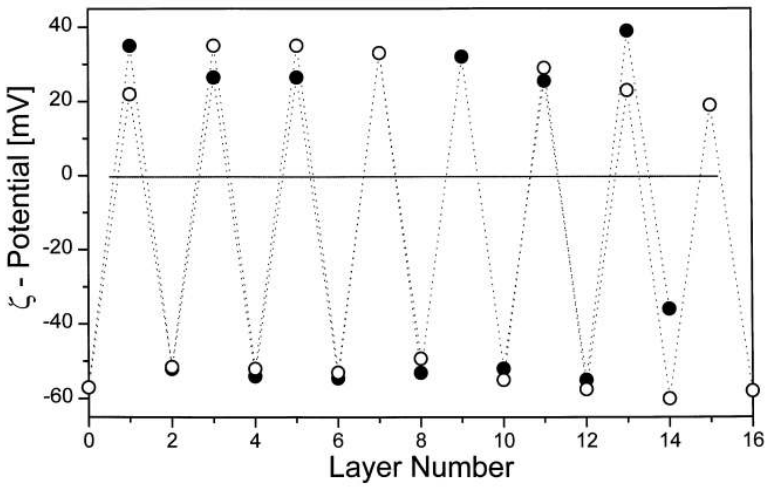

Figure 2.4: ζ-potential change of particles depending on the polymer layer number. □ PSS/PDADMAC; ■ BSA/PDADMAC; ○ PSS/PAH; △ DNA/PDADMAC [25].

and PSS/PAH. PDADMAC is poly(diallyldimethyl ammonium chloride (Figure 2.5 [35]), BSA is bovine serum albumin consisting of 583 amino acids, and DNA is deoxyribonucleic acid. The graph shows the oscillation of ζ-potential between -60 mV and +40 mV after the adsorption of polyanions and polycations, respectively.

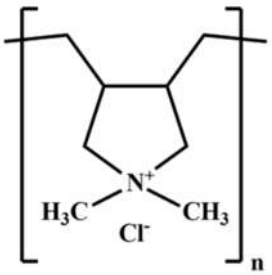

Figure 2.5: Chemical molecular formula of PDADMAC [35].

This charge overcompensation depends on several factors. This is a balance between the free energy gain from the ion pairing of polyelectrolyte chains and the entropy reduction due to the loss of degrees of freedom of the polymer [36].

The addition of salts also promotes overcompensation. This occurs because of the swelling of the polyelectrolyte in the layer, which leads to a decrease in repulsion between segments owing to the presence of more ions and water. This leads to an increase in charge overcompensation by the polymer from the solution. It is also worth mentioning that salt can be easily removed from the system, in contrast to the already adsorbed polyelectrolyte. Because of this important property, LbL assembly is possible, since otherwise polyelectrolytes can be easily stripped away by oppositely charged polymer solutions [37, 38]. Radiolabeling of all parts of the polyelectrolyte multilayers (polymers and counterions) demonstrated that no salt ions remained in the multilayer. The charge in the layer is balanced by oppositely charged polymer chains. In addition, it is assumed that overcompensation is at its peak value on the surface of the film and decays toward its depth site.

2.1.2.2 Polyelectrolyte multilayer growth

The consecutive adsorption of polyelectrolytes on the template led to an increase in the film thickness. The amount of adsorbed polymer is assumed to depend on the number of bilayers in two ways: linear and nonlinear (Figure 2.6) [28]. The bilayer is represented as A/B and the multilayer is referred to as $(A/B)_n$, where n is the number of bilayers.

Linear growth implies that the adsorbed amount remains constant for each layer. With each layer, the thickness of the film increased by a few nanometers, and this increase depended on the characteristic lengths of the polyanion and polycation. Some examples of polyelectrolytes that demonstrate linear growth are

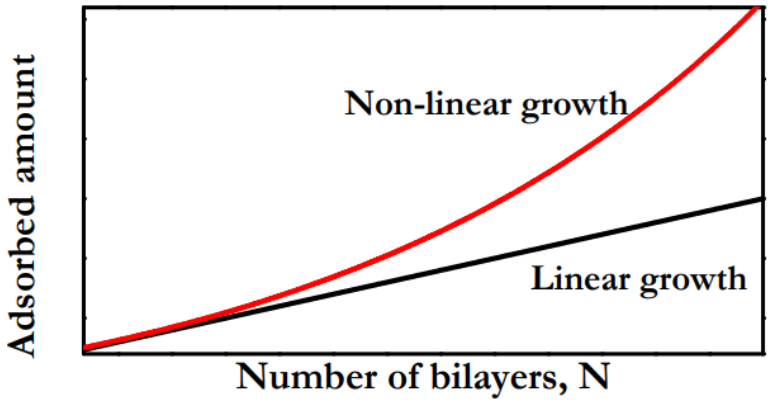

Figure 2.6: Schematic representation of linear and non-linear dependence of the adsorbed polymer on the number of bilayers [28].

$(PAH/PSS)_n$, $(PDADMAC/PSS)_n$ [39] (if the solution has low ionic strength), and $(PAH/PAA)_n$ (PAA is poly(acrylic acid) [40]. At the same time, nonlinear growth means that the adsorbed amount is different for each bilayer and does not depend only on the characteristic wavelengths of the polymers. Earlier mentioned PDADMAC and PSS exhibit nonlinear growth when assembled from a solution with high ionic strength [37]. Other examples of such polymers include $(PLL/HA)_n$ (poly(L-lysine)/hyaluronic acid) [41] and $(PGA/PLL)_n$ (PGA is poly(L-glutamic acid)) [42]. The chemical formulas of PAA, PLL, and PGA are shown in Figure 2.7.

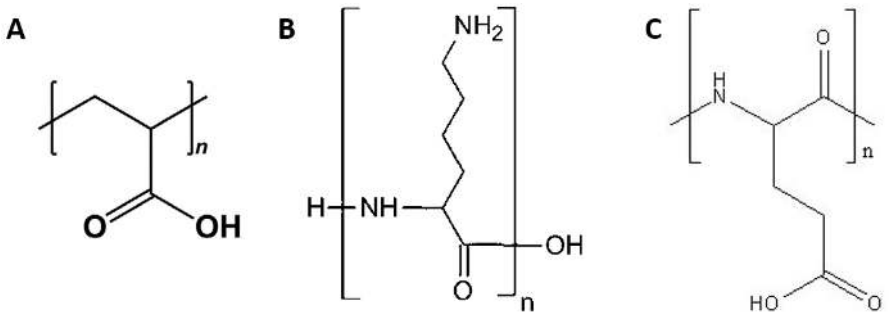

Figure 2.7: Molecular formulas of (A) PAA [43], (B) PLL [44], and (C) PGA [45].

The physical principles behind the differences between linear and nonlinear growth still raise questions. Nevertheless, they are commonly associated with the diffusion of adsorbing polymers into the multilayers [46]. Considering this and using the mean-field approach, the mechanism of nonlinear growth was theoretically explained in detail [47]. The layer thickness depends on the number of deposition steps in the geometrical progression.

$$L_{k+1} \simeq K L_k, \tag{2.1}$$

where parameter K depends on the ionic strength. A higher ionic strength leads to faster layer thickness growth. A lower polymer charge density also led to an increase in the parameter K.

To conclude the part of literature review on the synthesis of polymer microcapsules, this is a complicated yet beautifully simple process. Charge overcompensation of polymers results in the growth of polyelectrolyte layers, creating thin and soft shells for the delivery of various materials. The methods of cargo loading into capsules are discussed in the next section.

2.1.3 Encapsulation in Layer-by-Layer Capsules

A significant characteristic of polymer microcapsules is the possibility of loading them with various cargo. This approach reduces cargo cytotoxicity against cells, while preserving it from the external environment. Two strategies are commonly used to load the target substance into the microcapsules: pre-loading and post-loading.

2.1.3.1 Pre-loading

In the pre-loading approach, the cargo is encapsulated during the first stages of polymer capsule preparation. Usually, it is done by utilization of a porous core as a template for the subsequent layering of polymers. Many types of templates can be used in this case, including silica [48], melamine-formaldehyde particles [49], polystyrene [50], PLA particles [51], and others [52]. One of the most popular templates is calcium carbonate cores (vaterite form) [53]. The diameter of the particles ranges from 300 nm to 5 μm [54, 55]. Important features of vaterite include biocompatibility [56] and low cytotoxicity [57]. The particles also have a high loading capacity owing to their porous structure, and can be dissolved under relatively mild acidic conditions [58].

There are several approaches for loading cargo in vaterite cores, including co-precipitation, adsorption, and freezing. During coprecipitation, $CaCO_3$ particles are formed by the addition of salts directly to the cargo solution [59]. It is worth mentioning that drugs may influence the size and shape of the formed particles [55]. Moreover, some drugs may lose their activity owing to pH changes and the high ionic strength of the solution during vaterite synthesis [60]. Nevertheless, for water-soluble molecules, coprecipitation usually provides higher loading results in comparison to adsorption [60,61].

In the adsorption method, preliminarily prepared vaterite cores are placed in the cargo solution for loading [62]. This approach eliminates the side effects of coprecipitation, as previously mentioned. Moreover, it allows the encapsulation of

hydrophobic molecules dispersed in organic solvents because vaterite is stable in non-polar media [63, 64].

The loading in vaterite using the freezing method was introduced by German *et. al.* [65, 66]. $CaCO_3$ particles were added to the magnetic NPs suspension and frozen for 2 h. Then, they were thawed and a fresh solution of NPs was added. The thawing-freezing cycle was repeated several times. This approach allowed a threefold increase in the load of nanoparticles in the templates compared to the methods mentioned previously. Proteins were also loaded using this methodology, which resulted in four times more encapsulation than with conventional methods.

Therefore, the choice of pre-loading technique depends on the type of cargo, solvent, and need for low or high encapsulation values.

2.1.3.2 Post-loading

In the post-loading approach, the desired compound is loaded during the final stages of capsule synthesis. This can be achieved by changing capsule environment parameters, such as pH [67], ionic strength [68], and temperature [69]. These effects change the permeability of the shell, allowing the substance to enter the capsule interior. The capsules are then transferred to the primary condition, entrapping the cargo inside [62]. It is also crucial that the exposure of capsules to these conditions does not lead to irreversible changes in their structure. Otherwise, cargo leakage would occur [70].

The possibility of loading cargo with a wide range of molecular weights less than 1000 g/mol by changing the pH has been reported [71]. The capsules were made

from poly(methacrylic acid) (PMAA) and poly(N-vinylpyrrolidone) (PVPON), with additional chemical cross-linking of PMAA. The chemical formulas of PMAA and PVPON are shown in Figure 2.8 [71]. Alexa Fluor and DOX were chosen as the model cargo. Encapsulation of the material was performed at 7.5 pH when the capsule shell remained permeable. The capsules were then sealed with dextran at pH 5.5. Interestingly, positively charged Alexa Fluor was trapped in the capsule cavity, whereas negatively charged DOX accumulated in the capsule shell.

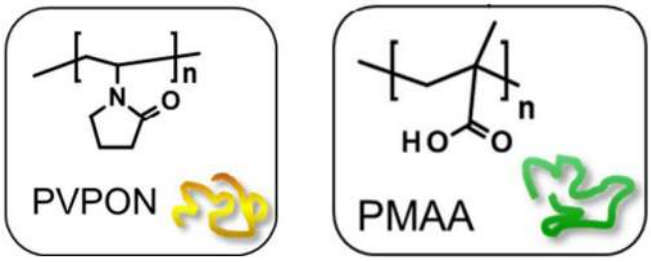

Figure 2.8: Chemical molecular formulas of PMAA and PVPON [71].

Another post-loading strategy combined both incubation with cargo and heat treatments [72]. Capsules were made from PArg and DS and incubated with the photodynamic therapy drug cholosens. Subsequently, the capsules were heated and demonstrated a slower release rate than the non-treated sample. Therefore, heat exposure ensured the entrapment of the drug by tightening the polymer shell.

An example of loading the cargo by thermal treatment was reported by Ermakov et al. [73]. The authors prepared two types of capsules: $(PDADMAC/PSS)_4$ and $(PArg/DS)_4$. RhB was used as a compound for loading. The results differed depending on capsule composition. For $(PDADMAC/PSS)_4$, heat increased the RhB loading for capsules with concentrations less than 3×10^9 unit/mL and

demonstrated a reversed effect at higher concentrations. At the same time, for $(PArg/DS)_4$, heat led to a decrease in the loading for all concentrations. The dependence of the loading efficacy on the capsule concentration might indicate that interactions between the capsule polymeric network and the compound play a role in this process, affecting both the pervasion and distribution of cargo. Part of the low-molecular-weight compound binds to the capsule shell, compensating for the charge, and part of the cargo diffuses through the polymeric matrix to the inner cavity. The heat treatment compensated for the inner charge and extrusion of the cargo associated with the capsule shell. This means that the higher the part of the substance associated with the capsule wall, the higher is the impact of heat on reducing the loading, which might be the case for $(PARG/DS)_4$ capsules.

Such a variety of loading methods provides great opportunities for material encapsulation depending on the researcher's goal, capsule composition, and actual cargo.

2.1.4 Properties of microcapsules

In this section, the properties of microcapsules are discussed from a cellular point of view. It is crucial to understand the mechanism of capsule internalization and the various impacts of capsules on cells to provide effective labeling and tracking.

2.1.4.1 Cellular internalization of capsules

Kastl et al. performed a detailed study of the mechanism of internalization of LbL polymer capsules by cells [74]. The authors used several methods: characterization of morphology, pharmacological and chemical inhibition of capsule internalization, and colocalization of capsules and organelles. This study revealed that multiple internalization pathways occur during uptake. First, electrostatic forces initiate the interaction between the cell and capsule. The phagocytic cup is then formed by the reorganization of actin and filopodia formation. In addition, for proper internalization, capsules require cholesterol-rich lipid domains to colocalize with lipid rafts. Since the capsule diameter is larger than that of lipid rafts, the environment of internalizing vesicles is acidic, and active dynamin is independent, lipid-raft-mediated macropinocytosis is supposed to take place at this early internalization stage. In addition to local cell surface polymerization of actin and vesicle acidification, co-localization with lysosomal-associated membrane protein 1 (LAMP1) is typical for phagolysosome maturation. Therefore, the phagocytic mechanism is activated to transport capsules to heterophagolysosomes. Many capsule parameters can affect the internalization process, such as the size, shape, stiffness, and surface charge, which will be discussed further.

Size

The size of the capsules is determined based on the size of the templates used for their production. The optimal diameter of a capsule for internalization depends on the cell line, application goal, and surface chemistry. Polymer capsules of 300

nm do 5 μm were reported to be internalized by cells [75–77].

For example, 300- and 500-nm polymer capsules were loaded with doxorubicin (DOX) and functionalized with the tumor-targeting DR5-B ligand to be internalized by the HCT 116 cell line (human colon cancer) [75]. The uptake was precisely observed for 7 h to conclude that smaller capsules were internalized faster than larger ones, reaching the same level at approximately 7 h.

In the study by Verkhovskii et al. Raw 264.7 cells were used to evaluate the uptake efficiency of magnetite-loaded capsules with sizes of 1 and 2.7 μm [76]. When 10 capsules per cell were added and incubated for 6 h, 93% of the cells captured 2.7 μm capsules and 79% of the cells captured 1 μm capsules. This could be explained by the lower probability of cell interaction with smaller capsules, as the cell confluence was 60% in this experiment. Therefore, increasing the confluence of cells may increase the uptake efficiency of capsules, regardless of their size.

Shape

The shape of the particles is known to influence the rate and degree of internalization by cells [78]. For example, cubic-shaped capsules exhibit higher uptake levels in breast cancer cells than spherical capsules [79]. This might be due to the greater adhesion gain for the cubic particle-cell interaction that compensates the energy for cell membrane deformation, leading to higher uptake rates.

Simultaneously, rod-shaped capsules internalized slower than spherical capsules [80]. This is attributed to the higher aspect ratio of the rod capsules, which reduces

the uptake values due to the larger average radius of the capsules.

Stiffness

Capsule stiffness also plays a role in the internalization. Polymer microcapsules have been reported to undergo deformation during phagocytosis [81]. The deformation of capsules was studied to reveal several regimes, such as a linearly elastic regime, plastic regime, and strain-hardening regime [82]. The change in capsule shape can be suppressed by prior thermal treatment to induce capsule shrinking or by the introduction of nanoparticles into the polymer shell [83]. Moreover, capsule stiffness depends on the number of layers deposited for shell formation. For example, soft capsules with fewer layers were internalized faster than hard capsules with more layers [84].

Surface charge

The surface charge of polymer capsules depends on the last layer of applied polymer. Cells are known to typically have a negative membrane charge; therefore, positively charged capsules attach to cells faster and stronger than negatively charged [85].

2.1.4.2 Capsule cytotoxicity

Evaluation of the cytotoxicity of polymer capsules is crucial for successful *in vitro* and *in vivo* experiments. Usually, a colorimetric assay (MTT assay) is used to evaluate cell viability. MTT assay is based on the reduction of tetrazolium salt (3-(4,5-dimethylthiazol-2-yl)-2,5-diphenyltetrazolium bromide) by metabolically active cells to formazan crystals. Purple formazan crystals are then diluted

with dimethyl sulfoxide (DMSO) and the absorption of the solution is analyzed. The cytotoxic effect of a material usually increases with the dose and exposure duration [86].

Typically, cytotoxic studies of polymer microcapsules have shown low toxicity. For example, for capsules made with polyarginine/dextran sulfate (PArg/DS) (chemical formulas are shown in Figure 2.9), the bone marrow-derived dendritic cell viability was reduced to 90% when 10 capsules per cell were added and to 80% at 30 capsules per cell concentration [87]. In the latter case, viability was impaired because capsules were added at the amounts that they sedimented on top of the cells, impairing the nutrient supply. A similar insignificant cytotoxicity at high capsule doses was reported for PSS/PAH capsules when added to fibroblast cells [88]. As for capsules based on BSA/TA, the viability of the RAW 264.7, macrophage cell line was high as well: approximately 90% when 50 capsules per cell were added [89]. Therefore, the cytotoxicity of the LbL polymer microcapsules is quite low.

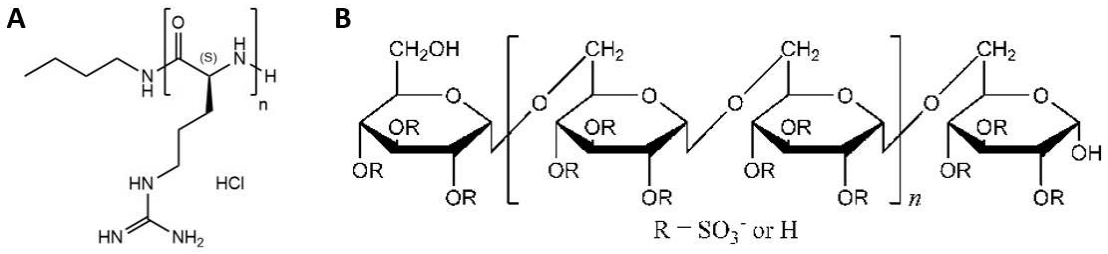

Figure 2.9: Chemical molecular formulas of (A) PArg [90] and (B) DS [91].

In conclusion, polymer microcapsules are perfect candidates for various cell applications. Capsules have low cytotoxicity and a soft shell composition, which

compliments their effective uptake. Mentioned features open possibilities for the delivery of various cargoes to cells, such as nanoparticles, dyes, and drugs.

2.1.5 Biomedical applications of polymer microcapsules

In the next section, various biological applications of microcapsules are discussed to create a vision for capsule application possibilities.

2.1.5.1 Drug delivery

Polymer microcapsules are promising candidates for drug delivery applications. Many studies have focused on anticancer therapy [75, 92, 93]. Recently, a study developed capsules containing the highly toxic drug DOX [93]. Quantum dots were used as fluorescent labels. The capsules demonstrated prolonged release under conditions similar to those in the living body. Other authors have utilized DOX as an anti-cancer treatment [75]. Simultaneously, to reduce the cytotoxic effect of the drug on the organism, capsules were loaded with a subtoxic amount of DOX and modified with a drug-specific DR5-B ligand to promote targeted drug delivery.

Polymer capsules also could be used for the release of antibiotics. In one study, silica particles were loaded with gentamicin and covered with polyelectrolyte layers [94]. This combination demonstrated a higher drug loading than silica particles without additional layers. Such capsules also provided sustained release of the drug over two weeks. In addition, the release was pH-responsive and was triggered by acidic conditions. In another approach, antibiotic release was triggered

by the presence of bacteria [95]. The capsule shell was composed of poly-L-lysine and hyaluronic acid and was loaded with vancomycin. The capsule wall was intact when exposed to protease due to the crosslinking of its components. At the same time, it started to degrade when exposed to Lys-X-specific protease IV from *Pseudomonas aeruginosa*.

2.1.5.2 Cell manipulation

A magnetic field can be used for the remote manipulation of cells [96]. For this purpose, capsules can be modified with magnetic nanoparticles (MNPs). Once cells internalize such capsules, they become sensitive to an external magnetic field and can be moved to the desired location. For example, capsules composed of PAH/PSS polyelectrolytes and magnetite could be effectively internalized by human mesenchymal stromal cells (hMSCs) [97]. These cells then could be sorted via a magnetic sorting system. Moreover, capsules did not affect the ability of MSCs to differentiate, which is important for stem cell therapy applications [98].

The concept of cell magnetic manipulation can also be paired with encapsulated cargo delivery. In work by Muslimov et al. [99], magnetic capsules were synthesized with PArg and DS and loaded with immobilized genetic material (mRNA). The capsules were introduced into hMCS and did not affect the cell proliferation capacity. Using magnetic sorting, transfection efficiency was increased, and an almost pure genetically modified cell line was obtained.

Not only individual single cells can be manipulated by using magnetic capsules. It was demonstrated that after cells internalized capsules packed with magnetite,

they could form spheroids, which are the building blocks of the cells [100]. Such spheroids now possess magnetic properties and could be used for magnetic patterning in tissue-engineering applications.

2.1.5.3 Bioreactors

Polymer microcapsules could be utilized as a platforms for various reactions. The possibility of precisely controlling the size, composition, functions, and shell thickness provides advantages for such applications [101]. Capsules can be used for enzyme-catalyzed biomineralization [102], enzyme-catalyzed polymerization [103] and bioenzyme reactions [104].

As an example of enzyme-catalyzed biomineralization, $CaCO_3$ synthesis has been carried out exclusively inside polyelectrolyte capsules [105]. For this purpose, capsules were loaded with urease in a water/ethanol mixture, which made them permeable to urease macromolecules [106]. The capsules were then dispersed in $CaCl_2$ and urea solution. Urease catalyzes the reaction inside the capsules, leading to the decomposition of urea and forming CO_3^{2-} inside the capsules. Carbonate anions reacted with Ca ions to form $CaCO_3$ which completely filled the capsule interior.

In enzyme-catalyzed polymerization, polymers can be synthesized inside the microcapsules. The idea behind such a reaction is based on the permeability of the capsule shell to the monomer. Simultaneously, biocatalysts and polymer chains cannot leave capsules because of their high molecular weights. In the study by Ghan et al. [107], 4-(2-Aminoethyl)phenol hydrochloride (tyramine) was used as

the monomer. In addition, horseradish peroxidase was encapsulated via a pH change in the solution and catalyzed the polymerization of tyramine inside the capsules.

Bioenzyme reactions can also be performed inside the capsules [104]. The samples prepared from protamine (PR) and DS LBL capsules were loaded with enzymes. The capsules were sequentially incubated in solutions of horseradish peroxidase (HRP) and glucose oxidase (GOx). Retention of enzymatic activity of the encapsulated peroxidase/glucose oxidase system was demonstrated.

2.1.5.4 Biosensors

Polymer microcapsules could be used as a platform for sensing applications, owing to various protocols for the integration and loading of cargo [108]. In addition, both reference and analyte-sensitive fluorochromes can be incorporated into the capsule to provide the basis for precise measurements [109].

The first capsule-based sensing system was developed for glucose monitoring [110,111]. In one of the studies, dissoluble cores were coated with layers of fluorescein isothiocyanate (FITC)-dextran, tetramethylrhodamine-Concanavalin A (TRITC-Con A) and PAH/PSS polyelectrolytes [111]. The mechanism of glucose detection was based on the formation of ultra-thin films between dextran and Con A. First, fluorescence spectrometry of the capsules revealed prominent peaks of both FITC and TRITC. After the addition of glucose, a stronger FITC peak appeared because dextran was displaced from the capsule, resulting in a decrease in energy transfer efficiency.

Another application of layer-by-layer polymer capsules is for pH detection. The first pH sensor was developed by Kreft *et al.* [112]. The microcapsules were loaded with seminaphtorhodafluor-1-dextran (SNARF-1-dextran) conjugate. Its fluorescence emission greatly depends on the pH of the environment and changes from green under acidic conditions to red under alkaline conditions. Because the capsule shell is permeable to ions, its fluorescence signal depends on the concentration of ions. Such capsules could be used in flow-cytometry-based assays for precise uptake measurements [113]. The localization of the capsules could be determined by detecting the fluorescence intensities in the green and red channels. Capsules inside the cells fluoresce in the green channel because of the acidic interior. At the same time, capsules on the cell membrane fluoresce in the red channel owing to an alkaline environment.

In conclusion, polymer microcapsules are a unique system. The capsule size can be precisely controlled and the choice of polymers for the capsule shell is wide. Capsules have low cytotoxicity and are easily taken up by various cell lines. Capsules can also be loaded with drugs, dyes, and nanoparticles (NPs). These properties make microcapsules attractive for cell-labeling and tracking applications.

2.2 Carbon nanodots

In this section, carbon nanodots (CNDs) are discussed because they played a role in the photoconversion of polymer capsules, reported previously [24], which

inspired the current work.

2.2.1 Carbon nanodots production

One of the first studies on CNDs was published in 2004 [114]. CNDs are considered a zero-dimensional materials. They are usually composed of carbon, oxygen, hydrogen, and nitrogen and have a diameter of less than 10 nm. Typically, CNDs are produced by either a top-down or bottom-up approach (Figure 2.10) [115].

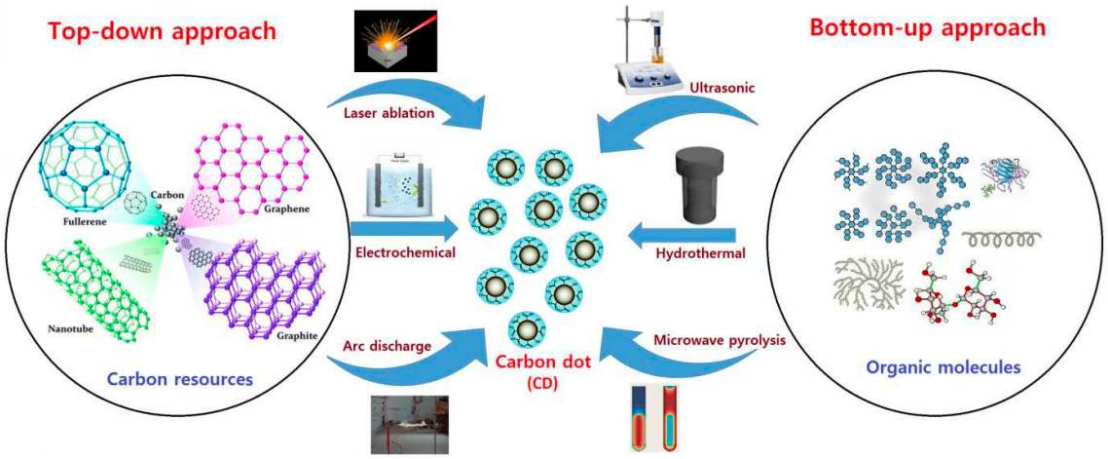

Figure 2.10: Schematic illustration of various production options of CNDs [115].

In top-down methods, higher-dimensional carbon resources, such as graphene, graphite, fullerene, and carbon nanotubes, are disrupted. This can be achieved by laser ablation [116], electrochemical synthesis [117], chemical oxidation [118], and arc discharge [119]. In laser ablation, particles are heated by a laser beam in a liquid. The reaction occurs in a cavitation bubble where the particles interact with the liquid. CNDs are formed during the plasma-cooling phase and diffuse into the solution [116]. In electrochemical synthesis, a redox reaction occurs under

the influence of an electric current applied between the two electrodes separated by the electrolyte [117]. In chemical oxidation, carbon materials are treated with strong oxidants such as sulfuric acid or hydrogen peroxide [118]. In arc discharge, a high current passes through the carbon cathode and anode electrodes, creating a helium plasma arc that evaporates carbon atoms [119].

Usually, CNDs produced by the top-down approach are not fluorescent, but this can be resolved by passivation of the surface of CNDs with various polar moieties [120]. A valuable benefit of top-down methods is that the prepared CNDs typically do not have structural uncertainty and possess a well-defined structure [121]. In addition to pure CNDs, various molecular precursors could be added to the reaction to dope the nanodot structure with N, S, or other atoms [122, 123].

In bottom-up methods, molecular precursors such as food waste, sugars, and citric acid are used. Carbonization of such carbon-containing sources can be achieved via microwave pyrolysis [124], hydrothermal treatment [125], or ultrasonification [126]. In microwave pyrolysis, CNDs are produced by the microwave irradiation of organic compounds [124]. In the hydrothermal treatment approach, a precursor mixed with water or an organic solvent was placed in the autoclave and heated to a high temperature (approximately 160-200 °C). CNDs were collected after complete cooling of the mixture [127]. In the ultrasonic method, carbon precursors in specific solvents are exposed to sonification. CNDs are formed because of the radiation energy produced, which leads to condensation and carbonization [126].

Bottom-up synthesis is difficult to control because multiple side products can be formed simultaneously with the CNDs, initiating the need for further purification. Therefore, the characteristics of these CNDs were highly dependent on the reaction conditions. Nevertheless, this approach is attractive because of its simplicity and the lack of additional processing of CNDs to impart fluorescence properties. Moreover, the bottom-up approach can provide a wider variety of CND structures than top-down methods [128]. The classification of the most common types of CNDs is presented in Figure 2.11) [129]. The core structure of nanoparticles can be amorphous or crystalline, whereas the surface can contain different polar or non-polar groups.

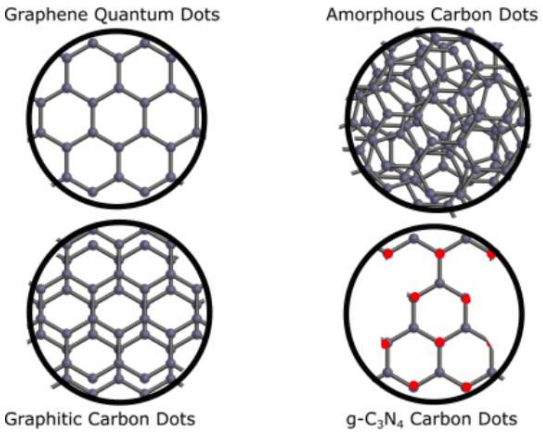

Figure 2.11: Commonly reported CND structures. Black dots – carbon atoms and red dots – nitrogen atoms [129].

Therefore, bottom-up synthesis is more suitable for the production of CNDs precisely in the capsule shell, which was done previously [24]. In the next section, the properties of CNDs will be discussed.

2.2.2 Carbon nanodots properties

2.2.2.1 Optical absorption

It was reported that the absorption of CNDs is high in the ultraviolet (UV) range, with the tail of the spectra present in the visible range (Figure 2.12a) [114]. Absorption peaks are usually observed between 260 and 320 nm. The absorption peak around 220-270 nm is related to the electron transition from π orbital to C=N bonds. An absorption peak around 280-350 is present because of the π to $\pi*$ transitions in the C=C bond and n to $\pi*$ transitions in C=O bonds. Finally, a peak around 350-600 nm in the visible range was associated with the electron transitions of the CND surface functional groups [130].

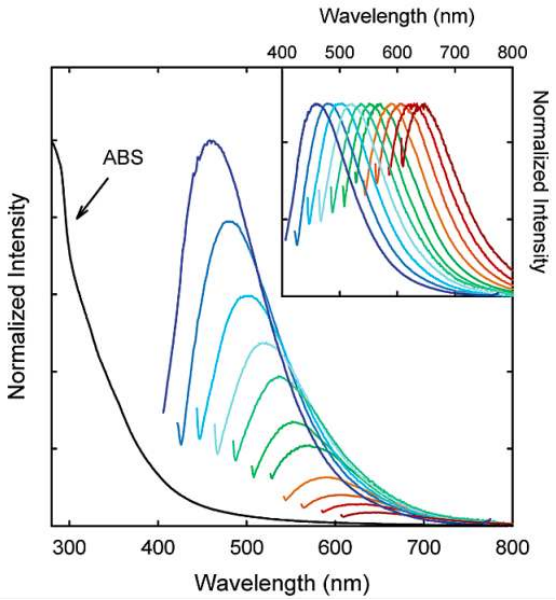

Figure 2.12: The absorption (ABS) and luminescence emission spectra of poly(propionyl ethyleneimine-co-ethyleneimine) (PPEI-EI) CNDs in water. The excitation wavelength is increased from 400 nm at the 20 nm step [114].

2.2.2.2 Photoluminescence

As for luminescence emission, the photoluminescence (PL) of CNDs depends on the excitation wavelength (Figure 2.12) [114]. Several mechanisms have been proposed to explain this phenomenon. The most common methods are based on the quantum confinement effect (QCE) and emissive surface-energy traps.

The QCE was confirmed by theoretical calculations. Using time-dependent density functional theory (TDDFT), the emission of graphene quantum dots (GQDs) with zigzag edges was calculated (Figure 2.13) [131]. Emission was observed from the deep UV to near-infrared regions with changes in the GQDs diameter from 0.46 to 2.31 nm. More specifically, the visible range was covered by the diameters of GQDs ranging from 0.89 to 1.80 nm, which correlates with the QCE. Other studies have also reported that the larger the CNDs, the higher the emission maximum wavelength [132]. In another study by Kim et al. [133], high-resolution transmission electron microscopy (HRTEM) was used to analyze CND's shape. It was concluded that the PL behaviour was attributed to the circular-to-polygonal-shape changes and edge-state variations of the GQDs at a diameter of 17 nm.

Another mechanism of PL is related to the surface peculiarities of CNDs, such as surface defects of passivated particles, triple carbene at the zigzag edges, oxygen-containing, and other functional groups [134]. For example, GQDs have been reported to exhibit pH-dependent PL emission, which is affected by protonation and deprotonation of surface functional groups [135]. In addition, various organic solvents cause different surface passivations of CNDs, leading to diverse emission

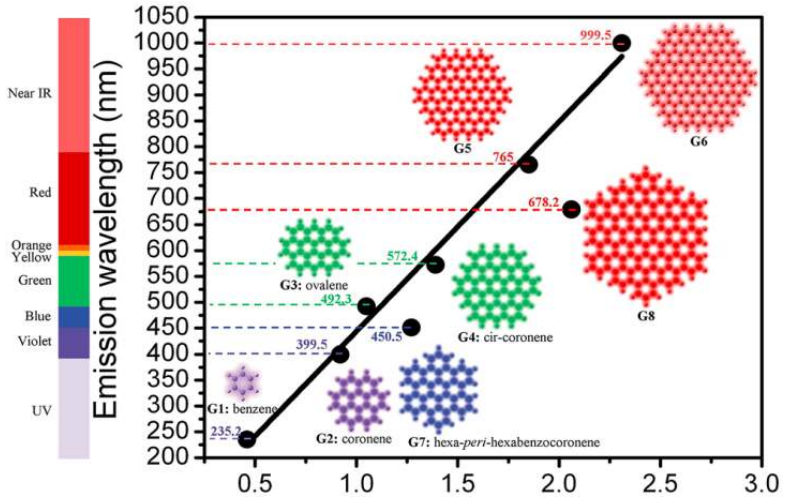

Figure 2.13: Emission wavelength of different sizes GQDs with different sizes obtained through TDDFT [131].

peak wavelengths [136]. Moreover, Lin et al. [130] reported that the energy gap was smaller in GQDs with zigzag edges than in those with armchair edges. Such a zigzag configuration is supposed to contain a triplet carbene state instead of a singlet carbene state. Therefore, PL emission might be connected to such a triplet carbene state that quench and recover under acidic or alkaline conditions. Nevertheless, the PL of CNDs is difficult to explain by a single mechanism, and a combination of models should be used for this task, which include the conjugation effect, defects, surface functional groups, and carbon core state [137].

2.2.2.3 Up-converted photoluminescence

Up-converted photoluminescence (UCPL) is observed when multiple photons are absorbed simultaneously, and light of a shorter wavelength is emitted in comparison to the original light source (anti-Stokes-type emission) [138]. Moreover, a

fixed emission peak at 540 nm upon near-infrared (NIR) irradiation was discovered, which did not change its position at various excitation wavelengths [139]. This means that regardless of the excitation parameters, emission occurs from the lowest single state of energy.

Nevertheless, there are studies on five types of CNDs that did not show UCPL properties [140]. The authors claimed that the UCPL in reality arose from the normal fluorescence excited by the leaking component from the second diffraction in the fluorescence spectrophotometer's monochromator. This leakage component can be eliminated by installing a long-pass filter in the excitation pathway of the spectrometer. Therefore, such an experiment suggests that UCPL detection should be performed thoroughly to avoid false positive results.

In conclusion, CNDs have unique optical properties, which highly depend on the size, surface passivation, and environment's pH. Therefore, their synthesis parameters should be carefully controlled to ensure the reproducibility of the results. In the next section, the applications of CNDs will be discussed.

2.2.3 Carbon nanodots applications

2.2.3.1 Photocatalysis

CNDs are known to exhibit photocatalytic properties, which means that they can accelerate chemical reactions upon photoexcitation. CNDs are attractive candidates for photocatalytic applications because of their optical absorption and electron transfer properties and the possibility of coupling them with other materials

(for example, Fe_2O_3 [141] and TiO_2 [142]). Currently, there are two viewpoints on the effect of CNDs on photocatalytic reactions (Figure 2.14) [142]. First, CNDs accept electrons from photoexcited semiconductors, facilitating charge transfer to the substrate and inhibiting the recombination of the excited electron-hole pairs. This raises the possibility that the reaction will proceed further [143]. Second, CNDs can act as semiconductors; after light absorption, the excited electron is transferred to the coupled semiconductor. This increases the catalytic activity throughout the visible range [144].

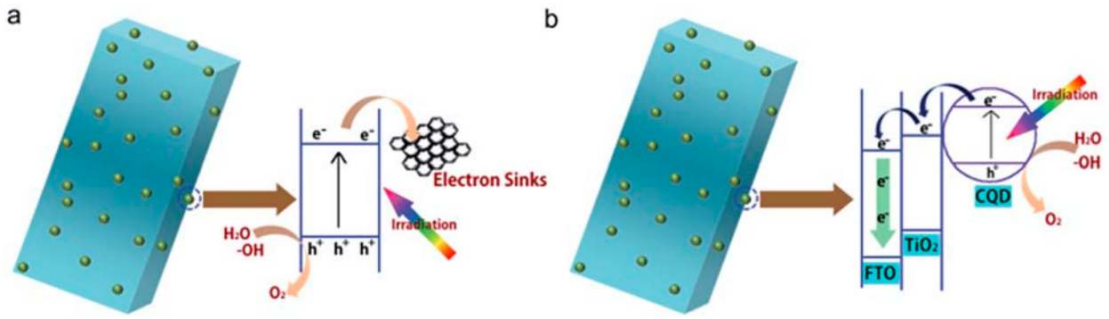

Figure 2.14: Proposed mechanism of photocatalytic activity of CNDs: (a) electron sink, (b) electron donor [142].

As an example of CND photocatalytic activity application, their nanocomposite with Fe_2O_3 was used for photodegradation of toxic benzene and methanol gases under visible light [141]. Also, carbon nanoparticles were prepared with gold coating as a potential photocatalyst for the reduction of atmospheric CO_2 or the production of H_2 from water [145].

2.2.3.2 Nanosensing applications

CND nanosensors are typically developed using two strategies: based on pure CNDs and by coupling CNDs with other materials. For example, pure CNDs can be used for ion detection, which was done for Ag^{2+} [146], Fe^{3+} [147], Pb^{2+} [148], and others. When the CNDs were dispersed in the solution with the target analyte, their fluorescence decreased, indicating the presence of the analyte. High sensitivity and selectivity can be achieved by modifying CNDs with functional groups that are sensitive to specific ions.

Supposedly due to the negative charge of CND, their application for the detection of cations is less common. Nevertheless, the detection of PO_3^{-4} and S^{2-} has been reported using a combination of CND with Eu^{3+} ions [149]. In addition, CNDs were adsorbed on the surface of gold nanoparticles, providing a system for SCN^- detection [150]. As an underlying mechanism, CND emission is reduced by cations and recovered in the presence of a detectable anion, which inhibits this effect.

2.2.3.3 Optoelectronic devices

CNDs are attractive candidates for optoelectronic devices owing to their strong absorption, tunable emission, and electron-donating/accepting properties. CNDs can be used in light-emitting diodes (LED) as fluorescence downconverters [151] because they absorb UV light and emit in the visible range. By adjusting the emission parameters and exploiting the high quantum yield, white LED can be

obtained. Moreover, CNDs can be used as active layers in electroluminescent devices [152]. In this case, the CNDs served as an emitting layer after charge injection in the multilayer structure.

Because the CND absorption spectrum has a tail in the visible range, it may be useful for solar cell production. Moreover, CNDs can be used as sensitizers in solar cells because they can easily accept and donate electrons [153, 154].

2.2.3.4 Biomedical applications

According to several studies, CNDs are nontoxic, which is crucial for various biomedical applications [155, 156]. One such application is bioimaging based on the bright PL of CNDs. For example, CNDs prepared from l-aspartic acid and d-glucose were reported to accumulate in C6 glioma cells [156]. Moreover, because CNDs can penetrate the blood-brain barrier, they can accumulate in mouse brain tumors, opening possibilities for tumor diagnosis.

In addition to imaging, CNDs can also be used for cancer treatment. For example, they have been reported to suppress the proliferation of tumor membranes, thus exerting angiogenic effects on vessels [157]. Moreover, there been used as antiviral agents [158]. For example, they physically blocked the passage of the hepatitis C virus into human lung cancer and monkey kidney cancer cells.

In conclusion, CNDs are non-toxic materials that can be easily produced from various sugar sources. Their unique optical properties make them attractive candidates for photocatalytic applications. In addition, their nontoxicity is favorable for biological applications. In the next section, the photoconversion phenomenon

will be discussed.

2.3 Photoconversion

Here, the photoconversion phenomenon is discussed using the example of fluorescent proteins (FPs). FPs are widely used in live-cell imaging [159]. They are usually expressed throughout the whole cell, which presents certain limitations for researchers. To overcome this problem, photoactivatable, photoconvertible, and photoswitchable fluorescent proteins can be used (Figure 2.15) [160]. Photoacti-

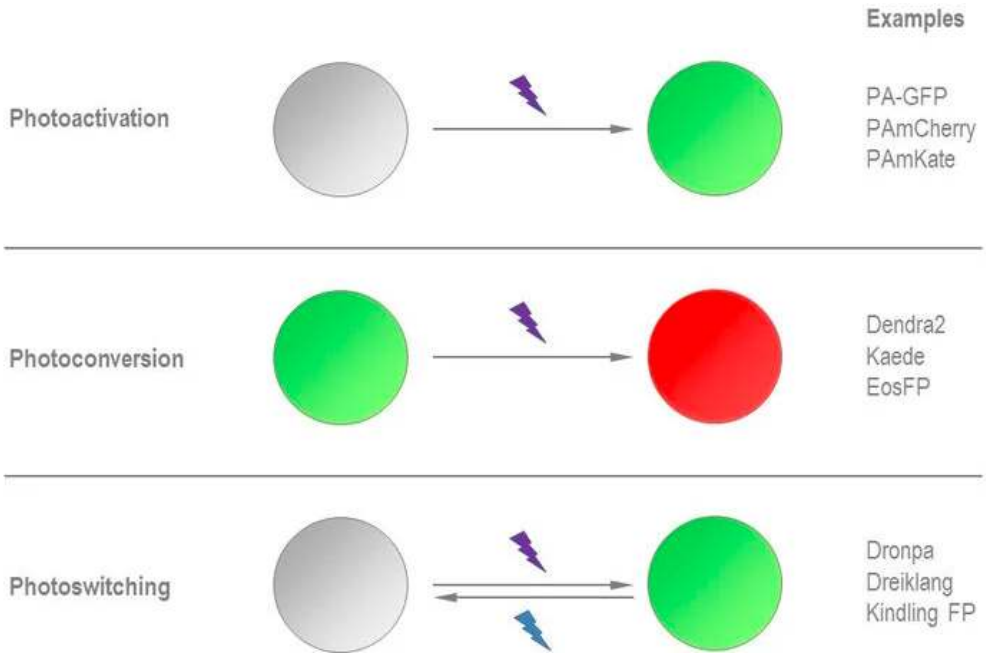

Figure 2.15: Schematic illustration of differences between photoactivatable, photoconvertible, and photoswitchable FP [160].

vatable FPs are initially in a non-fluorescent state and can be switched "on" to a fluorescent state after blue or violet light irradiation [161]. Photoactivatable FPs cannot return to their original states after irradiation. In contrast, photoswitch-

able FPs can be switched "on and off" multiple times owing to the light exposure at different wavelengths [162]. Photoconvertable FPs can irreversibly change their fluorescence emission spectra from green to red upon irradiation [163]. All three types of FPs have different mechanisms of action, and, for the purpose of this research, the photoconversion mechanism of FPs is covered further.

2.3.1 Photoconversion mechanism in fluorescent proteins

One of the first photoconvertible FP was found in the stony coral *Trachyphyllia geoffroyi* and was named Kaede [164]. Later, other members of Kaede's subfamily of FPs were discovered, which include EosFP [165], derived from stony coral *Lobophyllia hemprichii*, and Dendra [166] derived from octocoral *Dendronephthya sp.*.

Currently, many more types of photoconvertible FPs are available. They are reported to share three chromophore-forming amino acid residues His62-Tyr63-Gly64 located in the eleven-stranded β-barrel structure. Typically, they are numbered 62-64 but in some cases, their positions could be shifted due to loop insertions and N-terminal extensions. Examples of such proteins include Kaede, in which residues are numbered 65-67 [167].

The initial stage of photoconvertible FP maturation involves spontaneous creation of a green chromophore. It is based on a correctly folded protein and an internal main-chain cyclization reaction. The next step is two-electron oxidation facilitated by molecular oxygen, which acts as an electron acceptor, followed

by water removal [168, 169]. The mature form of the photoconvertible FP undergoes reverse protonation, which allows chromophore distortion by stimulating His62 activation [170]. In the next step, blue or UV irradiation of the protonated form of FP leads to photoconversion. The proposed photoconversion mechanism is illustrated in Figure 2.16 [163]. The proposed important bond rotations are

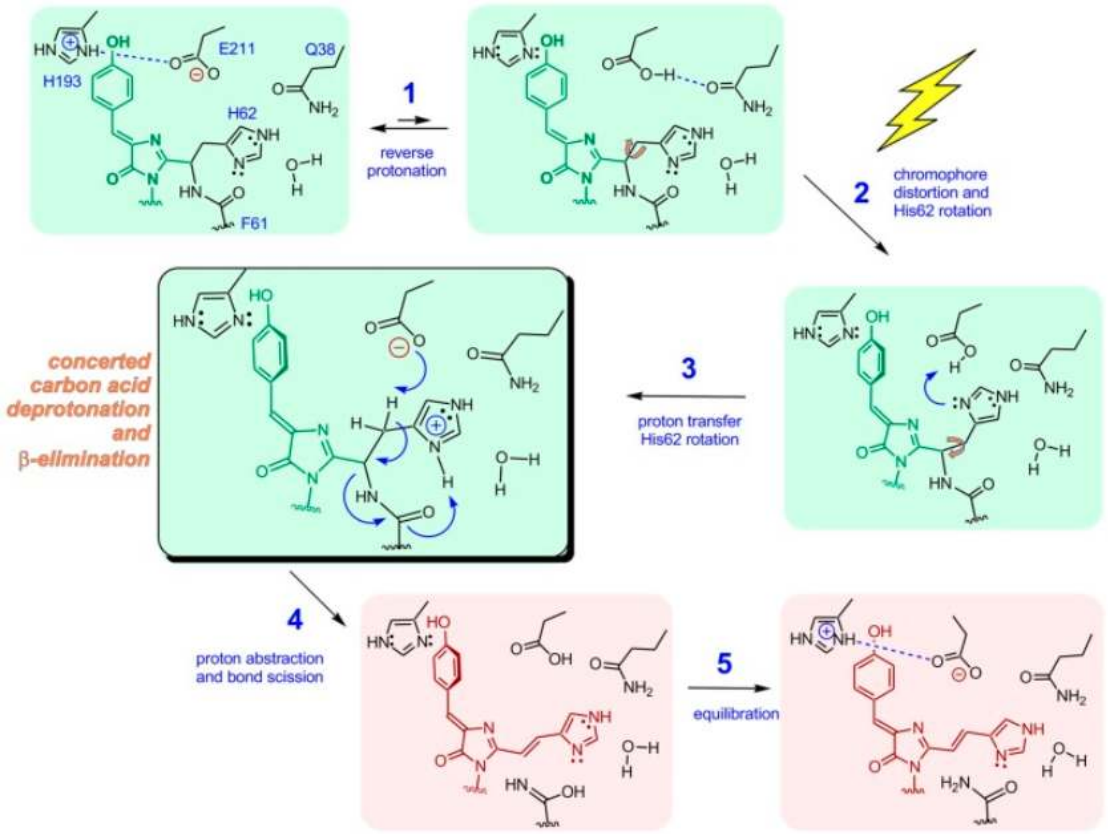

Figure 2.16: Proposed green-to-red photoconversion mechanism of photoconvertible FPs [163].

presented in Figure 2.17 [163]. Specifically, histidine residues are important for acquiring red fluorescence owing to light irradiation. As discussed, in the initial state, FP possesses a two-ring chromophore during cis-transfiguration (marked in green in Figure 2.16). UV light exposure leads to a series of events that change the

chemical structure of FP by backbone cleavage between the N and C α atoms of histidine. As a result, a Cα-Cβ double bond is formed, forming a new three-ring chromophore (marked in red in Figure 2.16). The formation of such an extended conjugation leads to a decrease in the energy gap between the highest occupied molecular orbital and the lowest unoccupied molecular orbital. This shifts the emission to a higher wavelength region of the spectrum. Such photoconverted FP also undergo a reversible process of protonation and deprotonation, transitioning between a nonfluorescent neutral state and a fluorescent anionic state [171].

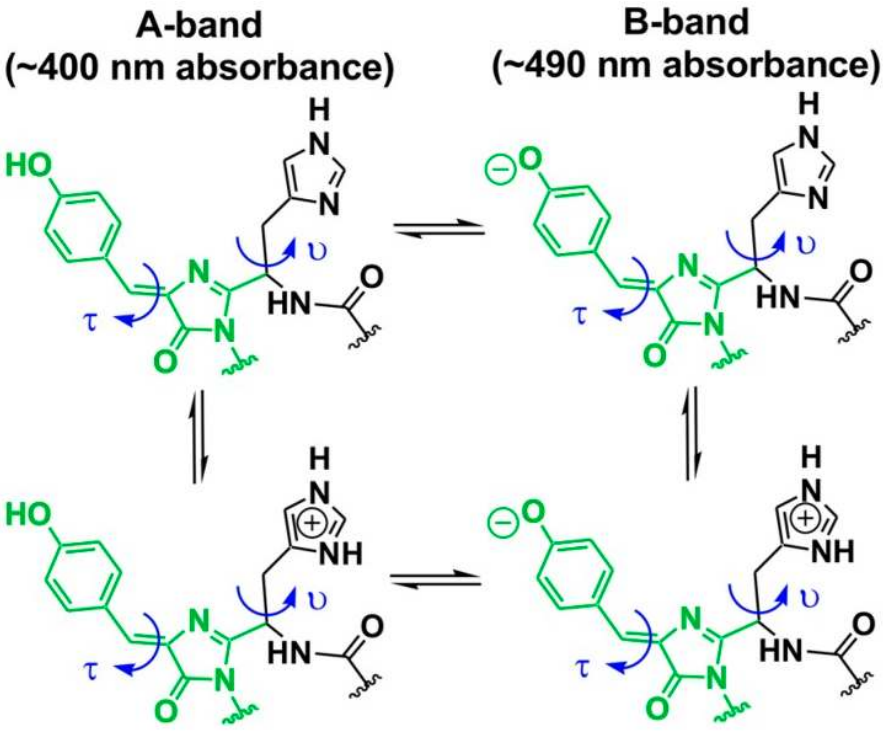

Figure 2.17: Proposed important bond rotations in photoconversion of photoconvertible FP. The rotation angles are τ – chromophoric β-methylene bridge, and υ – His62 side chain [163].

Both green-to-red and cyan-to-green photoconversions are possible in the case

of the PS-CFP and PS-CFP2 proteins [172, 173]. They contain the tripeptide Ser65-Tyr66-Gly67, which is initially in the neutral form (Figure 2.18O) [167]. Upon 405-nm light irradiation, the decarboxylation reaction of Glu222 alters the

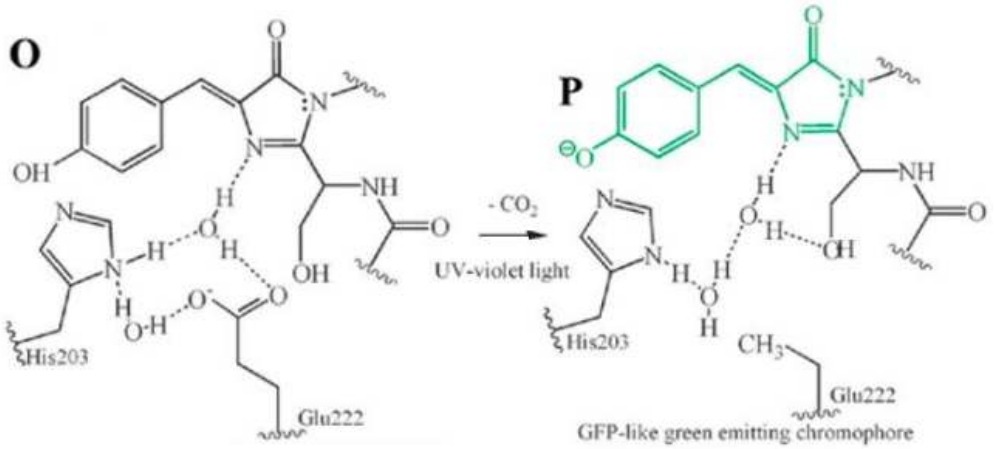

Figure 2.18: Cyan-to-green photoconversion of PS-CFP and PS-CFP2 proteins from (O) neutral form to (P) anionic form [167].

chromophore environment (marked green in Figure 2.18P [167]). This results in fluorescence of the protein in the green range [174].

Another mechanism for the photoconversion reaction is known as "oxidative redding" [175]. The reaction is illustrated in Figure 2.19 [167]. The green chro-

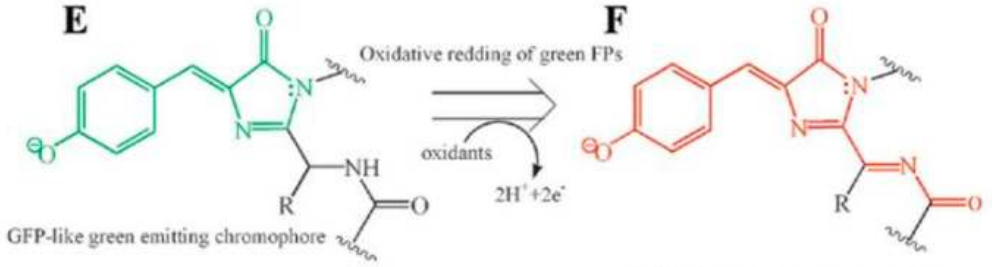

Figure 2.19: Redding reaction [167].

mophore in the excited state undergoes deprotonation and two-electron oxida-

tion, forming a chromophore that emits in the red range [176]. The low oxygen concentration is crucial for this reaction, since otherwise, radicals undergo rapid oxidation.

In conclusion, photoconvertible FPs have a unique chemical structure that consists of proteins and chromophores, making photoconversion possible in such system. Oxygen also plays a crucial role in the photoconversion reaction.

2.3.2 Photoconversion mechanism in organic dyes

Several organic fluorophores can also be photoconverted and used for cell labeling. Unlike FPs, organic fluorophores do not require genetic modification of the cells [177]. In this section, the photoconversions of cyanine, xanthene, and acridine dyes are discussed.

2.3.2.1 Cyanine dyes

Cyanines are synthetic dyes belonging to the polymethine group. Examples of cyanine dyes include Cyanine3 (Cy3), Cyanine3.5 (Cy3.5), Cyanine5 (Cy5), Cyanine5.5 (Cy5.5), Cyanine7 (Cy7), SYTO red dyes, DiR, and Alexa Fluor 647 (AF647).

The photoconversion mechanism is discussed in the example of Cy5, which fluoresces in the red range (Figure 2.20) [178]. The photoconversion of cyanine dyes is dependent on singlet oxygen, which is generated by the energy transfer to molecular oxygen from the excited triplet fluorophores due to laser irradiation [177, 179]. The produced singlet oxygen attacks the double bonds of the polymethine

chain, breaking the Π conjugations. The obtained compounds 1a-b and 2a-b then form 3a-b compound by undergoing two- or one-carbon bond cleavage reactions. 2a-b then binds to 3a-b, forming Cy3, which fluoresces in the yellow range.

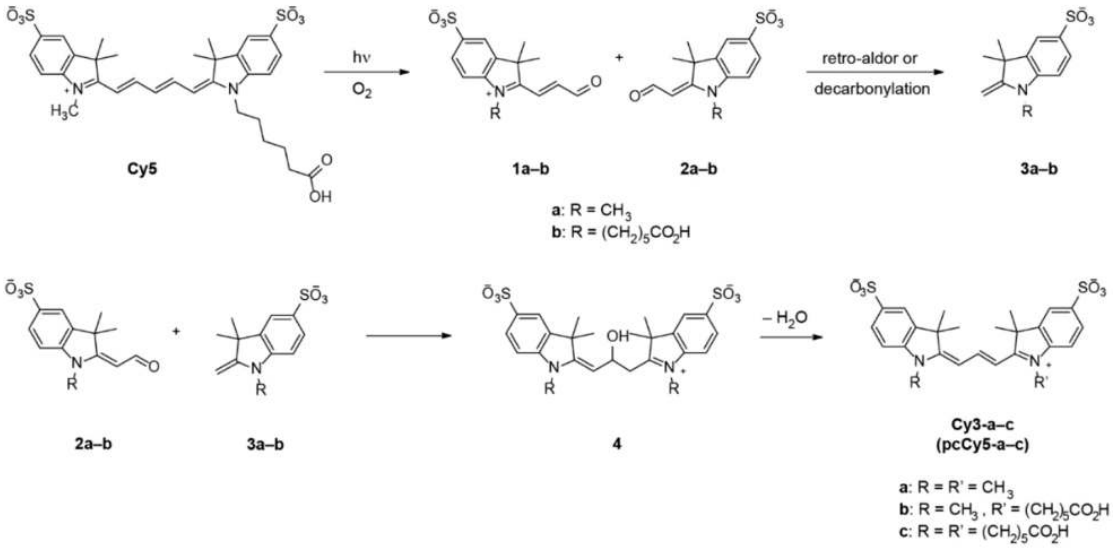

Figure 2.20: Mechanism of photoconversion from Cy5 to Cy3 upon red laser irradiation [178].

It has also been demonstrated that such photoinduced removal of a two-carbon unit occurs with Cy5.5 as well [178,180]. The photoconverted Cy5.5 demonstrated the fluorescence properties of Cy3.5 (Figure 2.21).

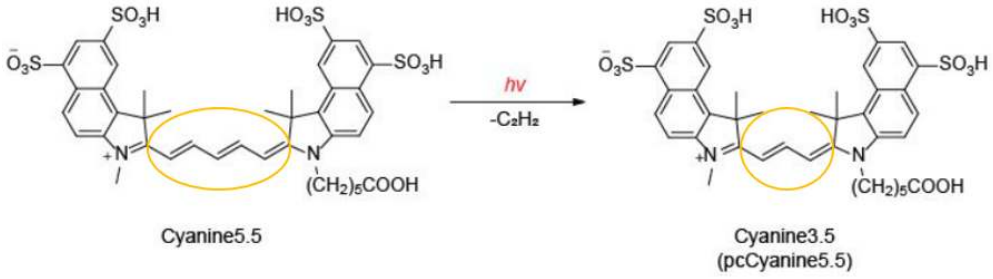

Figure 2.21: Photoconversion from Cy5.5 to Cy3.5 [178].

In another study, the mechanism of Cy7 photoconversion was explored [181].

Irradiation of Cy7 removes a two-carbon unit, providing Cy5, which is then photoconverted to Cy3. In this study, microtubules in COS7 cells were imaged using total internal reflection fluorescence (TIRF). Cells were irradiated with a 641 nm laser using a low irradiation intensity of 0.1 kW/cm^2 to minimize the photoconversion of Cy7 (Cy5 – red channel (679/41 nm) and Cy7 – infrared channel (835/35 nm). Over the course of laser exposure, the intensity of fluorescence increased in both Cy7 and Cy5 channels (Figure 2.22), followed by bleaching. The initial increase in the signal in the Cy7 channel is likely related to the disruption of Cy7 aggregates due to photoconversion and photobleaching. The delayed rise of the signal in the Cy5 channel might be due to the small proportion of Cy7, which is in a non-quenched monomeric state and undergoes photoconversion.

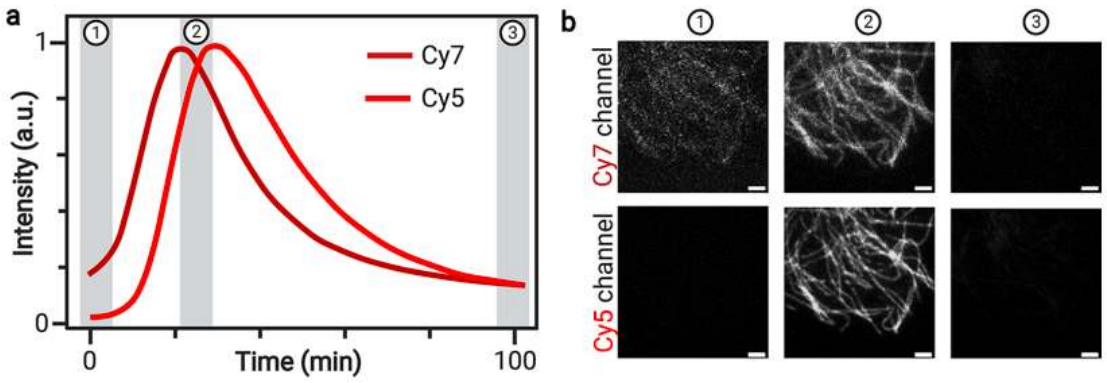

Figure 2.22: (a) Fluorescence signals recorded in the Cy7 channel and Cy5 channel over time. (b) Fluorescence imaging under irradiation intensity of 0.1 kW/cm^2 at corresponding time points [181].

In addition, high-resolution mass spectrometry (HRMS) analysis of the photoproduct of AF647 revealed the appearance of a peak shift that indicated the loss of the C_2H_2 group from AF647, causing blue-shifted photoconversion [178].

Another example of a cyanine photoconvertible dye is SYTO62 which contains a three-carbon polyene linker [180]. The photoconversion of the dye was inhibited in the presence of the singlet oxygen scavenger sodium azide. Simultaneously, photoconversion was stimulated after the addition of D_2O, which prolonged the singlet oxygen lifetime. Therefore, the photoconversion of SYTO62 also relies on photooxidation, as in the case of Cy5 and Cy7.

The presented results indicate that cyanine dyes containing three to seven carbons in polyene linkers can undergo photoconversion owing to the cleavage of the polymethine chain by singlet oxygen. These dyes can potentially be used for cell labeling and tracking.

2.3.2.2 Xanthene dyes

Xanthene dyes are organic compounds containing oxygen atom in a central heterocyclic structure and two more cyclic structures are attached to this central ring. Such a nucleus is called the xanthylium (1a) or dibenzo-pryan nucleus (xanthene) (1b) and acts as a chromophore (Figure 2.23) [182]. The amino or hy-

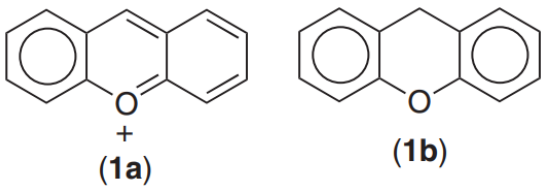

Figure 2.23: Proposed photooxidation pathway of RhB under visible light irradiation

droxyl groups act as auxochromes. Xanthene dyes have many applications, they

could be used for textile and paper staining, as antibacterial agents and biomarkers, and for fluorescence imaging. Xanthene dyes are divided into several groups: triphenylmethane derivatives, diphenylmethane derivatives, hydroxyl derivatives, aminohydroxy derivatives, and miscellaneous fluorescent derivatives [182]. The following discussion focuses on the first three groups for the purpose of this literature review.

Triphenylmethane derivatives

This group of dyes includes rhodamines that are chemically produced as triphenylmethane analog, 9-phenylxanthene. Examples of these dyes are rhodamine B (RhB), rhodamine 6G (Rh6G), rhodamine 123 (Rh123), and rhodamine 110 (Rh110).

For more than 50 years, RhB has been known to undergo stepwise photooxidation by active oxygen species, leading to the loss of its ethyl groups [183]. In addition, this causes blue shifts in the absorption and emission spectra of the dye (Figure 2.24) [184].

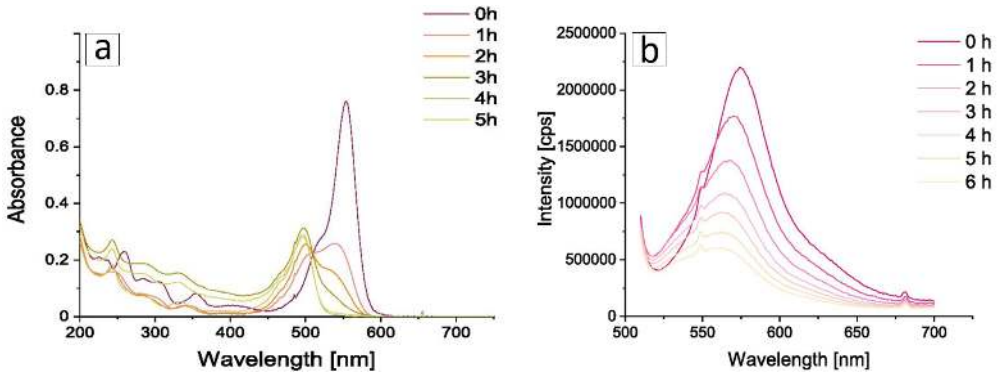

Figure 2.24: (a) Absorption and (b) fluorescence spectra changes of RhB under irradiation with 405 nm LED [184].

Using mass spectrometry and TiO_2/SiO_2 particles as a photocatalyst, Chen et al. proposed a pathway of photooxidation reaction of RhB [185] (Figure 2.25). It could be noticed that eventually RhB is transformed into Rh110 (m/z = 331,

HPLC peaks	Absorption maximum (min)	Retention time (min)	Corresponding intermediares of RhB	m/z	assigned substrates
IV	502	2.56	rhodamine 110 (Rh)	331.1 353.1	Rh^+ $Rh\text{-}Na^+$
III	514	3.34	N-ethyl-rhodamine 110 (MRh)	359.1 381.1	MRh^+ $MRh\text{-}Na^+$
II-B	529	4.67	N-ehyl-N'-ethyl-rhodamine 110 (MMRh)	387.1 409.1	$MMRh^+$ $MMRh\text{-}Na^+$
II-A	525	5.10	N,N-diethyl-rhodamine 110 (DRh)	387.1 409.1	DRh^+ $DRh\text{-}Na^+$
I	541	7.87	N,N-diehyl-N'-ethyl-rhodamine 110 (DMRh)	415.1 437.1	$DMRh^+$ $DMRh\text{-}Na^+$
RhB	556	12.75	Rhodamine B (RhB)	443.1 465.1	RhB^+ $RhB\text{-}Na^+$

Figure 2.25: Proposed photooxidation pathway of RhB under visible light irradiation [185].

$\lambda_{ex}/\lambda_{em}$ = 500/522 nm [186]). Thus, it is shifted to the blue region from the RhB spectra, which has the parameters $\lambda_{ex}/\lambda_{em}$ = 546/567 nm [187]. Moreover, the photoconversion effect was reported by Demina et al. [24]. RhB was loaded into the polymer microcapsules by thermal treatment, and the labels were photoconverted from red to green inside the cells.

Rh6G was also reported to undergo a deethylation reaction upon irradiation [188]. Absorption analyses after UV irradiation for different time intervals at neutral pH revealed a blue shift in the absorption spectra (Figure 2.26) [189]. In a recent study, the photoconversion properties of Rh6G were demonstrated in a Rhodamine 6G salicylaldehyde hydrazone-Zn complex as a material for photochromic devices [190]. When this complex was exposed to UV irradiation, the color changed from pale yellow to light pink.

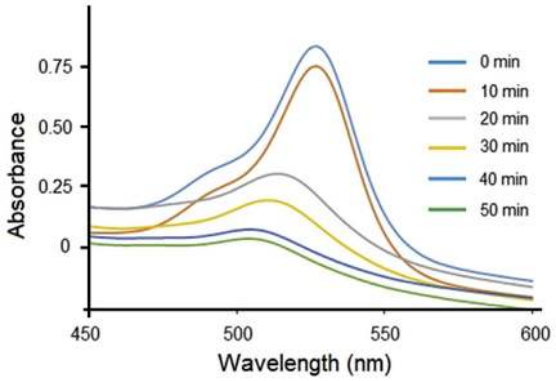

Figure 2.26: Absorbance of Rh6G depending on the irradiation time [189].

Therefore, triphenylmethane derivatives experience photoconversion due to the removal of ethyl groups. This property makes them attractive candidates for the production of photoconvertible cell labels.

Diphenylmethane derivatives

This group includes pyronins, which differ from rhodamines in the absence of a carboxyphenyl group. Examples include Acridine Red (AR), Pyronin Y (PyY), and Pyronin B (PyB) (Figure 2.27) [191]. AR is used for fabric coloring, PyY is used for staining RNA, and PyB is used for nucleic acid staining in the methyl green-pyronin method.

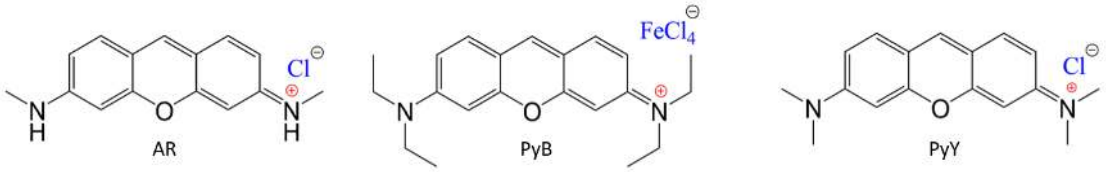

Figure 2.27: Chemical structures of Acridine Red, Pyronin Y, and Pyronin B [191].

Photoconversion of the above-mentioned dyes has not been reported in the literature. Nevertheless, there is an interesting study on a 9-dithianyl-pyronin deriva-

tive [192]. The researchers performed an extensive study of the photodegradation pathway of this compound. The transformation of the 9-dithianyl-pyronin derivative (1) upon light exposure leads to the formation of a 3,6-diamino-9H-xanthen-9-one derivative (2) (Figure 2.28a). Note that the absorbance of the obtained compounds (2) and (3) is shifted to shorter wavelengths (Figure 2.28b) [193].

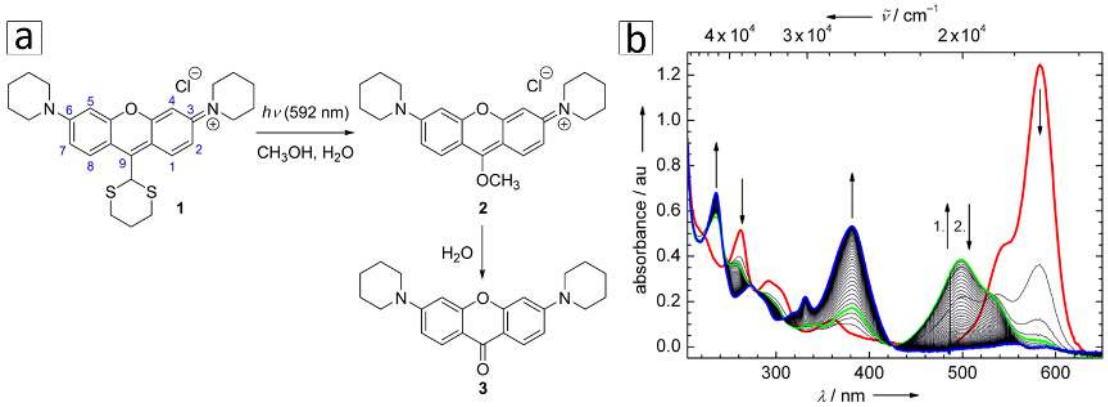

Figure 2.28: (a) 9-dithianyl-pyronin derivative (1) transformation upon irradiation to (2) and (3) compounds. (b) Absorption spectra measured in methanol of the compound (1) –red line, compound (2) – green line, (3) – blue line [193].

Therefore, pyronin dyes and their derivatives potentially exhibit photoconversion properties and might be used for studies on the synthesis of photoconvertible labels.

Hydroxyl derivatives

The main representative of this group is fluorescein, which is the building block of hydroxyl derivatives. In the case of fluorescein, a red spectral shift was observed in the absorbance spectrum with an increase in the pH value of the aqueous solution [194]. The same phenomenon of emission spectrum red shift was

detected with an increase in temperature [195]. Moreover, FITC conjugated with antibody IgG was reported to undergo photoconversion in cultured rat astrocytes [196].

Therefore, fluorescein also has the potential to be applied to the production of photoconvertible labels. To conclude for the whole group of xanthene dyes, there are several promising candidates for photoconvertible cell labels. Based on this literature, rhodamine, pyronin, and fluorescein dyes will be studied for such applications in the thesis.

2.3.2.3 Acridine dyes

Acridine is an organic compound with the formula $C_{13}H_9N$. It is an alkaloid related to the anthracene structure, where one of the central carbons is substituted by nitrogen [197]. Examples of acridine dyes include acridine orange (AO), acridine yellow (AY), acridine yellow G, and quinacrine.

AO is often used for cell staining. It diffuses through the cytoplasmic membrane of live cells and accumulates in organelles with low pH, such as lysosomes. It also intercalates with DNA and binds to RNA through stacking interactions [198]. AO has also been demonstrated to undergo a demethylation reaction upon irradiation, which leads to a blue shift in the absorption spectra (Figure 2.29) [199].

The identification of AO intermediates is presented in Figure 2.30, demonstrating that AO undergoes the consecutive removal of methyl groups. Moreover, AO was reported to undergo photoconversion when tested in rabbit retina tissue [196].

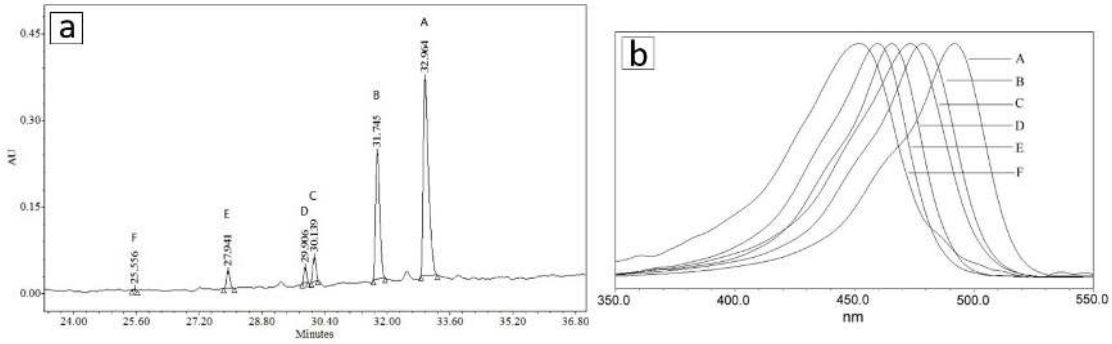

Figure 2.29: (a) HPLC chromatogram of AO solution after 2 h of irradiation with visible light (UV detector). (b) Absorbance spectra of corresponding AO intermediates [199].

HPLC peaks	*N*-de-methylation intermediates	Abbreviation	Retention time (min)	ESI-MS peaks (*m/z*)	Absorption maximum (nm)
A	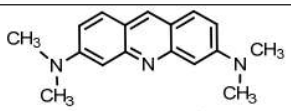	AO	32.964	266.18	491.6
B	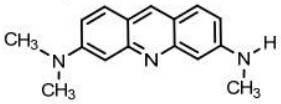	AO-M	31.745	252.07	478.2
C	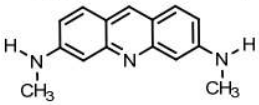	AO-MM	30.139	238.01	473.3
D	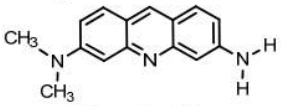	AO-D	29.906	238.14	466.0
E	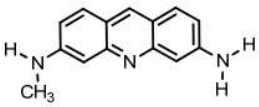	AO-DM	27.941	224.03	459.9
F	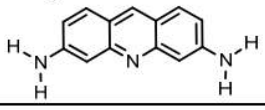	AO-DD	25.556	210.04	451.4

Figure 2.30: Identification of the N-de-methylation intermediates of AO [199].

As for AY, it was also reported to undergo a demethylation reaction upon irradiation, similar to AO (Figure 2.31) [200]. It has not been studied to show photoconversion properties previously, but it can still potentially be used for this

task.

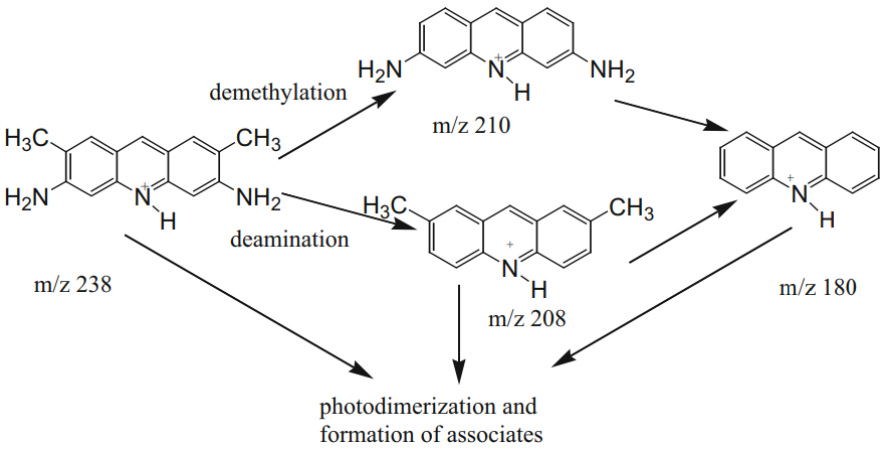

Figure 2.31: Proposed scheme of AY photodegradation [200].

Therefore, acridine dyes exhibit potential for the production of photoconvertible labels due to the demethylation of these dyes upon irradiation and the corresponding spectral shift.

2.3.2.4 Other dyes

Many more dyes were reported to undergo a blue shift upon light exposure. Examples include thiazine dyes [201], which were irradiated in the presence of PMAA and oxygen, demonstrating a considerable hypsochromic shift. Hoechst dye, which is used for nuclei staining, can be photoconverted from blue to green or even red. The same is true for 4',6-Diamidino-2-phenylindole (DAPI), which is widely used for DNA staining [202]. Methylated diazaxanthilidene shows red-shifted photoconversion by 6π electrocyclization to restore aromaticity, followed by an oxidation event [203]. Lucifer Yellow and FM 1-43FX were used for testing the photoconversion setup built by Dobson et al. [204]. Other examples of

photoconvertible dyes include propidium iodide, fluoro-gold, gast blue, diamidino yellow [205], ethidium bromide, norepinephrine, and others [196].

In conclusion, the photoconversion mechanism of various FPs and dyes was discussed. While FPs are widely used for cell labeling, various organic fluorescent dyes also exhibit potential for the production of capsule-based photoconvertible labels, such as cyanine, rhodamine, acridine, pyronine, which will be used for further studies. In the next section, cell labeling and tracking techniques are discussed.

2.4 Cell labeling techniques

There are several cell labeling and tracking techniques, such as fluorescent proteins [206], organic dyes [207], magnetic nanoparticles [208], bioluminescent probes [209], quantum dots [210], and radioactive isotope alternatives [211]. Methods and materials that possess photoconversion properties will be discussed more thoroughly in the next section to gain information about various tasks that are solved with cell labeling and tracking approach.

2.4.1 Fluorescent proteins

The discovery and development of fluorescent proteins were important steps in precisely studying the organization and function of various living systems (Figure 2.32) [206]. FPs are used not only for cell labeling but also for labeling proteins, organelles, and nucleic acids, as well as for other tasks.

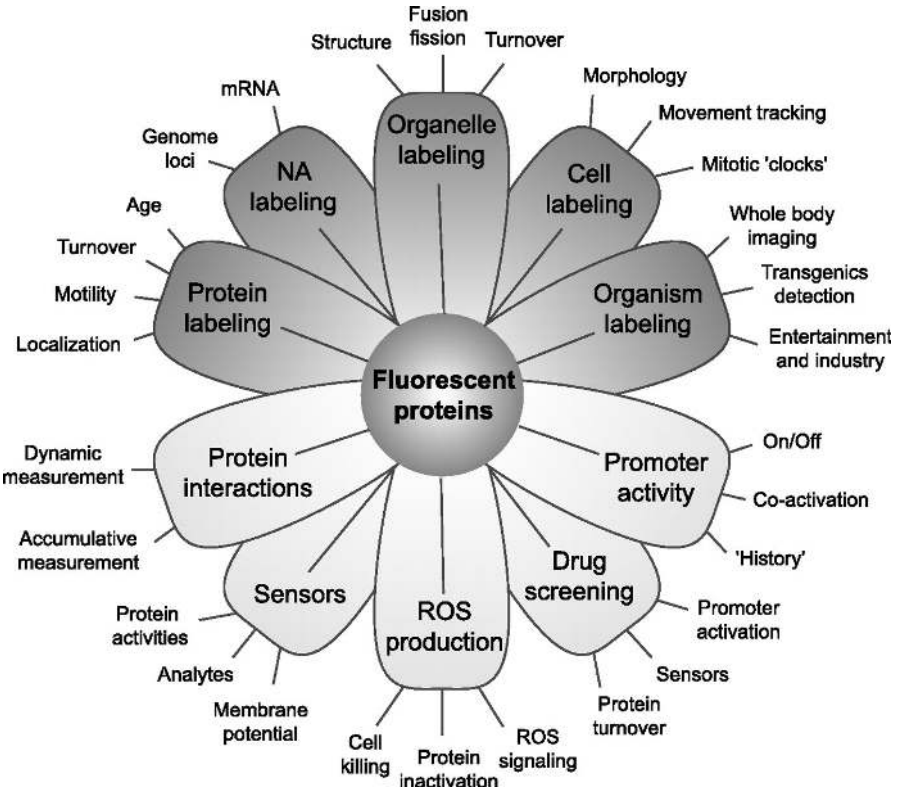

Figure 2.32: Areas of FP application [206].

In cell labeling applications, FPs can be used to visualize a specific cell type and analyze cell interactions in the environment of the whole organism, tissue, organ, or cell cultures. For example, hMSCs were transfected to express the photoconvertible fluorescent protein Dendra2 [6]. The cells were labeled and tracked in both 2D and 3D microenvironments (porous chitosan scaffolds, Matrigel, and alginate hydrogels). This approach allowed for the analysis of hMSC dynamics, cell morphology, and mobility in different 3D microenvironments for the future development of biomaterials for better stem cell recruitment and migration.

In the study by Hatta et al., the photoconvertible FP Kaede was used to study embryogenesis in zebrafish [10]. Cells were labeled in patterns of interest to track their movements. Using this technique, processes such as placode formation, neu-

rulation, and the navigation of early commissural axons in the hindbrain can be investigated. In another study, four photoconvertible FPs (PA-GFP, PS-CFP2, Kaede, and KikGR) were used to generate transgenic embryonic stem cells [212]. The KikGR protein was chosen as the most efficient for cell labeling. Subpopulations of embryonic stem cells in culture and groups of cells within mouse embryos cultured *ex utero* were photoconverted. The labeled cells could be observed for several days, providing valuable information about embryo development. For example, it could be determined if convergence or extension collective cell behaviour occurs in mouse embryos (Figure 2.33) [212]. For this, the rectangular region of interest (ROI) was labeled, and the height-to-width value was measured. The observed changes in the height-to-width ratio indicated a convergent extension behaviour type. The fate of the photoconverted cells could also be observed. For this, a small group of cells was labeled on the right side of the cardiac crescent of an embryo. After 12 h, the photoconverted cells were incorporated into the right side of the formed linear heart tube, indicating that they can contribute only to its right side.

In addition to zebrafish and mice, the chicken model was also used for cell fate tracking. For example, FPs were introduced into the neural tube of the avian embryo by electroporation to observe the migration of neural crest cells in real time [213]. In another study, chick neural crest cell behaviours within the rhombomere 4 migratory streams were studied using the photoconvertible KikGR [214].

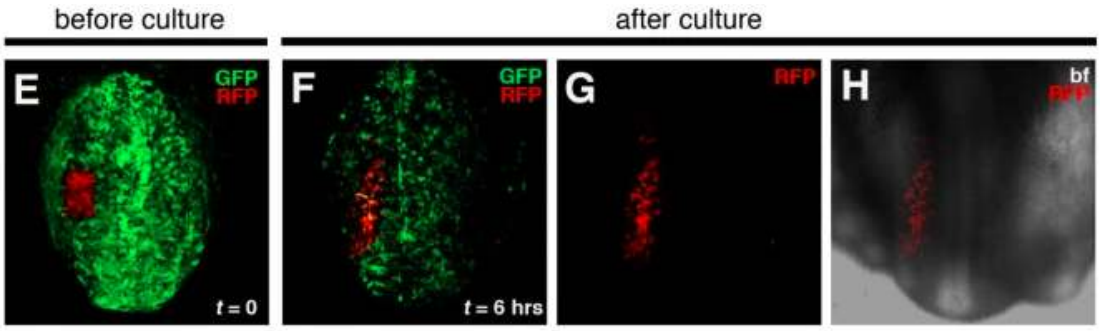

Figure 2.33: (E) Rectangular cell labeling at the start of embryo culture. (F) Migration of photoconverted cells after 6 h. (G) Red channel. (H) Overlay of the red channel and bright field image. The scale bar is 200 μm [212].

To conclude, photoconvertible FPs are a powerful tool for marking cells and observing changes in the selected cells over time. This approach offers the possibility of marking and re-sorting cells with certain requested characteristics for cultivation and growth (e.g., creation of purified cell lines) [215]. Nevertheless, this approach has its limitations: (i) some FPs exhibit toxicity [18] and a tendency to aggregate [16], (ii) a gradual decrease in the photoconverted fluorescent signal during cell doubling (i.e., daughter cells share a part of the converted protein among themselves until the signal disappears completely) [216], (iii) the inability to identify an individual cell among the marked ones, and (iv) the need for gene modification of the primary culture carrying the gene of the photoconvertible protein [163]. Gene modification is the main limitation to exploiting the resulting cell clones in personalized medicine because of the probability of random mutations occurring during transfection.

2.4.2 Organic fluorophores

Small-molecule organic fluorophores can also be used for cell labeling and tracking. The idea behind cell fate tracking within a population was demonstrated in the example of the commercial lipophilic membrane dye DiR (Figure 2.34) [207]. Here, the original single cell is stained with DiR (A). In the absence of photoconversion, later imaging of this area does not provide clear information on whether proliferation or migration occurred when more cells appeared (B). At the same time, photoconversion of DiR-labeled cells can provide information on cell division and differentiation. During division, the doubling of photoconverted cells will be observed (D). During differentiation, the GFP-reporter gene is turned on, changing the fluorescence of the cell to yellow (E).

In the mentioned research [207], hematopoietic stem/progenitor cells (HSPCs) were labeled with DiR and injected into lethally irradiated C57BL/6 mice. After *in vivo* photoconversion of these cells, the red-to-blue channel intensity ratio increased by 5.7 times compared to before the procedure. Then, the photoconverted cells were observed to track their proliferation and fate.

In another study, DiR was used for labeling, photoconversion, and tracking of ovarian cancer cells (OVCAR5) in monolayer cultures and spheroids, which could be used to study subpopulations of cells [7]. The photoconverted cells can then be selectively isolated using fluorescence-activated cell sorting (FACS). Additionally, melanoma cells were stained with DiR and injected retro-orbitally into zebrafish to create a melanoma xenograft model *in vivo*. A small area of melanoma cells was

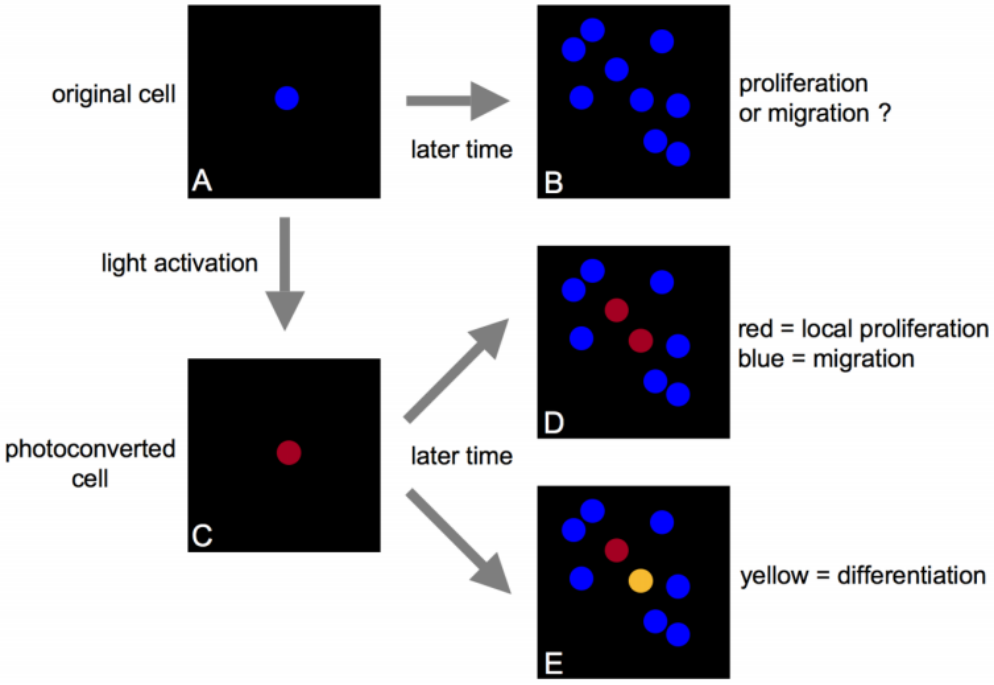

Figure 2.34: Scheme of *in vivo* photoconversion method to track the fate of an individual cell. (A) DiR-labeled cell. (B) Later, the same area was without photoconversion. (C) Photoconversion of the DiR-labeled cell, (D) cell proliferation and migration, and (E) cell differentiation [207].

then selected for photoconversion, and the spreading of these cells was observed over the course of a week. Such research paves the way for resolving tasks such as lineage tracing in the context of metastasis: which cells divide the most rapidly, which cells spread first, and which subpopulations of cells are resistant to therapy.

There are more examples of photoconvertible dyes in cell experiments. For example, methylated diazaxanthilidene was thoroughly studied for labeling HeLa cells [203]. Heng et al. developed boron dipyrromethenes (BODIPY) dye for blue-shifted photoconversion of cells [217]. Another scientific group proposed a new dual-activatable cell tracker (DACT) that relies on activation by both intra-

cellular carboxylesterases and light [22]. This dye was used for tracking cell-cell interactions and cell migration of splenocytes on a monolayer of immortalized lymphatic endothelial cells (imLEC).

Overall, such a variety of fluorescent photoconvertible dyes provides a wide range of fluorescence detection options. The discussed dyes often have bright fluorescence signals, and the staining procedure is quite simple [218]. Nevertheless, these dyes possess certain limitations. For example, DiI is highly cytotoxic, and its safe concentration greatly depends on the cell type [219]. Without a predefined safe concentration of the dye, dead cells might appear during culture preparation. Such debris from the dead cells would be taken up by other non-labeled cells, staining them and potentially distorting research results. In cases where there are no dead cells, DiI can still diffuse from labeled cells and stain other cell lines [220]. The same tendency was reported for Hoechst dye [221]. When labeled and non-labeled cells were co-cultivated, the transfer of this dye to more than 50% of non-labeled cells was observed within six hours after the start of the experiment. DAPI also stains non-labeled cells due to non-covalent binding to DNA [222]. Moreover, it does not penetrate the cell membrane effectively and cannot be used at higher concentrations due to cytotoxicity, which limits its labeling possibilities [223]. Additionally, dyes are diluted due to cell division, which leads to a decrease in the fluorescence intensity signal. Therefore, tracking is possible for up to three divisions [207].

Cyanine dyes can also exhibit cytotoxic properties [224], and the possibility

of their migration into neighboring unstained cells during co-cultivation has not been sufficiently studied. At the same time, their advantages include the potential for covalent cross-linking with biological molecules [225], as well as a wide choice of dyes with different excitation and fluorescence ranges, including those for near-infrared (NIR) (Cy 5.5, Cy7). Therefore, the development of a new form of the dye for cell labeling is required, which will be demonstrated in Chapter 5.

To conclude, the discussed challenges restrict the applicability of traditional optical labeling with non-covalently binding dyes in free form due to possible distortions in the interpretation of research results. Thus, leakage and dilution of the dye impact the accuracy and efficiency of long-term tracking studies, potentially leading to unreliable data and misinterpretations of cell behaviour over time. Addressing these issues is vital for improving research outcomes, enhancing our understanding of cellular mechanisms, and ensuring the safe and effective application of cell-based therapies in clinical settings.

Chapter 3. Materials and Methods

3.1 Materials

Poly(allylamine hydrochloride) (PAH, Mw = 17.5 kDa), poly(4-styrene sulfonate) sodium salt (PSS, Mw = 70 kDa), dextran sulfate sodium salt (DS, Mw = 40 kDa), calcium chloride dihydrate, sodium carbonate, sodium chloride, ethylenediaminetetraacetic acid (EDTA), and polyvinyl alcohol (PVA) were purchased from Sigma.

The fluorescent dyes rhodamine B (RhB), rhodamine 6G (Rh6G), pyronin B (PyB), fluorescein (Fl), acridine yellow (AY), acridine orange (AO), thiazine red (TR), and rhodamine B isothiocyanate (RITC) were purchased from Sigma. Cyanine 3.5 (Cy3.5) NHC ester, cyanine 5.5 (Cy5.5) NHC ester, and cyanine 7 (Cy7) NHC ester were purchased from Lumiprobe.

Dulbecco's modified Eagle's medium (DMEM), fetal bovine serum (FBS), phosphate-buffered saline (PBS), trypsin/EDTA solution, bovine serum albumin (BSA), Hoechst 33258, Calcein-AM fluorescent dye, and the MTT cell proliferation assay kit were purchased from Thermo Fisher Scientific. Dimethyl sulfoxide (DMSO) was purchased from Merck. DiIC18(5) (DiD) lipophilic tracer was obtained from Lumiprobe. Alpha-MEM and UltraGlutamin I were purchased from Lonza. Streptomycin was obtained from Biolot. The vital dye DRAQ-7 was purchased from BioLegend.

Antibodies that were used and purchased include: CD45 FITC (2D1) from BD Biosciences, CD105 PE (TEA3/17.1.1) from Beckman Coulter, CD34 PerCP-

Vio700 (AC136) from Miltenyi Biotec, and CD90 APC (5E10) from BioLegend.

All reagents were used directly as received without purification. Deionized (DI) water (specific resistivity higher than 18.2 MΩ·cm) from the Direct-Q water purification system was used to prepare all solutions.

3.2 Methods

3.2.1 Capsules synthesis with thermal treatment in PVA gel

3.2.1.1 Layer-by-layer polymer application

Capsule preparation was performed in two stages. During the first stage, layer-by-layer polymer capsules were synthesized as a base. For this, spherical calcium carbonate microparticles were prepared. Equal volumes (0.650 μl) of 1 M calcium chloride and 1 M sodium carbonate were combined under constant stirring in 3 mL of water. The obtained particles were washed twice with water and once with ethanol, and left to dry in a binder drying chamber at 60°C for 3 h. Once enough calcium carbonate microparticles were obtained, polyelectrolytes were applied, alternating PAH and PSS (1 mg/mL in 0.15 M NaCl). Each layer was adsorbed onto the vaterite particles for 10 min at the rotator and washed three times with water using centrifugation (1400 × g, 2 min) 3 times. Consequently, four PAH/PSS bilayers were obtained. EDTA 0.2 M solution was used to dissolve the $CaCO_3$ cores. Subsequently, a DS aqueous solution (2 mg mL^{-1}) was added to the capsules, and the sample was left on the rotator for 1 h. The suspension was then washed with

water three times using centrifugation.

3.2.1.2 Hydrothermal synthesis

For hydrothermal treatment, three PVA gel concentrations were prepared: 11.3, 17, and 22.6 wt%. PVA granules were added to water and left for 1 h to swell. Then, a water bath was used to heat the PVA with constant stirring until all the granules were dissolved. The capsules were dispersed in a dye-aqueous solution. Solution concentrations were different for each dye depending on their solubility: RhB, Rh6G, AO, and TR – 0.5 mg/mL; AY – 0.06 mg/mL; Fl and PyB – 0.05 mg/mL. The capsules were then mixed into the prepared PVA gels and placed in a high-pressure autoclave for thermal treatment (180°C, 3 h). The final concentrations of PVA gel after the addition of dye solution and capsules were 10, 15, and 20 wt%. After cooling, the capsules prepared in 10 and 15 wt% PVA gel were washed in DI water several times until the PVA gel was removed (5,600 × g, 4 min). The capsules prepared in 20 wt% PVA gel were heated using a water bath in the additional volume of water. Then, the gel was removed by centrifugation. The concentration of capsules was counted using a hemocytometer (Goryaev chamber).

3.2.1.3 Surface modification

After hydrothermal treatment, capsules with surface modification were also prepared. For this, PAH and PSS polymers were added to the capsules (1 mg mL^{-1} in 0.15 M NaCl). Each layer was adsorbed onto the particles for 10 min

on the rotator and washed three times with water using centrifugation. As a result, capsules with the following additional layer compositions were obtained: PVA/PAH/PSS, PVA/PAH, where PVA stands for the base capsules prepared in PVA gel.

3.2.2 Capsules synthesis without thermal treatment

3.2.2.1 Preparation of labeled PAH

RITC conjugation with PAH

PAH and RITC can bind through specific functional groups present in their molecular structures. PAH contains amine groups -NH_2, which act as nucleophiles in chemical reactions, participating in the covalent binding process. At the same time, RITC contains a reactive thiocarbamoyl group –N=C=S. This group is capable of forming covalent bonds with the nucleophilic functional groups present in PAH (Figure 3.1).

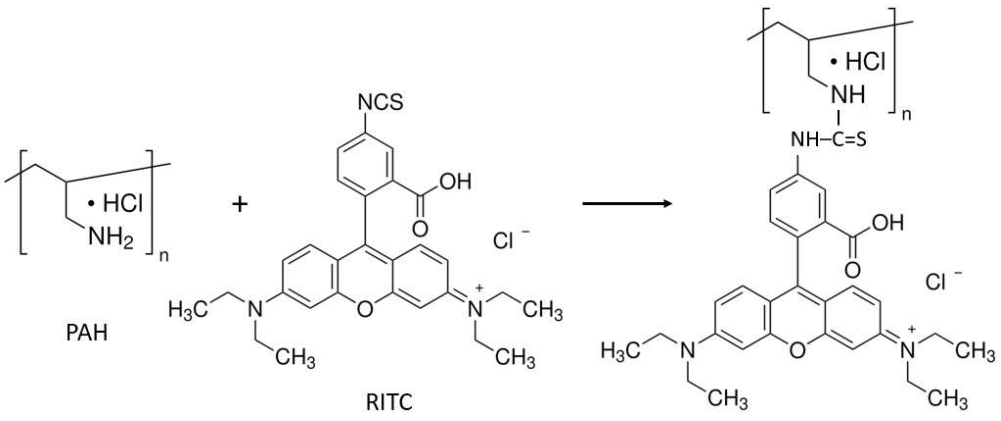

Figure 3.1: Scheme of RITC conjugation with PAH.

To prepare PAH-RITC, the following protocol was used. PAH was diluted in

a 1.3 M NaCl solution (100 mg in 7.6 mL). RITC was diluted in a 1:1 DMSO:H_2O solution (15.3 ml, 2 mg/mL). The two prepared solutions were combined and left for 24 h with constant stirring. After that, the labeled polymer was dialyzed in NaCl solution for four days. The NaCl solution was renewed several times. The final product was kept at -18 °C.

Cyanine NHS ester conjugation with PAH

Cyanine3.5 NHS ester contains a reactive N-hydroxysuccinimide (NHS) ester group. In the presence of primary amines (-NH_2), the NHS ester undergoes amidation, forming stable amide bonds with PAH (Figure 3.2) [226].

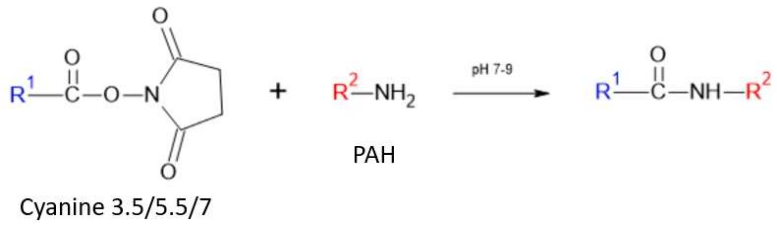

Figure 3.2: Scheme of cyanine 3.5 (or Cy5.5, or Cy7) NHS ester conjugation with PAH [226].

To prepare PAH-Cy3.5 (or Cy5.5, or Cy7), the following procedure was utilized. PAH was diluted in PBS (160 mg in 40 mL), and the pH was neutral. The Cy dye was diluted in ethanol (5 mg in 5 mL). Two mixtures were combined and left with constant stirring overnight at 4 °C. After that, the labeled polymer was dialyzed in NaCl solution for three days at 4 °C. The NaCl solution was renewed several times. The final product was kept at -18 °C.

3.2.2.2 Layer-by-layer polymer application

Capsules were made according to the LbL procedure described above. This means that after the preparation of the calcium carbonate cores, polyelectrolytes were applied consecutively. The only difference in the capsule shell was the presence of PAH-RITC or PAH-Cy3.5/Cy5.5/Cy7 as one of the layers. Therefore, after the dissolution of the inner core, the following capsules were obtained: (PAH/PSS/PAH-dye/PSS/$(PAH/PSS)_n$). No additional modifications were performed.

3.2.3 Cell studies

3.2.3.1 Mouse mesenchymal stem cells (mMSCs)

Cultivation of mMSCs and EPNT-5 cells

mMSCs were obtained at the Raisa Gorbacheva Research Institute of Pavlov University. EPNT-5 (mouse glioblastoma) cells were obtained from the Institute of Biochemistry and Physiology of Plants and Microorganisms, Saratov Scientific Center of the Russian Academy of Sciences (IBPPM RAS) collection. Stock vials of frozen mMSCs and EPNT-5 cells (1 mL) were thawed using a water bath (37 °C). Then, the cell suspension was transferred to 5 mL of warm (37 °C) DMEM (for mMSCs) or EMEM (for EPNT-5) growth medium (10% FBS, 1% penicillin/streptomycin), centrifuged (3 min, 1000 RPM), and placed on flasks with fresh growth medium for subsequent cultivation (37 °C, humidified atmo-

sphere with 5% CO_2). The medium was refreshed 24 h after defrosting. For routine maintenance in culture (passage), cells are seeded at a confluence of approximately 15-20% and grown to a confluence of approximately 80%. For passage, mMSCs and EPNT-5 cells were detached with trypsin/EDTA solution for 5 min.

Cell viability assay

mMSCs were plated on a 96-well plate at the amount of 5×10^3 cells per well and incubated for 12 h (37 °C, humidified atmosphere with 5% CO_2). Then, 1, 5, 10, 15, 20, and 25 microcapsules per cell were added in 100 μL of fresh DMEM growth medium to the wells (in 6 repetitions). The concentration of capsules for this step was calculated using a hemocytometer (Goryaev chamber). mMSCs without microcapsules were used as a positive control. After 24 and 48 h of incubation, the culture medium was replaced with 100 μL of fresh medium containing a 10% MTT stock solution (5 mg/mL in DPBS buffer) and incubated for 3 h at 37 °C. Then, the culture medium with MTT reagent was carefully removed, and 100 μL of DMSO solution was added to each well and incubated for 15 min using a thermoshaker (TS-100 Biosan) at 37 °C and 300 RPM to dissolve the formazan crystals. The absorbance of each well was measured at a wavelength of 570 nm using a spectrophotometer.

Influence of microcapsule amount on internalization efficiency and mMSCs proliferation

mMSCs were plated on a 12-well plate at the amount of 6×10^4 cells per well and incubated for 12 h under identical conditions. Next, 15, 20, and 25 capsules per

cell were added to the wells (in 3 repetitions) in 1 mL of fresh growth medium and incubated for 24 h to allow for internalization. Then, the culture medium was removed, and the cells were carefully washed three times with DPBS to remove uncaptured capsules. Next, the cells were stained using 150 μL of a stock solution with Calcein-AM and Hoechst 33258 in a serum-free medium, which was added to each well and incubated for 20 min. After staining, the cells were washed with a DPBS buffer. Fluorescence images were obtained from 3 randomly selected fields for each well to compare cell proliferation with and without microcapsules. Proliferation was calculated by the number of mMSCs cell nuclei (stained by Hoechst 33258) per 1 cm^2. Images were obtained using an inverted microscope Olympus IX73 (Olympus, Tokyo, Japan).

Then, 150 μL trypsin/EDTA solution was used to harvest the cells, which were then centrifuged (3 min, 1000 RPM) while adding an equivalent quantity of complete growth medium. Next, the medium with trypsin was removed, and cells were suspended in fresh DPBS supplemented with 2% FBS and measured using an ImageStream X Mark II Imaging flow cytometer (Luminex, USA). The measurement parameters were chosen analogously to those for C2C12 cells.

Cell mobility

mMSCs were plated in a 24-well plate at a density of 3×10^4 cells/well and incubated for 12 h. After this, microcapsules were added at concentrations of 15, 20, and 25 capsules per cell and incubated for 24 h. A scratch was made using a pipette tip according to the described protocol [227]. The mMSCs were

washed three times with DPBS to remove detached cells and non-internalized microcapsules. Next, 1 mL of medium with 2% FBS was added to each well. Cells without capsules under the same conditions served as a negative control, while cells without capsules in a medium supplemented with 10% FBS were selected as a positive control. Fluorescence images of mMSCs were obtained after staining with Calcein AM using a 4x\0.3 NA objective immediately after the scratch, and 12 and 24 h later. The migration stage was evaluated by calculating the area between the edges of the wound using ImageJ software.

mMSCs tracking into the EPNT-5 2D and 3D colony

For mMSCs tracking into 2D EPNT-5 cells colony, 2-well silicone inserts with a defined 500 μm cell-free gap were used. The silicone insert was placed on a μ-Dish 35 mm (Ibidi) with a 500 μm grid for the convenience of monitoring changes in the growth areas of cell colonies and to determine the position of labeled mMSCs. The EPNT-5 cells were stained with 0.1% DiD membrane dye in ethanol (2 μL of the solution was added to 200 μL of the medium for 30 min). Then, EPNT-5 cells and mMSCs (containing microcapsules) were placed in the well of the silicone insert (2×10^3 cells per well) and incubated for 12 h (5% CO_2 at 37 °C). Next, the silicone insert was removed, and the migration test was started.

For mMSCs tracking in 3D EPNT-5 cells, the colony used low adhesion 96-well floater plates SDL3D (SPL lifesciences, Korea) to grow spheroids. EPNT-5 (labeled DiD) and mMSCs (containing microcapsules) were mixed in a ratio of 5:1, respectively. Photoconversion of capsules into individual mMSCs and monitoring

of their migration in spheroids was carried out after 24 hours.

Fluorescence images of the area of interest were obtained using a confocal microscope before and 15 min, and 24, 48, and 72 h after microcapsule photoconversion. The settings for obtaining images and photoconversion of the microcapsules were similar to those described in the "Confocal laser scanning microscopy" section. EPNT-5 cells were visualized using a 671 nm laser with a detection range of 685–790 nm.

3.2.3.2 Human mesenchymal stromal cells (hMSC)

Cell preparation

hMSCs were obtained from the bone marrow of healthy donors who provided signed informed consent. The cells were isolated using a direct plating procedure [97]. Briefly, heparinized whole bone marrow was re-suspended in alpha-MEM supplemented with 100 IU/mL penicillin, 0.1 mg/mL streptomycin, 10% FBS, and 2 mM UltraGlutamin I. After the attachment of the cells to the culture plastic, the medium containing non-adherent cells was replaced with fresh culture medium. The culture medium was changed every 3 days until confluence was reached (80%). For passaging, hMSCs were detached using trypsin/EDTA solution for 5 min and replated at a density of 5.0×10^3 cells/cm^2. Cultures from the 2nd-3rd passage were used for further experiments.

Cell tracking

hMSCs were cultivated on 35 mm petri dishes (Ibidi GmbH, Martinsried, Germany) at a density of 3×10^4 cells per dish. The cells were stained with a 0.1%

solution of Cy 7 NHS ester in ethanol (6 μL of the solution was added to 200 μL of the medium for 30 min). This ensured stable hMSCs staining and clear visualization in the fluorescent mode of the confocal microscope for 7 days. Thermally treated photoconvertible microcapsules were added 24 h before the experiment at a ratio of 10 capsules per cell. Fluorescent images of hMSCs were obtained before and at 15 min, 1, 3, 5, and 7 d after microcapsule photoconversion using the confocal microscope. The settings for obtaining the images and photoconversion of the microcapsules were similar to those described later in the section "Confocal laser scanning microscopy." The cells were visualized using a 671 nm laser with a detection range of 685–790 nm.

3.2.3.3 Myocytes

Cultivation of C2C12 and Raw 264.7 cells

Stock vials of frozen C2C12 and Raw 264.7 cells were thawed in a water bath (37 °C) and then maintained in DMEM growth medium (10% FBS, 1% penicillin/streptomycin) at 37 °C in a humidified atmosphere with 5% CO_2. After 24 h, the medium was refreshed. For routine maintenance in culture (passage), cells are seeded at a confluence of approximately 10% and grown to a confluence of approximately 80%. For passage, C2C12 and Raw 264.7 cells were detached with trypsin/EDTA solution for 5 min.

Cell tracking

For cell tracking, 2-well silicone inserts with a defined cell-free gap (500 μm) were used. The silicone insert was placed on a μ-Dish 35 mm (Ibidi) with a 500 μm

grid. This was performed for the convenience of monitoring changes in the growth areas of cell colonies and to determine the position of labeled cells. Raw 264.7 were placed in the first well, and C2C12 (containing microcapsules) was placed in the second well (2×10^3 cells per well). After a 12-h incubation (5% CO_2 at 37 °C), the silicone insert was removed and the migration test was started. The cells were stained with a 0.1% DID membrane dye in ethanol (2 μL of the solution was added to 200 μL of the medium for 30 min). This ensured stable cell staining and clear visualization in the fluorescent mode of the confocal microscope during the 4 days of the experiment. Fluorescence images of the area of interest were obtained using a confocal microscope before and at 15 min, 24, 48, 72, and 96 h after microcapsule photoconversion. The settings for obtaining images and photoconversion of the microcapsules were similar to those described later in the section "Confocal laser scanning microscope." C2C12 and Raw 264.7 cells were visualized using a 671 nm laser with a detection range of 685–790 nm.

3.3 Instruments

3.3.1 Scanning electron microscopy

Scanning electron microscope (SEM) VEGA 3 LM, TESCAN (TESCAN, Czech Republic, Brno) was used for capsule morphology characterization (Figure 3.3 [228]). The samples were prepared by depositing a drop of the capsule suspension on copper tape and leaving it to dry at room temperature. Before imaging, the samples were coated with a thin gold film (approximately 5 nm thick) using a

Q150R ES Plus rotary-pumped coater (Quorum, England) to make them conductive. The voltage used for SEM imaging was 3-7 kV depending on the sample, the working distance was 15 mm, and the tilt was 15 degrees. SEM image analysis was performed using the ImageJ software.

Figure 3.3: Image of scanning electron microscope VEGA 3 LM [228].

In scanning electron microscopy, the electron beam is used to scan the sample [229]. When an electron beam interacts with a surface, signals are generated and detected by the detector. There are several types of detectors:

1. Secondary electron detector. Secondary electrons are emitted by the surface of the sample. Therefore, this detector is sensitive to the surface topography of the sample and is used to study the surface morphology.

2. Backscattered electrons detector. Backscattered electrons are produced due to elastic scattering from the deeper layers of the sample. This detector is sensitive to compositional contrast, so sample components having different compositions will have different grayscale shades in the BSE images. This allows visualization

of compositional differences between sample constituents.

3. Energy dispersive spectrometer. It allows for the determination of the elemental composition of the sample.

3.3.2 Focused ion beam scanning electron microscopy (FIB-SEM)

FIB-SEM was used to obtain images of cut capsules to evaluate their inner structure. A dual-beam scanning electron microscope, Tescan Solaris (Czech), was used (Figure 3.4). Before imaging, the samples were coated with a thin gold film using a Q150R ES Plus rotary-pumped coater (Quorum, England). The

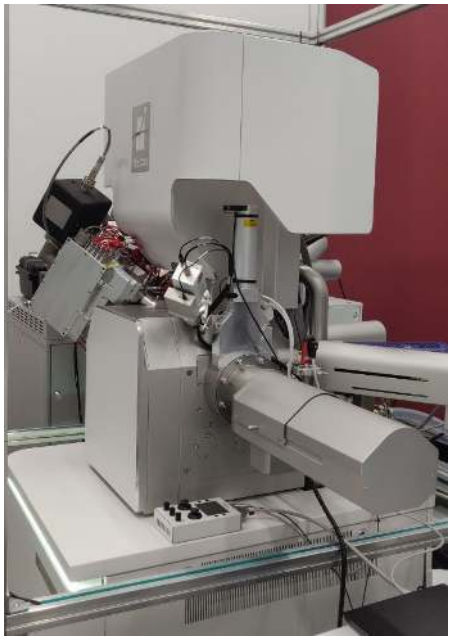

Figure 3.4: Image of FIB-SEM Tescan Solaris.

chosen parameters included the following: high voltage – 3 keV, stage tilt – 55°, acceleration voltage – 3 keV, beam current – 30 nA, dwell time – 10^{-7} s.

In FIB-SEM, the electron beam is used for sample visualization, and the ion

beam is used for analysis. The scheme of FIB-SEM is presented in Figure 3.5 [230]. The focused ion beam of heavy ions (usually gallium) is used to ablate a part of the sample [231]. Gallium ions have low surface free energy, a 29.8 °C melting point, low volatility, and low vapor pressure. Moreover, gallium ions are sufficiently heavy to break down a wide range of materials.

The ion beam interacts with the sample in a variety of ways. Ions collide with sample atoms and lose their energy. It could mostly occur via nuclear energy losses or electronic energy losses. Nuclear collisions might lead not only to sputtering of material atoms but also to back-scattered ions, secondary ion emission, and atom displacements. After several injections, the ion reaches a certain depth and remains in the sample [230].

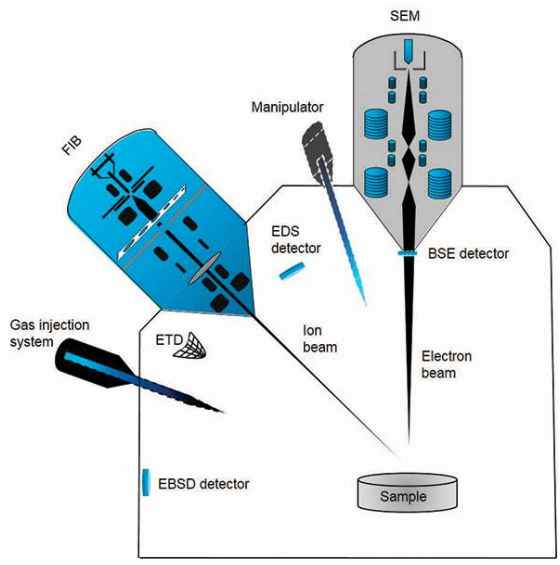

Figure 3.5: Common FIB-SEM scheme [230].

Etch speed and precision are tuned by ion beam intensity. The higher the current, the faster the ablation, but the resolution is lower. Also, non-targeted

surrounding material could be melted, and the amount of re-deposited material might increase. At each step, a fine sample thickness could be removed, followed by visualization by SEM. By repeating this cycle several times, a whole volume of the sample could be precisely visualized [232].

3.3.3 Fluorescence microscopy

Olympus IX73 inverted microscope (Olympus, Japan) was used for visualization of the capsules and cells (Figure 3.6). It is equipped with a 130 W mercury lamp as a source of light. The parameters of the cubes are the following: excitation 360-370 nm and emission 420-460 nm; excitation 470-495 nm and emission 510-550 nm; excitation 540-550 nm and emission 575-625 nm.

Figure 3.6: Olympus IX73 inverted microscope.

The fluorescence phenomenon includes the adsorption of a photon with higher energy and subsequent emission of the photon with lower energy since some energy

is lost in this process [233]. The higher energy photon has a shorter wavelength (excitation light), and the lower energy photon has a longer wavelength (emitted light). This phenomenon is called the Stokes shift.

The key principle of the fluorescence microscope is to separate the emitted light from the excitation beam. It is achieved by using optical filters in correlation to the spectra of the dyes used for sample staining. The scheme of the light path in the fluorescent microscope is presented in Figure 3.7 [233]. Here, excitation light from the mercury lamp is directed through excitation filter cube DM1 with a dichroic mirror. The light goes to the sample, and the emitted fluorescence light follows back to the emission cube DM2. Here, it is separated into two beams. The barrier B blocks excitation light from the detector. Emission filters Em1 and Em2 also block undesirable light. The final signal is detected by the detectors.

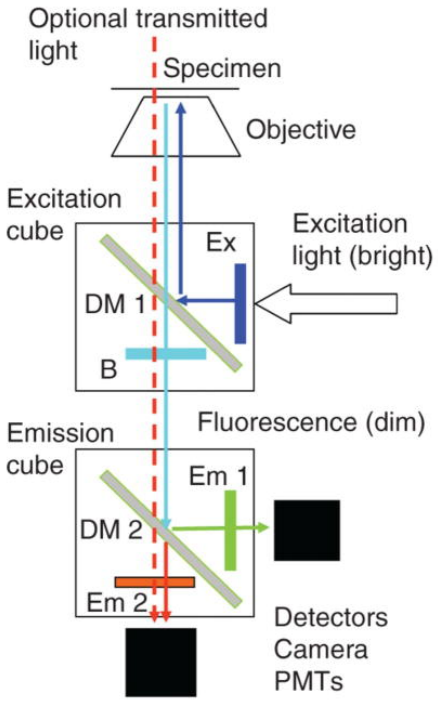

Figure 3.7: Scheme of the light path of a fluorescent microscope [233].

3.3.4 Confocal laser scanning microscopy (CLSM)

3.3.4.1 Confocal microscope

CLSM was performed using the Leica TCS SP8 X (Leica, Germany) for capsule characterization and cell experiment visualization (Figure 3.8). The microscope is equipped with 10x/0.40 NA, 20x/0.70 NA, and 40x/0.60 NA air objectives, as well as 40x/1.30 NA, 63x/1.40 NA, and 100x/1.44 NA oil objectives. The set of lasers includes 405, 458, 488, 514, 561, and 671 nm. The power of the 458, 488, and 514 nm lasers is 21.7 mW, the power of the 561 nm laser is 50 mW, and the power of the 671 nm laser is 100 mW.

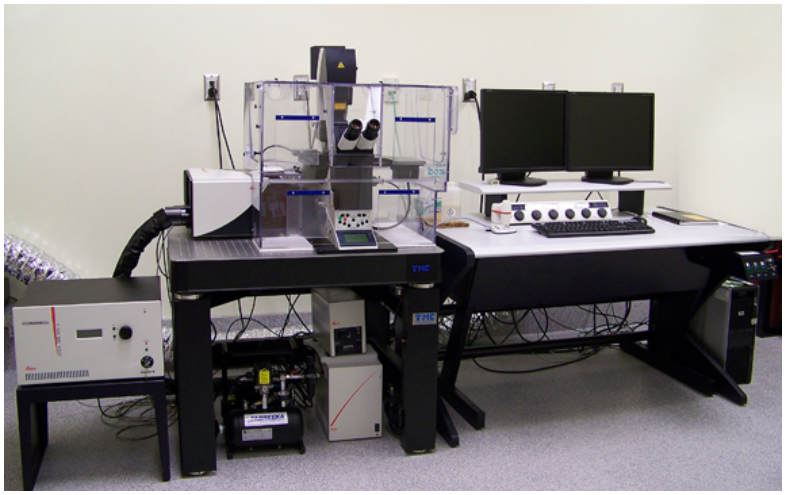

Figure 3.8: Image of CLSM Leica TCS SP8 X.

For capsule imaging, a drop of the sample was deposited on the slide and covered with a cover glass. The edges were sealed to prevent the movement of the capsules due to water evaporation. The cells were visualized in Petri dishes. The visualization system is located in the environmental chamber with temperature

and CO_2 for long-term imaging and tracking of the cells.

In a conventional fluorescence microscope, the entire sample is uniformly illuminated by the microscope's radiation source [234]. In the case of the confocal microscope, point illumination and a pinhole are used to exclude out-of-focus signal (Figure 3.9) [234]. Thus, fluorescent radiation is detected only from the focal plane. Therefore, the resolution of the image is much higher than what conventional fluorescence microscopes provide.

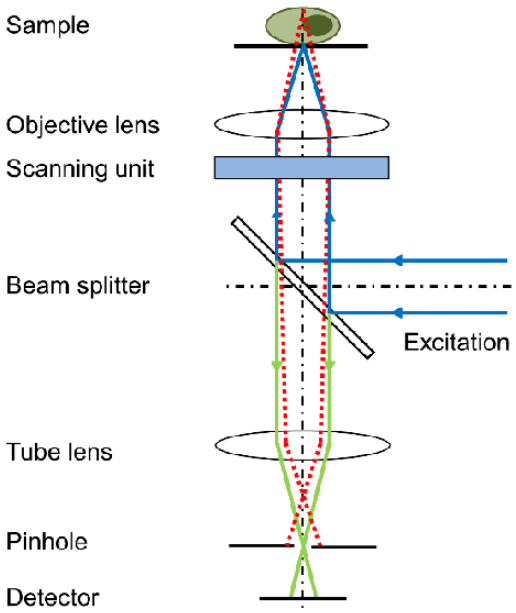

Figure 3.9: CLSM scheme [234].

Also, since only one fluorescent point is recorded, a scan of the sample is required to form a 2D or 3D raster image. The laser beam moves across the sample in an XY-plane using mirrors with a controlled angle of inclination. Slower scanning provides a better signal-to-noise ratio, which results in better contrast and higher resolution. Nevertheless, since most of the fluorescence signal is blocked

out, it leads to decreased intensity of the signal. To compensate for this, sensitive photodetectors and longer detector exposure are used. The optical signal is transformed into an electrical signal, which can be seen on the computer screen.

3.3.4.2 CLSM studies of fluorescent polymer microcapsules

Capsules imaging

Objective 20x/0.70 NA was used for CLSM imaging. Lasers with wavelengths of 405, 488, and 561 nm were used for microcapsule excitation and detection. The fluorescence of the capsules with dyes Fl, AY, AO, and TR was excited at 488 nm and detected in the range of 505–600 nm. For convenience, it is called the green channel. The fluorescence of the RhB, Rh6G, PyB, Cy3.5, and RITC dyes was excited at 561 nm and detected in the range of 580–620 nm for RhB, in the range of 580–670 for Rh6G and PyB, in the range of 580–630 for Cy3.5. For convenience, it is called the red channel. The fluorescence of the capsules with the dyes Cy5.5 and Cy7 was excited with a 671 nm laser and detected in the range of 686–790 nm, which is called the NIR channel.

The laser power densities (LPD) for the visualization of the samples were 9 kW/cm^2 for Fl, AY, AO, and TR; 6 kW/cm^2 for RhB, Cy3.5, and RITC; 18 kW/cm^2 for Rh6G and PyB; and 9 kW/cm^2 for Cy5.5 and Cy7.

Photoconversion

For the photoconversion procedure, the smallest possible scanning area was chosen, which corresponded to 12.11 $\times$ 12.11 μm with 512 $\times$ 512 pixels and a scanning speed of 10 Hz. For the photoconversion process, the observed area was magnified

to represent the capsules selected for the procedure. The laser power density used for the photoconversion process was 451 kW/cm^2 for RhB and Rh6G; 193, 322, and 451 kW/cm^2 for Cy3.5 and RITC; 180, 451, and 721 kW/cm^2 for Cy5.5. The signal from the photoconverted capsules was detected in the range 505–540 nm (excited with the 488 nm laser). The LPD for visualization in this channel was 9 kW/cm^2. Changes in the fluorescence intensities of the capsules before and after collecting the time series and performing photoconversion were evaluated using Gwyddion software [235].

Capsules photostability measurements

The photostability of the capsules containing the dyes was evaluated by collecting a time series of 15 scans at standard settings usually used for obtaining high-quality images of the cells. The settings included a 1024 × 1024 pixel spatial resolution, a 100 Hz scanning speed, and the following LPDs: 9 kW/cm^2 for Fl, AY, AO, and TR; 6 kW/cm^2 for RhB and Cy3.5; 18 kW/cm^2 for Rh6G and PyB; and 9 kW/cm^2 for Cy5.5.

λ-scans measurements

The λ-scans were recorded for capsules by excitation with lasers at 488 and 405 nm. The selected scan ranges were 505–700 and 420–600 nm, respectively, with a 20 nm detection bandwidth and a 5 nm λ-detection step size.

Measurement of capsules fluorescence intensity

Capsule fluorescence intensity was measured with Gwyddion software. The tool "Radial profiles" was utilized. In this tool, the line is used as the diameter of the

capsule to define a circular area (Figure 3.10). The center of the line is marked

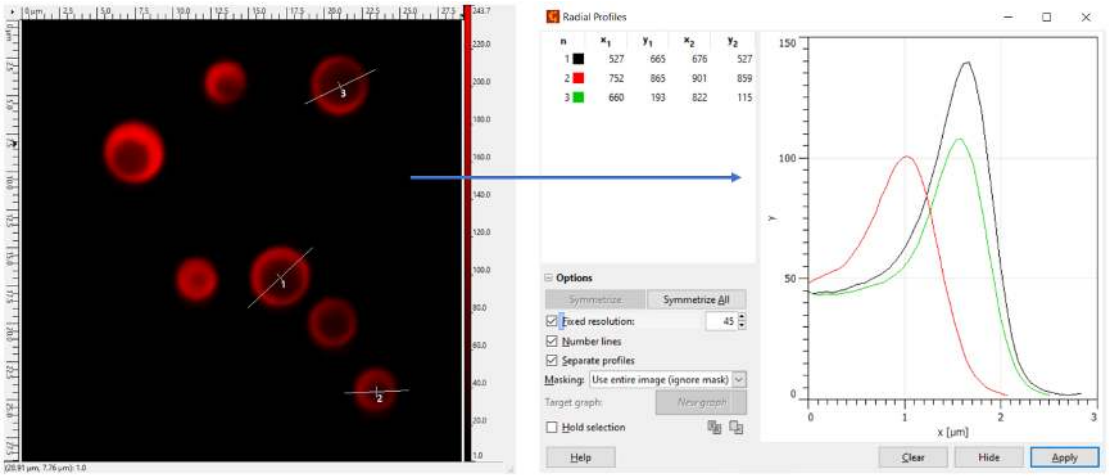

Figure 3.10: Gwyddion program interface when "Radial profiles" tool is used.

with a tick, and the best position of the tick can be adjusted in the program by clicking "Symmetrize". The profile of capsule fluorescence intensity is then obtained by angular averaging. The final graph demonstrates the dependence of fluorescence intensity on the radius of the capsules.

3.3.5 Zeta-sizer

Zetasizer Malvern Nano ZS (Malvern Panalytical, United Kingdom) was used to measure the zeta potential of the capsules (Figure 3.11). For this, semitransparent water solutions of samples were prepared and sonicated in an ultrasonic (US) bath before measurements.

The dynamic light scattering is used to measure the diameter of the particles. The particles dispersed in the solution are moving due to Brownian motion, which leads to the local fluctuations of particle concentrations. The following lo-

Figure 3.11: Image of zeta sizer Malvern Nano.

cal inhomogeneities of the refractive index lead to fluctuations in the intensity of scattered light when a laser beam passes through the sample. The received signal is analyzed using correlation spectroscopy, the autocorrelation function is calculated, and on this basis, the particle size distribution is constructed. For spherical particles that do not interact with each other, their size can be calculated using the Stokes-Einstein formula:

$$D = \frac{k_B T}{6\pi\eta R}, \tag{3.1}$$

where k_B – Boltzmann constant, T – absolute temperature, η – shear viscosity of the medium in which particles of radius R are suspended.

Zeta potential is the electrical potential at the shear plane. To measure zeta potential, a known constant voltage is applied to the electrodes. This leads to the migration of the particles to the electrode with the opposite charge. Since the voltage and the distance between the electrodes are known, the electrophoretic mobility can be determined, from which the zeta potential can then be calculated

with Henry's equation:

$$U_E = \frac{2\varepsilon\zeta}{3\eta} f(\kappa a), \tag{3.2}$$

where U_E – electrophoretic mobility, ε – dielectric constant, ζ – zeta-potential, κ – viscosity of the solution, and $f(\kappa a)$ – Henry's function.

3.3.6 Plate reader measurements

Plate reader Tecan Infinite 200 PRO (TECAN, Switzerland) was used for absorbance and fluorescence spectra measurements of the solutions (Figure 3.12). The plate reader combines both monochromator- and filter-based optics, which gives a wide range of wavelengths accessible for measurements. The absorbance spectral range is from 230 to 1000 nm. Fluorescence can be analyzed within the range of 280 to 850 nm. Parameters for fluorescence spectra excitation and detection of the dyes are listed in Table 3.1. Typically, 150 μL of the solution was added to a 96-well plate for the measurements.

Figure 3.12: Image of plate reader Tecan Infinite 200 PRO.

For absorbance measurements, a light with a specific wavelength illuminates the sample. The detector receives the light after it passes through the sample and

The dye	λ_{ex}	Detection range
RhB and Rh6G	455 nm	490–650 nm
PyB	470 nm	505–650 nm
Fl	440 nm	475–650 nm
AY	400 nm	435–650 nm
AO	425 nm	460–650 nm
TR	405 nm	540–650 nm
Cy3.5	530 nm	565–750 nm
Cy5.5	615 nm	650–850 nm
Cy7	685 nm	720–850 nm
RITC	495 nm	530-700 nm

Table 3.1: Parameters for fluorescence spectra detection of the dyes.

calculates the percentage of the light intensity decrease [236].

In fluorescence measurements, after illumination of the sample with the chosen light wavelength, the sample emits light. This fluorescence signal is collected by separating emitted light from excitation light by the filtering system. The final signal is measured with the detector.

3.3.7 Mass spectrometery

Mass spectrometer

Mass spectrometry (MS) was performed using a Q Exactive Hybrid Quadrupole-Orbitrap (Thermo Fisher Scientific, Figure 3.13). The mass spectrometer is used

to obtain information about the m/z value of the samples' ions. Moreover, MS spectra can demonstrate isotope masses. When ionized, molecules can disintegrate and produce fragment ions, which should be taken into account when analyzing the data. The general scheme of the equipment is presented in Figure 3.14 [237]. Three main components include an ionization source, mass analyzer, and detector.

Figure 3.13: Image of Q Exactive Hybrid Quadrupole-Orbitrap mass spectrometer.

In Orbitrap MS, electrospray ionization is used to transfer the sample to a gaseous state. After injection, the liquid is sprayed into a stream of hot nitrogen through the capillary. The charge from the nebulizer flows onto the formed liquid droplets. In a flow of hot nitrogen, the solvent in the droplet evaporates, its diameter decreases, and the surface charge increases. Then, a Coulomb explosion occurs – the droplet bursts and the charge goes to the molecules inside. The external electric field guides the ions further to a mass analyzer (MA).

Orbitrap MA consists of two electrodes: external and coaxial inner electrodes. The ions are trapped to rotate around the inner electrode in elliptical paths, and

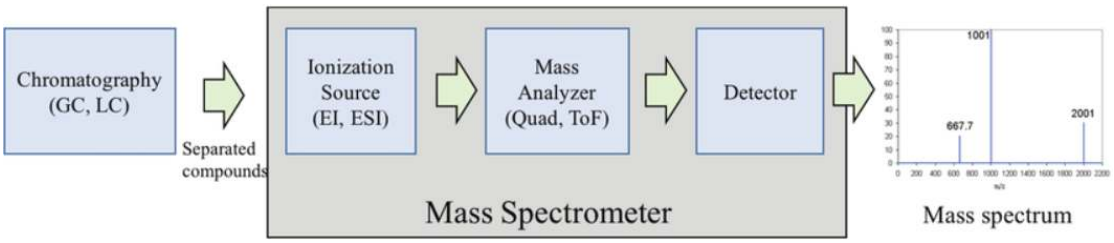

Figure 3.14: General scheme of the mass spectrometer [237].

they move back and forth along the axis of the central electrode. The current from the trapped ions is detected and converted into a mass spectrum using the Fourier transform of the resulting frequency signal. Therefore, the orbitrap also acts as a detector of ions. Angular frequency:

$$\omega = \frac{\sqrt{k}}{m/z}, \tag{3.3}$$

where k_B is the force constant of the potential, similar to the spring stiffness.

Sample preparation for mass spectrometry

For mass spectrometry measurements, RhB and R6G were prepared in three forms. The first was an initial solution of the dye in water (2 μM). The second form was a solution of the dye at a concentration of 1 μM, autoclaved with DS (0.3 μg/mL) for 3 h at 180°C. In the third form, the obtained solution was poured into a quartz cell and placed in a dark chamber. In the chamber, the solution was irradiated with a UV lamp (15 W, 254 nm peak) for 20 min for Rh6G and 30 min for RhB under constant stirring. Before the mass spectrometry measurements, the samples were diluted twice with a solution of equal parts of acetonitrile and water with 0.1 % formic acid. The injection volume was 200 μL. Ionization was performed with electrospray in positive mode. The detection range was 200–1000 m/z.

Chapter 4. Thermal Treatment in PVA Gel to Facilitate Photoconvertible Capsule Synthesis and Capsules' Characterization

4.1 Introduction

Cell tracking plays a crucial role in understanding the behaviour, migration, and fate of individual cells within large populations [8, 9, 238, 239]. The ability to trace cell pathways provides valuable insights into various biological processes, such as the interactions between cancer cells and immune cells [240]. This allows for the evaluation of the proliferation degree and rate for further selection of immune cells with the best characteristics. The subsequently created cell line derived from cell selection and purification holds potential for applications in tissue engineering and personalized medicine, specifically for targeted drug delivery to the tumor site.

Optical marking of cells has emerged as a powerful tool for cell tracking, offering the potential to label and monitor cells with high precision. This approach primarily relies on the use of genetically modified cells expressing GFP-like proteins such as Dreiklang [12], Dronpa [13], mTFP0.7 [241], rsCherryRev [242], IrisFPs [14], and others. The synthesis of GFP-like proteins in cells is achieved via transfection [15]. Although genetic modification is effective in certain cell types, it may not be feasible for all cell types. For example, fibroblasts [243], CHO cells [244], astrocytes [245], neural cells [246], and other cells exhibit the potential for effective

transfection. Nevertheless, significant challenges arise when working with some cell lines, for instance, primary cultures [247], especially stem cells [20], thereby limiting the applicability of traditional optical labeling techniques with GFP-like proteins. Particularly for stem cells, the process of transfection gives rise to concerns regarding the potential for utilizing these cells in the scope of personalized medicine. Another conventional approach for cell labeling is the use of lipophilic membrane dyes. Nevertheless, they often experience leakage from cells, and the intensity of the signal is reduced over time due to cell division [21, 22].

As an alternative to transfection, previous studies proposed the utilization of polymer microcapsules [24]. Capsules function as microreactors that combine rhodamine B (RhB) as a fluorescent dye and carbon nanodots (CNDs) as a photocatalytic agent. Upon subjecting the polymer capsules to laser radiation, a photocatalytic reaction occurs within the capsule, resulting in alterations in the emission spectra of RhB. Polymer capsules are highly advantageous as tracking labels because of their low toxicity [88], ease of internalization by diverse cell types, and prolonged retention within cells [248]. These properties make them a desirable option for cell tracking purposes. However, several challenges persist in this approach. One such challenge is the need to explore additional fluorescent dyes that emit in different spectral ranges, thereby expanding the possibilities of cell tracking. Another unresolved issue is connected to the significant loss of capsules during hydrothermal treatment. It happens primarily due to capsules melting together when synthesis is performed in a dye-aqueous solution. Subsequent filtration to

remove fused capsules further increases the capsule loss.

This chapter focuses on the development of stable, scalable, and easy-to-reproduce labels for cell tracking as an alternative to GFP-like proteins and lipophilic dyes. Several concentrations of polyvinyl alcohol (PVA) gel (10, 15, and 20 wt%) were tested as a medium for capsule thermal treatment to increase their production yield. The effect of the additional dextran sulfate (DS) as a source of CNDs on capsule intensity and morphology was investigated. Rhodamine 6G (Rh6G), pyronin B (PyB), fluorescein (Fl), acridine yellow (AY), acridine orange (AO), and thiazine red (TR) were investigated in comparison to previously reported RhB. Capsule morphology was examined using scanning electron microscopy (SEM) and focused ion beam SEM. Capsules with various dyes were examined for their brightness of fluorescence, photostability, and photoconversion ability with CLSM. The photoconversion mechanism was studied using mass spectrometry.

4.2 High yield production of fluorescent capsules synthesis via PVA gel

A recent study [24] revealed that carbonized polyelectrolyte capsules containing RhB retained high fluorescence after thermal treatment, exhibited photoconversion properties, and were stable for cell tracking. This type of capsule was prepared according to a previously described method based on PSS and PAH polymers [249]. DS was also applied to the capsules as a source of CNDs, which were formed during

thermal treatment and played the role of a catalyst for the photoconversion of the dye during laser irradiation [250]. The dye encapsulation in microcapsules was performed through hydrothermal synthesis in water, which presented certain limitations. The capsules sank to the bottom of the autoclave and formed a single layer. If too many capsules were placed in the autoclave, capsules would remain in contact, leading to their fusion at high temperatures. Aggregates of capsules thermally treated in water can be seen in Figure 4.1. Therefore, an additional filtration step was required to remove large aggregates. Both the limit of capsule load in the autoclave and the filtration step caused a reduction in the production yield.

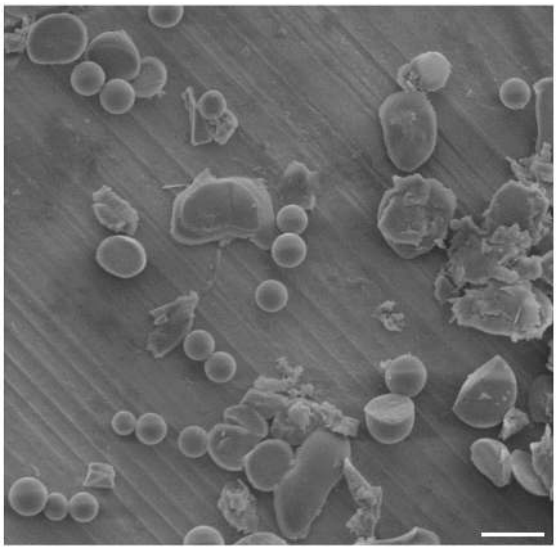

Figure 4.1: SEM image of polymer microcapsules after thermal treatment in water (scale bar is 5 μm).

Therefore, in the first phase of this research, the last stage of synthesis was modified to increase the production yield of capsules. To achieve that, PVA gel was

used as the medium for capsules instead of water during thermal treatment. PVA is a water-soluble, non-toxic, biocompatible, and biodegradable polymer [251], which is important for the production of materials for use in biological systems. It is also thermally stable since it decomposes around 220 °C [252], which makes PVA gel a perfect candidate as a medium for capsule production.

To select the most optimal concentration of PVA gel, three options were prepared: 10, 15, and 20 wt% (Figure 4.2). The represented percentages of the gel correspond to the final concentration achieved after the addition of capsule suspension and dye solution to the gel. Such concentrations were chosen since PVA gel concentrations higher than 20 wt% is too viscous [253, 254]. As a model dye, RhB was used since it has already been demonstrated to possess photoconversion properties in capsules [24]. After thermal treatment and complete cooling, the 10 and 15 wt% PVA gels were removed by washing the capsules several times with room temperature water and centrifuging.

Nevertheless, 20 wt% PVA gel was problematic to separate from capsules, since it did not dissolve in room temperature water. Maximum PVA concentration in water was reported to be 25 wt% [253], which is usually prepared by freeze-drying or heating to 90-100 °C [255]. Commonly used concentrations of PVA gels include those below 20 wt% [254]. Therefore, there was the a need to heat up again a highly concentrated 20 wt% PVA gel with capsules in additional water. It allowed both to dissolve the PVA gel and reduce its concentration to approximately 2 wt%. Then, the PVA gel was removed as usual with water and centrifuging. Such an additional

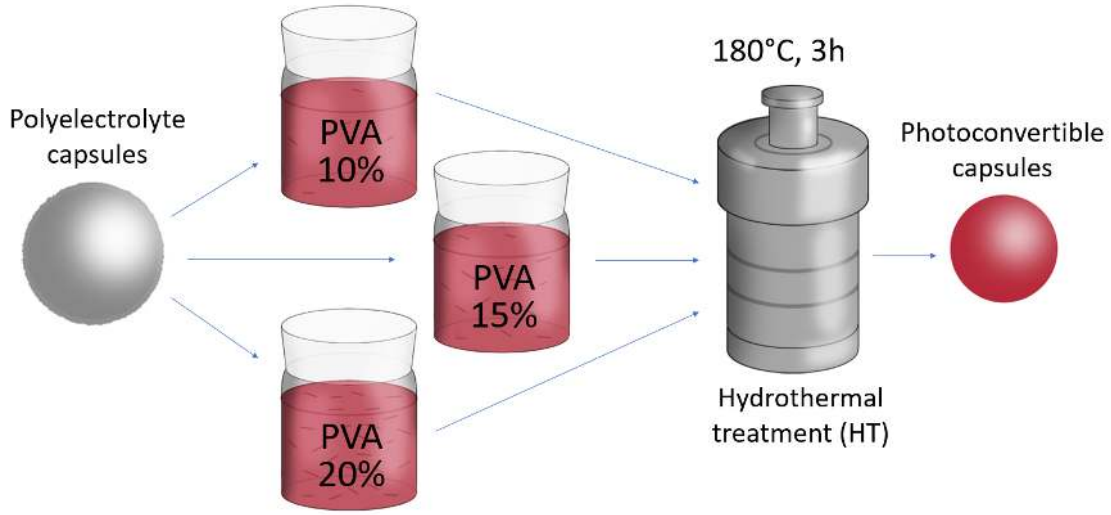

Figure 4.2: Scheme of the preparation of the thermally treated microcapsules in 10, 15, and 20 wt% PVA gel with RhB.

manufacturing step complicates the process of capsule production in 20% PVA gel, making this concentration option less desirable for further application.

In addition to PVA, other polymers can potentially be used as a medium for capsule synthesis. For example, poly(ethylene oxide) (PEO), which is water-soluble, biocompatible, and biodegradable, and it decomposes around 320 °C [256], demonstrating high thermal stability. Depending on the PEO molecular weight, similar to the PVA viscosities could be obtained [257]. Another option for capsule treatment medium might be water-soluble and biocompatible polyvinylpyrrolidone (PVP), which decomposes around 380 °C [258]. In addition, polyacrylic acid (PAA) is also water-soluble and biocompatible, and it starts to decompose between 230 and 300 °C [259]. Therefore, it can be potentially used for capsule thermal treatment. Nevertheless, concentrations of polymer gels should be carefully adjusted to obtain appropriate viscosity.

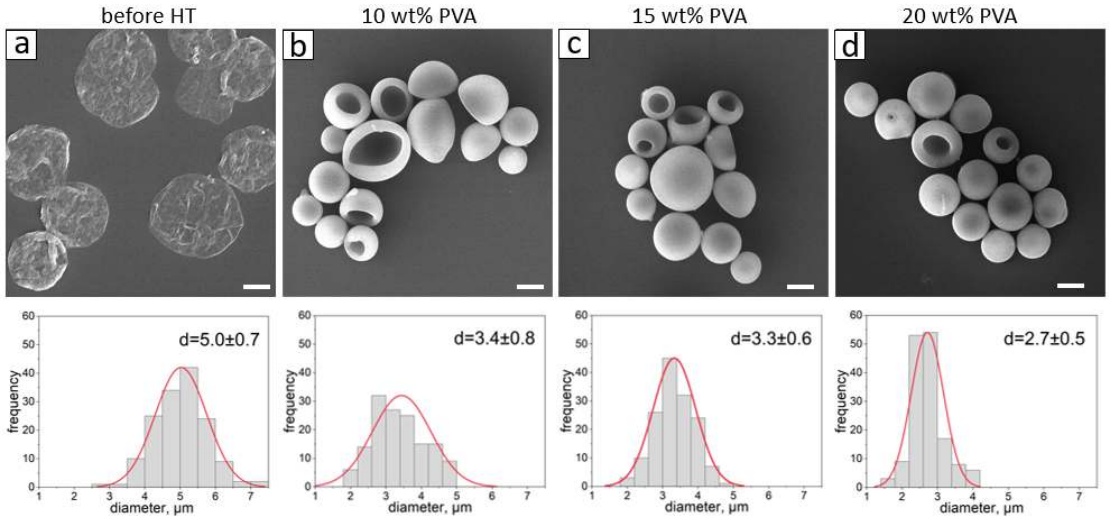

Figure 4.3: SEM images of capsules (a) before and after thermal treatment in (b) 10, (c) 15 and (d) 20 wt% PVA gel with corresponding histograms of diameters distribution (scale bar is 2 μm).

SEM images of capsules prepared in 10, 15, and 20 wt% PVA gel and capsules before thermal treatment are presented in Figure 4.3. The diameter turned out to be 5.0 $\pm$ 0.7 μm for the initial capsules and approximately 30% less for the capsules after thermal treatment in 10 and 15 wt% PVA gel (Figure 4.3). The decrease in capsule size due to the thermal treatment was also observed by other researchers [260]. This is related to the increased mobility of the polymer chains and hydrophobic interactions.

At the same time, the diameter of capsules made in 20 wt% PVA gel was 2.7 $\pm$ 0.5 μm, which is almost half the size of the initial capsules. Supposedly, it happened due to the earlier described additional step of heating this sample in excess water to remove the gel. The reduced percentage and, therefore, viscosity of the gel allowed capsules to shrink tighter under exposure to high temperature

due to the increased mobility of polymer chains [260].

In addition to the decrease in size, SEM also demonstrated a change in the capsules' shape. Thus, dried capsules without hydrothermal treatment collapsed due to the absence of a hard core. At the same time, capsules after heat treatment retained a spherical shape, which also indirectly indicates compaction of the polymer layers and an increase in the thickness of the shell. Moreover, the dent in part of the capsules could be observed, indicating that capsules fold upon drying due to the thin polymer shell. This data was supported by FIB-SEM images (Figure 4.4). After the cutting with the ion beam, the presence of the cavity in polymer

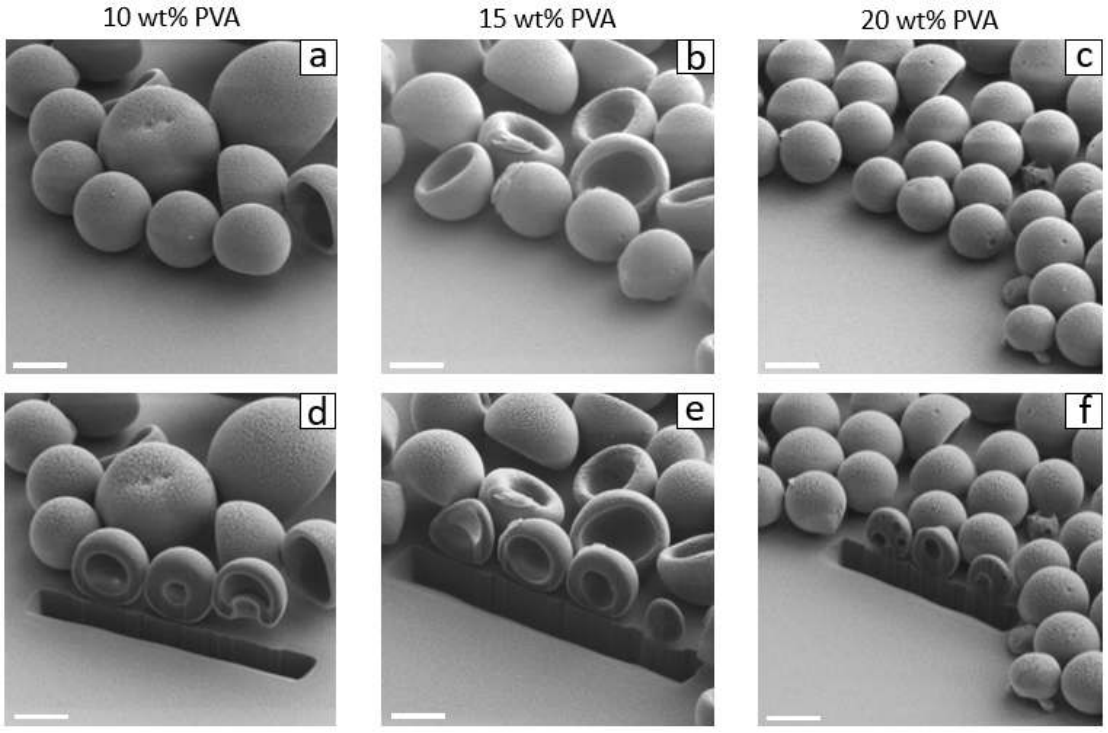

Figure 4.4: FIB-SEM images of capsules before and after cut with ion beam. Capsules prepared in 10 (a,d), 15 (b,e), and 20 (c,f) wt% PVA gel (scale bar is 2 μm).

capsules could be observed. Also, the formation of the dent can be seen in Figure 4.4d. The thickness of the capsule shell increased due to the compression of polymer layers under high temperatures.

The appropriately high viscosity of the PVA gel [261] allowed the capsules to remain separate from each other in the thickness of the gel during thermal treatment. This prevented the capsules from fusing during autoclaving and eliminated the need for further filtration (Figure 4.3). In addition, more capsules could be placed in the autoclave in this approach because capsules were distributed in the volume of the reactor and not only at the bottom. As a result, the capsule yield in one synthesis using PVA gel increased by at least 250 times in comparison to the synthesis in water, which was counted using a hemocytometer (Goryaev chamber).

To choose the most optimal PVA concentration, photoconversion of capsules was performed. CLSM images are presented in Figure 4.5a-c, demonstrating the possibility to photoconvert capsules prepared in all three PVA concentration options. It means that the use of PVA gel for capsule synthesis did not affect the presence of the photoconversion effect. Λ-scans of capsules also demonstrated the presence of a spectra blue shift for all the samples (Figure 4.5d-f). The shifted spectra could be detected in the range 505–540 nm, which allowed for the observation the photoconversion effect.

Using CLSM images, angularly averaged intensities of capsules in red and green channels were extracted (Figure 4.6). According to the Student's t-Test, a statistically significant difference in intensity values between 10 and 15 wt% PVA

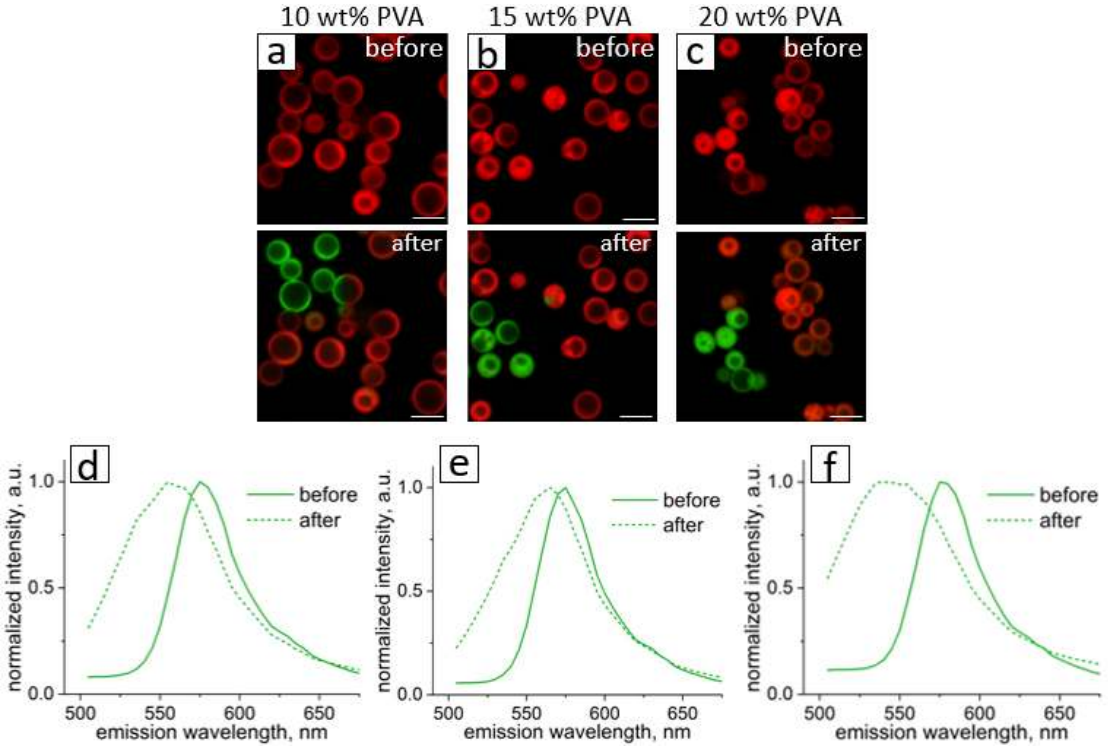

Figure 4.5: CLSM images of capsules prepared in (a) 10, (b) 15, and (c) 20 wt% PVA gel with RhB before and after photoconversion (scale bar is 5 μm). Λ-scans of capsules prepared in (d) 10, (e) 15, and (f) 20 wt% PVA gel with RhB before and after photoconversion.

was observed in both red and green channels. It means that the thermal treatment of capsules in 15 and 20 wt% PVA gel indeed provides a higher intensity signal in comparison to treatment in 10 wt% PVA. It might mean that in the case of 10 wt% PVA, a lower amount of RhB was encapsulated due to a lower concentration of PVA gel. RhB has an overall positive charge, capsules have a negative charge, and PVA is a non-ionic polymer. As was explained earlier [73], RhB diffused through the capsule into the inner cavity and bound to the capsule shell. Heat treatment caused the compensation of the inner charge, removing some part of RhB from

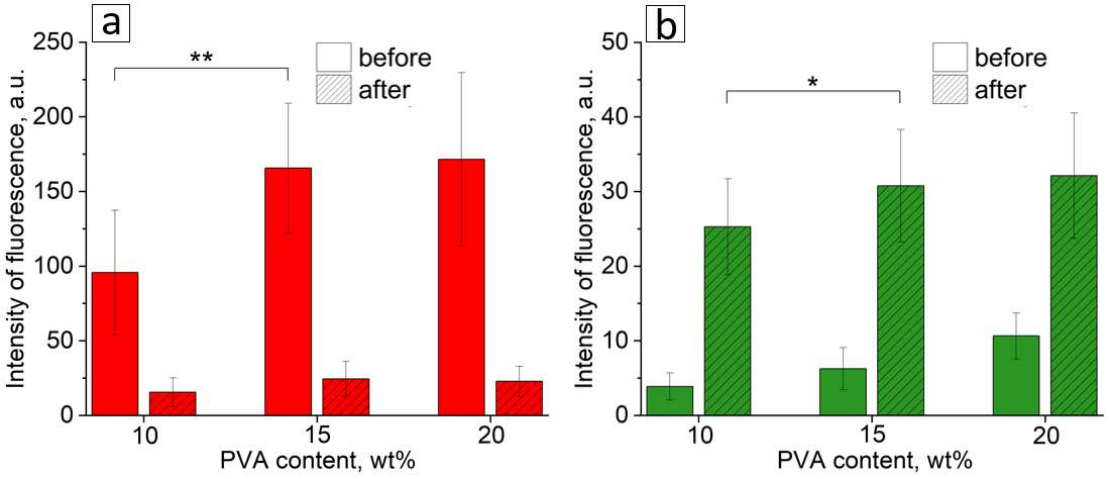

Figure 4.6: Angularly averaged intensities of capsules (prepared in 10, 15, and 20 wt% PVA) in (a) red and (b) green channels before and after photoconversion. **P<0.001, *P<0.05

the shell. At the same time, the higher the PVA concentration, the lower the apparent diffusion coefficient (ADC) [262]. Therefore, RhB could be released from the capsules more easily into the matrix of a lower-concentration PVA gel due to the higher ADC. As a result, the fluorescence intensity of capsules treated in 10 wt% PVA came out lower.

Taking into account the need for an additional heating step of the 20 wt% PVA gel in excess water to purify capsules and lower fluorescence intensity of capsules prepared in 10 wt% gel, the most optimal gel concentration was chosen to be 15 wt%. This concentration was used further for the preparation of all the samples. Overall, the utilization of PVA gel as a medium for capsule synthesis allowed for the optimization and scaling up of the production yield of capsules by hundreds of times.

4.3 Carbon nanodots influence on photoconvertible capsules

In the initially published article [24], DS was used as a source of carbon for CNDs synthesis in the capsules. Such CNDs were proposed to act as a photocatalyst for the photoconversion reaction. Here, the effect of DS application on the capsule surface before thermal treatment was investigated. For this, capsules containing RhB with and without DS were synthesized using thermal treatment. Also, similar capsules containing no dye were prepared. SEM images and histograms of the capsule diameters are present in Figure 4.7.

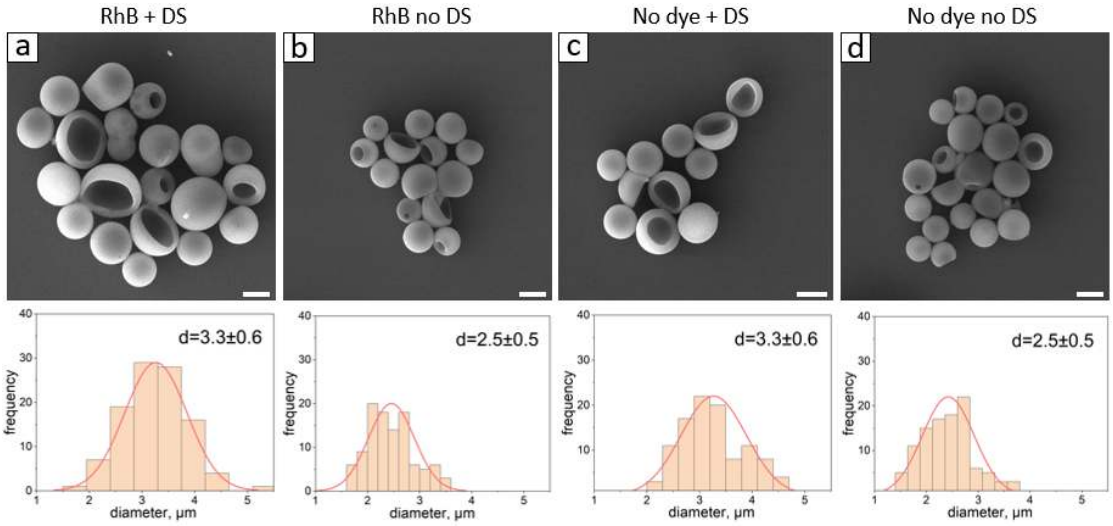

Figure 4.7: SEM images and corresponding histograms of diameters of capsules after thermal treatment in PVA gel (a) with RhB and DS applied on the capsule surface, (b) with Rh B and no DS, (c) without the dye and with applied DS, (d) without the dye and no DS (scale bar is 2 μm).

According to the obtained data, the diameter of capsules containing DS as an outer layer was 3.3 $\pm$ 0.6 μm, while the diameter of capsules without DS was

smaller: 2.5 ± 0.5 μm. This phenomenon is related to the odd or even amount of layers in the capsule shell [263]. The addition of an extra DS layer created a different ratio between positively and negatively charged polyelectrolytes. This led to a different ratio between electrostatic force, which expands the capsule shell, and hydrophobic force caused by unfavorable interaction between the polymer and water, which shrinks the capsule shell [264]. The excess of negative charge due to the presence of the DS layer leads to a higher value of electrostatic force, which makes capsules shrink less under the high temperatures [263].

4.3.1 Capsules containing RhB with and without DS

The possibility to photoconvert capsules containing RhB without DS was also analyzed, and CLSM images are presented in Figure 4.8a. Also, λ-scans of capsules

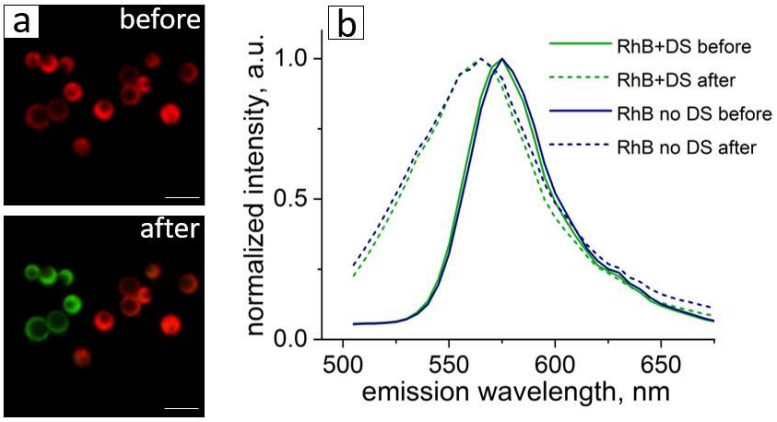

Figure 4.8: (a) CLSM images of capsules containing RhB without application of DS before and after photoconversion (scale bar is 5 μm). (b) Λ-scans of capsules with RhB with and without DS before and after photoconversion.

with and without DS are presented in Figure 4.8b, which are almost identical. It

means that CNDs from DS sources are not obligatory to achieve photoconversion of capsules.

Moreover, fluorescent intensities of labels with and without DS were compared before and after photoconversion in red and green channels (Figure 4.9). The data

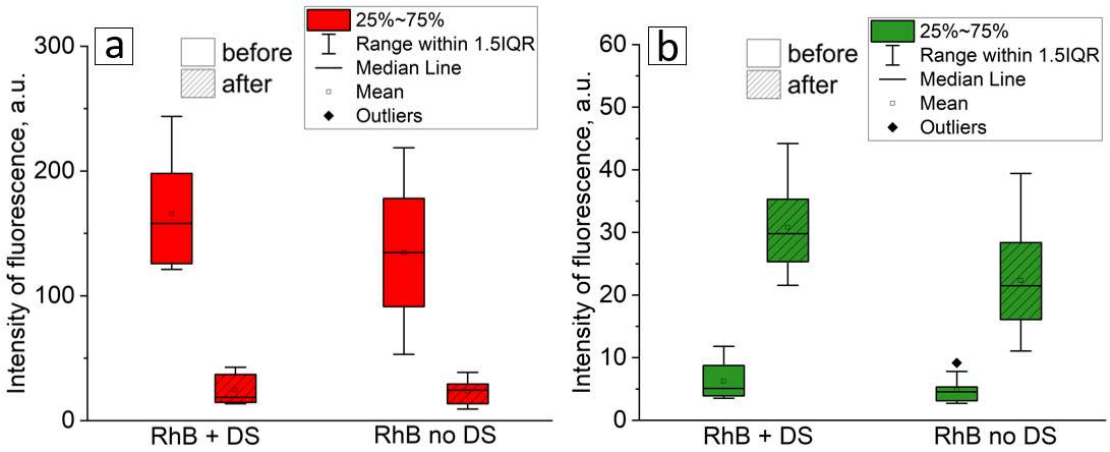

Figure 4.9: Box plot of capsule intensities before and after photoconversion (containing RhB with and without DS) in (a) red and (b) green channels.

is depicted as a box plot to show the distributions of intensity values. Whiskers mark the range where the data are present. Notably, for capsules with DS, all the intensity values in the red channel before photoconversion are higher than 120 a.u., while for capsules without DS, intensity values start from approximately 50 a.u. Nevertheless, according to the Student's t-test, P=0.053, which makes the data difference between these two sets of data not statistically significant. In the green channel, all intensity values of capsules with DS are higher than 20 a.u. after photoconversion, while for capsules without DS, the lowest intensity value is approximately 11 a.u. Also, P=0.007 for these two sets of values, which makes the data difference statistically significant.

Taking into account the overall higher intensity values of capsules with DS in both channels (which is statistically significant in the green channel), the capsules with DS are preferable as potential cell labels, since they can provide a higher and narrower range of fluorescence intensity. This could be connected to the fact that DS has a negative charge, which stimulates the diffusion of positively charged RhB molecules into capsules and binds to the capsule shell. This might give a more uniform loading of the dye into the capsules.

4.3.2 Capsules containing no dye with and without DS

CLSM images of the capsules containing no dye, with or without the outer layer of DS, were obtained (Figure 4.10a,b). The capsules fluoresced in the green channel. The irradiation of the capsules with a 561 nm laser was performed to mimic the photoconversion procedure (irradiated capsules are marked with ovals). The fluorescence intensities of capsules before and after the procedure are presented in Figure 4.10c. No change in intensity was observed. Moreover, the intensities of both samples are similar, indicating that DS did not affect the fluorescence signal.

Λ-scans of capsules were recorded using 405 and 488 nm lasers for excitation. The resulting spectra are different (green and violet lines), which means that they depend on the excitation wavelength. It indirectly indicates that CNDs are present in capsules since they are well known to exhibit excitation-dependent fluorescence [265]. Therefore, CNDs are formed during the thermal treatment of the capsules with or without the additional DS. Indeed, CNDs could be synthesized

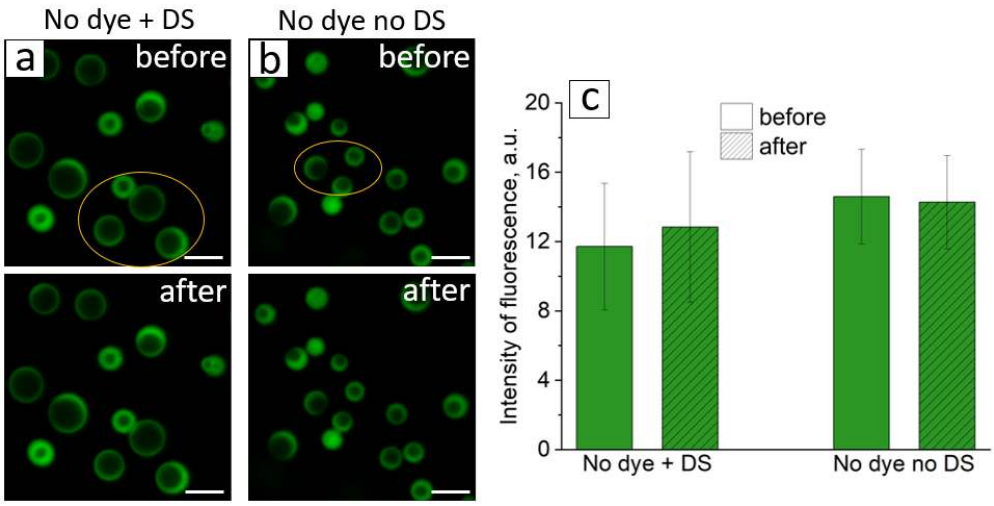

Figure 4.10: CLSM images of capsules (containing no dye) (a) with DS and (b) without DS before and after 561 nm laser irradiation (scale bar is 5 μm). (c) Corresponding angular intensities of capsules before and after 561 nm laser irradiation.

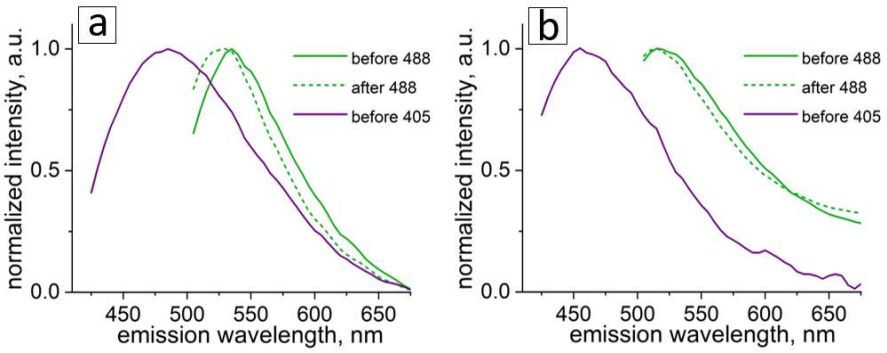

Figure 4.11: Λ-scans of capsules (containing no dye) (a) with DS and (b) without DS before and after 561 nm laser irradiation. Green lines correspond to the excitation of λ-scan at 488 nm, violet line corresponds to the excitation of λ-scan at 405 nm.

from other capsule components, such as polystyrene sulfonate [266]. Potentially, polyallylamine hydrochloride can also be used as a source of carbon for CNDs [267].

To conclude, photoconvertible polymer microcapsules could be synthesized both with and without DS. Nevertheless, the addition of DS allowed for obtaining capsules with bigger diameters, which is preferable for cell labeling. Moreover, the presence of DS provided capsules with higher fluorescence intensity. All of that makes capsules with DS more attractive for further application. Therefore, DS is used for the synthesis of the capsules in this chapter.

4.4 Encapsulation of fluorescent dyes

In addition to RhB, other dyes have been reported to exhibit blue spectral shifts upon irradiation. Several of them were chosen as fluorescent in the red channel, similar to RhB: Rh6G [189], PyB as an analog of rhodamine dyes [191], and TR [201]. Other dyes were chosen as fluorescent in the green channel, which might give more opportunities for labeling in different spectral ranges: Fl [268], AY [200], and AO [199]. Moreover, all of them, except Fl, have methyl groups that are often removed during radiation exposure, causing a blue shift of the dye spectra. The dyes were selected for further investigation in this research as promising candidates for the synthesis of photoconvertible labels. The objective was to assess the potential of loading these dyes into capsules while preserving their inherent fluorescent properties. The scheme of the capsule synthesis is presented in Figure 4.12.

SEM images of the capsules before and after treatment in the PVA gel for each of the seven dyes were obtained (Figure 4.13). The diameters of the capsules were

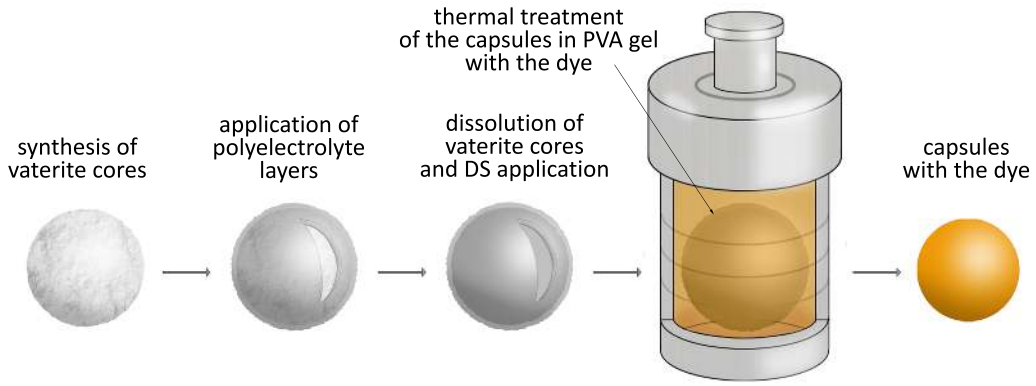

Figure 4.12: Scheme of the preparation of the thermally treated microcapsules in PVA gel with the dye.

calculated using ImageJ based on at least 150 capsules; histograms are present in Figure 4.14.

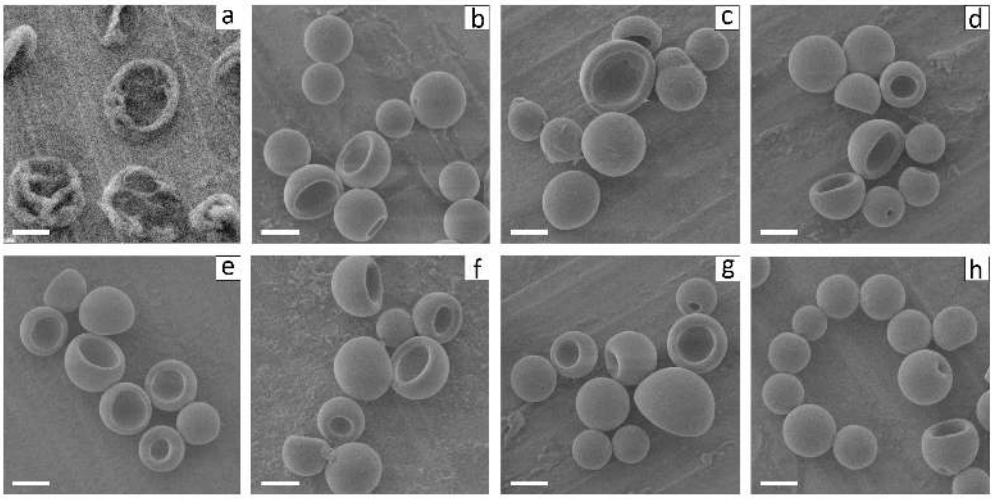

Figure 4.13: SEM images of polymer microcapsules before (a) and after thermal treatment in PVA gel with Rhodamine B (b), Rhodamine 6G (c), Pyronin B (d), Fluorescein (e), Acridine Yellow (f), Acridine Orange (g), and Thiazine Red (h) (scale bar is 2 μm).

CLSM images of the capsules are presented above each size data point (Figure

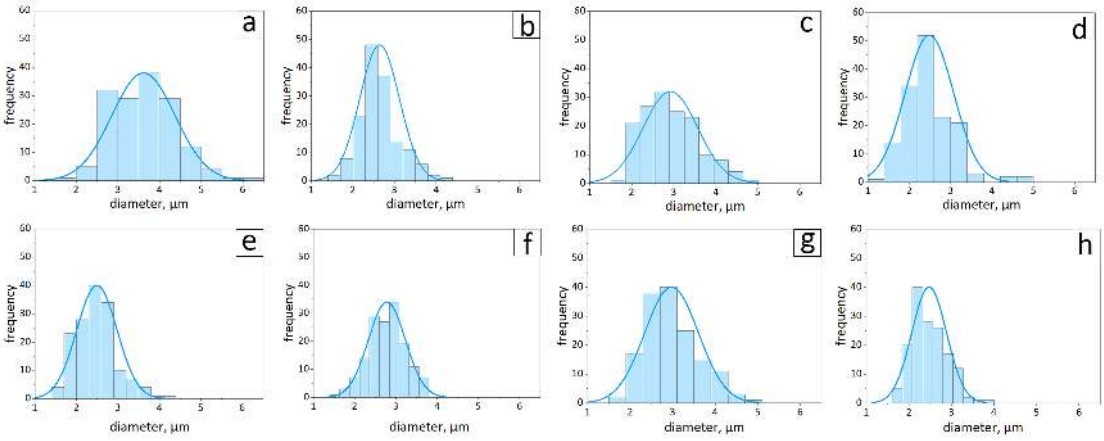

Figure 4.14: Histograms of polymer microcapsule size distribution before (a) and after thermal treatment in PVA gel. Microcapsules are loaded with Rhodamine B (b), Rhodamine 6G (c), Pyronin B (d), Fluorescein (e), Acridine Yellow (f), Acridine Orange (g), and Thiazine Red (h).

4.15). The excitation and emission parameters were tuned based on the possibility of locating them as close as possible to the fluorescence spectra of the dyes. The dye excitation and emission spectra are presented in Figure 4.16.

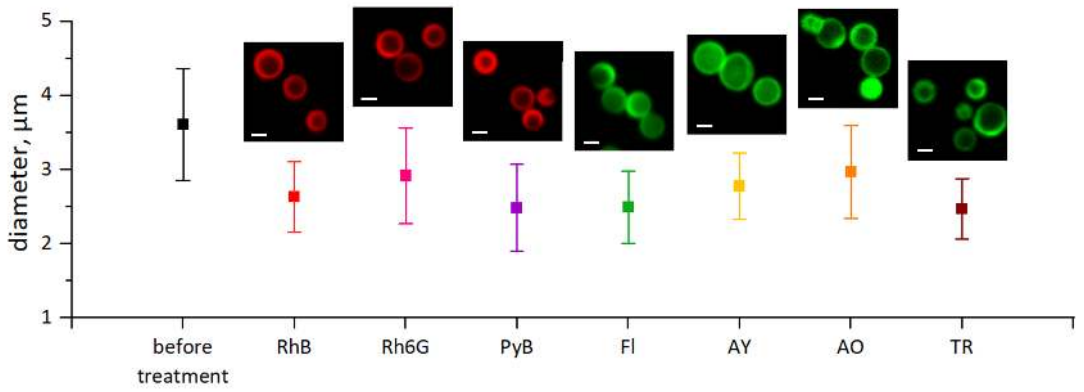

Figure 4.15: Graph of the capsule diameters before and after thermal treatment with the dyes RhB, Rh6G, PyB, Fl, AY, AO, and TR with the corresponding CLSM images (scale bar is 2 μm).

For capsules containing RhB, fluorescence was excited by a 561 nm laser and detected in the range of 580–620 nm. Rh6G and PyB were excited by a 561 nm laser and detected in the range of 580–670 nm, which is referred to as the red channel for ease of perception. Fl, AY, AO, and TR were excited by a 488 nm laser and detected in the range of 505–600 nm, which is referred to as the green channel. The applied excitation wavelengths and detection ranges of the capsules conformed to those of the dye excitation and emission spectra (Figure 4.16), except for TR.

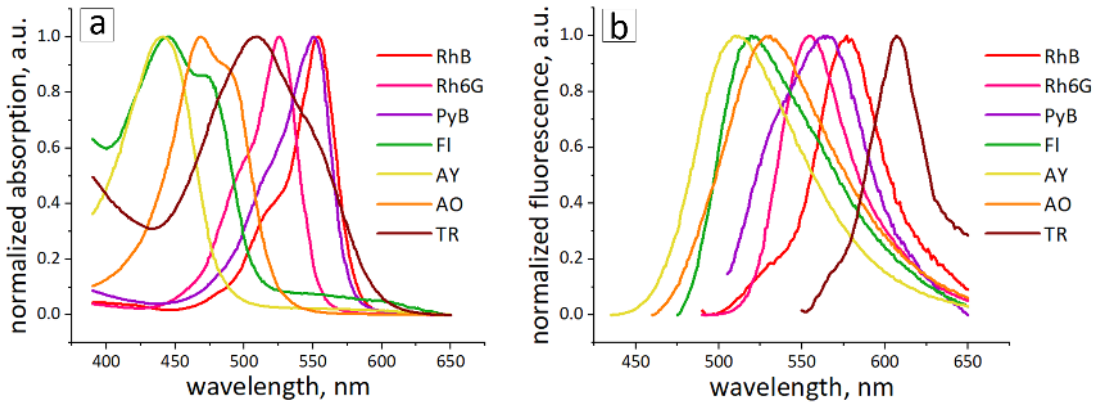

Figure 4.16: Normalized absorption (a) and fluorescence (b) spectra of the dye solutions.

TR has an excitation wavelength maximum of 509 nm and an emission wavelength maximum of 607 nm (Figure 4.16). Therefore, it is supposed to be excited with a 561 nm laser and visualized in the red channel. Nevertheless, capsules with TR were detected in the green channel. Most probably, such a change in fluorescence parameters is associated with the effects of high temperature and pressure during hydrothermal synthesis, which indirectly indicates a change in the structure

of the dye. Since capsules containing TR still exhibited noticeable fluorescence in the green channel, the sample was further investigated. Thus, temperature treatment of microcapsules during hydrothermal synthesis provided the encapsulation of a wide range of low molecular weight dyes due to the ability of polyelectrolyte layers to compress under high temperatures, which is consistent with the results of other authors [269]. Note that encapsulated dyes retained their fluorescent properties while only one of them changed its spectral properties after encapsulation (Figure 4.15).

4.5 Fluorescence intensity of capsules containing selected dyes

Stable bright fluorescence of labels is a crucial parameter for prolonged cell tracking. Therefore, the fluorescence intensity values of the capsules were also analyzed. This was performed by obtaining a series of angularly averaged intensity profiles from CLSM images. Images were obtained with equal laser settings in separate channels (except for RhB, which is further explained). The obtained values were normalized separately for the dyes in the red (RhB, Rh6G, and PyB) and green (Fl, AY, AO, and TR) channels (Figure 4.17a). The fluorescence intensities of the capsules varied across the samples. The difference in intensity is related to the excitation and detection conditions of the dyes. λ-scans are presented in Figure 4.17. Red rectangles correspond to the 580–620/670 nm detection ranges (red channel), and green rectangles correspond to the 505–600 nm detection range of the confocal microscope (green channel). These parameters were set to obtain

confocal images. Such parameters were less optimal for Rh6G, PyB, AY, AO, and TR, as can be seen from their λ-scans, but could not be changed due to the discreteness of the lasers included in the design of the confocal microscope. RhB exhibited the highest intensity among the dyes in the red channel. Therefore, a lower laser power density (LPD) and a narrower detection region were chosen for this dye (Figure 4.17b-d).

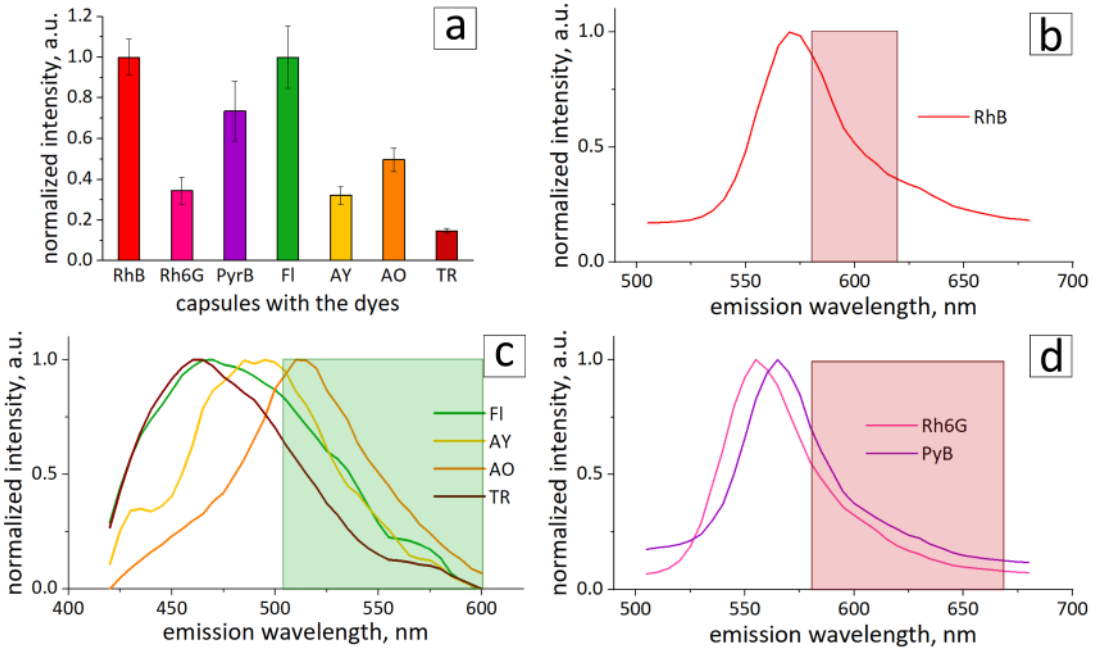

Figure 4.17: (a) Angularly averaged fluorescence intensities of the capsules with dyes RhB, Rh6G, and PyB (detection range 580–620/670 nm, red channel) and Fl, AY, AO, and TR (detection range 505–600 nm, green channel). λ-scans of capsules with (b) RhB, (c) Rh6G, and PyB (488 nm excitation). λ-scans of capsules with (d) Fl, AY, AO, and TR (405 nm excitation). Red and green rectangles correspond to the detection ranges 580–620/670 nm and 505–600 nm, respectively.

Fl exhibited the highest fluorescence intensity in the green channel. Its emission

maximum was located farther from the detection region than those of AY and AO. Nevertheless, it has a higher quantum yield (0.79 against 0.47 and 0.2 for AY and AO, respectively) [270–272]; therefore, its intensity is higher. It is usually sufficient to increase the laser intensity and gain to obtain bright confocal images to overcome the weak fluorescence. Nevertheless, it would have had a high impact on the stability of the dyes, which was further demonstrated.

4.6 Study of the photostability of the dyes in the capsules

One of the most important characteristics of cell labels is their photostability during long-term tracking for several days. The fluorescent label must withstand prolonged detection and imaging processes. To evaluate the photostability of the dyes in the capsules, bleaching tests were performed. Time-series confocal scans of 15 frames were obtained at standard laser settings used to record high-quality images of the cells. The fluorescence intensities of the capsules before and after the time series were calculated by angularly averaging the intensity profiles. The intensities are presented in Figure 4.18 and were normalized to the data before the bleaching test.

According to the obtained graph, capsules containing RhB and Rh6G lost approximately 10% of their fluorescence intensity after the procedure. PyB dye intensity was reduced by 40%. Fl, AY, AO, and TR lost approximately 75% of their fluorescence intensity. This means that even if the laser intensity and gain are increased to obtain brighter confocal images, it will lead to even more rapid

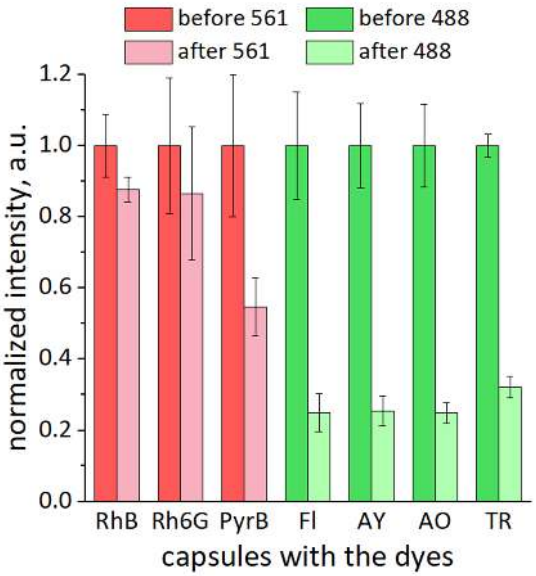

Figure 4.18: Normalized changes in the fluorescence intensity of the dyes before and after the bleaching test.

bleaching of these dyes. Low fluorescence intensity and photostability made dyes Fl, AY, AO, and TR unfavorable for long-term tracking. Therefore, these four dyes were excluded from further studies. The following experiments were performed on capsules containing RhB, Rh6G, and PyB dyes.

4.7 Photoconversion on capsules with RhB, Rh6G, and PyB

The photoconversion abilities of capsules containing RhB, Rh6G, and PyB were analyzed. CLSM images before and after the photoconversion procedure are presented in Figure 4.19. The fluorescence of the capsules was excited at 561 nm and detected in the range 580–620/670 nm.

Photoconversion was performed using a laser with a wavelength of 561 nm. The increased signal after photoconversion appeared in the range of 505–540 nm

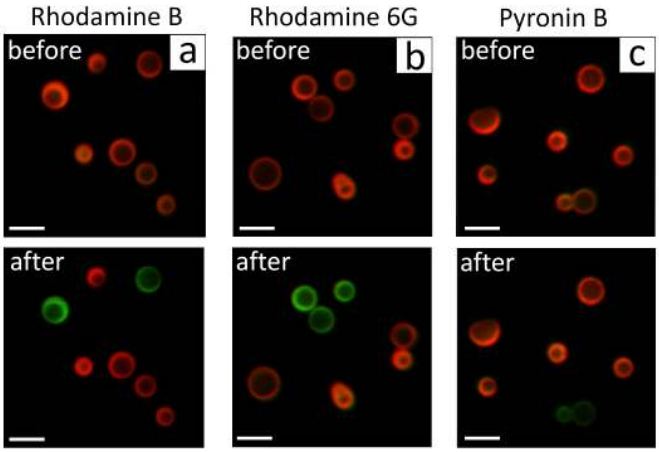

Figure 4.19: CLSM images of thermally treated microcapsules in PVA gel with RhB (a), Rh6G (b), and PyB (c) before and after photoconversion (scale bar is 5 μm).

for RhB and Rh6G excited by the laser with a 488 nm wavelength. At the same time, no such effect was observed for PyB.

For each sample, angularly averaged profiles of the fluorescence intensities were extracted from the CLSM images before and after the procedure. The intensities changed both in the green and red channels for RhB and Rh6G (Figure 4.20ab,de). The fluorescence signal was significantly reduced in the red channel and considerably increased in the green channel. Thus, the desired photoconversion effect was observed due to changes in the intensity of the signal in the red and green channels. The photoconversion of capsules with RhB correlates with the data obtained earlier for capsules with this dye made by hydrothermal treatment in water [24]. Both RhB and Rh6G belong to the rhodamine family [273]. Therefore, the photoconversion effect for Rh6G might correlate with similarities in the chemical structure of these two dyes [274].

Due to the laser exposure, the intensity of capsules with PyB was reduced in the red channel but remained at the same level in the green channel (Figure 4.20hi). Therefore, the signal in the green channel was insufficient to detect it for labeling purposes. Low stability of the pyronin dye was demonstrated previously [275], which correlates with the obtained results. At the same time, a blue shift of λ-scan under 488 nm excitation in the case of PyB was also observed (Figure 4.20j). Supposedly, a blue shift is present owing to the decrease in the signal in the red channel. In other words, because part of the spectral signal was detected in the green channel (505–540 nm) before photoconversion, it became more prominent after the bleaching of the dye in the red channel. This effect resulted in a blue shift of capsule spectra.

Additionally, λ-scans of capsules containing RhB and Rh6G under 488 nm excitation before and after photoconversion were recorded (Figure 4.20c,f). For both dyes, a blue shift of the spectra was observed after laser irradiation. A similar phenomenon of absorbance spectra blue shift upon irradiation was demonstrated previously for both RhB and Rh6G dyes [185, 189]. To justify the observed effect for emission spectra, solutions of RhB and Rh6G dyes were prepared after thermal treatment with DS. The solutions were exposed to UV radiation to mimic the influence of the laser. The changes in the fluorescence spectra are shown in Figure 4.23. The fluorescence spectrum of RhB demonstrated the growth of a left shoulder peak due to UV radiation. The fluorescence spectrum of Rh6G exhibited a blue shift upon UV irradiation. Therefore, the observed changes in the dyes'

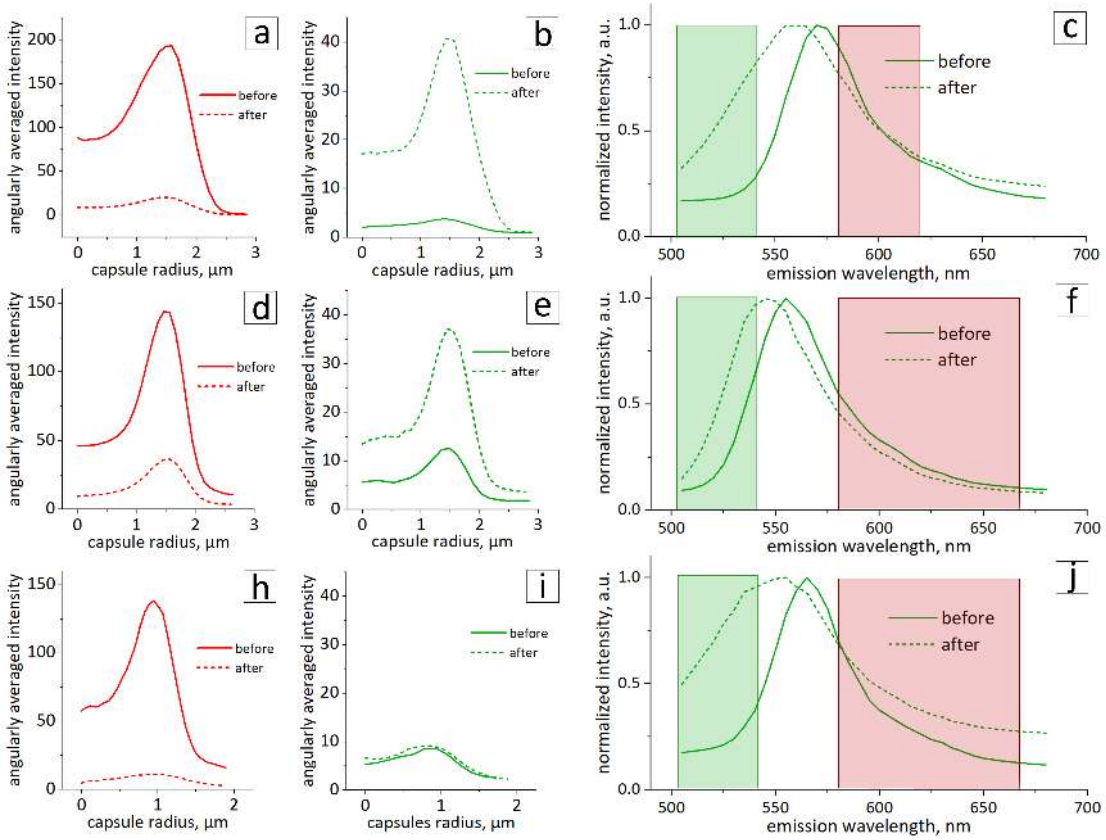

Figure 4.20: Changes in the angularly averaged fluorescence intensity of the capsules before and after laser irradiation in the red and green channels of RhB (a,b), Rh6G (d,e), and PyB (h,i). Capsule emission spectra under 488 nm excitation before and after laser conversion for RhB (c), Rh6G (f), and PyB (j) (green and red rectangles correspond to the 505–540 and 580–620/670 nm detection ranges of the confocal microscope, respectively).

fluorescence spectra after UV exposure support the blue shift of capsules' λ-scans upon laser irradiation.

In the previous studies, it was shown that the efficiency of microcapsule photoconversion depends significantly on the wavelength, and the optimum wavelength was reported to be 554 nm (absorption peak of RhB) [24]. Also, in different

studies, the possibility of the photoconversion of microcapsules using the most common constant and pulsed lasers at 532 nm was evaluated [276]. In this thesis, a standard confocal laser with a wavelength of 561 nm was used for the photoconversion. Taken together, this data shows that the developed fluorescent labels can be photoconverted using various types of lasers (at least in the range of 532–561 nm). This makes the developed approach useful for a wide range of researchers. Note that the photoconversion settings must be optimized for a particular optical system.

Since PyB did not demonstrate photoconversion ability, it was not studied further. Therefore, subsequent mass spectrometric studies were performed only for RhB and Rh6G.

4.8 Mass spectrometric study of RhB and Rh6G photoconversion mechanism

Previously, it was suggested that capsule photoconversion is possible due to RhB going through several deethylation steps under laser irradiation in combination with CNDs acting as a catalyst [24]. To verify this hypothesis, mass spectrometry of RhB and Rh6G aqueous solutions was performed. Dye solutions were prepared according to the same thermal treatment scheme as that used for the capsules. Aqueous solutions of the dyes without thermal treatment were used as the controls. The mass spectrometry results obtained for six prepared samples are shown in Figure 4.21.

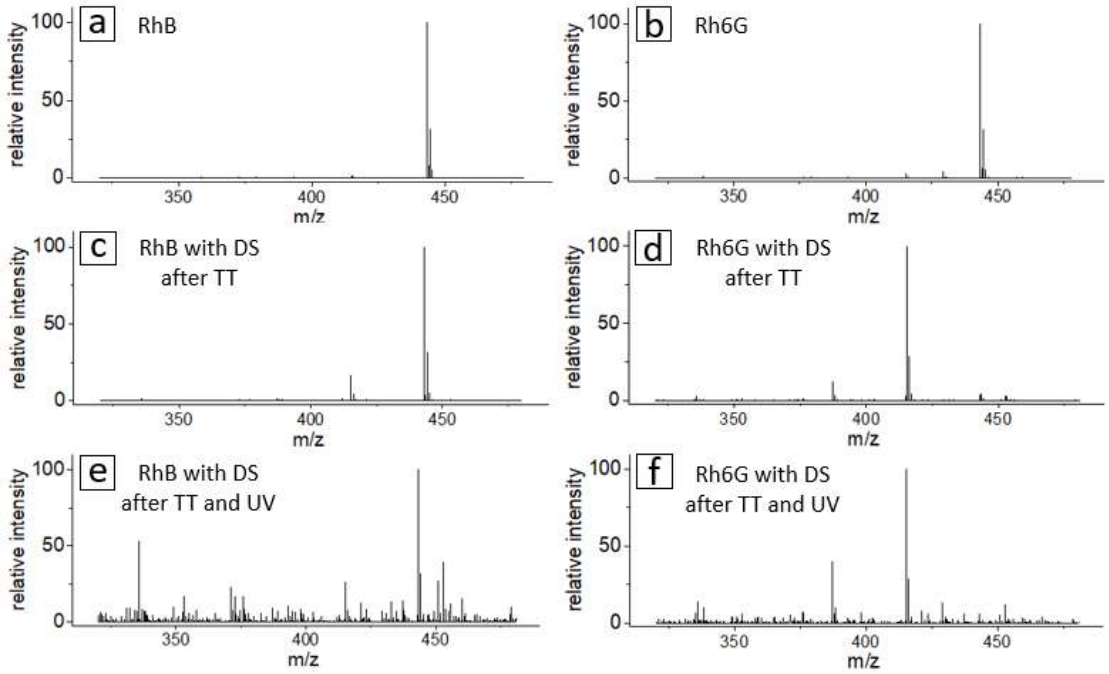

Figure 4.21: Mass spectrometry of RhB and Rh6G solutions (a,b), RhB and Rh6G solutions with DS after TT (c,d), and after UV irradiation (e,f).

According to mass spectra, after thermal treatment, a fragment ion with 415.2 m/z appeared for both RhB and Rh6G. Nevertheless, in the case of RhB, the vast majority of ions were still the original molecule of the dye (443.2 m/z). At the same time, the fragment ion with 415.2 m/z was present in a maximum concentration in the Rh6G solution, while the amount of the original molecule of this dye drastically decreased.

Also, after the UV irradiation, other forms of RhB and Rh6G appeared with the removed ethylene groups. Values of m/z and corresponding lost groups are summarized in Table 4.1. The numbers in brackets indicate the numbers of the ethylene groups.

The previously proposed photooxidation pathway of RhB [185] and Rh6G [188]

Table 4.1: Interpretation of the removed groups of fragment ions of Rhodamine B and Rhodamine 6G after thermal treatment and UV irradiation.

Rhodamine B		**Rhodamine 6G**	
m/z	loss	m/z	loss
443.2		443.2	
415.2	C_2H_4	415.2	C_2H_4
387.2	C_2H_4 (2)	401.2	$C_2H_4, CH_3\cdot$
359.2	C_2H_4 (3)	387.2	C_2H_4 (2)
331.3	C_2H_4 (4)	372.2	C_2H_4 (2), $NH_2\cdot$
		359.2	$C_2H_4, CH_3\cdot, C_2H_5NH\cdot$

is presented in Figure 4.22. Here, the detected fragment ions in the studied solutions are marked with blue ovals. The lost groups are also written out with their locations marked with red ovals.

A similar deethylation effect was observed for the photooxidation of RhB intermediates [185] and the Rh6G dye [188]. The removal of ethylene groups leads to a change in the chemical structure of the dye. Such intermediates begin to fluoresce in a shorter wavelength range, providing the basis for the desired photoconversion effect in polymer capsules. In addition to other studies [185,188], this blue spectral shift was also confirmed by the change in fluorescence spectra of the dyes after UV irradiation (Figure 4.23). RhB exhibited noticeable growth of shoulder peaks at 536 nm, and Rh6G showed a 3 nm blue shift after UV irradiation. Thus, mass

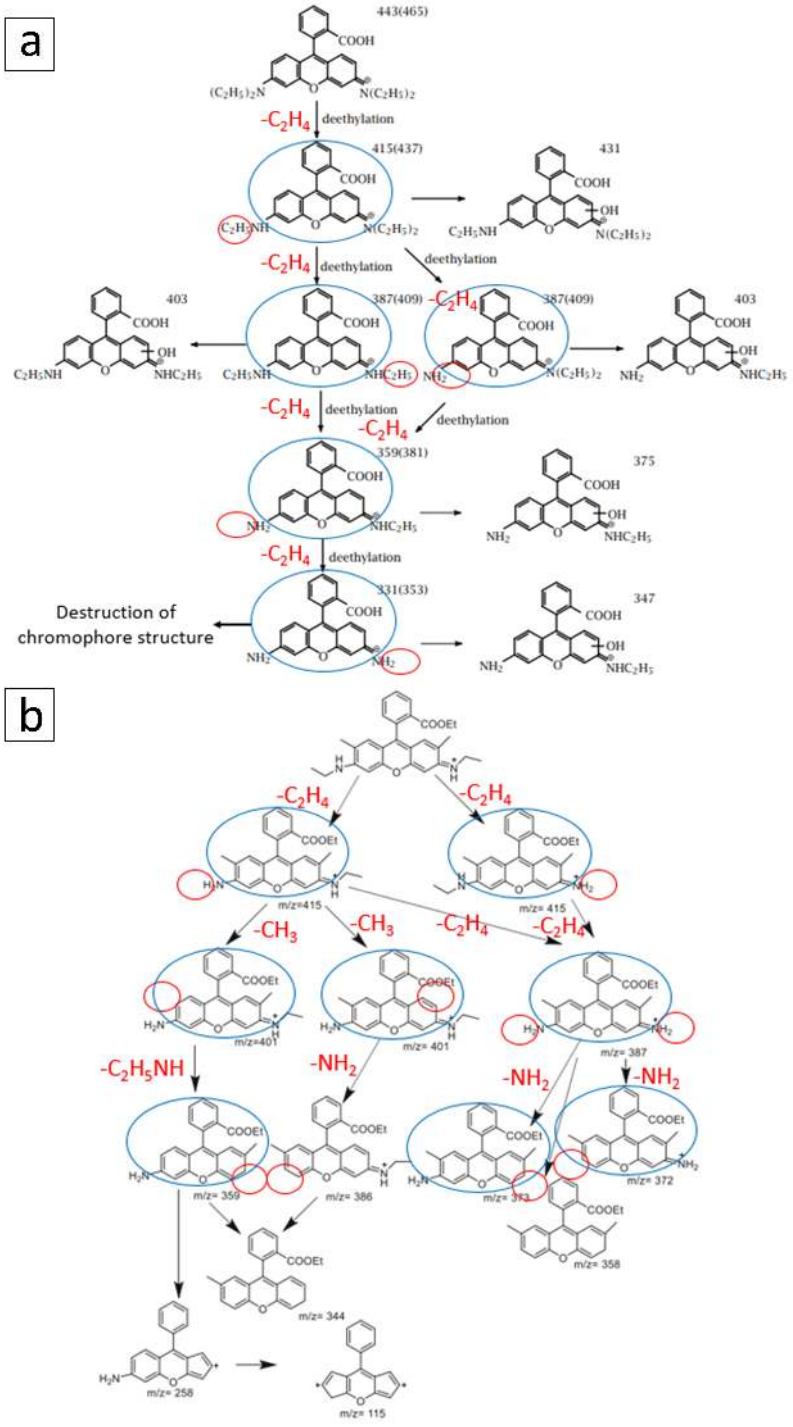

Figure 4.22: Photooxidation pathways of (a) RhB [185] and (b) Rh6G [188]. Fragment ions present in the solutions after UV irradiation are marked with blue ovals. The location of the removed groups is marked with red ovals.

spectrometry confirmed that the spectral shifts of RhB and Rh6G in the capsules were due to the deethylation reaction.

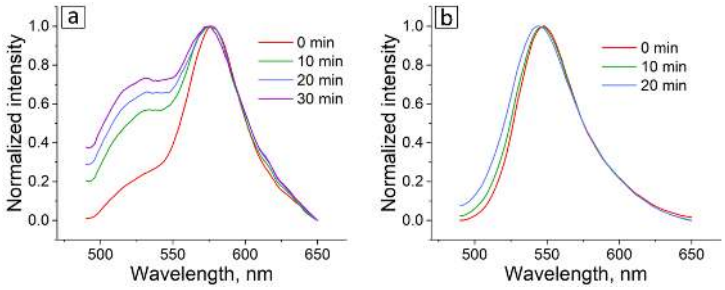

Figure 4.23: Normalized fluorescence spectra of the RhB (a) and Rh6G (b) dye solutions after thermal treatment with DS before and after UV irradiation for 10, 20, and 30 minutes.

4.9 Capsules' surface modification

In this section, the effect of surface modification using positively and negatively charged polyelectrolytes on capsule photoconversion properties will be demonstrated and discussed. As a model dye, RhB will be used since the 561 nm confocal laser is more optimal for the excitation of this dye than for Rh6G.

Three types of capsules were prepared (Figure 4.24). Sample 1 is regular capsules thermally treated in PVA gel with RhB. Sample 2 and sample 3 are capsules additionally covered with layers of PAH and PAH/PSS, respectively. For convenience, samples were named according to the outer layer of the capsules: PVA, PSS, and PAH.

The Zeta potential of capsules is presented in Table 4.2. PVA and PSS capsules had a negative charge of around -18 mV and an outer layer of cationic PAH

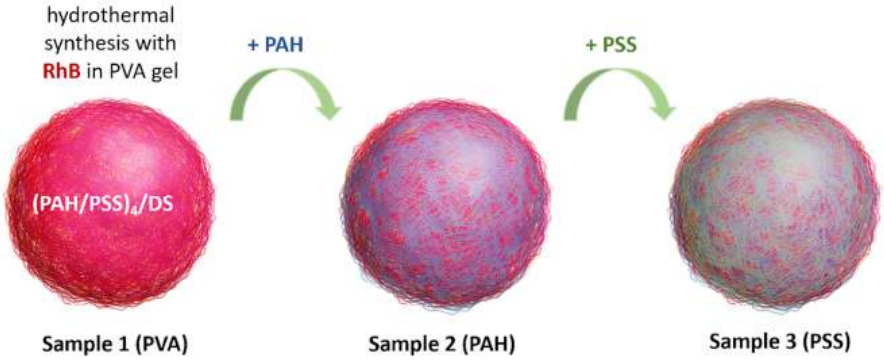

Figure 4.24: Scheme of polymer microcapsules surface modification with PAH and PSS polymers.

increased the charge of capsules to -7.6 mV. PAH is a weak polyelectrolyte that is pH-dependent, so it cannot always completely compensate for the negative charge of capsules to become positive [31].

Sample	Z_p, mV
PVA capsules	-17.5 ± 1.2
PAH capsules	-7.6 ± 0.6
PSS capsules	-18.5 ± 2.6

Table 4.2: Zeta potential of polymer microcapsules.

CLSM images of PVA capsules and those modified with PSS and PAH polymers are presented in Figure 4.25. Here, photoconversion of capsules was performed using the same LPD but changing the duration of one-pixel irradiation from 0.2 to 0.6 ms. According to the obtained images, capsules retained their photoconversion properties after the addition of extra polymer layers. Thus, surface modification did not affect the possibility of photoconverting capsules. Indeed, the usual double

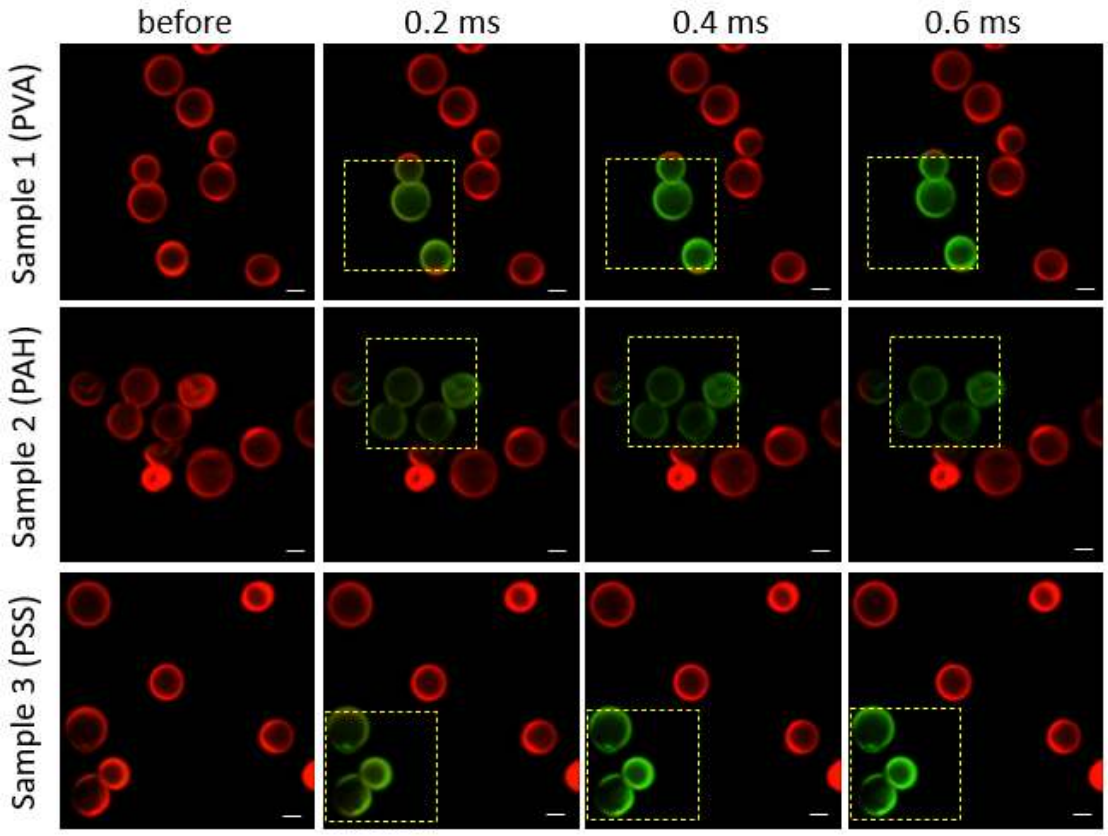

Figure 4.25: Photoconversion of microcapsules using 561 nm laser depending on the duration of one-pixel irradiation. The laser exposure area is marked with a yellow square (size - 500 × 500 pixels (20 × 20 μm)). Excitation – 488 nm, emission: 505 – 540 nm (green channel), 505 – 540 nm (red channel). The scale bar is 2 μm.

thickness of the capsule shell prepared by the LbL approach is about 50 nm in the case of six bilayers [277]. It means that a single or double additional polyelectrolyte layer is even thinner, which is not an obstacle for the confocal laser.

The change in fluorescence intensity of capsules after each irradiation step in the green and red channels is presented in Figure 4.26a-c. It could be noted that the intensity of the signal in the green channel increases, reaching the plateau at

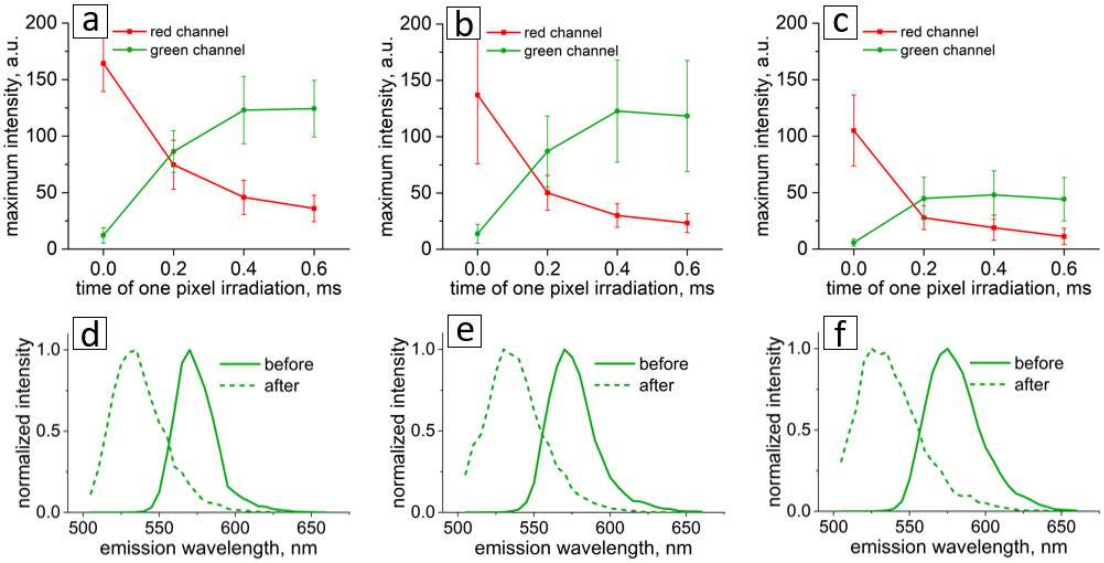

Figure 4.26: Changes in fluorescence intensity of capsules without (a) and with an outer layer of PSS (b) and PAH (c) depending on irradiation duration of one pixel in green and red channels. Corresponding λ-scans of capsules (d-f) before and after one-pixel laser irradiation for 0.4 ms.

around the 0.4 ms mark. In the red channel, the intensity decreases, reaching close to minimum values at around 0.4 ms as well. Therefore, further irradiation is not required to provide the highest fluorescence signal of photoconverted capsules. Moreover, λ-scans of capsules (Figure 4.26d-f) demonstrated a blue shift of capsules' spectra, which was discussed above. Therefore, the optimal parameters of photoconversion of capsules containing RhB using a 561 nm laser are an LPD is 451 kW/cm^2 and a one-pixel irradiation duration of 0.4 ms. The discussed three types of polymer microcapsules will be used for cell experiments in Chapter 6. The difference between the viability and uptake efficiency of these samples will be discussed.

4.10 Conclusions

A comprehensive protocol for the synthesis of fluorescent polymer capsules in the PVA gel was elaborated. This protocol allowed for increasing the yield of capsules from one synthesis by at least 250 times. Also, additional DS on capsule shells provided a higher and narrower intensity of fluorescence signal before and after photoconversion.

This method of photoconvertible capsule synthesis using PVA gel also offers ease of replication and enables the encapsulation of various dyes within capsules. The encapsulated dyes exhibited robust fluorescence after thermal treatment. Also, the fluorescence intensity of the capsules containing the dyes varied depending on their fluorescence spectra and confocal detection regions. Nevertheless, during the bleaching assay, Fl, AY, AO, and TR dyes displayed low photostability. The rest of the encapsulated dyes, RhB, Rh6G, and PyB, demonstrated high photostability. During further studies, RhB and Rh6G were found to have photoconversion properties, while PyB did not possess this characteristic. This photoconversion effect was evident when comparing the fluorescence intensities before and after the procedure. A significant decrease was observed in the 580–620/670 nm detection range, and a noticeable increase was seen in the 505–540 nm detection range. Mass spectrometry analysis revealed that the rhodamine dyes underwent several deethylation steps under conditions similar to those of the photoconversion procedure. Consequently, new compounds with blue spectral shifts

were formed, enabling the visualization of the capsules in the green channel following laser irradiation [185, 188]. This supports the proposed hypothesis regarding the presence of a deethylation reaction during the photoconversion process.

Both RhB- and Rh6G-containing capsules can be used for cell labeling. In the case of using the 561 nm laser and the 580-620 nm detection range, RhB-containing capsules were more suitable for further experiments, since these parameters are more optimal for the RhB dye than for Rh6G. Therefore, capsules containing RhB also require less power density for photoconversion than capsules with Rh6G. It is more favorable for cell experiments where cells should remain alive after laser radiation. Despite this, capsules containing Rh6G still may be useful for cell tracking.

The absence of genetic modification when using the developed labels for marking cells eliminates the risk of spontaneous mutations. Therefore, our polymer labels can be considered for personalized medicine, for example, in cancer treatment and stem cell therapy.

Chapter 5. Non-thermal Layer-by-layer Synthesis of Photoconvertible Capsules and their Characterization

5.1 Introduction

In the previous chapter, thermally treated polymer microcapsules with RhB and Rh6G were proposed as fluorescent labels for cell tracking. During the synthesis of these capsules, the encapsulation of the dyes occurs while autoclaving capsules in the PVA solution with the dye at 180 °C for 3 h. Also, during this process, CNDs are formed, acting as a photocatalyst during photoconversion. Nevertheless, not all dyes can withstand the high temperatures that are required for this type of synthesis. For example, TR did not survive during thermal treatment, as was discovered in Chapter 4. Depending on the temperature and duration, thermal treatment can cause dyes to degrade due to the breaking of the chemical bonds within the dye molecules [278, 279]. It changes the dyes' inherent absorption and fluorescence properties, excluding them from further labeling and photoconversion applications.

Moreover, there is still the need for broadening the variety of photoconvertible dyes to other detection ranges, since now only RhB and Rh6G are available (excitation 561 nm, detection 580–620/670 nm with CLSM). Studies on the far-red fluorescent dyes are especially promising since labels with such dyes hold the potential for tracking cells in the tissues [280]. It is due to the presence of a

near-infrared (NIR) window (650–900 nm), where light has the highest penetration level into biological tissue [281]. For example, changes in glioblastoma cells in brain tissue were tracked with luminescent nanoparticles [280]. Other studies include tracking transplanted stem cells using fluorescent nanoparticles [282]. Nevertheless, some particles for tracking are produced containing cytotoxic heavy metals such as Pb, Hg, or Cd [283, 284] or rare earth metals [285]. At the same time, polymer microcapsules are well known for their low cytotoxicity and high uptake efficiency by cells [88, 248]. Therefore, the application of such microparticles for NIR imaging would provide a label with low toxicity for cell tracking in the tissues.

This chapter is dedicated to the development of an alternative approach to photoconvertible capsule synthesis that does not require thermal treatment. It was studied using the dyes Cy3.5, Cy5.5, Cy7 and RITC. The possibility of broadening the ranges of photoconversion options using these dyes was assessed. Photoconversion parameters were analyzed by changing laser power density (LPD) and the duration of one pixel irradiation (one pixel area is equal to 560 nm^2). The photostability of capsules containing cyanine dyes was evaluated.

5.2 Non-thermal approach to photoconvertible capsule synthesis

In the previous chapter, capsules were thermally treated in PVA gel to induce encapsulation of the dye in the capsule. Nevertheless, not all dyes can withstand

the thermal treatment, which was demonstrated above for TR. Therefore, as a first step in the studies, an alternative approach was proposed that did not require thermal treatment. Model dyes Cy3.5, Cy5.5, and Cy7 were chosen since they were reported to exhibit a photoconversion effect [180] and could be bonded to PAH. Also, RITC was utilized as a control dye since RhB is known to retain the photoconversion effect after the thermal treatment.

To analyze if cyanine dyes could withstand thermal treatment in the first place, the solutions of the PAH labeled with the dyes Cy3.5, Cy5.5, and Cy7 were thermally treated according to the procedure described earlier (3 h, 180 °C). Fluorescence intensities of the labeled PAH-dye solutions were recorded before and after the procedure (Figure 5.1). According to the obtained spectra, fluorescence inten-

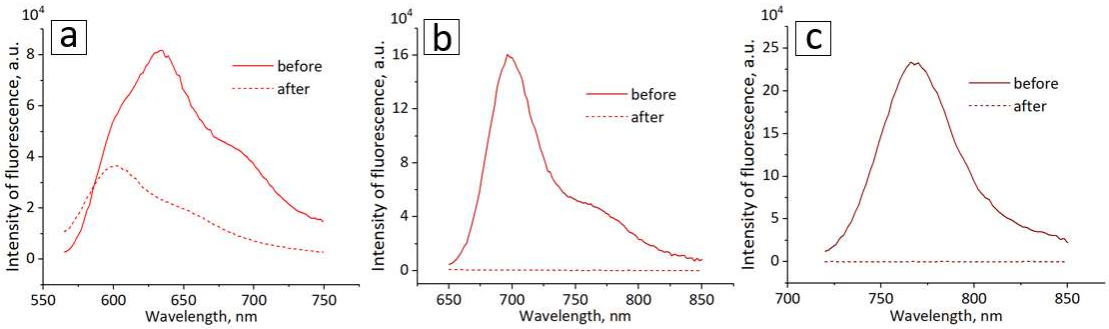

Figure 5.1: Fluorescence intensities of the (a) PAH-Cy3.5, (b) PAH-Cy5.5, and (c) PAH-Cy7 aqueous solutions before and after thermal treatment

sities of the PAH-Cy5.5 and PAH-Cy7 decreased dramatically to zero values after the thermal treatment. This means that the dyes did not withstand the high temperature and should be encapsulated in the capsules without thermal treatment to save their fluorescent properties. As for PAH-Cy3.5, its intensity decreased by

around two times after thermal treatment, and the peak of intensity shifted by 32 nm. Such changes in the spectrum nature might be connected with changes in the chemical structure of the dye, which could affect its ability to undergo photoconversion [286]. Therefore, the Cy3.5 dye should also be encapsulated without thermal treatment to preserve its fluorescence properties.

To prepare photoconvertible capsules (Figure 5.2) loaded with the target dye

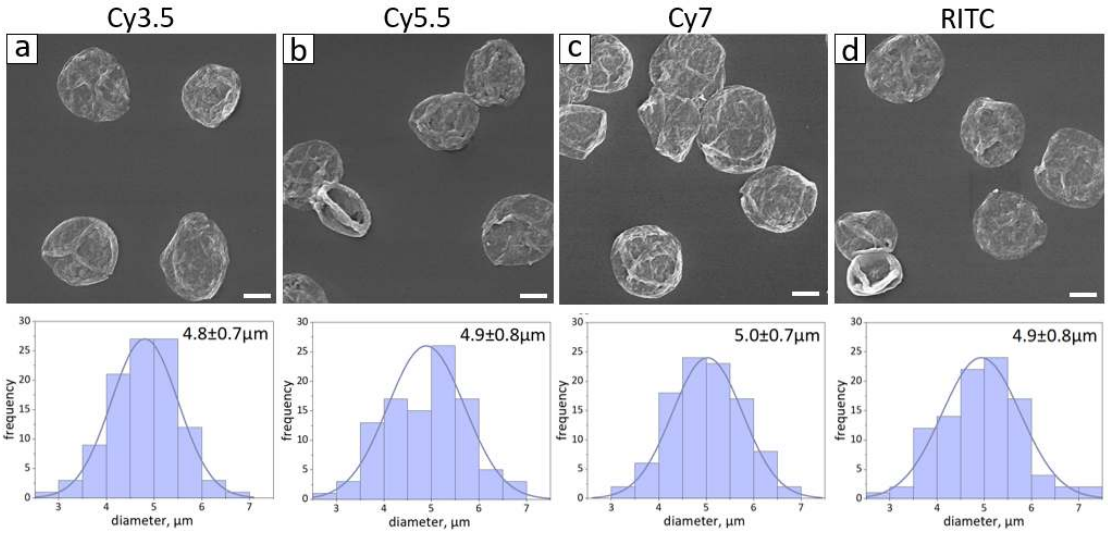

Figure 5.2: SEM images and histograms of the size distribution of LbL polymer microcapsules with RITC, Cy3.5, Cy5.5, and Cy7. The scale bar is 2 μm.

without thermal treatment, PAH labeled with the dyes Cy3.5, Cy5.5, Cy7, or RITC was used for capsule synthesis as a component of the shell instead of the middle layer of regular PAH, which led to the encapsulation of the dye.

The histograms of size distribution are presented below each SEM image (Figure 5.2). The average diameter of capsules with Cy3.5 is 4.8 $\pm$ 0.7 μm, those with Cy5.5 are 4.9 $\pm$ 0.8 μm, those with Cy7 are 5.0 $\pm$ 0.7 μm, and those with RITC are 4.9 $\pm$ 0.8 μm.

5.3 Photoconversion of LbL capsules with Cy3.5

Absorbance and fluorescence spectra of Cy3.5 and PAH-Cy3.5 were recorded (Figure 5.3). It should be noted that both spectra experienced a redshift. This effect was noticed previously when the cyanine dye bound to DNA [287], which could be connected to the low ratio of twisted dimer configurations due to binding to PAH [288]. Moreover, the absorption spectra have broadened significantly after binding to DNA. A similar effect was also reported for cyanine dyes [289], which could be explained by the aggregation of the dye due to binding to PAH. Therefore, the spectra of the dye changed after conjugation with the PAH polymer.

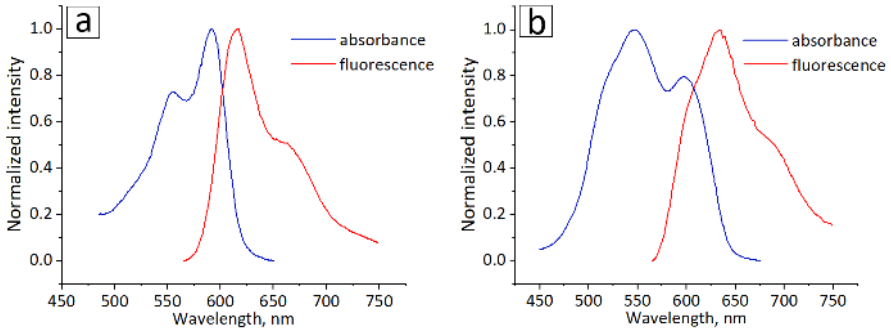

Figure 5.3: Normalized absorbance and fluorescence spectra of Cy3.5 (a) and PAH-Cy3.5 (b).

In the next stage, it was verified that after conjugation and encapsulation into the shells of the Cy3.5 microcapsules, the dye retained the ability to be photoconverted using CLSM. The microcapsules with encapsulated Cy3.5 were excited with the 561 nm laser, and the emission range was 580–630 nm (red channel). The fluorescence signal after photoconversion was excited with the laser 488 nm

and the emission range was 505–540 nm (green channel). To choose the optimal photoconversion parameters, LPD and duration of one pixel irradiation were changed. The utilized LPDs for Cy3.5 photoconversion were 193, 322, and 451 kW/cm^2. The duration of one pixel irradiation was changed from 0.05 to 0.15 ms. According to the obtained CLSM images, the encapsulated form of Cy3.5 can be photoconverted (Figure 5.4). It corresponds to the previously reported photoconversion feature of this dye [180].

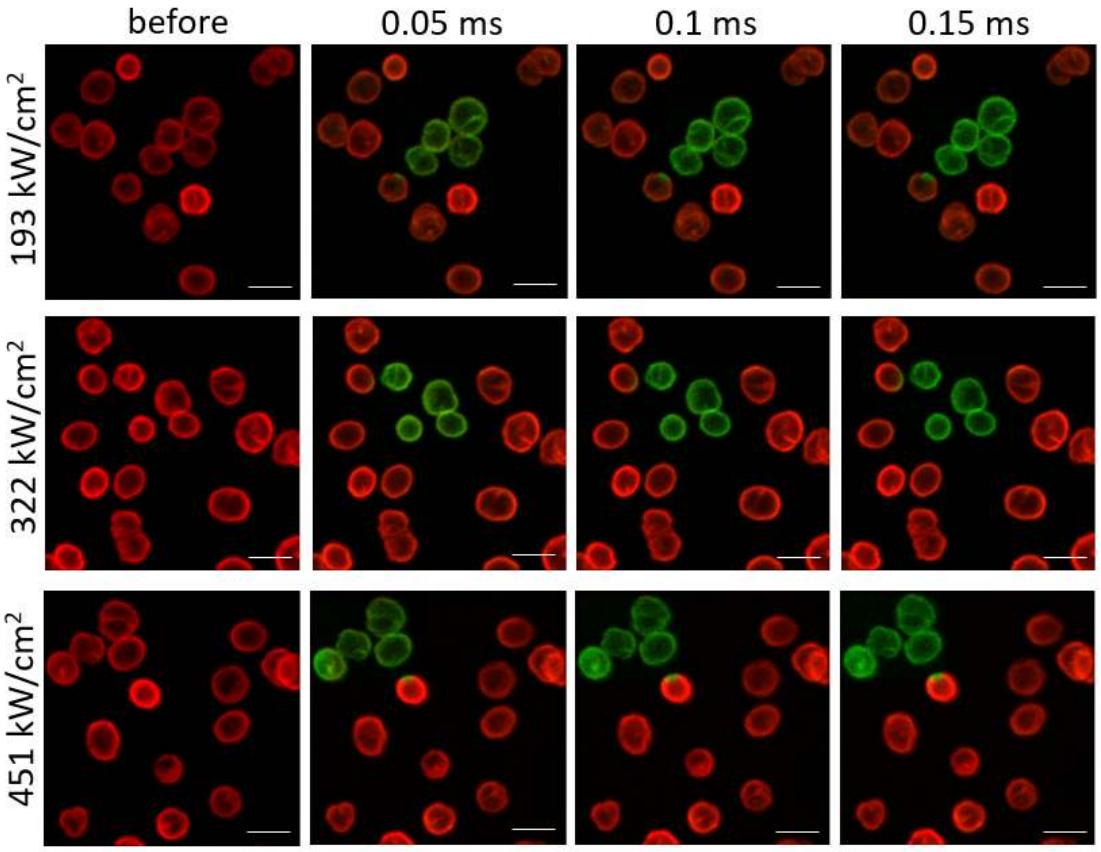

Figure 5.4: (a) CLSM images of microcapsules with encapsulated Cy3.5 before and after photoconversion depending on the duration of one pixel irradiation at 193, 322, and 451 kW/cm^2 LPD. The scale bar is 5 μm.

Changes in the lambda scans of encapsulated Cy3.5 depending on the duration

of one pixel irradiation and LPD in the green channel (ex. 488 nm, em. 505-540 nm) and red channel (ex. 561 nm, em. 580-630 nm) are reported in Figure 5.5a-c. It should be noted that no left peak in the lambda scans was initially observed. Nevertheless, when irradiation started, the peak in the blue region started to grow, providing the signal for detection in the green channel (the range of 505-540 nm). The growth of the shoulder peak was higher, the bigger the utilized LPD.

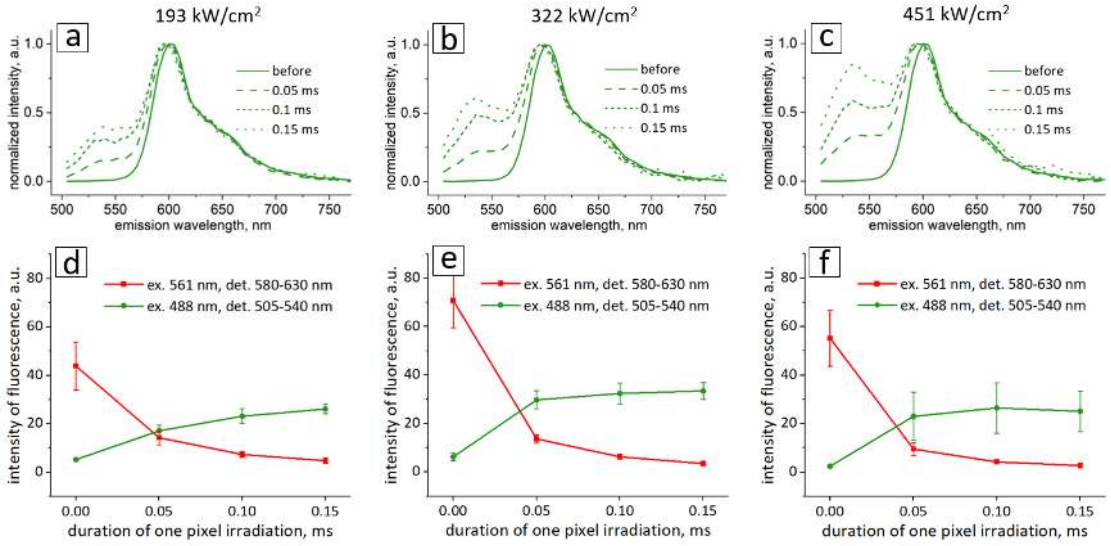

Figure 5.5: λ-scans of capsules with Cy3.5 before and after photoconversion depending on the duration of one pixel irradiation at (b) 193, (c) 322, and (d) 451 kW/cm^2 laser power density. Corresponding changes in intensity over time under irradiation at (d) 193, (e) 322, and (f) 451 kW/cm^2 LPD.

Moreover, changes in fluorescence intensity varied depending on the utilized LPD (Figure 5.5d-f). At 193 kW/cm^2, the intensity in the green channel increased but did not reach a maximum plateau, as in the case of 322 and 451 kW/cm^2 LPD. For the last two LPDs, the maximum intensity in the green channel and minimum intensity in the red channel were reached at around 0.1 ms of one pixel irradiation.

Therefore, there was no need for a longer laser irradiation, and a 0.1 ms time point was chosen as the more optimal. Also, since no significant difference in intensities was observed between 322 and 451 kW/cm^2 LPDs, the lower LPD was chosen to reduce the dose of irradiation in the following cell experiments. This means that LPD of 322 kW/cm^2 and a duration of one pixel irradiation of 0.1 ms were set as the most optimal parameters for photoconversion of encapsulated Cy3.5.

5.4 Photoconversion of LbL capsules with Cy5.5

Absorption and fluorescence spectra were recorded for Cy5.5 and PAH-Cy5.5 (Figure 5.6). As for PAH-Cy3.5, a similar effect of absorbance spectrum broadening was observed, which has already been discussed [289].

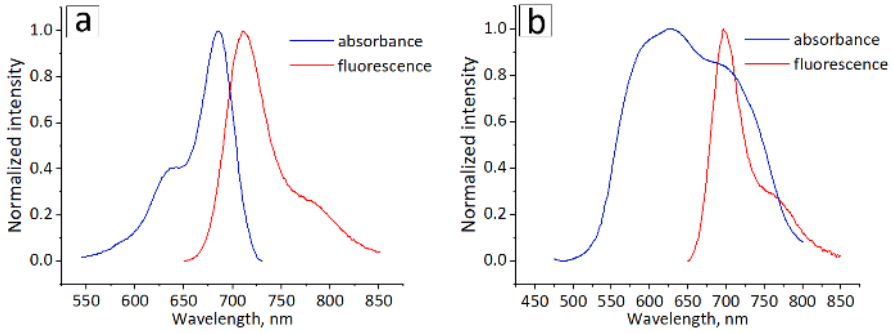

Figure 5.6: Normalized absorbance and fluorescence spectra of Cy5.5 (a) and PAH-Cy5.5 (b).

Analogously to the previous section for encapsulated Cy3.5, the possibility to photoconvert encapsulated Cy5.5 was assessed using CLSM. The sample was excited with a 671 nm laser, and the emission range was 686–790 nm (NIR channel). The fluorescence signal after photoconversion was excited with the 488 nm laser,

and the detection range was 505–540 nm (green channel). CLSM images of microcapsules with Cy5.5 before and after photoconversion with 180, 451, and 721 kW/cm^2 LPD at different one pixel irradiation durations are presented in Figure 5.7. According to the obtained images, successful photoconversion of encapsulated Cy5.5 was achieved. It corresponds to the reported photoconversion property of this dye [180].

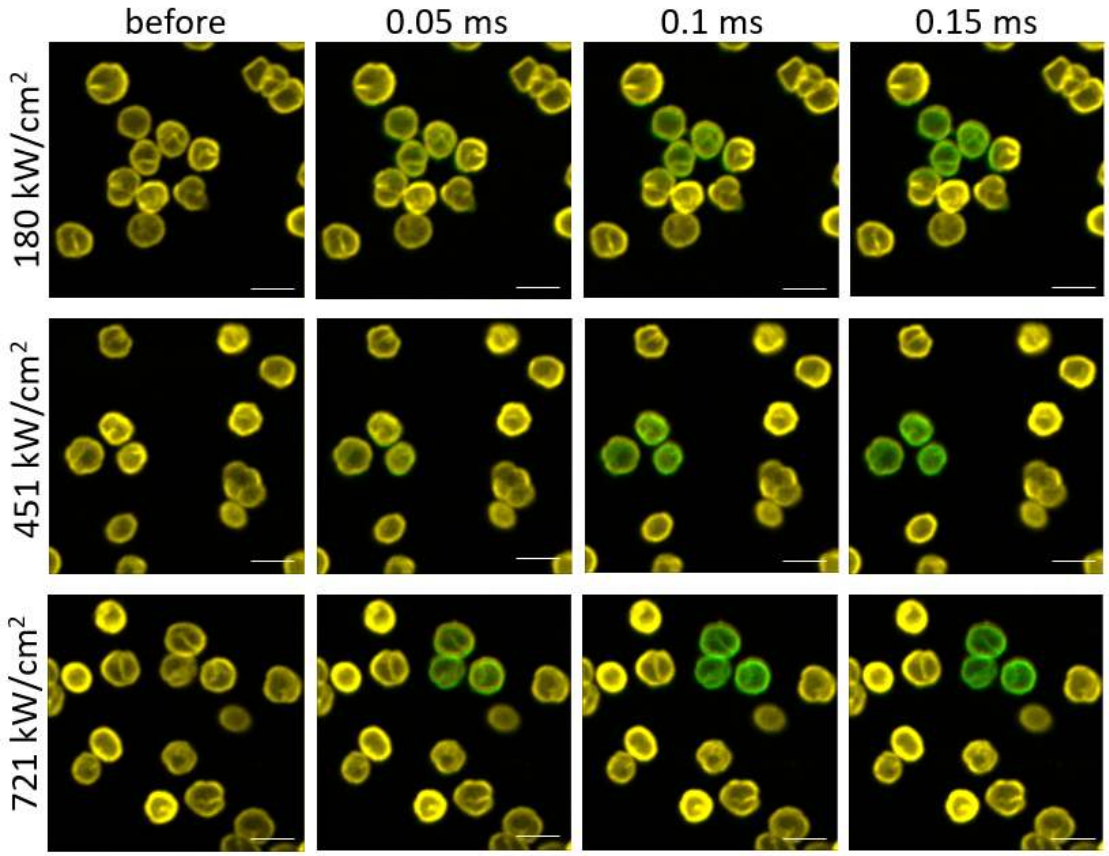

Figure 5.7: CLSM images of capsules with Cy5.5 before and after photoconversion depending on the duration of one pixel irradiation at 180, 451, and 721 kW/cm^2 LPD. Scale bar is 5 μm

Lambda scans of encapsulated Cy5.5 depending on the duration of one pixel irradiation and LPD are presented in Figure 5.8a-c. It can be noted from the

lambda scan data that the peak in the region of the initial signal detection (686–790 nm) was reduced after laser irradiation. At the same time, there was a peak in the blue region that provided the possibility to obtain the photoconversion effect.

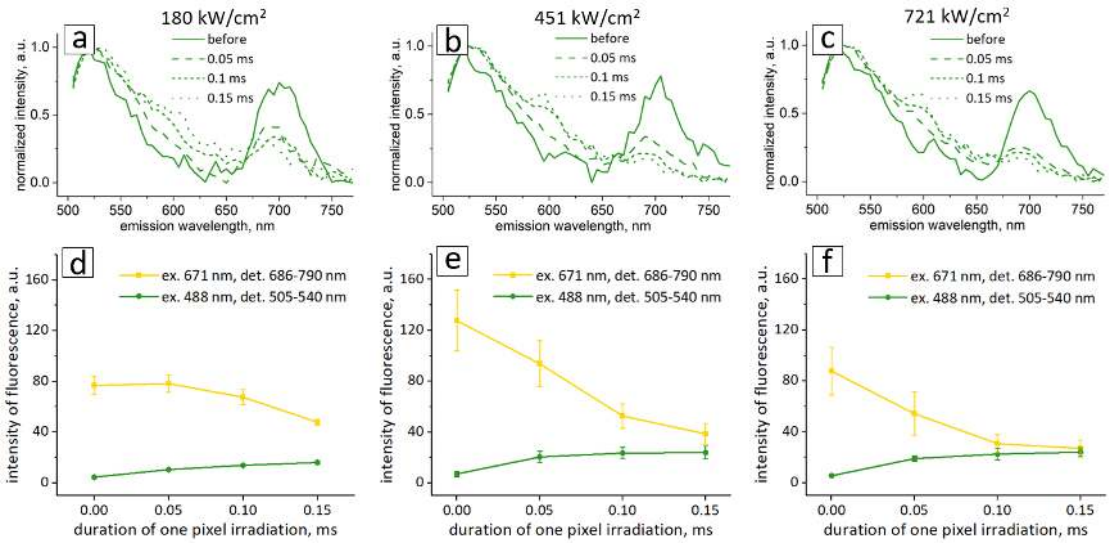

Figure 5.8: λ-scans of capsules with Cy5.5 before and after photoconversion depending on the duration of one pixel irradiation at (b) 180, (c) 451, and (d) 721 kW/cm^2 laser power density. Corresponding changes in intensity over time under irradiation at (d) 180, (e) 451, and (f) 721 kW/cm^2 laser power density.

The fluorescence intensity changes of encapsulated Cy5.5 were different depending on the applied LPD (Figure 5.8d-f). For 180 kW/cm^2 LPD, intensities in both channels did not reach a plateau, indicating that laser intensity was not sufficient for complete photoconversion during 0.15 ms of one pixel irradiation duration. At the same time, intensities in both channels came to approximately the same value at 0.15 ms in the case of 721 kW/cm^2 LPD, reaching the plateau. A similar effect was observed in the case of 451 kW/cm^2 LPD, demonstrating that only the signal in the green channel reached the maximum saturation value of

intensity, while the yellow-colored NIR channel did not. Therefore, the most optimal parameters for photoconversion were chosen as 721 kW/cm^2 LPD and 0.15 ms of one pixel irradiation.

As a result, photoconversion of both encapsulated Cy3.5 and Cy5.5 from red and NIR channels to the green channel was successful. It means that the covalent conjugation of cyanine dyes with PAH and their encapsulation in polyelectrolyte layers did not affect their photoconversion property, as reported previously [180]. Indeed, photoconversion of these dyes happens due to the cleavage of double bonds of the polymethine chain, leading to the removal of the C_2H_2 group and a blue spectra shift [178]. This polymethine chain does not participate in covalent bonding with PAH, and it is not affected by the encapsulation process, allowing the photoconversion of the encapsulated cyanine dyes.

5.5 Photoconversion of LbL capsules with Cy7

Absorbance and fluorescence spectra of Cy7 and PAH-Cy7 are presented in Figure 5.9. A similar effect of absorbance spectrum broadening was present for PAH-Cy7 as well, as with the rest of the dyes [289].

Capsules containing Cy7 were excited with a 671 nm laser and detected in the region of 686–790 nm. CLSM images of capsules before and after various combinations of LPD and duration of irradiation are presented in Figure 5.10a.

From the CLSM images, the photoconversion effect of capsules containing Cy7 was not as profound as in the case of Cy3.5 and Cy5.5. Indeed, the calculation of

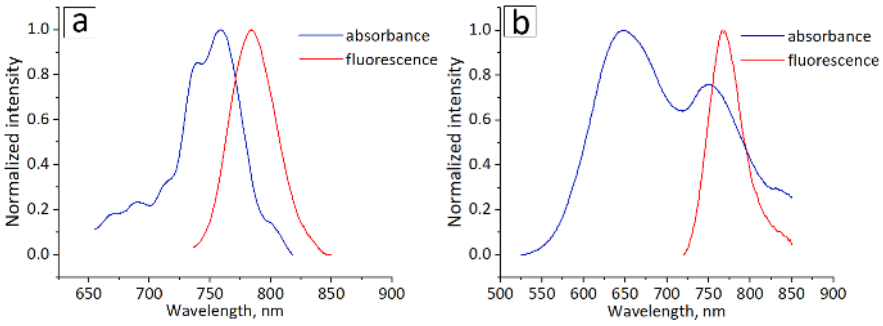

Figure 5.9: Normalized absorbance and fluorescence spectra of Cy7 (a) and PAH-Cy7 (b).

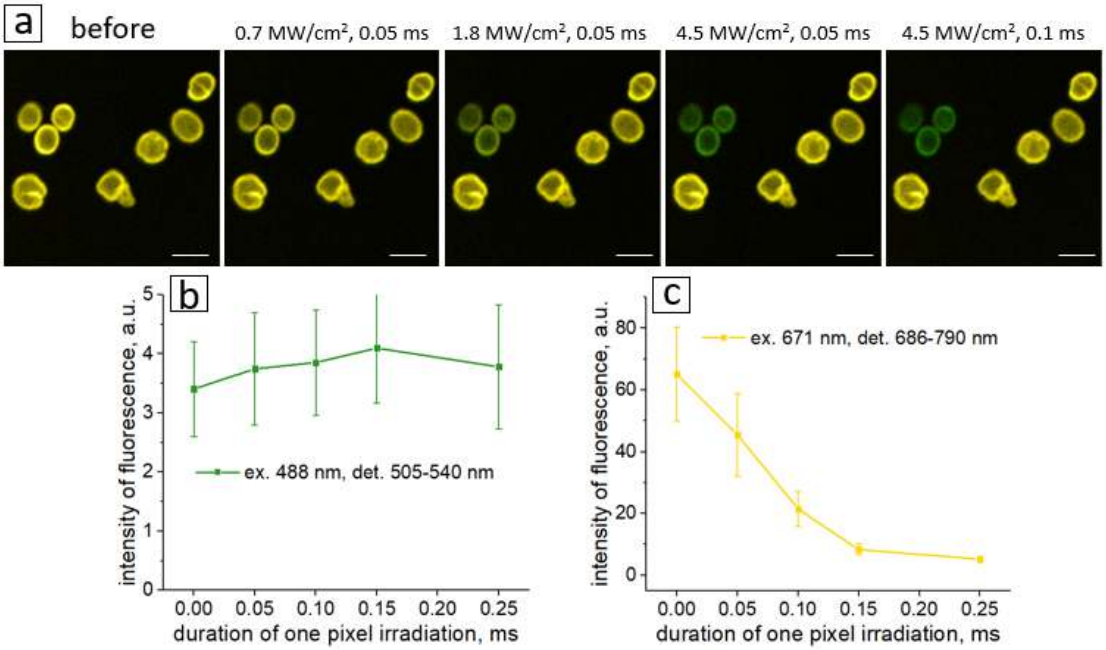

Figure 5.10: (a) CLSM images of capsules with Cy7 before and after photoconversion depending on the duration of one pixel irradiation at LPD of 0.7, 1.8, and 4.5 MW/cm^2. The scale bar is 5 μm. (b) Changes in the capsule's fluorescence intensity depending on the duration of one pixel irradiation. Each irradiation time point corresponds to its CLSM image and LPD of 0.7, 1.8, and 4.5 MW/cm^2

capsules' fluorescence intensity revealed low values of the signal (less than 5 a.u. in comparison to 20-30 a.u. for Cy3.5 and Cy5.5) (Figure 5.10b). Nevertheless, the graph revealed a small trend of intensity increase upon irradiation. The decline of the fluorescence intensity at 0.25 ms indicates the bleaching of the dye due to high LPD and longer one pixel irradiation duration. The intensity of capsules in the NIR channel is reduced, most probably due to both photobleaching and photoconversion (Figure 5.10c). A similar effect of simultaneous Cy7 bleaching and photoconversion was observed earlier [181]. Cells were irradiated with a 640 nm laser at a low LPD of 0.1 kW/cm^2. That led to the appearance of the photoconverted signal in the red channel. Since in the current study, the signal is absent in the red channel and was observed only in the green channel, the removal of two C_2H_4 groups occurs, forming the Cy3 product [181].

It is also worth mentioning that the 671 nm laser is not optimal for the excitation of the Cy7 dye, since its emission peak is 769 nm (Figure 5.9). It means that the distance between laser excitation and the actual fluorescence of the dye is 98 nm. Therefore, a 671 nm laser can excite a small portion of the dye fluorescence, which makes this laser not optimal for such a task. Indeed, such a dye is often used in NIR spectroscopy, where higher wavelengths from 780 to 2500 nm are utilized [290, 291]. Therefore, it might be the reason why the photoconversion effect of Cy7 is less prominent than that of Cy3.5 and Cy5.5 dyes.

5.6 Photoconversion of LbL capsules with RITC

Absorbance and fluorescence spectra of RITC and PAH-RITC were recorded (Figure 5.11). After the conjugation of RITC, its absorbance spectrum broadened

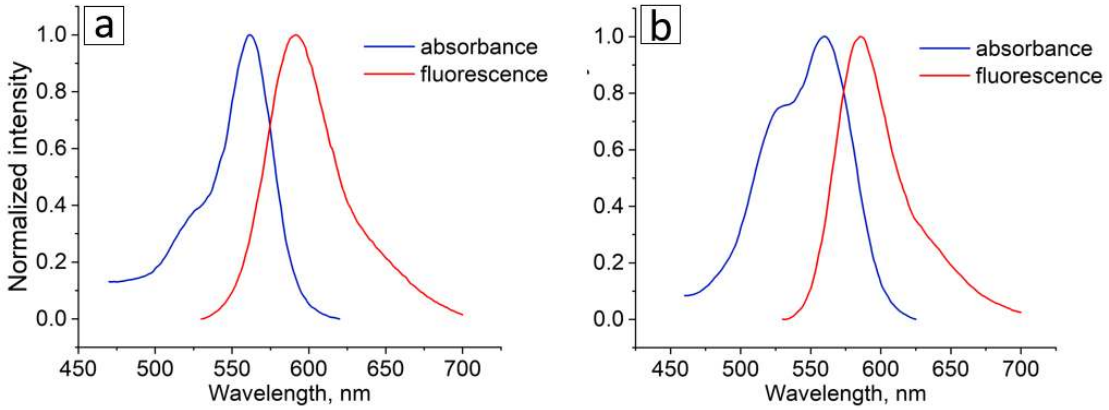

Figure 5.11: Normalized absorbance and fluorescence spectra of RITC (a) and PAH-RITC (b).

[289], while peak maxima stayed relatively close to the original positions.

CLSM studies were performed for RITC dye bound to PAH as an analog of free RhB, which was studied in the previous chapter. CLSM images of capsules containing RITC before and after photoconversion are presented in Figure 5.12. The utilized duration of irradiation and LPD were the same as for Cy3.5 since both dyes have the same parameters of excitation and detection. According to the obtained images, photoconversion of capsules containing RITC was achieved. Therefore, it is possible not only for free RhB dye, as was reported previously [24], but also for RITC chemically bound to the polymer.

Λ-scans of capsules are present in Figure 5.13a-c, demonstrating that the blue

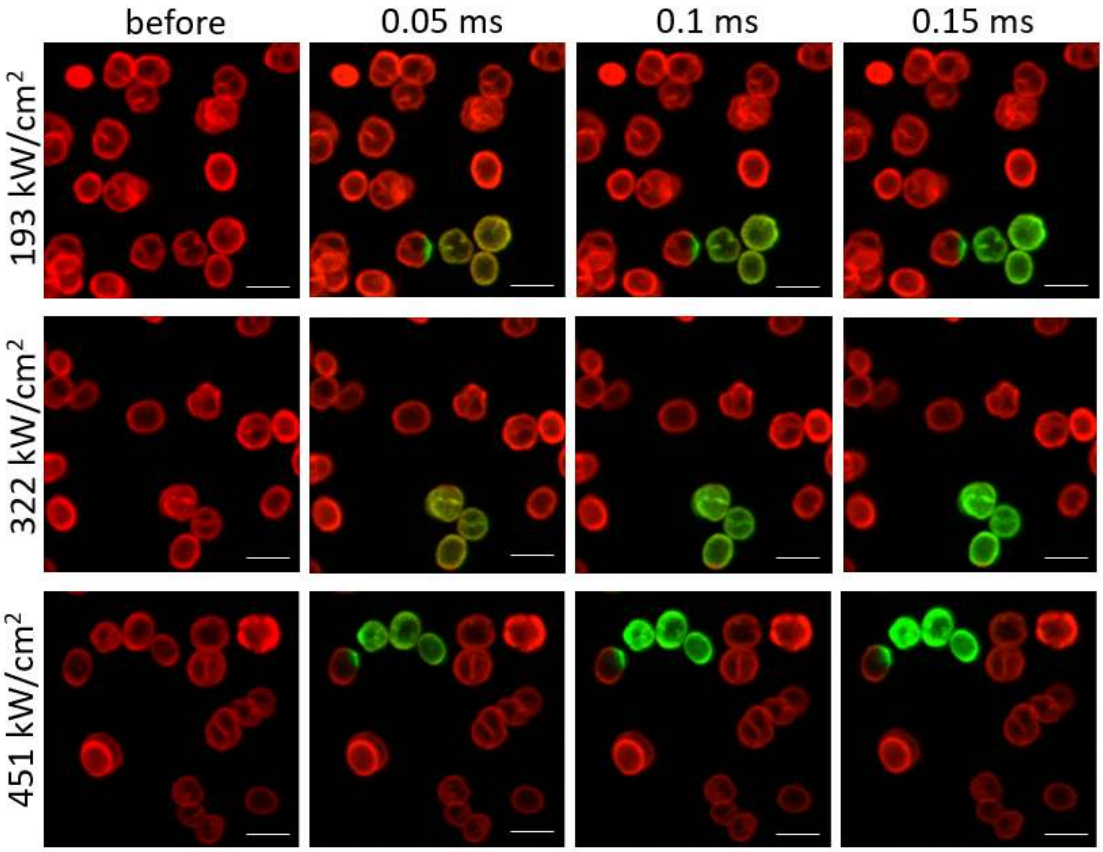

Figure 5.12: CLSM images of capsules with PAH-RITC before and after photoconversion depending on the duration of one pixel irradiation at 193, 322, and 451 kW/cm^2 LPD. The scale bar is 5 μm.

shift of the spectra increases with the duration of laser exposure. The degree of the left shoulder rises also higher the bigger the utilized LPD. It indicates a greater impact of the laser with higher intensity on the photoconversion degree.

Changes in fluorescence intensity of capsules in the green and red channels are presented in Figure 5.13d-f. The pattern was similar in the case of 193 and 322 kW/cm^2 LPD. The continuous close-to-linear rise or decrease in intensity with time was noticed. Notably, when 451 kW/cm^2 LPD was utilized, it gave almost two times a higher increase in intensity at 0.15 ms in the green channel in comparison

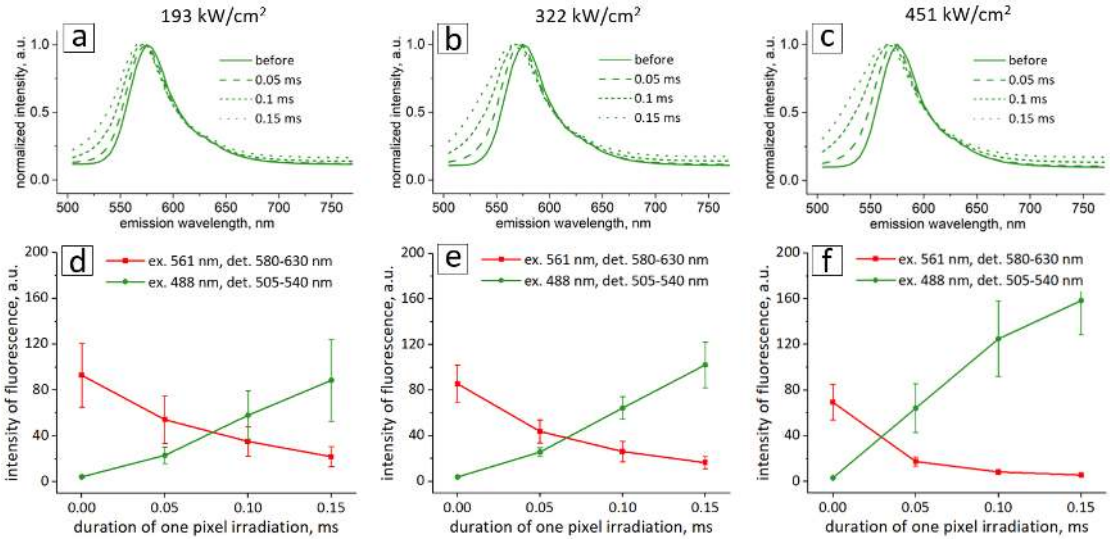

Figure 5.13: λ-scans of capsules with RITC before and after photoconversion depending on the duration of one pixel irradiation at (b) 193, (c) 322, and (d) 451 kW/cm^2 laser power density. Corresponding changes in intensity over time under irradiation at (d) 193, (e) 322, and (f) 451 kW/cm^2 laser power density.

to other LPDs. A plateau of minimal intensity in the red channel was reached at the 0.1 ms mark. Therefore, optimal photoconversion parameters for capsules containing RITC include 451 kW/cm^2 LPD, as was reported previously [24], and the duration of irradiation of 0.1 or 0.15 ms, depending on the desired brightness of the signal in the green channel.

5.7 Photostability of capsules containing Cy3.5 and Cy5.5

Cell labels are supposed to be photostable to provide a reliable fluorescence signal during prolonged detection and imaging processes. A bleaching test was conducted to assess the photostability of capsules containing Cy3.5 and Cy5.5

dyes, since Cy7 demonstrated a less prominent photoconversion effect, and RhB is well known to be photostable. The fluorescence intensities of capsules before and after the bleaching were calculated and normalized to the values at the start of the experiment (Figure 5.14). Interestingly, the intensity of the capsules for Cy3.5 did

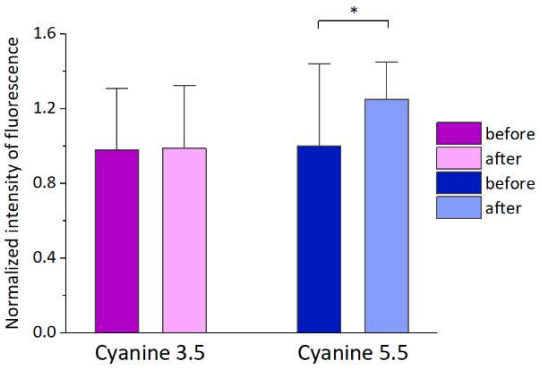

Figure 5.14: Normalized changes in the fluorescence intensity of the Cy3.5 and Cy5.5 dyes before and after the bleaching test. *P < 0.05

not change after the bleaching, while it increased for the sample with Cy5.5. It is known that dyes can form aggregates, resulting in the quenching of some part of the fluorescence signal [292, 293]. The laser exposure might induce photochemical reactions in the dye molecules that potentially can distort some dye molecules in the aggregates [294]. This might reduce the number of active molecules in the aggregates and thus lower the quenching effect and increase fluorescence. Therefore, Cy3.5 and Cy5.5 dyes demonstrated high photostability as potential cell labels.

5.8 Conclusions

In this chapter, a new approach to the synthesis of photoconvertible capsules that do not require thermal treatment was proposed. Capsules with the dyes Cy3.5, Cy5.5, Cy7, and RITC were prepared. Capsules containing Cy3.5, Cy5.5, and RITC demonstrated profound photoconversion ability. Capsules containing Cy3.5 and RITC were excited with the 561 nm laser and detected in the range 580–630 nm. Capsules containing Cy5.5 and Cy7 were excited with the 671 nm laser and detected in the range 686–790 nm. After photoconversion, the capsules were excited with a 488 nm laser and detected in the range 505–540 nm. As for capsules containing Cy7, the photoconversion effect was less prominent. Presumably, it is because the maximum wavelength of the 671 nm laser used in CLSM is not optimal for the excitation of this dye, since its detection peak is located at 769 nm.

Optimal parameters of photoconversion (the duration of one pixel laser irradiation and LPD) were selected for all of the photoconverted dyes by analyzing the changes in the capsules' fluorescence intensity. For capsules containing Cy3.5, optimal parameters were found to be 322 kW/cm^2 and 0.1 ms; for capsules containing Cy5.5 – 721 kW/cm^2 and 1.5 ms; for capsules containing RITC – 451 kW/cm^2 and 0.1 or 0.15 ms. Such a set of parameters could be used as a guideline for adjusting the parameters of different setups of confocal microscope lasers.

Another advantage of the proposed non-thermal encapsulation approach is the possibility of loading drugs in such microcapsules and combining both photocon-

vertible cell labeling and drug delivery [75]. Nevertheless, drugs might degrade upon laser radiation during photoconversion, forming potentially toxic products, and this possibility should be carefully addressed [295].

The newly developed capsules containing Cy5.5, which is a near-infrared fluorescent dye, provide the additional option of labeling region to Cy3.5, RITC, and previously reported RhB and Rh6G. Moreover, it also opens up the possibility of detecting capsules deeper in the tissue by taking advantage of near-infrared windows in biological tissue (650–900 nm) [296]. For example, it might give the ability to observe such labels in brain tissue [297].

Chapter 6. Photoconvertible Polymer Capsules For Cell Labeling and Tracking

6.1 Introduction

The following chapter is focused on the characterization of photoconvertible polymer microcapsules in biological systems. Both types of capsules prepared with thermal (Chapter 4) and non-thermal treatment (Chapter 5) are expected to be applicable for cell tracking. In this chapter, capsules prepared with thermal treatment were chosen for cell experiments for several reasons. The decrease in size during synthesis leads to the increase in shell thickness and stiffness. Therefore, capsules can be observed as separate bright "beads" in the cells that do not deform and do not collapse with each other. A smaller diameter of capsules is also beneficial for uptake by smaller cells (for example, fibroblasts [298]). At the same time, regular LbL capsules prepared without thermal treatment can deform due to their thin soft shell [299]. This might lead to their adhesion to each other and complicate the distinction of separate capsules in the cell for effective labeling. Note that such LbL capsules potentially could be used for drug delivery since no heating is required for their production, which is crucial for the drug. Moreover, this synthesis technique is suitable for the dyes that do not withstand thermal treatment. Nevertheless, for the goals of this research, thermally treated capsules were chosen for labeling experiments, taking into account their discussed advantages over LbL capsules. Samples discussed at the end of Chapter 4 are used: capsules

thermally treated in PVA gel with RhB and capsules additionally covered with layers of PAH and PAH/PSS. Application and exploration of photoconvertible polymer microcapsules are done for various cell lines. The experiments on mouse mesenchymal stromal cells (mMSCs) are discussed in detail in this Chapter and the approbation of the labeling and tracking approach on myoblasts (C2C12) and human mesenchymal stromal cells (hMSCs) is briefly discussed.

MSCs are the cornerstone, hope, and fear of modern cancer therapy [252]. According to MSCs' inherent tumor-tropic properties, their use as a "Trojan horse" has been proposed to deliver encapsulated drug forms into the tumor more effectively [300]. Nevertheless, there is a growing number of oncology studies showing that MSCs have dual characteristics in relation to cancer development. It has been shown that in the early stages, they are able to reduce the accumulation of reactive oxygen species and DNA damage, providing a tumor suppressor effect. At a late stage, MSCs manifest themselves as tumor promoters and stimulate epithelial-mesenchymal transition and metastasis [301]. Such growing controversy regarding the utility of MSCs in cancer therapy requires detailed *in vitro* and *in vivo* studies of their interactions with tumors.

Today, one of the key approaches for studying the behaviour and properties of individual cells in heterogeneous populations is the use of photoconvertible GFP-like proteins like Dronpa [13], mTFP0.7 [241], IrisFPs [14], and others. This technique makes it possible to mark a defined cell or cell ensemble using localized laser exposure. Since the effect of protein photoconversion is irreversible,

researchers can track the changes that occur in selected cells over time [6, 215]. This approach offers the possibility of not only tracing the destiny of individual cells in heterogeneous populations but also of marking and re-sorting cells with certain requested characteristics for cultivation and growth (e.g., the creation of purified cell lines) [302]. However, this approach has its limitations: (i) some GFP-like proteins exhibit toxicity [303] and a tendency to aggregate [304], (ii) a gradual decrease in the photoconverted fluorescent signal during cell doubling (i.e., daughter cells share a part of the converted protein among themselves until the signal disappears completely) [216], (iii) the inability to identify an individual cell among the marked ones, and (iv) the need for gene modification of the primary culture carrying the gene of the photoconvertible protein [163]. Gene modification is the main limitation to exploit the resulting cell clones in personalized medicine because of the probability of random mutations occurring during transfection.

Another cell labeling approach includes the use of lipophilic membrane dyes [203, 207, 217]. For example, DiR membrane dye exhibits high fluorescent stability for a long time, and it is suitable for both in vitro and in vivo tracking studies [207]. It can be photoconverted by laser irradiation, which allows the labeling and tracking of one or several cells in the population [7]. This advantage is critical for studying the properties of complex heterogeneous populations. Individually labeled cells can be sorted for targeted DNA or RNA sequencing [305, 306], or to obtain a purified cell line with the desired properties [307]. Nevertheless, membrane dyes can stain other cells in populations that are in close contact [308]. On

top of that, it does not make it possible to identify an individual cell of interest among several already marked ones in the case of photoconversion.

In the previous study, a promising new highly stable fluorescent photoconversion label was presented. This label is a thermally treated polymer multilayer microcapsule loaded with the fluorescent dye Rhodamine B (RhB), which can be easily internalized by various cell lines and reliably detected in the cytoplasm [24, 276]. Cells are capable of internalizing several microcapsules, which makes it possible to combine photoconverted and unconverted labels inside one cell and create color coding. This allows the identification of the specific cells among several marked cells. In addition, this method does not require genetic modification of the cell line.

In this Chapter, photoconvertible polymer microcapsules thermally treated in PVA gel with RhB and modified surfaces were explored in cell experiments on mMSC. The influence of capsule number (with different surface charges) on the viability, internalization efficiency, proliferation, and mobility of mMSCs was assessed. Finally, the migration of individual mMSCs within 2D and 3D EPNT-5 glioblastoma cell colonies was studied using photoconvertible microcapsules. The approbation of such a labeling and tracking technique on two more cell lines (myoblasts (C2C12) and hMSC) was discussed.

6.1.1 Selection of the optimal ratio of capsules per cell for effective and safe labeling of mMSCs and cell mobility

The correctly selected ratio of capsules per cell is of fundamental importance for the successful internalization of capsules into the cytoplasm in sufficient quantities without harm to their morphofunctional state. It is worth noting that the optimal ratio to ensure effective and safe labeling varies significantly among different cell types [24], so it must be carefully selected in each specific case. In this regard, at the first stage of cell experiments, the viability of mMSCs was assessed by metabolic activity at 24 and 48 h after adding 0, 1, 5, 10, 15, 20, and 25 capsules per cell. Three types of samples were used, which were discussed in Chapter 4. Sample 1 is regular capsules thermally treated in PVA gel with RhB. Sample 2 and sample 3 are capsules additionally covered with layers of PAH and PAH/PSS, respectively. For convenience, samples were named according to the outer layer of the capsules: PVA, PAH, and PSS.

Samples 1 (PVA) and 3 (PSS) did not have a statistically significant cytotoxic effect at all ratios of capsules per cell either 24 or 48 h after their addition (compared to the control) (Figure 6.1a). In contrast, the addition of sample 2 (PAH) was accompanied by a statistically significant decrease in metabolic activity even when adding 5 capsules (after 24 hours) and 1 capsule (after 48 hours) per cell. For this sample, a smooth trend of decreasing metabolic activity was found depending on the number of microcapsules added after both 24 and 48 h. It is important to

note that even the highest concentrations tested (15, 20, and 25 capsules per cell) did not reduce metabolic activity by more than 30 %. The difference in mMSCs' metabolic activity after the addition of 15 and 25 capsules per cell also did not exceed 6 % at the studied time points. Therefore, the internalization efficiency of different types of capsules at these concentrations was assessed in detail.

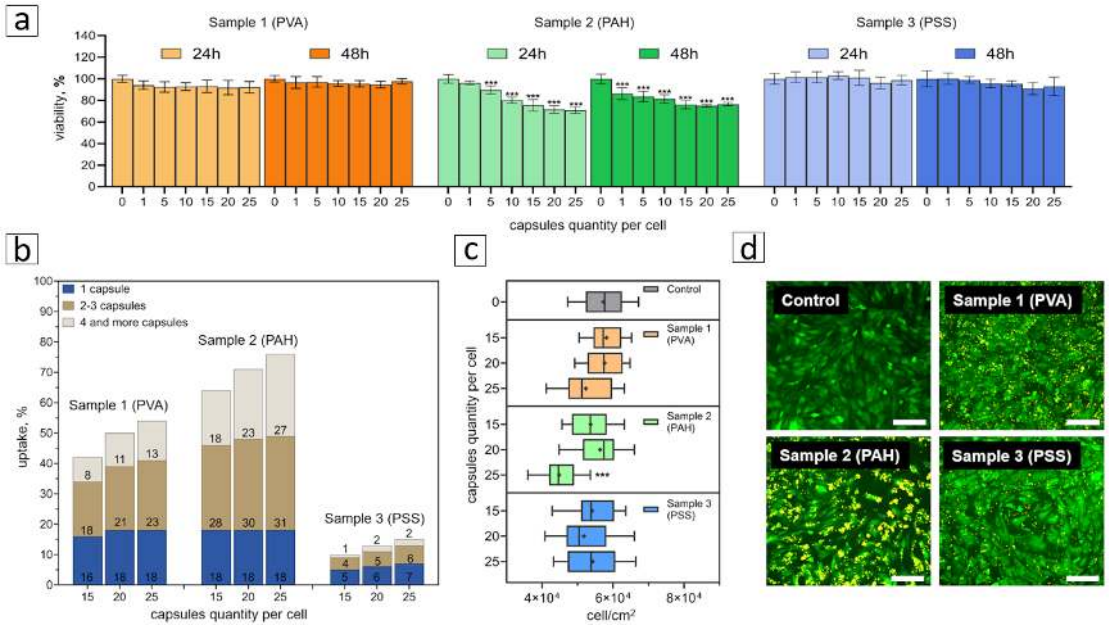

Figure 6.1: (a) Dependence of the metabolic activity of mMSCs on the number of added microcapsules with various surface modifications. ***P $<$ 0.001. (b) Dependence of the percentage of cells in the population that internalized the microcapsules 24 h after incubation with different concentrations. (c) The influence of the amount of microcapsules on mMSCs cell proliferation at different initial cell densities 24 h after incubation. ***P $<$ 0.001. (d) Fluorescence images of mMSCs (green) 24 h after cultivation with 25 capsules per cell (microcapsules are yellow). The scale bar is 200 μm.

As expected, internalization efficiency increased with an increasing number of

capsules per cell (Figure 36.1b). A common tendency for all types of capsules was also observed to increase the proportion of cells capturing 2-3 or more than 4 capsules. The percentage of cells that captured only 1 capsule was not significantly different. It is noteworthy that sample 2 (PAH) was internalized better than the rest of the samples. The efficiency of its internalization was 63.5 ± 6.4, 71 ± 2.8, and 75.9 ± 0.9 % for the ratios of 15, 20, and 25 capsules per cell, respectively. Sample 1 (PVA) was internalized by mMSCs less efficiently – 42.1 ± 5.1, 49.8 ± 1.7, and 54.5 ± 4.5 %, respectively. The worst results were obtained for the sample 3 (PSS) – the internalization efficiency did not exceed 7.3 ± 0.2 % at the highest capsule concentration.

The addition of PVA and PSS-modified capsules did not have a statistically significant effect on mMSC proliferation at all concentrations tested (Figure 6.1c). Significant differences in proliferation were only found when PAH-modified capsules were added at a rate of 25 capsules per cell.

The difference in the interaction of different types of capsules with cells was especially clearly visible in fluorescent images 24 h after incubation (Figure 6.1d). Capsules that were not internalized and did not interact with the cell membrane were removed during washing. The images were fully correlated with the internalization data obtained by flow cytometry. PAH-modified capsules densely covered the mMSCs' membrane, while PSS-modified capsules were visualized as single objects. This effect may be because the cell membrane has a negative charge; therefore, more positively charged capsules (like PAH-modified capsules) are at-

tached to cells faster and stronger than negatively charged capsules, which was reported previously [85]. At the same time, it was reported that particles with a more positive charge have a more pronounced cytotoxic effect [309], which is fully consistent with the presented data (Figure 6.1a). Capsules and other micro and nanocontainers with a pronounced negative charge (like PSS-modified capsules) are usually used for delivery through the bloodstream precisely due to low adhesion to the cell membranes [310] and as a result of a longer circulation time [311]. It is interesting that even despite the slight difference between the samples PSS and PVA in electrokinetic ζ-potential (Table 4.2), the difference in the effectiveness of internalization was pronounced to a significant extent (Figure 6.1b).

Analysis of the mMSCs' mobility using a scratch test revealed a small statistically significant difference for a sample of microcapsules modified with PSS at the addition of 25 capsules per cell compared to the negative control at 12 h (Figure 6.2). This difference leveled out at the 24-hour mark. This generally indicates the absence of a significant effect of all selected types and concentrations of capsules on cell mobility.

The identified trend showed the greatest promise of using PAH-modified capsules for mMSCs' labeling in a ratio of 20 capsules per cell. Under these conditions, optimal internalization efficiency was achieved without significantly affecting metabolic activity, cell motility, and proliferation.

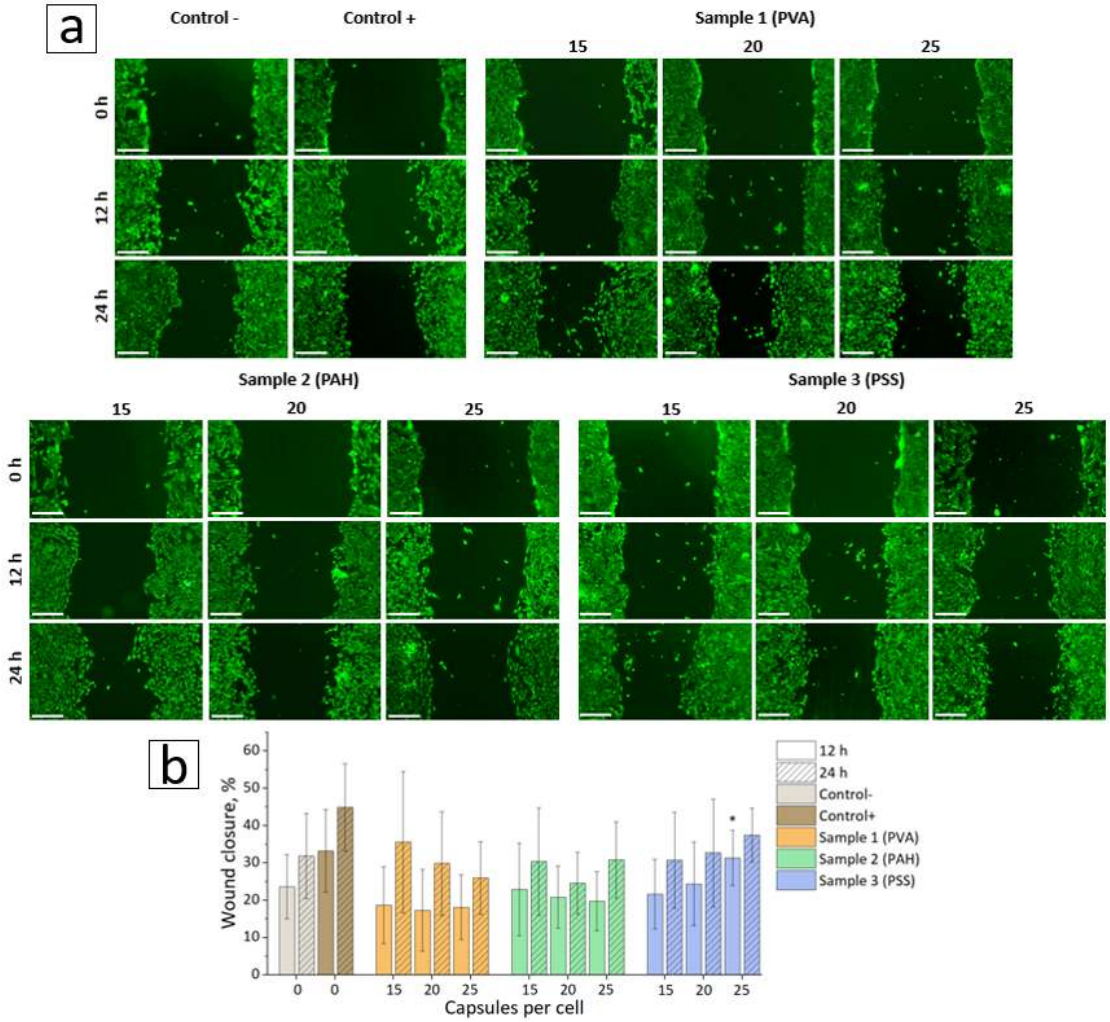

Figure 6.2: (a) Fluorescence images of the wound closure for mMSCs (green) at 0, 12, and 24 h after cultivation with different concentrations of photoconvertible microcapsules. The scale bar is 500 μm. (b) Graph of wound closure over time for mMSCs. *P < 0.05.

6.1.2 Tracking the migration of individual mMSCs labeled using photo-converted microcapsules in 2D u 3D EPNT-5 glioblastoma cells colony

At the next stage of cell experiments, the possibility of monitoring mMSCs' migration into glioblastoma cells (EPNT-5) colonies was studied during joint co-

cultivation. For this, the mMSCs (labeled with GFP and microcapsules) and EPNT-5 (labeled with DiD) were placed into 2 wells of silicone inserts with a defined cell-free gap (500 μm). The silicone insert was placed on a μ-Dish with a 500 μm grid for the convenience of monitoring changes in growth areas of cell colonies and determining the position of labeled cells. After 12 h of incubation, the silicone insert was removed (Figure 6.3). Note that mMSCs were placed into the well 24 h after internalization of the microcapsules (20 capsules per cell) and they had normal adhesion and morphology despite the presence of capsules inside. Monitoring of the cell migration continued for the next 72 h until the colonies completely merged. Notably, the merging of colonies was accompanied by the beginning of the process of DiD label transfer onto the mMSCs' membrane, which made further monitoring of migration difficult. Simultaneously, the capsules localized inside of mMSCs were an additional marker that allowed for reliable identification. As expected, it was the mMSCs that actively migrated to the glioblastoma colonies, while the EPNT-5 cells did not change their localization. Moreover, the active movement toward the colony of cancer cells began only after 24 hours.

Two cells at the border of the mMSCs' colony were laser-labeled at the beginning of the experiment (Figure 6.3). Labeled and their daughter cells (4 cells at the 48 h of the experiment) tended to move in the direction of the glioblastoma colony. At the same time, after 2 days of the experiment, tracking labeled cells became difficult. This was probably due to the high confluence of cells in the studied area, the loss of some cells during daily washing with DPBS buffer, and

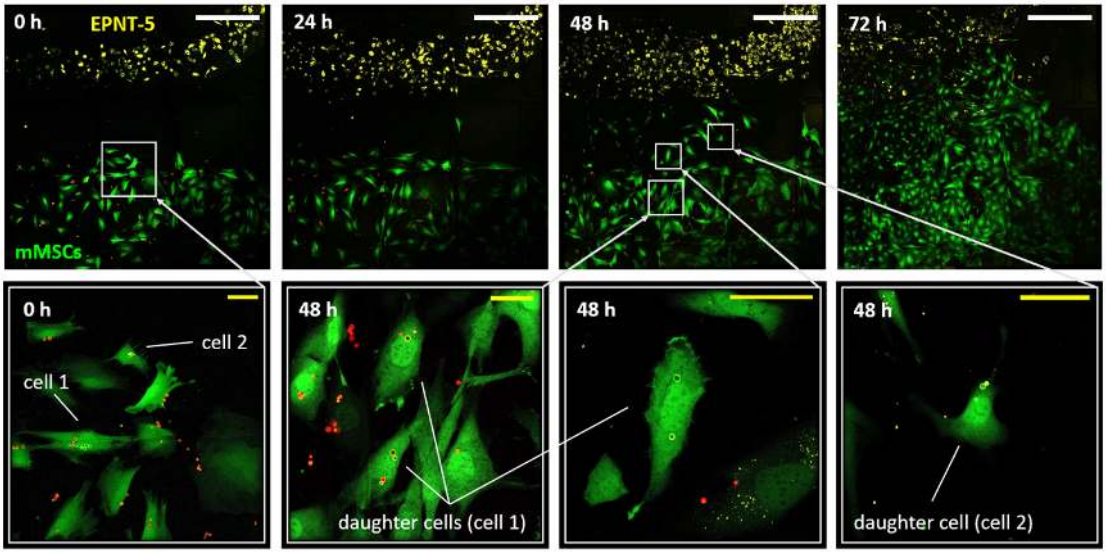

Figure 6.3: Migration of mMSCs (green) into a population of EPNT-5 glioblastoma cells (yellow) at 0, 24, 48, and 72 h. Cell 1 and Cell 2 were additionally labeled with photoconverted (green) PAH-modified microcapsules. Daughter cells shared converted capsules during doubling. Non-converted capsules are red. The white scale bar is 500 μm, and yellow is 50 μm.

the replacement of the medium.

Note that cell doubling led to the division of converted and non-convertible capsules between daughter cells. This required daily monitoring to record the new color coding that the daughter cells received. At the same time, the initial number of capsules (internalized by the cell and converted) was a natural limitation for tracking daughter cells. This is especially relevant and should be taken into account when tracking cells with a short doubling period (12-24 h). Nevertheless, the bright and stable fluorescence of the photoconverted microcapsules was maintained throughout the entire monitoring period, which was a significant

advantage compared to photoconvertible proteins. After photoconversion, new fluorescent proteins are continuously produced by the cell expressing the original color. As a result, a significant loss of the photoconverted signal occurs through protein turnover, and the photoconverted cells revert to their original color within 24 hours after photoconversion [216]. On the contrary, photoconversion of the lipophilic dye is permanent. Once photoconverted, the cell does not reacquire the original fluorescence signal, and the photoconverted signal is passed on to the daughter cells. It was reported that the progeny of a photoconverted cell can be tracked over at least three cell doublings, but the brightness of the signal will decrease by half with each cell doubling [207].

To monitor cells inside the 3D glioblastoma culture, the number of cells was initially selected to allow visualization of all cells in the spheroid (Figure 6.4). Spheroids consisting of 600-3000 cells allowed visualization of only the outer layer of cells (about 70 μm deep). This made migration monitoring impossible in a living spheroid without special optical clearing techniques. In this regard, the number of cells was reduced to 75, with a ratio of mMSCs to EPNT-5 of 1:5, respectively. It was still possible to view all the cells in the spheroid during 3D reconstruction with this number of cells.

Observation of individually labeled mMSCs in the spheroid made it possible to identify them for at least 48 hours (Figure 6.5a). 3D reconstruction confirmed the localization of photoconverted capsules in the mMSCs' cytoplasm both immediately and 48 h after the experiment started (Figure 6.5b). At the same time,

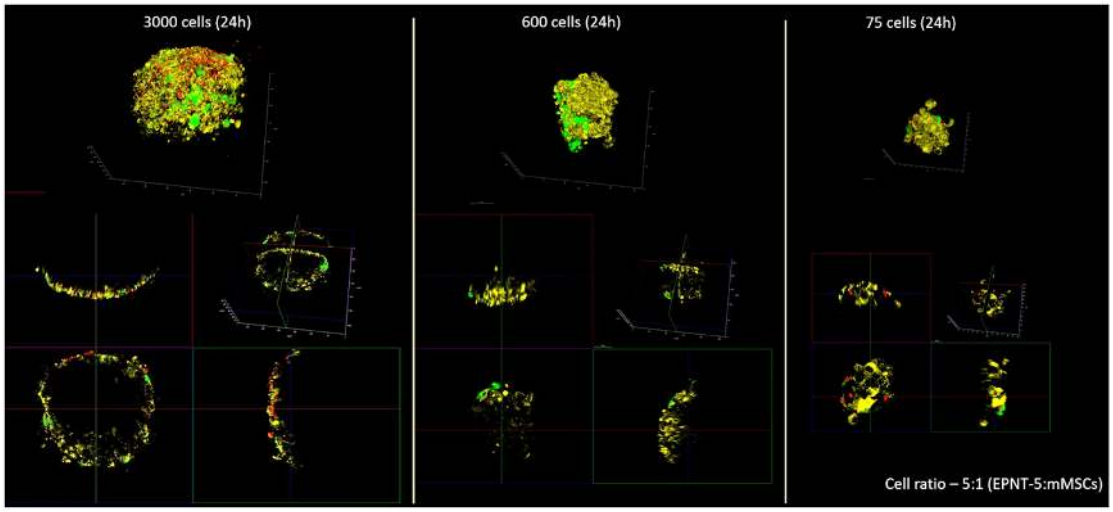

Figure 6.4: Fluorescence images of mMSCs (green) and the EPNT-5 glioblastoma cell spheroid (yellow) 24 h after placing a mixed cell suspension into the wells of low-adhesion 96-well floater plates SDL3D. Non-converted capsules – red.

continuous growth of the spheroid was observed, which ultimately led to the impossibility of identifying all the cells in it. This experiment also noted the ability of the lipophilic dye DiD to migrate to the mMSCs membrane from EPNT-5 cells' membrane already 24 h after the start of the experiment (48 h from the start of spheroid formation). At the same time, the transfer of photoconverted microcapsules from mMSCs to EPNT-5 was not noticed.

In general, the migration tracking of individual mMSCs in 2D and 3D EPNT-5 glioblastoma cells colonies showed a significant advantage of microcapsules in comparison with the DiD dye labeling.

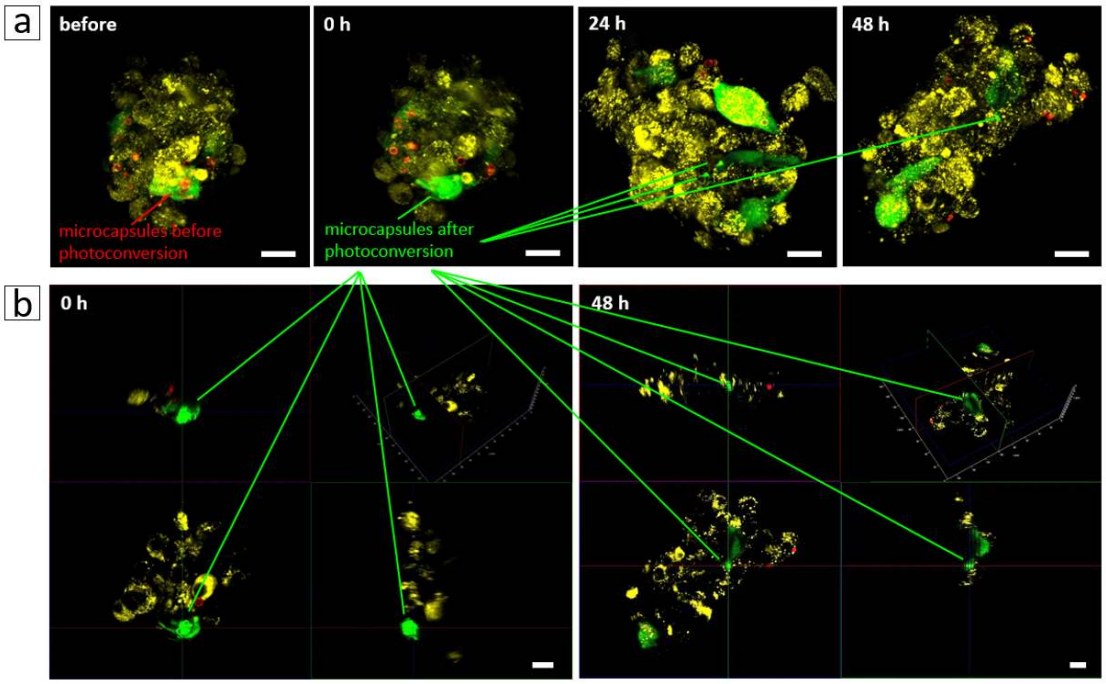

Figure 6.5: (a) Migration of mMSCs (green) in EPNT-5 glioblastoma cells spheroid (yellow) at 0, 24, and 48 h. Photoconverted capsules are green, and non-converted capsules are red. (b) 3D reconstruction of the EPNT-5 glioblastoma cell spheroid with labeled mMSCs at 0 and 48 h after photoconversion. Scale bar – 20 µm. The scale bar is 20 μm.

6.1.3 Approbation of photoconvertible microcapsules for myoblasts (C2C12) and hMSCs labeling and tracking

The developed photoconvertible polymer capsules were also approbated on hMSCs and myoblasts (C2C12). In this section, the results of the experiments will be briefly discussed to analyze how photoconvertible polymer capsules affect two additional cell lines.

6.1.3.1 hMSCs

hMSCs are at the center of the biomedical research community because of their unique properties, namely: multipotency [312–314], self-renewal capacity [315], long-term *ex vivo* proliferation capacity [316, 317], ability to migrate to tissue injury areas [318,319], and immune modulation [320]. These cells can also secrete anti-inflammatory cytokines [321] and hide themselves from the immune system [322]. hMSCs have great potential in targeted [323, 324] and regenerative [325] medicine and have already been applied in clinical practice [326]. The ability of hMSCs to differentiate into multiple lineages opens up broad prospects for tissue engineering [317]. Nevertheless, the possibility of spontaneous differentiation (e.g., by cancer cells or fibroblasts [327, 328]) raises concerns. At the same time, the ability of the cells to migrate in a directed manner and carry cargo to a site of damage has wide potential [329]. Therefore, the study of the fundamental issues of hMSCs' interaction with healthy and pathological cells and the processes of their migration and differentiation remain extremely relevant.

In this regard, the developed photoconvertible polymer microcapsules were used for hMSCs' labeling and tracking. The efficiency of capsule internalization is directly related to the added capsule concentration. A ratio of 10 capsules per cell is optimal, causing 46 ± 2 % of all cells to be labeled. The consequent increase in the number of capsules led to a critical decrease in cell viability and a change in morphology. At the same time, a higher ratio of capsules to cells does not have a significant effect on the cell immunophenotype.

The capsules have been internalized and retained inside hMSCs for at least 7 days (Figure 6.6a,b). Cells are known to have exocytosis machinery, when after uptake, digestion, and nutrient absorption, cells remove undigested particles to the outside. The duration of capsule retention inside the cells depends on the cell line and polymers used for the production of the capsules. For example, microcapsules based on biodegradable PArg and DS were broken down by macrophages within 24 h [240]. At the same time, the capsules prepared with non-biodegradable polymers PAH and PSS polymers can be observed in cells for several days [330]. It was demonstrated in a work by Luo et al., where capsules remained inside C2C12 cells for 34 days [248].

In addition, it is likely that the capsules will retain a bright fluorescent signal for a long time (several weeks or months) because their composition is based on non-biodegradable polyelectrolytes [330]. The developed approach made it possible to track the trajectory of the movement of several individual cells for several days, as well as the fate of daughter cells after doubling, without additional marking for 4 days (Figure 6.6c). Some of the photoconverted microcapsules may have been lost by cells during the tracking process. This was probably due to their localization on the membrane and incomplete internalization by the cell at the time of marking (Figure 6.6d)

Even though the converted and non-converted capsules were split between the daughter cells randomly, the brightness of the label is preserved, and the new color code can be automatically "assigned" to the daughter cells. These new

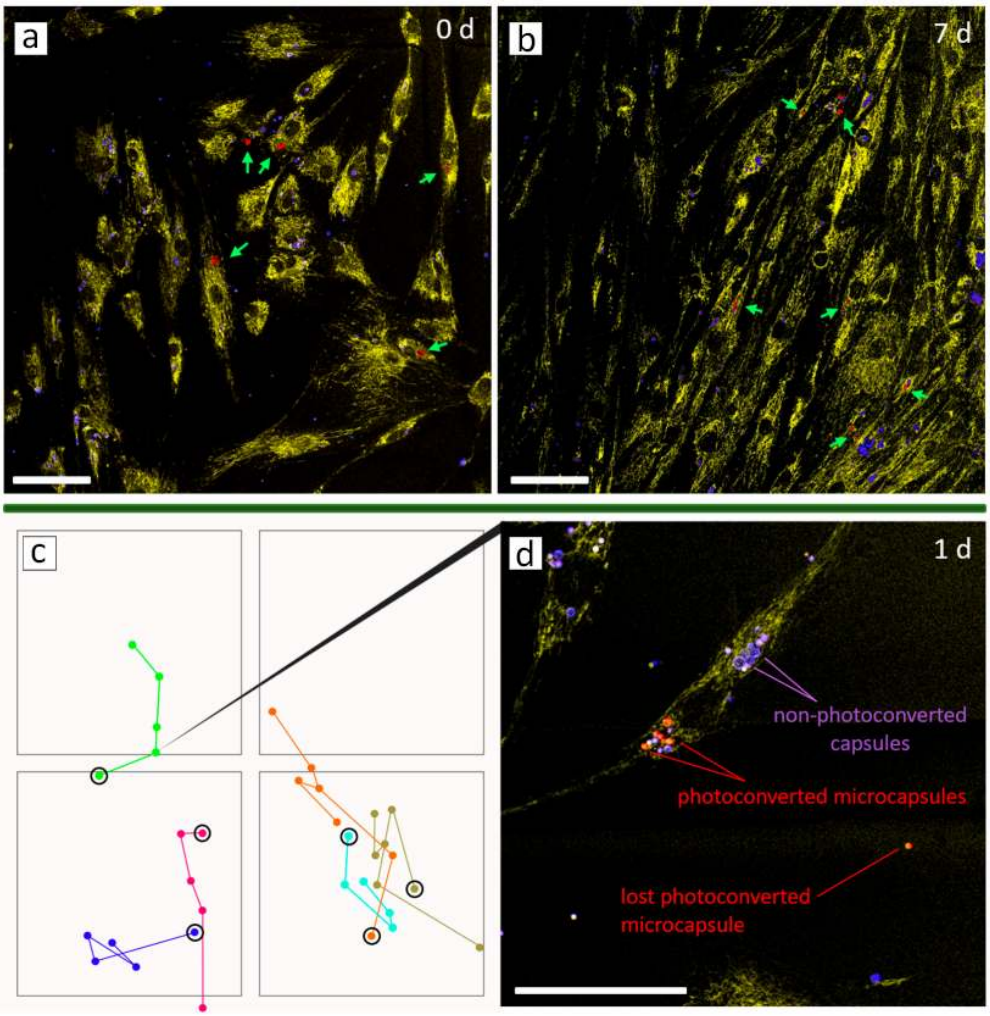

Figure 6.6: CLSM images of hMSCs with microcapsules at 0 (a) and 7 (b) days after labeling (hMSCs – yellow (Cy7), non-photoconverted microcapsules – blue, photoconverted – red). Green arrows indicate the photoconverted microcapsules. The scale bar is 100 μm. (c) Tracking diagram of six cells over 4 days. The dots circled in black indicate day 0. The remaining dots show the position of the nucleus of the labeled cell every 24 h. The side of each square is 500 μm. Tracks of individual cell movement are marked with different colors. (d) Image of one of the marked cells 1 day after the tracking commenced. The scale bar is 50 μm.

codes can be traced during subsequent monitoring. Reliable tracing of hMSCs and their daughter cells was performed for 1.5 or 2 doubling periods before the culture reached 100% confluence (with an initial confluence value of 25-30%). Nevertheless, it is possible to start the experiment with lower confluence values (10-15%) for some cell cultures that are less sensitive to their microenvironment than hMSCs. In this case, the multiple doublings will eventually lead to the appearance of daughter cells with no capsules or too few capsules to assign them a "color code." The repeated addition of microcapsules for labeling can help solve this problem. Note that the current approach using photoconvertible proteins has no possibility of individual cell coding. The fluorescent signal starts to dilute within the first few hours after protein photoconversion due to the continuous synthesis of new unconverted molecules. The splitting of the converted protein during cell doubling also decreases the detectable signal until its complete disappearance after 48-72 h [216].

6.1.3.2 Myoblasts (C2C12)

Despite significant progress in pharmacological and surgical fields, ischemic heart disease is the leading cause of morbidity and mortality worldwide [331, 332]. Ischemic injury leads to cardiomyocyte loss, followed by fibrosis, resulting in impaired contractile function of the heart [333]. In contrast to skeletal muscle, the cardiomyocyte turnover rate in the adult heart is limited [334]. This is due to the relative inability of adult mammalian cardiomyocytes to reenter the cell cycle and the apparent absence of a stem cell population that could proliferate

and differentiate into myoblasts (myocyte precursors) [335].

It has been reported that human myoblast transplantation into minipig myocardium after ischemic heart injury also has attractive effects on cardiac repair [336]. The few studies on patients also demonstrated the potential of autologous skeletal myoblast transplantation into the post-infarction scar or ischemic area for the restoration of contractile function of the heart [337,338]. Nevertheless, the complications of transplantation and mechanisms of myoblast migration have not been fully elucidated [336]. Therefore, the development of reliable methods for labeling and tracking myoblasts and the study of their migration and interaction with surrounding tissue is extremely relevant for regenerative medicine.

Thermally treated polyelectrolyte microcapsules with RhB showed promise as a bright, stable, and reliable marker for the detection of myocytes in a colony of macrophages. Uptake reached 73 $\pm$ 3 % at a ratio of 15 capsules per cell. Note that the efficiency of microcapsule uptake depended on the degree of cell confluence and increased with an increase in the initial cell density. This is most probably associated with the increasing probability of interaction between the capsule shell and the cell membrane at a higher initial cell density. The metabolic activity of C2C12 cells tended to decrease with an increase in the number of microcapsules, nevertheless, values did not decrease below 80 %. This should be considered when planning experiments and choosing the optimal ratio of capsules per cell. Simultaneously, the capsules did not affect the mobility of C2C12 cells at any of the studied ratios (5, 10, and 15 capsules per cell).

The fluorescent capsules in the cytoplasm of C2C12 cells allowed the reliable identification of this type of cell (Figure 6.7). Observations of C2C12 and Raw264.7 cell colonies during co-cultivation for 96 allowed to identify several trends in their interactions (Figures 6.7a-e). The myoblasts actively moved towards the macrophage colony starting from the first day of the experiment and entered the macrophage colony after approximately 72 h. During this period, they covered a distance of 500 μm.

Two cells at the border of the C2C12 colony were laser-labeled at the beginning of the experiment. The tracking diagram of them demonstrated their migration pathways for both the initial and daughter cells (Figure 6.6f). Confocal imaging before and after photoconversion is presented in Figures 6.6g and 6.6h, respectively. Individual myoblast cells (labeled using photoconversion) and daughter cells tended to move in the direction of the macrophage colony, although they moved at different speeds. The Raw 264.7 cells did not leave the initial adhesion area their ability for active migration, which may indirectly indicate the ability of myoblasts to inhibit macrophage motility.

6.2 Conclusions

Three types of capsules with surface modifications were used for the cell experiments on mMSCs. Sample 1 (PVA) and sample 3 (PSS) demonstrated low cytotoxicity at all added capsule-to-cell ratios (15, 20, and 25 capsules per cell). Sample 2 (PAH) demonstrated a gradual decrease in cell viability with an in-

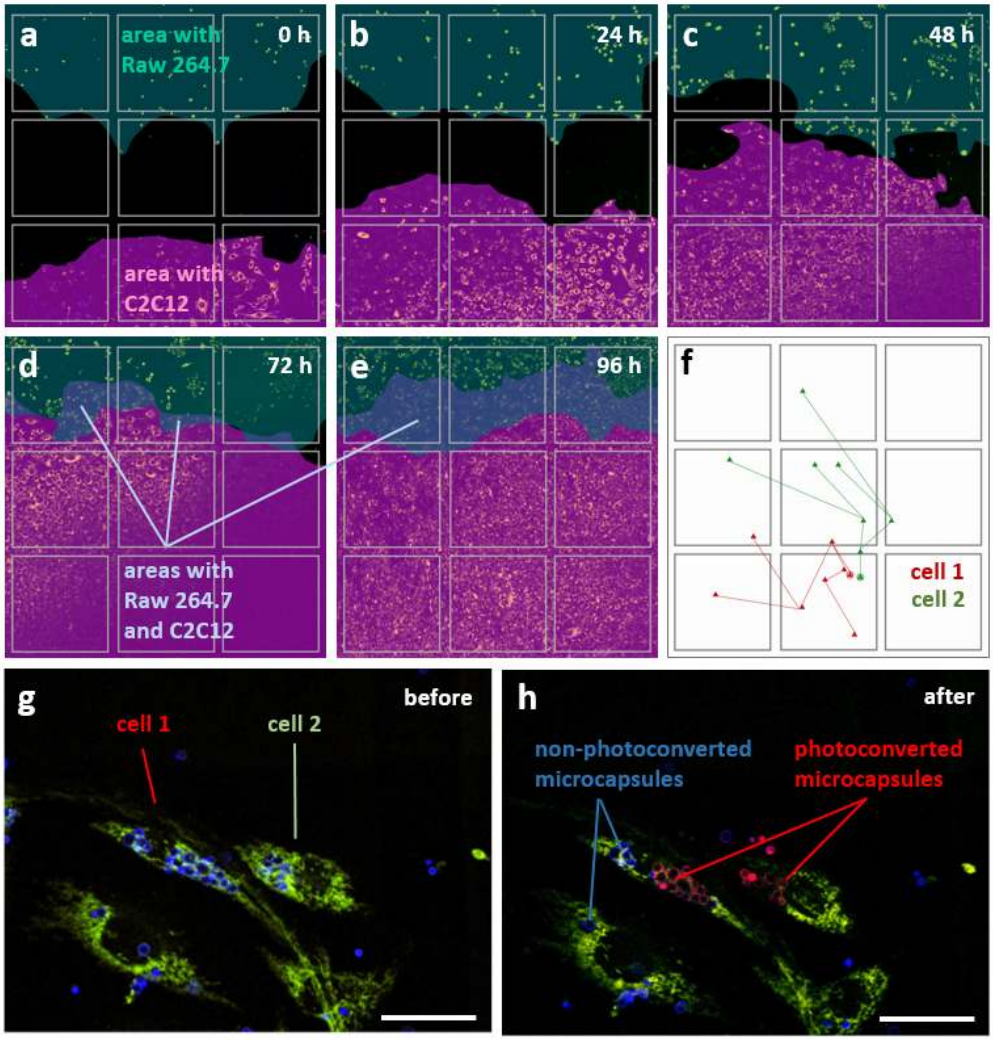

Figure 6.7: (a) Fluorescence images of C2C12 cells with internalized capsules and RAW 264.7 cells at 0 h (RAW 264.7 cells are stained with DiD (yellow)). (b-e) Fluorescence images showing the changes in the borders of the cells after 24, 48, 72, and 96 h (the area with RAW 264.7 is green, and area with C2C12 is violet). (f) Tracking diagram of two labeled cells over four days. Day 0 is marked with a circle. (g-h) Fluorescence images of two cells before (blue) and after (red) photoconversion of the capsules.

crease in capsule concentration. Nevertheless, metabolic activity was not reduced by more than 30 % even at a concentration of 25 capsules per cell. At the same time, sample 2 (PAH) demonstrated the highest uptake values: approximately 76 % for the ratio of 25 capsules per cell. Interestingly, the internalization efficiency was very low for sample 3 (PSS): approximately 7 %. This phenomenon is closely connected to the fact that the cell membrane has a negative charge, and more positively charged particles are attached to it more strongly and at a higher rate [85]. Capsules also did not affect mMSCs' mobility.

For the labeling and tracking experiments, sample 2 (PAH) was chosen as the most promising candidate at the concentration of 20 capsules per cell. The migration of mMSCs into the glioblastoma cells colony was studied. Labeled mMSC cells moved in the direction of glioblastoma, as well as the daughter cells, which could be identified as well. Migration of stem cells in the glioblastoma spheroid was also observed. It was possible to label mMSCs and identify them for at least 48 hours. Both 2D and 3D studies demonstrated that the lipophilic membrane DiD dye, originally used to stain glioblastoma cells, contaminated the membrane of mMSC cells after 24 h from the start of the experiment. At the same time, the transfer of polymer capsules was not noticed, making them an attractive alternative to lipophilic dyes.

Photoconvertible microcapsules were also approbated for studies on C2C12 and hMSCs. For hMSCs, 10 capsules per cell were optimal for labeling, causing 46 $\pm$ 2% of all cells to be labeled. Also, capsules did not have a significant effect on

the cell immunophenotype. hMSCs were labeled and tracked for 4 days without additional marking. For C2C12 cells, 15 capsules per cell were optimal, causing 73 ± 3% of the cells to be labeled. The metabolic values did not decrease below 80%. The capsules did not affect the mobility of C2C12 cells at any of the studied ratios (5, 10, and 15 capsules per cell). The capsules were used to label C2C12 cells and observe their migration to the Raw264.7 colony.

The developed photoconvertible microcapsules have broad prospects for creating stable purified lines because of their ability to detect each cell from the labeled group as well as the absence of gene modification. There is a need to select and isolate specific cell populations from heterogeneous cultures [339]. For example, after labeling, morphologically competent cells can be sorted and clones with the requested characteristics may be obtained. Cells that are capable of rapid doubling or directional movement can be selected and expanded for further use in regenerative medicine.

In general, all the data obtained indicate that labeling with thermally treated polyelectrolyte microcapsules with RhB could be a promising approach for studying the processes of interaction between different cell lines. This is especially important for stromal/stem cells, including tumor cells, as they are widely differentiable. The developed strategy could become key to understanding their fate in the long-term cell-to-cell cultivation of the whole population.

Chapter 7. General Conclusions and Future Work

7.1 General conclusions

Two protocols for the synthesis of fluorescent photoconvertible polymer microcapsules were elaborated. The first one utilized PVA gel as a medium for capsule thermal treatment that initiated the dye encapsulation and formation of CNDs. This protocol allowed for increasing the yield of capsules from one synthesis by at least 250 times in comparison to a similar synthesis in water. The encapsulated dyes exhibited robust fluorescence after thermal treatment, except for TR, which did not withstand high-temperature treatment for the dye encapsulation (180 °C). RhB and Rh6G were found to be photostable and to exhibit photoconversion properties from the 580–620/670 detection region (561 nm laser excitation) to the 505–540 detection region (488 nm laser excitation). Mass spectrometry studies revealed that the rhodamine dyes underwent several deethylation steps under conditions similar to those of the photoconversion procedure. Consequently, new compounds with blue spectral shifts were formed, enabling the visualization of the capsules in the green channel after photoconversion.

Both RhB- and Rh6G-containing capsules can be used for cell labeling. In the case of using the 561 nm laser and 580-620 nm detection range, RhB-containing capsules were more suitable for cell experiments, since these parameters are more optimal for RhB dye than for Rh6G. Therefore, capsules containing RhB require less power density for photoconversion than capsules with Rh6G. This is more favorable for cell experiments where cells should remain alive after laser radiation.

Despite this, capsules with Rh6G still may be useful for cell tracking.

The second presented protocol for the synthesis of photoconvertible capsules did not require thermal treatment. Capsules with the dyes Cy3.5, Cy5.5, Cy7, and RITC were prepared. Capsules containing Cy3.5, Cy5.5, and RITC demonstrated profound photoconversion ability, while for Cy7 this effect was less prominent. Capsules containing Cy3.5 and RITC were excited with the 561 nm laser and detected in the range 580–630 nm. Capsules containing Cy5.5 and Cy7 were excited with the 671 nm laser and detected in the range of 686–790 nm. After photoconversion, the capsules were excited with a 488 nm laser and detected in the range 505–540 nm. Therefore, the sample with Cy5.5 (and potentially Cy7) provided a new detection option in the NIR region in addition to the dyes detected in the red channel. Moreover, it also opens up the possibility of detecting capsules deeper in the tissue by taking advantage of near-infrared windows in biological tissue (650–900 nm) [296].

Thermally treated photoconvertible polymer microcapsules with RhB have been used for cell labeling and tracking experiments on mMSCs. Modification of capsules with polyallylamine hydrochloride showed the best potential for intracellular uptake of capsules without significantly affecting viability, motility, and proliferation (the ratio of 20 capsules per cell turned out to be optimal). The tracking of the migration of labeled MSCs within glioblastoma cell colonies in both 2D and 3D models revealed the superior performance of microcapsules compared to conventional lipophilic dyes. The ability to reliably identify labeled cells over an

extended period without significant signal decay presents a notable advantage for long-term tracking studies. The technique developed in this study holds promise for advancing the understanding of MSC-tumor interactions and for facilitating the development of innovative approaches for cancer treatment.

This tracking and labeling technique using photoconvertible polymer capsules was also tested on myocytes (C2C12) and hMSCs. For hMSCs, a ratio of 10 capsules per cell was optimal, causing 46 ± 2% of all cells to be labeled while preserving cell viability. Also, capsules did not have a significant effect on the cell immunophenotype. The developed approach made it possible to track the trajectory of the movement of several individual cells for several days, as well as the fate of daughter cells after doubling, without additional marking for 4 days. Capsules were also reliably internalized by C2C12 cells, and uptake reached 73 ± 3% at a ratio of 15 capsules per cell. The metabolic values did not decrease below 80%. Moreover, the capsules did not affect the mobility of C2C12 cells. The capsules were used to label C2C12 cells and observe their migration to the Raw264.7 colony.

In the future, such capsules can provide a unique coding system for cell labeling and tracking via a combination of variously-colored labels. The capsules also can be used for individual labeling of the cells and will remain a bright fluorescence signal for at least 7 days of detection. Moreover, capsules serve as an alternative to lipophilic dyes, which often stain non-labeled cells [23], and green fluorescent proteins generated due to genetic modification of the cells. Proposed polymer

labels eliminate the risk of genetic mutations [20], which is important in the case of personalized medicine.

7.2 Future work

There are several directions for future studies on photoconvertible polymer microcapsules. For example, if stable and non leaking dyes that fluoresce in the green channel are be found and tested, that could provide one more labeling and tracking opportunity in addition to the red and NIR channels discussed in this thesis. Another possible task is to create stable purified lines of cells with specific characteristics using photoconvertible microcapsules. Labeled cells can be selected and isolated from heterogeneous cultures based on the desired set of parameters [339]. For example, it could be the most active and mobile cells. Cells that are capable of rapid doubling or directional movement are especially promising for this task, giving the ability to be rapidly expanded for further use in regenerative medicine. Another interesting task is investigating photoconvertible label uptake by cells in the tissues. The possibility of the photoconversion of internalized polymer capsules in the tissue can be investigated in this experiment. The possibility of the subsequent visualization of labeled cells for up to several days can also be analyzed. Another variation of this task is the injection in the tissue with the cells that have already captured the photoconvertible capsules. The possibility of their photoconversion can also be analyzed. This approach can be used to study glioma development, for example, or the migration of stem cells in the tissue.

Bibliography

[1] Bingcheng Yi, Qi Xu, and Wei Liu. An overview of substrate stiffness guided cellular response and its applications in tissue regeneration. *Bioactive Materials*, 15:82–102, September 2022.

[2] Hosseinkhani Mohsen, Mehrabani Davood, Hassan Karimfar Mohammad, Bakhtiyari Salar, Manafi Amir, and Shirazi Reza. Tissue engineered scaffolds in regenerative medicine. *World Journal of Plastic Surgery*, 3:3–7, December 2014.

[3] Hu Zhang and Kuo-Kang Liu. Optical tweezers for single cells. *Journal of The Royal Society Interface*, 5(24):671–690, April 2008.

[4] Feng Guo, Zhangming Mao, Yuchao Chen, Zhiwei Xie, James P. Lata, Peng Li, Liqiang Ren, Jiayang Liu, Jian Yang, Ming Dao, Subra Suresh, and Tony Jun Huang. Three-dimensional manipulation of single cells using surface acoustic waves. *Proceedings of the National Academy of Sciences*, 113(6):1522–1527, January 2016.

[5] Frederick Gertz and Alexander Khitun. Biological cell manipulation by magnetic nanoparticles. *AIP Advances*, 6(2), February 2016.

[6] Hugo R. Caires, Maria Gomez-Lazaro, Carla M. Oliveira, David Gomes, Denisa D. Mateus, Carla Oliveira, Cristina C. Barrias, Mário A. Barbosa, and Catarina R. Almeida. Finding and tracing human msc in 3d microen-

vironments with the photoconvertible protein dendra2. *Scientific Reports*, 5(1), May 2015.

[7] Sam Osseiran, Lauren A. Austin, Taylor M. Cannon, Chuan Yan, David M. Langenau, and Conor L. Evans. Longitudinal monitoring of cancer cell subpopulations in monolayers, 3d spheroids, and xenografts using the photoconvertible dye dir. *Scientific Reports*, 9(1), April 2019.

[8] Dirk Dormann and Cornelis J Weijer. Imaging of cell migration. *The EMBO Journal*, 25(15):3480–3493, August 2006.

[9] Rui Tang, Christopher W Murray, Ian L Linde, Nicholas J Kramer, Zhonglin Lyu, Min K Tsai, Leo C Chen, Hongchen Cai, Aaron D Gitler, Edgar Engleman, Wonjae Lee, and Monte M Winslow. A versatile system to record cell-cell interactions. *eLife*, 9, October 2020.

[10] Kohei Hatta, Hitomi Tsujii, and Tomomi Omura. Cell tracking using a photoconvertible fluorescent protein. *Nature Protocols*, 1(2):960–967, August 2006.

[11] Cornelia Halin, J. Rodrigo Mora, Cenk Sumen, and Ulrich H. von Andrian. In vivo imaging of lymphocyte trafficking. *Annual Review of Cell and Developmental Biology*, 21(1):581–603, November 2005.

[12] Tanja Brakemann, Andre C Stiel, Gert Weber, Martin Andresen, Ilaria Testa, Tim Grotjohann, Marcel Leutenegger, Uwe Plessmann, Henning Urlaub, Christian Eggeling, Markus C Wahl, Stefan W Hell, and Stefan

Jakobs. A reversibly photoswitchable gfp-like protein with fluorescence excitation decoupled from switching. *Nature Biotechnology*, 29(10):942–947, September 2011.

[13] Ryoko Ando, Hideaki Mizuno, and Atsushi Miyawaki. Regulated fast nucleocytoplasmic shuttling observed by reversible protein highlighting. *Science*, 306(5700):1370–1373, November 2004.

[14] Virgile Adam, Mickaël Lelimousin, Susan Boehme, Guillaume Desfonds, Karin Nienhaus, Martin J. Field, Joerg Wiedenmann, Sean McSweeney, G. Ulrich Nienhaus, and Dominique Bourgeois. Structural characterization of irisfp, an optical highlighter undergoing multiple photo-induced transformations. *Proceedings of the National Academy of Sciences*, 105(47):18343–18348, November 2008.

[15] Agnieszka Fus-Kujawa, Pawel Prus, Karolina Bajdak-Rusinek, Paulina Teper, Katarzyna Gawron, Agnieszka Kowalczuk, and Aleksander L. Sieron. An overview of methods and tools for transfection of eukaryotic cells in vitro. *Frontiers in Bioengineering and Biotechnology*, 9, July 2021.

[16] Yurii G. Yanushevich, Dmitry B. Staroverov, Alexander P. Savitsky, Arkady F. Fradkov, Nadya G. Gurskaya, Maria E. Bulina, Konstantin A. Lukyanov, and Sergey A. Lukyanov. A strategy for the generation of non-aggregating mutants of anthozoa fluorescent proteins. *FEBS Letters*, 511(1–3):11–14, December 2001.

[17] Satoshi Karasawa, Toshio Araki, Takeharu Naai, Hideaki Mizuno, and Atsushi Miyawaki. Cyan-emitting and orange-emitting fluorescent proteins as a donor/acceptor pair for fluorescence resonance energy transfer. *Biochemical Journal*, 381(1):307–312, June 2004.

[18] J. Paul Taylor, John Hardy, and Kenneth H. Fischbeck. Toxic proteins in neurodegenerative disease. *Science*, 296(5575):1991–1995, June 2002.

[19] Christopher D. Link, Virginia Fonte, Brian Hiester, John Yerg, Jmil Ferguson, Susan Csontos, Michael A. Silverman, and Gretchen H. Stein. Conversion of green fluorescent protein into a toxic, aggregation-prone protein by c-terminal addition of a short peptide. *Journal of Biological Chemistry*, 281(3):1808–1816, January 2006.

[20] Aaron Liew, Franck M. André, Léa L. Lesueur, Marie-Amélie De Ménorval, Timothy O'Brien, and Lluis M. Mir. Robust, efficient, and practical electrogene transfer method for human mesenchymal stem cells using square electric pulses. *Human Gene Therapy Methods*, 24(5):289–297, October 2013.

[21] Fanny Mousseau, Jean-François Berret, and Evdokia K. Oikonomou. Design and applications of a fluorescent labeling technique for lipid and surfactant preformed vesicles. *ACS Omega*, 4(6):10485–10493, June 2019.

[22] Elias A. Halabi, Jorge Arasa, Salome Püntener, Victor Collado-Diaz, Cornelia Halin, and Pablo Rivera-Fuentes. Dual-activatable cell tracker

for controlled and prolonged single-cell labeling. *ACS Chemical Biology*, 15(6):1613–1620, April 2020.

[23] Sandra Strassburg, Nigel W. Hodson, Patrick I. Hill, Stephen M. Richardson, and Judith A. Hoyland. Bi-directional exchange of membrane components occurs during co-culture of mesenchymal stem cells and nucleus pulposus cells. *PLoS ONE*, 7(3):e33739, March 2012.

[24] Polina A. Demina, Olga A. Sindeeva, Anna M. Abramova, Ekaterina S. Prikhozhdenko, Roman A. Verkhovskii, Ekaterina V. Lengert, Andrei V. Sapelkin, Irina Yu. Goryacheva, and Gleb B. Sukhorukov. Fluorescent convertible capsule coding systems for individual cell labeling and tracking. *ACS Applied Materials & Interfaces*, 13(17):19701–19709, April 2021.

[25] Gleb B. Sukhorukov, Edwin Donath, Sean Davis, Heinz Lichtenfeld, Frank Caruso, Victor I. Popov, and Helmuth Möhwald. Stepwise polyelectrolyte assembly on particle surfaces: a novel approach to colloid design. *Polymers for Advanced Technologies*, 9(10–11):759–767, October 1998.

[26] Gero Decher, Birgit Lehr, Klaus Lowack, Yuri Lvov, and Johannes Schmitt. New nanocomposite films for biosensors: layer-by-layer adsorbed films of polyelectrolytes, proteins or dna. *Biosensors and Bioelectronics*, 9(9–10):677–684, 1994.

[27] R.K. Iler. Multilayers of colloidal particles. *Journal of Colloid and Interface Science*, 21(6):569–594, June 1966.

[28] Ana Mateos-Maroto, Irene Abelenda-Núñez, Francisco Ortega, Ramón G. Rubio, and Eduardo Guzmán. Polyelectrolyte multilayers on soft colloidal nanosurfaces: A new life for the layer-by-layer method. *Polymers*, 13(8):1221, April 2021.

[29] G. Decher, J.D. Hong, and J. Schmitt. Buildup of ultrathin multilayer films by a self-assembly process: Iii. consecutively alternating adsorption of anionic and cationic polyelectrolytes on charged surfaces. *Thin Solid Films*, 210–211:831–835, April 1992.

[30] Edwin Donath, Gleb B. Sukhorukov, Frank Caruso, Sean A. Davis, and Helmuth Möhwald. Novel hollow polymer shells by colloid-templated assembly of polyelectrolytes. *Angewandte Chemie International Edition*, 37(16):2201–2205, September 1998.

[31] Rashida N. Smith, Mark McCormick, Christopher J. Barrett, Linda Reven, and Hans W. Spiess. Nmr studies of pah/pss polyelectrolyte multilayers adsorbed onto silica. *Macromolecules*, 37(13):4830–4838, June 2004.

[32] JF Joanny. Polyelectrolyte adsorption and charge inversion. *The European Physical Journal B-Condensed Matter and Complex Systems*, 9(1):117–122, 1999.

[33] Regine v Klitzing. Internal structure of polyelectrolyte multilayer assemblies. *Physical Chemistry Chemical Physics*, 8(43):5012–5033, 2006.

[34] Kan Tang and Nicolaas A. M. Besseling. Formation of polyelectrolyte multilayers: ionic strengths and growth regimes. *Soft Matter*, 12(4):1032–1040, 2016.

[35] Thichakorn Sungoradee and Kawee Srikulkit. Preparation and characterizations of pss/pdadmac polyelectrolyte complex hydrogel. *Polymers*, 14(9):1699, April 2022.

[36] Joseph B. Schlenoff and Stephan T. Dubas. Mechanism of polyelectrolyte multilayer growth: charge overcompensation and distribution. *Macromolecules*, 34(3):592–598, January 2001.

[37] Jad A. Jaber and Joseph B. Schlenoff. Mechanical properties of reversibly cross-linked ultrathin polyelectrolyte complexes. *Journal of the American Chemical Society*, 128(9):2940–2947, February 2006.

[38] Joseph B. Schlenoff, Hiep Ly, and Ming Li. Charge and mass balance in polyelectrolyte multilayers. *Journal of the American Chemical Society*, 120(30):7626–7634, July 1998.

[39] Eduardo Guzmán, Hernán A. Ritacco, Francisco Ortega, and Ramón G. Rubio. Growth of polyelectrolyte layers formed by poly(4-styrenesulfonate sodium salt) and two different polycations: New insights from study of adsorption kinetics. *The Journal of Physical Chemistry C*, 116(29):15474–15483, July 2012.

[40] Erik Johansson, Eva Blomberg, and Lars Wågberg. Adhesive interaction between polyelectrolyte multilayers of polyallylamine hydrochloride and polyacrylic acid studied using atomic force microscopy and surface force apparatus. *Langmuir*, 25(5):2887–2894, February 2009.

[41] C. Picart, Ph. Lavalle, P. Hubert, F. J. G. Cuisinier, G. Decher, P. Schaaf, and J.-C. Voegel. Buildup mechanism for poly(l-lysine)/hyaluronic acid films onto a solid surface. *Langmuir*, 17(23):7414–7424, October 2001.

[42] Ph. Lavalle, C. Gergely, F. J. G. Cuisinier, G. Decher, P. Schaaf, J. C. Voegel, and C. Picart. Comparison of the structure of polyelectrolyte multilayer films exhibiting a linear and an exponential growth regime: An in situ atomic force microscopy study. *Macromolecules*, 35(11):4458–4465, April 2002.

[43] Shameek Vats, Lawrence W. Honaker, Margaret W. Frey, Francesco Basoli, and Jan P.F. Lagerwall. Electrospinning ethanol–water solutions of poly(acrylic acid): Nonlinear viscosity variations and dynamic taylor cone behavior. *Macromolecular Materials and Engineering*, 307(2), November 2021.

[44] Chongsuk Ryou, William B. Titlow, Charles E. Mays, Younsoo Bae, and Sehun Kim. The suppression of prion propagation using poly-l-lysine by targeting plasminogen that stimulates prion protein conversion. *Biomaterials*, 32(11):3141–3149, April 2011.

[45] SCBT. Poly-l-glutamic acid. https://www.scbt.com/p/poly-l-glutamic-acid-25513-46-6-alt, 2024 (accessed May 27, 2024).

[46] Donald L. Elbert, Curtis B. Herbert, and Jeffrey A. Hubbell. Thin polymer layers formed by polyelectrolyte multilayer techniques on biological surfaces. *Langmuir*, 15(16):5355–5362, June 1999.

[47] Andrey V. Subbotin and Alexander N. Semenov. The structure of polyelectrolyte complex coacervates and multilayers. *Macromolecules*, 54(3):1314–1328, January 2021.

[48] Faeze Kazemi-Andalib, Maryam Mohammadikish, Unes Sahebi, and Adeleh Divsalar. Layer-by-layer synthesis of the ph-responsive hollow microcapsule and investigation of its drug delivery and anticancer properties. *Journal of Pharmaceutical Sciences*, 112(4):1072–1080, April 2023.

[49] Ajay J. Khopade and Frank Caruso. Two-component, ultrathin microcapsules prepared by a core-mediated layer-by-layer approach. *Chemistry of Materials*, 16(11):2107–2112, April 2004.

[50] T. V. Bukreeva, I. V. Marchenko, B. V. Parakhonskiy, and Yu. V. Grigor'ev. Formation of silver nanoparticles on shells of polyelectrolyte capsules using silver-mirror reaction. *Colloid Journal*, 71(5):596–602, October 2009.

[51] Valentin V. Lulevich, Denis Andrienko, and Olga I. Vinogradova. Elasticity of polyelectrolyte multilayer microcapsules. *The Journal of Chemical Physics*, 120(8):3822–3826, February 2004.

[52] Bogdan V. Parakhonskiy, Alexey M. Yashchenok, Manfred Konrad, and Andre G. Skirtach. Colloidal micro- and nano-particles as templates for polyelectrolyte multilayer capsules. *Advances in Colloid and Interface Science*, 207:253–264, May 2014.

[53] Dmitry V. Volodkin, Natalia I. Larionova, and Gleb B. Sukhorukov. Protein encapsulation via porous caco3 microparticles templating. *Biomacromolecules*, 5(5):1962–1972, August 2004.

[54] Alexey V. Ermakov, Sergei V. Chapek, Ekaterina V. Lengert, Petr V. Konarev, Vladimir V. Volkov, Vladimir V. Artemov, Mikhail A. Soldatov, and Daria B. Trushina. Microfluidically assisted synthesis of calcium carbonate submicron particles with improved loading properties. *Micromachines*, 15(1):16, December 2023.

[55] Daria B. Trushina, Tatiana V. Bukreeva, Mikhail V. Kovalchuk, and Maria N. Antipina. Caco3 vaterite microparticles for biomedical and personal care applications. *Materials Science and Engineering: C*, 45:644–658, December 2014.

[56] Santoshkumar Biradar, Prabakaran Ravichandran, Ramya Gopikrishnan, Virupaxi Goornavar, Joseph C. Hall, Vani Ramesh, Sudhakar Baluchamy,

Robert B. Jeffers, and Govindarajan T. Ramesh. Calcium carbonate nanoparticles: Synthesis, characterization and biocompatibility. *Journal of Nanoscience and Nanotechnology*, 11(8):6868–6874, August 2011.

[57] Bogdan Parakhonskiy, Mikhail V Zyuzin, Alexey Yashchenok, Susana Carregal-Romero, Joanna Rejman, Helmuth Möhwald, Wolfgang J Parak, and Andre G Skirtach. The influence of the size and aspect ratio of anisotropic, porous caco3 particles on their uptake by cells. *Journal of Nanobiotechnology*, 13(1), September 2015.

[58] Daria B. Trushina, Tatiana N. Borodina, Sergei Belyakov, and Maria N. Antipina. Calcium carbonate vaterite particles for drug delivery: Advances and challenges. *Materials Today Advances*, 14:100214, June 2022.

[59] Yu. I. Svenskaya, A.M. Pavlov, D.A. Gorin, D.J. Gould, B.V. Parakhonskiy, and G.B. Sukhorukov. Photodynamic therapy platform based on localized delivery of photosensitizer by vaterite submicron particles. *Colloids and Surfaces B: Biointerfaces*, 146:171–179, October 2016.

[60] A. S. Vikulina, N. A. Feoktistova, N. G. Balabushevich, A. G. Skirtach, and D. Volodkin. The mechanism of catalase loading into porous vaterite caco3 crystals by co-synthesis. *Physical Chemistry Chemical Physics*, 20(13):8822–8831, 2018.

[61] Alexander I. Petrov, Dmitry V. Volodkin, and Gleb B. Sukhorukov. Protein-calcium carbonate coprecipitation: A tool for protein encapsulation.

Biotechnology Progress, 21(3):918–925, September 2008.

[62] Liesbeth J. De Cock, Stefaan De Koker, Bruno G. De Geest, Johan Grooten, Chris Vervaet, Jean Paul Remon, Gleb B. Sukhorukov, and Maria N. Antipina. Polymeric multilayer capsules in drug delivery. *Angewandte Chemie International Edition*, 49(39):6954–6973, July 2010.

[63] Neng Qiu, Huabing Yin, Bozhi Ji, Norbert Klauke, Andrew Glidle, Yongkui Zhang, Hang Song, Lulu Cai, Liang Ma, Guangcheng Wang, Lijuan Chen, and Wenwen Wang. Calcium carbonate microspheres as carriers for the anticancer drug camptothecin. *Materials Science and Engineering: C*, 32(8):2634–2640, December 2012.

[64] Jin-Long Wu, Chao-Qun Wang, Ren-Xi Zhuo, and Si-Xue Cheng. Multi-drug delivery system based on alginate/calcium carbonate hybrid nanoparticles for combination chemotherapy. *Colloids and Surfaces B: Biointerfaces*, 123:498–505, November 2014.

[65] Sergei V. German, Marina V. Novoselova, Daniil N. Bratashov, Polina A. Demina, Vsevolod S. Atkin, Denis V. Voronin, Boris N. Khlebtsov, Bogdan V. Parakhonskiy, Gleb B. Sukhorukov, and Dmitry A. Gorin. High-efficiency freezing-induced loading of inorganic nanoparticles and proteins into micron- and submicron-sized porous particles. *Scientific Reports*, 8(1), December 2018.

[66] Marina V. Novoselova, Denis V. Voronin, Tatiana O. Abakumova, Polina A. Demina, Arsenii V. Petrov, Vladimir V. Petrov, Timofei S. Zatsepin, Gleb B. Sukhorukov, and Dmitry A. Gorin. Focused ultrasound-mediated fluorescence of composite microcapsules loaded with magnetite nanoparticles: In vitro and in vivo study. *Colloids and Surfaces B: Biointerfaces*, 181:680–687, September 2019.

[67] Qinghe Zhao and Bingyun Li. ph-controlled drug loading and release from biodegradable microcapsules. *Nanomedicine: Nanotechnology, Biology and Medicine*, 4(4):302–310, December 2008.

[68] G. Ibarz, L. Dähne, E. Donath, and H. Möhwald. Smart micro- and nanocontainers for storage, transport, and release. *Advanced Materials*, 13(17):1324, September 2001.

[69] Weixing Song, Qiang He, Helmuth Möhwald, Yang Yang, and Junbai Li. Smart polyelectrolyte microcapsules as carriers for water-soluble small molecular drug. *Journal of Controlled Release*, 139(2):160–166, October 2009.

[70] Ekaterina V. Skorb and Helmuth Möhwald. "smart" surface capsules for delivery devices. *Advanced Materials Interfaces*, 1(6), July 2014.

[71] Veronika Kozlovskaya, Jun Chen, Oleksandra Zavgorodnya, Mohammad B. Hasan, and Eugenia Kharlampieva. Multilayer hydrogel capsules of in-

terpenetrated network for encapsulation of small molecules. *Langmuir*, 34(39):11832–11842, September 2018.

[72] Alexey V. Ermakov, Roman A. Verkhovskii, Irina V. Babushkina, Daria B. Trushina, Olga A. Inozemtseva, Evgeny A. Lukyanets, Vladimir J. Ulyanov, Dmitry A. Gorin, Sergei Belyakov, and Maria N. Antipina. In vitro bioeffects of polyelectrolyte multilayer microcapsules post-loaded with water-soluble cationic photosensitizer. *Pharmaceutics*, 12(7):610, June 2020.

[73] Alexey V. Ermakov, Olga A. Inozemtseva, Dmitry A. Gorin, Gleb B. Sukhorukov, Sergei Belyakov, and Maria N. Antipina. Influence of heat treatment on loading of polymeric multilayer microcapsules with rhodamine b. *Macromolecular Rapid Communications*, 40(5), May 2018.

[74] Lena Kastl, Daniel Sasse, Verena Wulf, Raimo Hartmann, Josif Mircheski, Christiane Ranke, Susana Carregal-Romero, José Antonio Martínez-López, Rafael Fernández-Chacón, Wolfgang J. Parak, Hans-Peter Elsasser, and Pilar Rivera Gil. Multiple internalization pathways of polyelectrolyte multilayer capsules into mammalian cells. *ACS Nano*, 7(8):6605–6618, July 2013.

[75] Anastasia Gileva, Daria Trushina, Anne Yagolovich, Marine Gasparian, Leyli Kurbanova, Ivan Smirnov, Sergey Burov, and Elena Markvicheva. Doxorubicin-loaded polyelectrolyte multilayer capsules modified with antitumor dr5-specific trail variant for targeted drug delivery to tumor cells. *Nanomaterials*, 13(5):902, February 2023.

[76] Roman Verkhovskii, Alexey Ermakov, Olga Sindeeva, Ekaterina Prikhozhdenko, Anastasiia Kozlova, Oleg Grishin, Mikhail Makarkin, Dmitry Gorin, and Daniil Bratashov. Effect of size on magnetic polyelectrolyte microcapsules behavior: Biodistribution, circulation time, interactions with blood cells and immune system. *Pharmaceutics*, 13(12):2147, December 2021.

[77] Tatiana A. Kolesnikova, Raghavendra Palankar, and Mathias Winterhalter. *Polymer Capsules and Electroporation*, page 789–792. Springer International Publishing, 2015.

[78] Julie A. Champion and Samir Mitragotri. Role of target geometry in phagocytosis. *Proceedings of the National Academy of Sciences*, 103(13):4930–4934, March 2006.

[79] Jenolyn F. Alexander, Veronika Kozlovskaya, Jun Chen, Thomas Kuncewicz, Eugenia Kharlampieva, and Biana Godin. Cubical shape enhances the interaction of layer-by-layer polymeric particles with breast cancer cells. *Advanced Healthcare Materials*, 4(17):2657–2666, October 2015.

[80] Olga Shimoni, Yan Yan, Yajun Wang, and Frank Caruso. Shape-dependent cellular processing of polyelectrolyte capsules. *ACS Nano*, 7(1):522–530, December 2012.

[81] Alumdena Muñoz Javier, Oliver Kreft, Maximilian Semmling, Susanne Kempter, Andre G. Skirtach, Oliver T. Bruns, Pablo del Pino, Mathieu F. Bedard, Joachim Rädler, Josef Käs, Christian Plank, Gleb B. Sukhorukov,

and Wolfgang J. Parak. Uptake of colloidal polyelectrolyte-coated particles and polyelectrolyte multilayer capsules by living cells. *Advanced Materials*, 20(22):4281–4287, November 2008.

[82] Ali Ghaemi, Alexandra Philipp, Andreas Bauer, Klaus Last, Andreas Fery, and Stephan Gekle. Mechanical behaviour of micro-capsules and their rupture under compression. *Chemical Engineering Science*, 142:236–243, March 2016.

[83] Matthieu F. Bédard, Almudena Munoz-Javier, Renate Mueller, Pablo del Pino, Andreas Fery, Wolfgang J. Parak, Andre G. Skirtach, and Gleb B. Sukhorukov. On the mechanical stability of polymeric microcontainers functionalized with nanoparticles. *Soft Matter*, 5(1):148–155, 2009.

[84] Raimo Hartmann, Marcel Weidenbach, Martin Neubauer, Andreas Fery, and Wolfgang J. Parak. Stiffness-dependent in vitro uptake and lysosomal acidification of colloidal particles. *Angewandte Chemie International Edition*, 54(4):1365–1368, December 2014.

[85] Almudena Muñoz Javier, Oliver Kreft, Alicia Piera Alberola, Christian Kirchner, Bernd Zebli, AndreiS. Susha, Elias Horn, Susanne Kempter, Andre G. Skirtach, Andrey L. Rogach, Joachim Rädler, Gleb B. Sukhorukov, Martin Benoit, and Wolfgang J. Parak. Combined atomic force microscopy and optical microscopy measurements as a method to investigate particle uptake by cells. *Small*, 2(3):394–400, January 2006.

[86] Nastassja Lewinski, Vicki Colvin, and Rebekah Drezek. Cytotoxicity of nanoparticles. *Small*, 4(1):26–49, January 2008.

[87] S. De Koker, B. G. De Geest, C. Cuvelier, L. Ferdinande, W. Deckers, W. E. Hennink, S. C. De Smedt, and N. Mertens. In vivo cellular uptake, degradation, and biocompatibility of polyelectrolyte microcapsules. *Advanced Functional Materials*, 17(18):3754–3763, November 2007.

[88] C. Kirchner, A. Javier, A. Susha, A. Rogach, O. Kreft, G. Sukhorukov, and W. Parak. Cytotoxicity of nanoparticle-loaded polymer capsules. *Talanta*, 67(3):486–491, September 2005.

[89] Maria V. Lomova, Anna I. Brichkina, Maxim V. Kiryukhin, Elena N. Vasina, Anton M. Pavlov, Dmitry A. Gorin, Gleb B. Sukhorukov, and Maria N. Antipina. Multilayer capsules of bovine serum albumin and tannic acid for controlled release by enzymatic degradation. *ACS Applied Materials & Interfaces*, 7(22):11732–11740, May 2015.

[90] Iris Biotech. Polyarginine. `https://www.iris-biotech.de/global/blog/polyarginine/`, 2024 (accessed May 27, 2024).

[91] Bao-Lin Chu, Qinzhong Feng, Zhihua Wang, and Jin-Ming Lin. Enantiomeric separation of two antiparkinsonian drugs by electrokinetic chromatography using dextran sulfate. *Chromatographia*, 70(5–6):817–824, August 2009.

[92] Varsha Sharma, Joel Vijay, M.R. Ganesh, and Anandhakumar Sundaramurthy. Multilayer capsules encapsulating nimbin and doxorubicin for cancer chemo-photothermal therapy. *International Journal of Pharmaceutics*, 582:119350, May 2020.

[93] Daria Kalenichenko, Galina Nifontova, Alexander Karaulov, Alyona Sukhanova, and Igor Nabiev. Designing functionalized polyelectrolyte microcapsules for cancer treatment. *Nanomaterials*, 11(11):3055, November 2021.

[94] Yazan Al Thaher. Tailored gentamicin release from silica nanocarriers coated with polyelectrolyte multilayers. *Colloids and Surfaces A: Physicochemical and Engineering Aspects*, 614:126210, April 2021.

[95] Marina Craig, Annika Altskär, Lars Nordstierna, and Krister Holmberg. Bacteria-triggered degradation of nanofilm shells for release of antimicrobial agents. *Journal of Materials Chemistry B*, 4(4):672–682, 2016.

[96] Wen Li, Zhengqing Yan, Jinsong Ren, and Xiaogang Qu. Manipulating cell fate: dynamic control of cell behaviors on functional platforms. *Chemical Society Reviews*, 47(23):8639–8684, 2018.

[97] Kirill V. Lepik, Albert R. Muslimov, Alexander S. Timin, Vladislav S. Sergeev, Dmitry S. Romanyuk, Ivan S. Moiseev, Elena V. Popova, Igor L. Radchenko, Alexander D. Vilesov, Oleg V. Galibin, Gleb B. Sukhorukov, and Boris V. Afanasyev. Mesenchymal stem cell magnetization: Magnetic

multilayer microcapsule uptake, toxicity, impact on functional properties, and perspectives for magnetic delivery. *Advanced Healthcare Materials*, 5(24):3182–3190, November 2016.

[98] Matthew S. Alexander, Juan Carlos Casar, and Norio Motohashi. Stem cell differentiation and therapeutic use. *Stem Cells International*, 2015:1–2, 2015.

[99] Albert R. Muslimov, Alexander S. Timin, Aleksandra V. Petrova, Olga S. Epifanovskaya, Alena I. Shakirova, Kirill V. Lepik, Andrey Gorshkov, Eugenia V. Il'inskaja, Andrey V. Vasin, Boris V. Afanasyev, Boris Fehse, and Gleb B. Sukhorukov. Mesenchymal stem cells engineering: Microcapsules-assisted gene transfection and magnetic cell separation. *ACS Biomaterials Science & Engineering*, 3(10):2314–2324, September 2017.

[100] Elizaveta V. Koudan, Mikhail N. Zharkov, Mikhail V. Gerasimov, Saida Sh. Karshieva, Aleksandra D. Shirshova, Vladimir V. Chrishtop, Vladimir A. Kasyanov, Aleksandr A. Levin, Vladislav A. Parfenov, Pavel A. Karalkin, Frederico D. A. S. Pereira, Stanislav V. Petrov, Nikolay A. Pyataev, Yusef D. Khesuani, Vladimir A. Mironov, and Gleb B. Sukhorukov. Magnetic patterning of tissue spheroids using polymer microcapsules containing iron oxide nanoparticles. *ACS Biomaterials Science & Engineering*, 7(11):5206–5214, October 2021.

[101] Weijun Tong and Changyou Gao. Multilayer microcapsules with tailored

structures for bio-related applications. *Journal of Materials Chemistry*, 18(32):3799, 2008.

[102] Aimin Yu, Ian Gentle, Gaoqing Lu, and Frank Caruso. Nanoassembly of biocompatible microcapsules for urease encapsulation and their use as biomimetic reactors. *Chemical Communications*, (20):2150, 2006.

[103] Tatsiana Shutava, Zhiguo Zheng, Vijay John, and Yuri Lvov. Microcapsule modification with peroxidase-catalyzed phenol polymerization. *Biomacromolecules*, 5(3):914–921, March 2004.

[104] Nadezda G. Balabushevich, Gleb B. Sukhorukov, and Natalia I. Larionova. Polyelectrolyte multilayer microspheres as carriers for bienzyme system: Preparation and characterization. *Macromolecular Rapid Communications*, 26(14):1168–1172, July 2005.

[105] Alexei Antipov, Dmitry Shchukin, Yuri Fedutik, Irina Zanaveskina, Vera Klechkovskaya, Gleb Sukhorukov, and Helmuth Möhwald. Urease-catalyzed carbonate precipitation inside the restricted volume of polyelectrolyte capsules. *Macromolecular Rapid Communications*, 24(3):274–277, March 2003.

[106] Yuri Lvov, Alexei A. Antipov, Arif Mamedov, Helmuth Möhwald, and Gleb B. Sukhorukov. Urease encapsulation in nanoorganized microshells. *Nano Letters*, 1(3):125–128, March 2001.

[107] Rohit Ghan, Tatsiana Shutava, Amish Patel, Vijay T. John, and Yuri Lvov. Enzyme-catalyzed polymerization of phenols within polyelectrolyte microcapsules. *Macromolecules*, 37(12):4519–4524, May 2004.

[108] Joseph J. Richardson, James W. Maina, Hirotaka Ejima, Ming Hu, Junling Guo, Mei Y. Choy, Sylvia T. Gunawan, Lien Lybaert, Christoph E. Hagemeyer, Bruno G. De Geest, and Frank Caruso. Versatile loading of diverse cargo into functional polymer capsules. *Advanced Science*, 2(1–2), January 2015.

[109] Loretta L. del Mercato, Azhar Z. Abbasi, and Wolfgang J. Parak. Synthesis and characterization of ratiometric ion-sensitive polyelectrolyte capsules. *Small*, 7(3):351–363, December 2010.

[110] J. Quincy Brown, Rohit Srivastava, Huiguang Zhu, and Michael J. McShane. Enzymatic fluorescent microsphere glucose sensors:evaluation of response under dynamic conditions. *Diabetes Technology & Therapeutics*, 8(3):288–295, June 2006.

[111] Swetha Chinnayelka and Michael J. McShane. Glucose-sensitive nanoassemblies comprising affinity-binding complexes trapped in fuzzy microshells. *Journal of Fluorescence*, 14(5):585–595, September 2004.

[112] Oliver Kreft, Almudena Muñoz Javier, Gleb B. Sukhorukov, and Wolfgang J. Parak. Polymer microcapsules as mobile local ph-sensors. *Journal of Materials Chemistry*, 17(42):4471, 2007.

[113] Maximilian Semmling, Oliver Kreft, Almudena Muñoz Javier, Gleb B. Sukhorukov, Josef Käs, and Wolfgang J. Parak. A novel flow-cytometry-based assay for cellular uptake studies of polyelectrolyte microcapsules. *Small*, 4(10):1763–1768, October 2008.

[114] Ya-Ping Sun, Bing Zhou, Yi Lin, Wei Wang, K. A. Shiral Fernando, Pankaj Pathak, Mohammed Jaouad Meziani, Barbara A. Harruff, Xin Wang, Haifang Wang, Pengju G. Luo, Hua Yang, Muhammet Erkan Kose, Bailin Chen, L. Monica Veca, and Su-Yuan Xie. Quantum-sized carbon dots for bright and colorful photoluminescence. *Journal of the American Chemical Society*, 128(24):7756–7757, May 2006.

[115] Bibekananda De and Niranjan Karak. Recent progress in carbon dot–metal based nanohybrids for photochemical and electrochemical applications. *Journal of Materials Chemistry A*, 5(5):1826–1859, 2017.

[116] Agata Kaczmarek, Jacek Hoffman, Jerzy Morgiel, Tomasz Mościcki, Leszek Stobiński, Zygmunt Szymański, and Artur Małolepszy. Luminescent carbon dots synthesized by the laser ablation of graphite in polyethylenimine and ethylenediamine. *Materials*, 14(4):729, February 2021.

[117] Daniele Rocco, Vyali Georgian Moldoveanu, Marta Feroci, Martina Bortolami, and Fabrizio Vetica. Electrochemical synthesis of carbon quantum dots. *ChemElectroChem*, 10(3), January 2023.

[118] Reyna Berenice González-González, Lucy Teresa González, Marc Madou, César Leyva-Porras, Sergio Omar Martinez-Chapa, and Alberto Mendoza. Synthesis, purification, and characterization of carbon dots from non-activated and activated pyrolytic carbon black. *Nanomaterials*, 12(3):298, January 2022.

[119] F. J. Chao-Mujica, L. Garcia-Hernández, S. Camacho-López, M. Camacho-López, M. A. Camacho-López, D. Reyes Contreras, A. Pérez-Rodríguez, J. P. Peña-Caravaca, A. Páez-Rodríguez, J. G. Darias-Gonzalez, L. Hernandez-Tabares, O. Arias de Fuentes, E. Prokhorov, N. Torres-Figueredo, E. Reguera, and L. F. Desdin-García. Carbon quantum dots by submerged arc discharge in water: Synthesis, characterization, and mechanism of formation. *Journal of Applied Physics*, 129(16), April 2021.

[120] Zhen-An Qiao, Yifan Wang, Yang Gao, Hongwei Li, Tianyi Dai, Yunling Liu, and Qisheng Huo. Commercially activated carbon as the source for producing multicolor photoluminescent carbon dots by chemical oxidation. *Chemical Communications*, 46(46):8812, 2010.

[121] Gregory Ethan LeCroy, Sumit Kumar Sonkar, Fan Yang, L. Monica Veca, Ping Wang, Kenneth N. Tackett, Jing-Jiang Yu, Eugeniu Vasile, Haijun Qian, Yamin Liu, Pengju (George) Luo, and Ya-Ping Sun. Toward structurally defined carbon dots as ultracompact fluorescent probes. *ACS Nano*, 8(5):4522–4529, April 2014.

[122] Long Wang, Yidan Bi, Jia Gao, Yijia Li, Hong Ding, and Lan Ding. Carbon dots based turn-on fluorescent probes for the sensitive determination of glyphosate in environmental water samples. *RSC Advances*, 6(89):85820–85828, 2016.

[123] Juan Zhou, Yong Yang, and Chun-yang Zhang. A low-temperature solid-phase method to synthesize highly fluorescent carbon nitride dots with tunable emission. *Chemical Communications*, 49(77):8605, 2013.

[124] Xinyun Zhai, Peng Zhang, Changjun Liu, Tao Bai, Wenchen Li, Liming Dai, and Wenguang Liu. Highly luminescent carbon nanodots by microwave-assisted pyrolysis. *Chemical Communications*, 48(64):7955, 2012.

[125] Ngo Khoa Quang, Nguyen Ngoc Hieu, Vo Van Quoc Bao, Vo Thi Phuoc, Le Xuan Diem Ngoc, Luong Quang Doc, Nguyen Minh Tri, Le Vu Truong Son, Le Van Thanh Son, and Che Thi Cam Ha. Hydrothermal synthesis of carbon nanodots from waste wine cork and their use in biocompatible fluorescence imaging. *New Carbon Materials*, 37(3):595–602, June 2022.

[126] Jiali Xu, Kai Cui, Tianyu Gong, Jinyang Zhang, Zhirou Zhai, Linrui Hou, Fakhr uz Zaman, and Changzhou Yuan. Ultrasonic-assisted synthesis of n-doped, multicolor carbon dots toward fluorescent inks, fluorescence sensors, and logic gate operations. *Nanomaterials*, 12(3):312, January 2022.

[127] Gadisa Deme, Abebe Belay, Dinsefa Mensur Andoshe, Gemechu Barsisa, Diriba Tsegaye, Solomon Tiruneh, and Cherinet Seboka. Effect of hydrother-

mal reaction temperature on fluorescent properties of carbon quantum dots synthesized from lemon juice for adsorption applications. *Journal of Nanomaterials*, 2023:1–10, January 2023.

[128] Pranjal D. Modi, Vaibhavkumar N. Mehta, Vimalkumar S. Prajapati, Swati Patel, and Jigneshkumar V. Rohit. *Bottom-up approaches for the preparation of carbon dots*, page 15–29. Elsevier, 2023.

[129] Alice Sciortino, Andrea Cannizzo, and Fabrizio Messina. Carbon nanodots: A review—from the current understanding of the fundamental photophysics to the full control of the optical response. *C*, 4(4):67, December 2018.

[130] Liangxu Lin and Shaowei Zhang. Creating high yield water soluble luminescent graphene quantum dots via exfoliating and disintegrating carbon nanotubes and graphite flakes. *Chemical Communications*, 48(82):10177, 2012.

[131] Mahasin Alam Sk, Arundithi Ananthanarayanan, Lin Huang, Kok Hwa Lim, and Peng Chen. Revealing the tunable photoluminescence properties of graphene quantum dots. *J. Mater. Chem. C*, 2(34):6954–6960, 2014.

[132] Jan Belza, Ariana Opletalová, and Kateřina Poláková. Carbon dots for virus detection and therapy. *Microchimica Acta*, 188(12), November 2021.

[133] Sung Kim, Sung Won Hwang, Min-Kook Kim, Dong Yeol Shin, Dong Hee Shin, Chang Oh Kim, Seung Bum Yang, Jae Hee Park, Euyheon Hwang, Suk-Ho Choi, Geunwoo Ko, Sunghyun Sim, Cheolsoo Sone, Hyoung Joon

Choi, Sukang Bae, and Byung Hee Hong. Anomalous behaviors of visible luminescence from graphene quantum dots: Interplay between size and shape. *ACS Nano*, 6(9):8203–8208, August 2012.

[134] Ju Tang, Jin Zhang, Yunfei Zhang, Yiming Xiao, Yanli Shi, Yunhua Chen, Lan Ding, and Wen Xu. Influence of group modification at the edges of carbon quantum dots on fluorescent emission. *Nanoscale Research Letters*, 14(1), September 2019.

[135] Dengyu Pan, Jingchun Zhang, Zhen Li, and Minghong Wu. Hydrothermal route for cutting graphene sheets into blue-luminescent graphene quantum dots. *Advanced Materials*, 22(6):734–738, February 2010.

[136] Shoujun Zhu, Junhu Zhang, Chunyan Qiao, Shijia Tang, Yunfeng Li, Wenjing Yuan, Bo Li, Lu Tian, Fang Liu, Rui Hu, Hainan Gao, Haotong Wei, Hao Zhang, Hongchen Sun, and Bai Yang. Strongly green-photoluminescent graphene quantum dots for bioimaging applications. *Chemical Communications*, 47(24):6858, 2011.

[137] Lin Cui, Xin Ren, Mengtao Sun, Haiyan Liu, and Lixin Xia. Carbon dots: Synthesis, properties and applications. *Nanomaterials*, 11(12):3419, December 2021.

[138] Youfu Wang and Aiguo Hu. Carbon quantum dots: synthesis, properties and applications. *Journal of Materials Chemistry C*, 2(34):6921, June 2014.

[139] Xiaofang Jia, Jing Li, and Erkang Wang. One-pot green synthesis of optically ph-sensitive carbon dots with upconversion luminescence. *Nanoscale*, 4(18):5572, 2012.

[140] Xiaoming Wen, Pyng Yu, Yon-Rui Toh, Xiaoqian Ma, and Jau Tang. On the upconversion fluorescence in carbon nanodots and graphene quantum dots. *Chem. Commun.*, 50(36):4703–4706, 2014.

[141] Hengchao Zhang, Hai Ming, Suoyuan Lian, Hui Huang, Haitao Li, Lili Zhang, Yang Liu, Zhenhui Kang, and Shuit-Tong Lee. Fe2o3/carbon quantum dots complex photocatalysts and their enhanced photocatalytic activity under visible light. *Dalton Transactions*, 40(41):10822, 2011.

[142] Shilei Xie, Hua Su, Wenjie Wei, Mingyang Li, Yexiang Tong, and Zongwan Mao. Remarkable photoelectrochemical performance of carbon dots sensitized tio2under visible light irradiation. *J. Mater. Chem. A*, 2(39):16365–16368, August 2014.

[143] Hyoung-il Kim, Gun-hee Moon, Damián Monllor-Satoca, Yiseul Park, and Wonyong Choi. Solar photoconversion using graphene/tio2 composites: Nanographene shell on tio2 core versus tio2 nanoparticles on graphene sheet. *The Journal of Physical Chemistry C*, 116(1):1535–1543, December 2011.

[144] Xing Zhang, Fang Wang, Hui Huang, Haitao Li, Xiao Han, Yang Liu, and Zhenhui Kang. Carbon quantum dot sensitized tio2 nanotube arrays for

photoelectrochemical hydrogen generation under visible light. *Nanoscale*, 5(6):2274, 2013.

[145] Li Cao, Sushant Sahu, Parambath Anilkumar, Christopher E. Bunker, Juan Xu, K. A. Shiral Fernando, Ping Wang, Elena A. Guliants, Kenneth N. Tackett, and Ya-Ping Sun. Carbon nanoparticles as visible-light photocatalysts for efficient co2 conversion and beyond. *Journal of the American Chemical Society*, 133(13):4754–4757, March 2011.

[146] Sonaimuthu Mohandoss, Subramanian Palanisamy, SangGuan You, Jae-Jin Shim, and Yong Rok Lee. Rapid detection of silver ions based on luminescent carbon nanodots for multicolor patterning, smartphone sensors, and bioimaging applications. *Analytical Methods*, 13(47):5719–5726, 2021.

[147] Yongchao Du, Yaxi Li, Yunliang Liu, Naiyun Liu, Yuanyuan Cheng, Qiuzhong Shi, Xiang Liu, Zhimin Tao, Yumeng Guo, Jianguo Zhang, Najmeh Askaria, and Haitao Li. Stalk-derived carbon dots as nanosensors for fe3+ ions detection and biological cell imaging. *Frontiers in Bioengineering and Biotechnology*, 11, April 2023.

[148] Arnab Ghosh and Gopal Das. Environmentally benign synthesis of fluorescent carbon nanodots using waste pet bottles: highly selective and sensitive detection of pb2+ions in aqueous medium. *New Journal of Chemistry*, 45(19):8747–8754, 2021.

[149] Heng Xin Zhao, Li Qin Liu, Zhong De Liu, Yi Wang, Xi Juan Zhao, and Cheng Zhi Huang. Highly selective detection of phosphate in very complicated matrixes with an off–on fluorescent probe of europium-adjusted carbon dots. *Chemical Communications*, 47(9):2604, 2011.

[150] Dan Zhao, Chuanxia Chen, Lixia Lu, Fan Yang, and Xiurong Yang. A dual-mode colorimetric and fluorometric "light on" sensor for thiocyanate based on fluorescent carbon dots and unmodified gold nanoparticles. *The Analyst*, 140(24):8157–8164, 2015.

[151] Qiao-Ling Chen, Cai-Feng Wang, and Su Chen. One-step synthesis of yellow-emitting carbogenic dots toward white light-emitting diodes. *Journal of Materials Science*, 48(6):2352–2357, November 2012.

[152] Yuanfei Ding, Feng Zhang, Jiacong Xu, Yanqin Miao, Yongzhen Yang, Xuguang Liu, and Bingshe Xu. Synthesis of short-chain passivated carbon quantum dots as the light emitting layer towards electroluminescence. *RSC Advances*, 7(46):28754–28762, 2017.

[153] Adam Marinovic, Lim S. Kiat, Steve Dunn, Maria-Magdalena Titirici, and Joe Briscoe. Carbon-nanodot solar cells from renewable precursors. *ChemSusChem*, 10(5):1004–1013, February 2017.

[154] Melis Özge Alaş and Rükan Genç. *Carbon nanodot integrated solar energy devices*, page 497–535. Elsevier, 2021.

[155] Huiquan Tao, Kai Yang, Zhen Ma, Jianmei Wan, Youjiu Zhang, Zhenhui Kang, and Zhuang Liu. In vivo nir fluorescence imaging, biodistribution, and toxicology of photoluminescent carbon dots produced from carbon nanotubes and graphite. *Small*, 8(2):281–290, November 2011.

[156] Min Zheng, Shaobo Ruan, Shi Liu, Tingting Sun, Dan Qu, Haifeng Zhao, Zhigang Xie, Huile Gao, Xiabin Jing, and Zaicheng Sun. Self-targeting fluorescent carbon dots for diagnosis of brain cancer cells. *ACS Nano*, 9(11):11455–11461, October 2015.

[157] R. M. Shereema, T. V. Sruthi, V. B. Sameer Kumar, T. P. Rao, and S. Sharath Shankar. Angiogenic profiling of synthesized carbon quantum dots. *Biochemistry*, 54(41):6352–6356, October 2015.

[158] Alexandre Barras, Quentin Pagneux, Famara Sane, Qi Wang, Rabah Boukherroub, Didier Hober, and Sabine Szunerits. High efficiency of functional carbon nanodots as entry inhibitors of herpes simplex virus type 1. *ACS Applied Materials & Interfaces*, 8(14):9004–9013, April 2016.

[159] Gert-Jan Kremers, Sarah G. Gilbert, Paula J. Cranfill, Michael W. Davidson, and David W. Piston. Fluorescent proteins at a glance. *Journal of Cell Science*, 124(2):157–160, January 2011.

[160] Leica. Photoactivatable, photoconvertible, and photoswitchable fluorescent proteins. `https://www.leica-microsystems.com/science-lab/life-science/`

photoactivatable-photoconvertible-and-photoswitchable-fluorescent-proteins/, 2017 (accessed April 09, 2024).

[161] Jennifer Lippincott-Schwartz and George H. Patterson. Photoactivatable fluorescent proteins for diffraction-limited and super-resolution imaging. *Trends in Cell Biology*, 19(11):555–565, November 2009.

[162] Longteng Tang and Chong Fang. Photoswitchable fluorescent proteins: Mechanisms on ultrafast timescales. *International Journal of Molecular Sciences*, 23(12):6459, June 2022.

[163] Rebekka Wachter. Photoconvertible fluorescent proteins and the role of dynamics in protein evolution. *International Journal of Molecular Sciences*, 18(8):1792, August 2017.

[164] Ryoko Ando, Hiroshi Hama, Miki Yamamoto-Hino, Hideaki Mizuno, and Atsushi Miyawaki. An optical marker based on the uv-induced green-to-red photoconversion of a fluorescent protein. *Proceedings of the National Academy of Sciences*, 99(20):12651–12656, September 2002.

[165] Jörg Wiedenmann, Sergey Ivanchenko, Franz Oswald, Florian Schmitt, Carlheinz Röcker, Anya Salih, Klaus-Dieter Spindler, and G. Ulrich Nienhaus. Eosfp, a fluorescent marker protein with uv-inducible green-to-red fluorescence conversion. *Proceedings of the National Academy of Sciences*, 101(45):15905–15910, October 2004.

[166] Nadya G Gurskaya, Vladislav V Verkhusha, Alexander S Shcheglov, Dmitry B Staroverov, Tatyana V Chepurnykh, Arkady F Fradkov, Sergey Lukyanov, and Konstantin A Lukyanov. Engineering of a monomeric green-to-red photoactivatable fluorescent protein induced by blue light. *Nature Biotechnology*, 24(4):461–465, March 2006.

[167] Olesya V. Stepanenko, Olga V. Stepanenko, Daria M. Shcherbakova, Irina M. Kuznetsova, Konstantin K. Turoverov, and Vladislav V. Verkhusha. Modern fluorescent proteins: from chromophore formation to novel intracellular applications. *BioTechniques*, 51(5):313–327, November 2011.

[168] Lauren J. Pouwels, Liping Zhang, Nam H. Chan, Pieter C. Dorrestein, and Rebekka M. Wachter. Kinetic isotope effect studies on the de novo rate of chromophore formation in fast- and slow-maturing gfp variants. *Biochemistry*, 47(38):10111–10122, August 2008.

[169] Liping Zhang, Hetal N. Patel, Jason W. Lappe, and Rebekka M. Wachter. Reaction progress of chromophore biogenesis in green fluorescent protein. *Journal of the American Chemical Society*, 128(14):4766–4772, March 2006.

[170] Hanseong Kim, Taisong Zou, Chintan Modi, Katerina Dörner, Timothy J. Grunkemeyer, Liqing Chen, Raimund Fromme, Mikhail V. Matz, S. Banu Ozkan, and Rebekka M. Wachter. A hinge migration mechanism unlocks the evolution of green-to-red photoconversion in gfp-like proteins. *Structure*, 23(1):34–43, January 2015.

[171] Xin Li, Lung Wa Chung, Hideaki Mizuno, Atsushi Miyawaki, and Keiji Morokuma. Competitive mechanistic pathways for green-to-red photoconversion in the fluorescent protein kaede: A computational study. *The Journal of Physical Chemistry B*, 114(49):16666–16675, November 2010.

[172] Dmitriy M Chudakov, Vladislav V Verkhusha, Dmitry B Staroverov, Ekaterina A Souslova, Sergey Lukyanov, and Konstantin A Lukyanov. Photoswitchable cyan fluorescent protein for protein tracking. *Nature Biotechnology*, 22(11):1435–1439, October 2004.

[173] Dmitriy M Chudakov, Sergey Lukyanov, and Konstantin A Lukyanov. Tracking intracellular protein movements using photoswitchable fluorescent proteins ps-cfp2 and dendra2. *Nature Protocols*, 2(8):2024–2032, August 2007.

[174] J. Nathan Henderson, Rinat Gepshtein, Josef R. Heenan, Karen Kallio, Dan Huppert, and S. James Remington. Structure and mechanism of the photoactivatable green fluorescent protein. *Journal of the American Chemical Society*, 131(12):4176–4177, March 2009.

[175] Alexey M Bogdanov, Alexander S Mishin, Ilia V Yampolsky, Vsevolod V Belousov, Dmitriy M Chudakov, Fedor V Subach, Vladislav V Verkhusha, Sergey Lukyanov, and Konstantin A Lukyanov. Green fluorescent proteins are light-induced electron donors. *Nature Chemical Biology*, 5(7):459–461, April 2009.

[176] Dmitry A. Gorbachev, Elizaveta F. Petrusevich, Adil M. Kabylda, Eugene G. Maksimov, Konstantin A. Lukyanov, Alexey M. Bogdanov, Mikhail S. Baranov, Anastasia V. Bochenkova, and Alexander S. Mishin. A general mechanism of green-to-red photoconversions of gfp. *Frontiers in Molecular Biosciences*, 7, July 2020.

[177] Elana M. S. Stennett, Monika A. Ciuba, and Marcia Levitus. Photophysical processes in single molecule organic fluorescent probes. *Chem. Soc. Rev.*, 43(4):1057–1075, 2014.

[178] Yoonjung Cho, Hyeong Jeon An, Taehoon Kim, Chulbom Lee, and Nam Ki Lee. Mechanism of cyanine5 to cyanine3 photoconversion and its application for high-density single-particle tracking in a living cell. *Journal of the American Chemical Society*, 143(35):14125–14135, August 2021.

[179] Marcia Levitus and Suman Ranjit. Cyanine dyes in biophysical research: the photophysics of polymethine fluorescent dyes in biomolecular environments. *Quarterly Reviews of Biophysics*, 44(1):123–151, November 2010.

[180] Sheldon J. J. Kwok, Myunghwan Choi, Brijesh Bhayana, Xueli Zhang, Chongzhao Ran, and Seok-Hyun Yun. Two-photon excited photoconversion of cyanine-based dyes. *Scientific Reports*, 6(1), March 2016.

[181] harth S. Matikonda, Dominic A. Helmerich, Mara Meub, Gerti Beliu, Philip Kollmannsberger, Alexander Greer, Markus Sauer, and Martin J. Schnermann. Defining the basis of cyanine phototruncation enables a new ap-

proach to single-molecule localization microscopy. *ACS Central Science*, 7(7):1144–1155, June 2021.

[182] Paul Wight. Xanthene dyes, December 2000.

[183] N. A. Evans. Photofading of rhodamine dyes: I—identification of some rhodamine b photoproducts. *Journal of the Society of Dyers and Colourists*, 86(4):174–177, April 1970.

[184] Anna Jakimińska, Miłosz Pawlicki, and Wojciech Macyk. Photocatalytic transformation of rhodamine b to rhodamine-110 – the mechanism revisited. *Journal of Photochemistry and Photobiology A: Chemistry*, 433:114176, December 2022.

[185] Feng Chen, Jincai Zhao, and Hisao Hidaka. Highly selective deethylation of rhodamine b: Adsorption and photooxidation pathways of the dye on the tio_2/sio_2 composite photocatalyst. *International Journal of Photoenergy*, 5(4):209–217, 2003.

[186] AAT Bioquest. Spectrum [rhodamine 110]. `https://www.aatbio.com/fluorescence-excitation-emission-spectrum-graph-viewer/rhodamine_110`, 2024 (accessed April 12, 2024).

[187] AAT Bioquest. Spectrum [rhodamine b]. `https://www.aatbio.com/fluorescence-excitation-emission-spectrum-graph-viewer/rhodamine_b`, 2024 (accessed April 12, 2024).

[188] Tahir Rasheed, Muhammad Bilal, Hafiz M. N. Iqbal, Hongbo Hu, and Xuehong Zhang. Reaction mechanism and degradation pathway of rhodamine 6g by photocatalytic treatment. *Water, Air, & Soil Pollution*, 228(8), July 2017.

[189] Rajnish Kaur, Kowsalya Vellingiri, Ki-Hyun Kim, A.K. Paul, and Akash Deep. Efficient photocatalytic degradation of rhodamine 6g with a quantum dot-metal organic framework nanocomposite. *Chemosphere*, 154:620–627, July 2016.

[190] Ashok Mandi, Nandagopal Bar, Debrupa Biswas, Arindam Ray, Keya Ghosh, Dhrubajyoti Mondal, Gourab Kanti Das, and Pranesh Chowdhury. Rhodamine 6g salicylaldehyde hydrazone-zn complex: Synthesis, characterization, photochromism, understanding, and application. *Journal of Luminescence*, page 120611, April 2024.

[191] Xian-Fu Zhang, Jianlong Zhang, and Xulin Lu. The fluorescence properties of three rhodamine dye analogues: Acridine red, pyronin y and pyronin b. *Journal of Fluorescence*, 25(4):1151–1158, July 2015.

[192] Marek Martínek, Jiří Váňa, Peter Šebej, Rafael Navrátil, Tomáš Slanina, Lucie Ludvíková, Jana Roithová, and Petr Klán. Photochemistry of a 9-dithianyl-pyronin derivative: A cornucopia of reaction intermediates lead to common photoproducts. *ChemPlusChem*, 85(10):2230–2242, July 2020.

[193] Peter Štacko, Peter Šebej, Aneesh Tazhe Veetil, and Petr Klán. Carbon–carbon bond cleavage in fluorescent pyronin analogues induced by yellow light. *Organic Letters*, 14(18):4918–4921, August 2012.

[194] E. A. Slyusareva, M. A. Gerasimov, A. G. Sizykh, and L. M. Gornostaev. Spectral and fluorescent indication of the acid-base properties of biopolymer solutions. *Russian Physics Journal*, 54(4):485–492, September 2011.

[195] Yogeshwar Nath Mishra, Fahed Abou Nada, Stephanie Polster, Elias Kristensson, and Edouard Berrocal. Thermometry in aqueous solutions and sprays using two-color lif and structured illumination. *Optics Express*, 24(5):4949, February 2016.

[196] J H Sandell and R H Masland. Photoconversion of some fluorescent markers to a diaminobenzidine product. *Journal of Histochemistry & Cytochemistry*, 36(5):555–559, May 1988.

[197] Lipiar K. M. O. Goni, Mohammad A. Jafar Mazumder, Divya B. Tripathy, and Mumtaz A. Quraishi. Acridine and its derivatives: Synthesis, biological, and anticorrosion properties. *Materials*, 15(21):7560, October 2022.

[198] Vadim A. Byvaltsev, Liudmila A. Bardonova, Naomi R. Onaka, Roman A. Polkin, Sergey V. Ochkal, Valerij V. Shepelev, Marat A. Aliyev, and Alexander A. Potapov. Acridine orange: A review of novel applications for surgical cancer imaging and therapy. *Frontiers in Oncology*, 9, September 2019.

[199] Chung-Shin Lu, Chiing-Chang Chen, Ling-Kuen Huang, Peir-An Tsai, and Hsiao-Fang Lai. Photocatalytic degradation of acridine orange over nabio3 driven by visible light irradiation. *Catalysts*, 3(2):501–516, May 2013.

[200] N. P. Smirnova, N. I. Surovtseva, T. V. Fesenko, E. M. Demianenko, A. G. Grebenyuk, and A. M. Eremenko. Photodegradation of dye acridine yellow on the surface of mesoporous tio2, sio2/tio2 and sio2 films: spectroscopic and theoretical studies. *Journal of Nanostructure in Chemistry*, 5(4):333–346, July 2015.

[201] Neil Wotherspoon and Gerald Oster. Light induced spectral shift of the thiazine dyes in the bound state1. *Journal of the American Chemical Society*, 79(15):3992–3995, August 1957.

[202] Travis J. Karg and Kent G. Golic. Photoconversion of dapi and hoechst dyes to green and red-emitting forms after exposure to uv excitation. *Chromosoma*, 127(2):235–245, December 2017.

[203] Rachel M. Lackner, Christopher L. Johnny, and David M. Chenoweth. *Photoconvertible diazaxanthilidene dyes for live cell imaging*, page 379–388. Elsevier, 2020.

[204] Katharine L. Dobson, Carmel L. Howe, Yuri Nishimura, and Vincenzo Marra. Dedicated setup for the photoconversion of fluorescent dyes for functional electron microscopy. *Frontiers in Cellular Neuroscience*, 13, July 2019.

[205] Marina Bentivoglio and Hong-Sen Su. Photoconversion of fluorescent retrograde tracers. *Neuroscience Letters*, 113(2):127–133, May 1990.

[206] Dmitriy M. Chudakov, Mikhail V. Matz, Sergey Lukyanov, and Konstantin A. Lukyanov. Fluorescent proteins and their applications in imaging living cells and tissues. *Physiological Reviews*, 90(3):1103–1163, July 2010.

[207] Alicia L. Carlson, Joji Fujisaki, Juwell Wu, Judith M. Runnels, Raphaël Turcotte, Cristina Lo Celso, David T. Scadden, Terry B. Strom, and Charles P. Lin. Tracking single cells in live animals using a photoconvertible near-infrared cell membrane label. *PLoS ONE*, 8(8):e69257, August 2013.

[208] C Lalande, S Miraux, SM Derkaoui, S Mornet, R Bareille, JC Fricain, JM Franconi, C Le Visage, D Letourneur, J Amédée, and AK Bouzier-Sore. Magnetic resonance imaging tracking of human adipose derived stromal cells within three-dimensional scaffolds for bone tissue engineering. *European Cells and Materials*, 21:341–354, April 2011.

[209] Juli R. Bagó, Elisabeth Aguilar, Maria Alieva, Carolina Soler-Botija, Olaia F. Vila, Silvia Claros, José A. Andrades, José Becerra, Nuria Rubio, and Jerónimo Blanco. In vivobioluminescence imaging of cell differentiation in biomaterials: A platform for scaffold development. *Tissue Engineering Part A*, 19(5–6):593–603, March 2013.

[210] Barbara J Muller-Borer, Maria C Collins, Philip R Gunst, Wayne E Cascio, and Alan P Kypson. Quantum dot labeling of mesenchymal stem cells.

Journal of Nanobiotechnology, 5(1):9, 2007.

[211] Franz Josef Gildehaus, Florian Haasters, Inga Drosse, Erika Wagner, Christian Zach, Wolf Mutschler, Paul Cumming, Peter Bartenstein, and Matthias Schieker. Impact of indium-111 oxine labelling on viability of human mesenchymal stem cells in vitro, and 3d cell-tracking using spect/ct in vivo. *Molecular Imaging and Biology*, 13(6):1204–1214, November 2010.

[212] Sonja Nowotschin and Anna-Katerina Hadjantonakis. Use of kikgr a photoconvertible green-to-red fluorescent protein for cell labeling and lineage analysis in es cells and mouse embryos. *BMC Developmental Biology*, 9(1), September 2009.

[213] Danny A. Stark and Paul M. Kulesa. An in vivo comparison of photoactivatable fluorescent proteins in an avian embryo model. *Developmental Dynamics*, 236(6):1583–1594, May 2007.

[214] Paul M. Kulesa, Jessica M. Teddy, Danny A. Stark, Sarah E. Smith, and Rebecca McLennan. Neural crest invasion is a spatially-ordered progression into the head with higher cell proliferation at the migratory front as revealed by the photoactivatable protein, kikgr. *Developmental Biology*, 316(2):275–287, April 2008.

[215] T. Mutoh, T. Miyata, S. Kashiwagi, A. Miyawaki, and M. Ogawa. Dynamic behavior of individual cells in developing organotypic brain slices

revealed by the photoconvertable protein kaede. *Experimental Neurology*, 200(2):430–437, August 2006.

[216] Michio Tomura, Naoki Yoshida, Junko Tanaka, Satoshi Karasawa, Yoshihiro Miwa, Atsushi Miyawaki, and Osami Kanagawa. Monitoring cellular movement in vivo with photoconvertible fluorescence protein "kaede" transgenic mice. *Proceedings of the National Academy of Sciences*, 105(31):10871–10876, August 2008.

[217] Heng Li, Qi Zhang, Xing Guo, Weibin Bu, Huiquan Zuo, Lijuan Jiao, Zhongxin Li, Changjiang Yu, Shaozhen Wang, and Erhong Hao. Dual-color photoconvertible bodipy dyes based on visible-light photouncaging of nitrobenzyl moieties for living-cell imaging. *Advanced Optical Materials*, 12(6), October 2023.

[218] Fränze Progatzky, Margaret J. Dallman, and Cristina Lo Celso. From seeing to believing: labelling strategies for in vivo cell-tracking experiments. *Interface Focus*, 3(3):20130001, June 2013.

[219] Ching-Shwun Lin, Zhong-Cheng Xin, Jican Dai, and Tom F Lue. Commonly used mesenchymal stem cell markers and tracking labels: Limitations and challenges. *Histol. Histopathol.*, 28(9):1109–1116, September 2013.

[220] M.C. Kruyt, J. de Bruijn, M. Veenhof, F.C. Oner, C.A. van Blitterswijk, A.J. Verbout, and W.J.A. Dhert. Application and limitations of chloromethyl-

benzamidodialkylcarbocyanine for tracing cells used in bone tissue engineering. *Tissue Engineering*, 9(1):105–115, February 2003.

[221] N Mohorko, N Kregar-Velikonja, G Repovs, M Gorensek, and M Bresjanac. An in vitro study of hoechst 33342 redistribution and its effects on cell viability. *Human & Experimental Toxicology*, 24(11):573–580, November 2005.

[222] Paula Castanheira, Leonardo Torquetti Torquetti, Débora Rodrigues Soares Magalhãs, Marcio B. Nehemy, and Alfredo M. Goes. Dapi diffusion after intravitreal injection of mesenchymal stem cells in the injured retina of rats. *Cell Transplantation*, 18(4):423–431, April 2009.

[223] Daniele Zink, Nicolas Sadoni, and Ernst Stelzer. Visualizing chromatin and chromosomes in living cells. *Methods*, 29(1):42–50, January 2003.

[224] Alexander R. Nödling, Emily M. Mills, Xuefei Li, Davide Cardella, Edward J. Sayers, Shih-Hsiung Wu, Arwyn T. Jones, Louis Y. P. Luk, and Yu-Hsuan Tsai. Cyanine dye mediated mitochondrial targeting enhances the anti-cancer activity of small-molecule cargoes. *Chemical Communications*, 56(34):4672–4675, 2020.

[225] Virginia Wycisk, Katharina Achazi, Ole Hirsch, Christian Kuehne, Jens Dernedde, Rainer Haag, and Kai Licha. Heterobifunctional dyes: Highly fluorescent linkers based on cyanine dyes. *ChemistryOpen*, 6(3):437–446, April 2017.

[226] AAT Bioquest. Amine reactive dyes and probes for conjugation. https://www.aatbio.com/catalog/amine-reactive-dyes-and-probes-for-conjugation, 2024 (accessed March 28, 2024).

[227] Bronson I. Pinto, Nathan D. Cruz, Oscar R. Lujan, Catherine R. Propper, and Robert S. Kellar. In vitro scratch assay to demonstrate effects of arsenic on skin cell migration. *Journal of Visualized Experiments*, (144), February 2019.

[228] TESCAN. Tescan vega. https://www.tescan.com/product/sem-for-materials-science-tescan-vega/, 2023 (accessed March 1, 2024).

[229] Om Prakash Choudhary and Priyan ka. Scanning electron microscope: Advantages and disadvantages in imaging components. *International Journal of Current Microbiology and Applied Sciences*, 6(5):1877–1882, May 2017.

[230] Annalena Wolff. Fib scheme. https://analyticalscience.wiley.com/content/article-do/focused-ion-beams-overview-technology-and-its-capabilities, 2020 (accessed Fabruary 14, 2024).

[231] Meltem Sezen. *Focused Ion Beams (FIB) — Novel Methodologies and Recent Applications for Multidisciplinary Sciences.* InTech, February 2016.

[232] C. Chiappini and C. Almeida. *Silicon nanoneedles for drug delivery*, page 144–167. Elsevier, 2014.

[233] Michael J. Sanderson, Ian Smith, Ian Parker, and Martin D. Bootman. Fluorescence microscopy. *Cold Spring Harbor Protocols*, 2014(10):pdb.top071795, October 2014.

[234] Herbert Schneckenburger and Verena Richter. Laser scanning versus widefield—choosing the appropriate microscope in life sciences. *Applied Sciences*, 11(2):733, January 2021.

[235] David Nečas and Petr Klapetek. Gwyddion. `http://gwyddion.net/`, 2024 (accessed May 27, 2024).

[236] TECAN. Infinite 200 pro. `https://lifesciences.tecan.com/plate_readers/infinite_200_pro`, 2015 (accessed March 1, 2024).

[237] Dai Hai Nguyen, Canh Hao Nguyen, and Hiroshi Mamitsuka. Recent advances and prospects of computational methods for metabolite identification: a review with emphasis on machine learning approaches. *Briefings in Bioinformatics*, 20(6):2028–2043, August 2018.

[238] Tomoaki Nagai, Tomohiro Ishikawa, Yasuhiro Minami, and Michiru Nishita. Tactics of cancer invasion: solitary and collective invasion. *The Journal of Biochemistry*, 167(4):347–355, January 2020.

[239] Aurelie Evrard, Bastiaan O. R. Bargmann, Kenneth D. Birnbaum, Mark Tester, Ute Baumann, and Alexander A. T. Johnson. *Fluorescence-Activated Cell Sorting for Analysis of Cell Type-Specific Responses to Salinity Stress in Arabidopsis and Rice*, page 265–276. Humana Press, 2012.

[240] Anastasiia Yu. Sapach, Olga A. Sindeeva, Mikhail V. Nesterchuk, Alexandra A. Tsitrina, Oksana A. Mayorova, Ekaterina S. Prikhozhdenko, Roman A. Verkhovskii, Arsen S. Mikaelyan, Yuri V. Kotelevtsev, and Gleb B. Sukhorukov. Macrophage in vitro and in vivo tracking via anchored microcapsules. *ACS Applied Materials & Interfaces*, 14(46):51579–51592, November 2022.

[241] J. Nathan Henderson, Hui-wang Ai, Robert E. Campbell, and S. James Remington. Structural basis for reversible photobleaching of a green fluorescent protein homologue. *Proceedings of the National Academy of Sciences*, 104(16):6672–6677, April 2007.

[242] Andre C. Stiel, Martin Andresen, Hannes Bock, Michael Hilbert, Jessica Schilde, Andreas Schönle, Christian Eggeling, Alexander Egner, Stefan W. Hell, and Stefan Jakobs. Generation of monomeric reversibly switchable red fluorescent proteins for far-field fluorescence nanoscopy. *Biophysical Journal*, 95(6):2989–2997, September 2008.

[243] Jie Chao, Tiffany Peña, Dean G. Heimann, Chris Hansen, David A. Doyle, Ujwal R. Yanala, Timothy M. Guenther, and Mark A. Carlson. Expression

of green fluorescent protein in human foreskin fibroblasts for use in 2d and 3d culture models. *Wound Repair and Regeneration*, 22(1):134–140, January 2014.

[244] M. Palm, C. Baumstark-Khan, and G. Horneck. *Green Fluorescent Protein (GFP) Expression in Mammalian Cells After UV-Irradiation*, page 311–316. Springer Netherlands, 1999.

[245] Hiroyuki Katayama, Akitsugu Yamamoto, Noboru Mizushima, Tamotsu Yoshimori, and Atsushi Miyawaki. Gfp-like proteins stably accumulate in lysosomes. *Cell Structure and Function*, 33(1):1–12, 2008.

[246] Janine Walter, Sascha Hausmann, Thomas Drepper, Michael Puls, Thorsten Eggert, and Marcel Dihné. Flavin mononucleotide-based fluorescent proteins function in mammalian cells without oxygen requirement. *PLoS ONE*, 7(9):e43921, September 2012.

[247] Elizabeth Dreskin, Michelle Collins, Joseph Terefe, Luis Ugozzoli, and Teresa Rubio. Optimizing electroporation conditions in primary and other difficult-to-transfect cells. *Journal of biomolecular techniques : JBT*, 19:328–34, 01 2009.

[248] Dong Luo, David J. Gould, and Gleb B. Sukhorukov. Local and sustained activity of doxycycline delivered with layer-by-layer microcapsules. *Biomacromolecules*, 17(4):1466–1476, March 2016.

[249] Mikhail V. Zyuzin, Alexander S. Timin, and Gleb B. Sukhorukov. Multilayer capsules inside biological systems: State-of-the-art and open challenges. *Langmuir*, 35(13):4747–4762, March 2019.

[250] Sue Jiun Phang and Lling-Lling Tan. Recent advances in carbon quantum dot (cqd)-based two dimensional materials for photocatalytic applications. *Catalysis Science & Technology*, 9(21):5882–5905, 2019.

[251] Nan Jiang, Bo Qi, Xinyu Fan, Ling Yao, Yi Wang, Zeyu Zhao, Yongqing Xu, and Mohd Hasmizam Razali. Fabrication of biocompatible and biodegradable polyvinyl alcohol/sodium alginate blend polymers incorporating ca2+ doped tio2 nanocomposite 3d scaffold for biomedical applications. *Journal of Saudi Chemical Society*, 27(6):101758, November 2023.

[252] Xiaoli Zhang, Na Li, Ying Zhu, and Wei Wen. The role of mesenchymal stem cells in the occurrence, development, and therapy of hepatocellular carcinoma. *Cancer Medicine*, 11(4):931–943, January 2022.

[253] Christie M. Hassan, Patrina Trakampan, and Nicholas A. Peppas. *Water Solubility Characteristics of Poly(vinyl alcohol) and Gels Prepared by Freezing/Thawing Processes*, page 31–40. Springer US, 2002.

[254] Roberto G. Ramírez-Chavarría, Argelia Pérez-Pacheco, Emiliano Terán, and Rosa M. Quispe-Siccha. Study of polyvinyl alcohol hydrogels applying physical-mechanical methods and dynamic models of photoacoustic signals. *Gels*, 9(9):727, September 2023.

[255] Ying Chen, Jie Li, Jiawei Lu, Meng Ding, and Yi Chen. Synthesis and properties of poly(vinyl alcohol) hydrogels with high strength and toughness. *Polymer Testing*, 108:107516, April 2022.

[256] G. Gordon Cameron, Malcolm D. Ingram, M. Younus Qureshi, Helen M. Gearing, Luigi Costa, and Giovanni Camino. The thermal degradation of poly(ethylene oxide) and its complex with nacns. *European Polymer Journal*, 25(7–8):779–784, January 1989.

[257] Koblan Wilfried Ebagninin, Adel Benchabane, and Karim Bekkour. Rheological characterization of poly(ethylene oxide) solutions of different molecular weights. *Journal of Colloid and Interface Science*, 336(1):360–367, August 2009.

[258] Masaru Nakada, Hiroyuki Ishida, and Yoshitomo Furushima. Structural and dynamical characterisation of intermediate water interacting polyvinyl pyrrolidone. *Materialia*, 12:100743, August 2020.

[259] Beata Grabowska, Sylwia Cukrowicz, Karolina Kaczmarska, Sylwia Żymankowska-Kumon, Artur Bobrowski, Bożena Tyliszczak, and Natalia Maria Mrówka. Thermostability of organobentonite modified with poly(acrylic acid). *Materials*, 16(10):3626, May 2023.

[260] Karen Köhler, Dmitry G. Shchukin, Helmuth Möhwald, and Gleb B. Sukhorukov. Thermal behavior of polyelectrolyte multilayer microcapsules. 1. the

effect of odd and even layer number. *The Journal of Physical Chemistry B*, 109(39):18250–18259, September 2005.

[261] A. Babaie, S. Madadkhani, and B. Stoeber. Evaporation-driven low reynolds number vortices in a cavity. *Physics of Fluids*, 26(3), March 2014.

[262] Dita Puspita Sari and Darminto Darminto. Measurement of hydrogen diffusion through pva hydrogel using magnetic resonance imaging method in comparison with consistency assessment using digital penetrometer. *Jurnal Fisika dan Aplikasinya*, 9(2):86, October 2013.

[263] A. V. Dubrovskii, L. I. Shabarchina, Yu. A. Kim, and B. I. Sukhorukov. Investigation of the influence of temperature on polyelectrolyte microcapsules. *Glass Physics and Chemistry*, 33(3):226–231, June 2007.

[264] Karen Köhler, Helmuth Möhwald, and Gleb B. Sukhorukov. Thermal behavior of polyelectrolyte multilayer microcapsules: 2. insight into molecular mechanisms for the pdadmac/pss system. *The Journal of Physical Chemistry B*, 110(47):24002–24010, October 2006.

[265] Manisha Mondal and Subhamay Pramanik. A mechanism for excitation-dependent emission from carbon nanodots. *Materials Letters: X*, 18:100195, June 2023.

[266] Jerald Y. Q. Teo, Xin Ting Zheng, Debbie Hwee Leng Seng, Hui Kim Hui, Pei Lin Chee, Xiaodi Su, Xian Jun Loh, and Jason Y. C. Lim. Waste

polystyrene-derived sulfonated fluorescent carbon nanoparticles for cation sensing. *ChemistrySelect*, 7(36), September 2022.

[267] Anjali Banger, Sakshi Gautam, Sapana Jadoun, Nirmala Kumari Jangid, Anamika Srivastava, Indra Neel Pulidindi, Jaya Dwivedi, and Manish Srivastava. Synthetic methods and applications of carbon nanodots. *Catalysts*, 13(5):858, May 2023.

[268] N. O. Mchedlov-Petrossyan and V. V. Ivanov. Effect of the solvent on the absorption spectra and protonation of fluorescein dye anions. *Russian Journal of Physical Chemistry*, 81(1):112–115, January 2007.

[269] K. Köhler and G. B. Sukhorukov. Heat treatment of polyelectrolyte multilayer capsules: A versatile method for encapsulation. *Advanced Functional Materials*, 17(13):2053–2061, July 2007.

[270] R. E. Kellogg and R. G. Bennett. Radiationless intermolecular energy transfer. iii. determination of phosphorescence efficiencies. *The Journal of Chemical Physics*, 41(10):3042–3045, November 1964.

[271] John. Olmsted. Calorimetric determinations of absolute fluorescence quantum yields. *The Journal of Physical Chemistry*, 83(20):2581–2584, October 1979.

[272] B. Soep, A. Kellmann, M. Martin, and L. Lindqvist. Study of triplet quantum yields using a tunable dye laser. *Chemical Physics Letters*, 13(3):241–244, March 1972.

[273] M.R. Mohebbifar. Investigation of thermal lens performance of rhodamine 6g and rhodamine b at different concentration using pump/probe laser thermal lens spectroscopy. *Optik*, 242:166902, September 2021.

[274] Bruno R. V. Ferreira, Deleon N. Correa, Marcos N. Eberlin, and Pedro H. Vendramini. Fragmentation reactions of rhodamine b and 6g as revealed by high accuracy orbitrap tandem mass spectrometry. *Journal of the Brazilian Chemical Society*, 2016.

[275] Anthony Romieu, Garance Dejouy, and Ibai E. Valverde. Quest for novel fluorogenic xanthene dyes: Synthesis, spectral properties and stability of 3-imino-3h-xanthen-6-amine (pyronin) and its silicon analog. *Tetrahedron Letters*, 59(52):4574–4581, December 2018.

[276] P. A. Demina, O. A. Sindeeva, A. M. Abramova, M. S. Saveleva, G. B. Sukhorukov, and I. Y. Goryacheva. Fluorescent polymer markers photoconvertible with a 532 nm laser for individual cell labeling. *Journal of Biophotonics*, 16(6), February 2023.

[277] Dmitry A. Gorin, Sergey A. Portnov, Olga A. Inozemtseva, Zofia Luklinska, Alexey M. Yashchenok, Anton M. Pavlov, Andre G. Skirtach, Helmuth Möhwald, and Gleb B. Sukhorukov. Magnetic/gold nanoparticle functionalized biocompatible microcapsules with sensitivity to laser irradiation. *Physical Chemistry Chemical Physics*, 10(45):6899, 2008.

[278] Thao L. Nguyen and Mahmoud A. Saleh. Thermal degradation of azobenzene dyes. *Results in Chemistry*, 2:100085, January 2020.

[279] Cheunsoon Ahn, Xia Zeng, Longchun Li, and S Kay Obendorf. Thermal degradation of natural dyes and their analysis using hplc-dad-ms. *Fashion and Textiles*, 1(1), November 2014.

[280] Chiao-Ling Cheng, Ming-Hsien Chan, Sheng-Jan Feng, Michael Hsiao, and Ru-Shi Liu. Long-term near-infrared signal tracking of the therapeutic changes of glioblastoma cells in brain tissue with ultrasound-guided persistent luminescent nanocomposites. *ACS Applied Materials & Interfaces*, 13(5):6099–6108, January 2021.

[281] Lucas A Lane, Ruiyang Xue, and Shuming Nie. Emergence of two near-infrared windows for in vivo and intraoperative sers. *Current Opinion in Chemical Biology*, 45:95–103, August 2018.

[282] Guangcun Chen, Yejun Zhang, Chunyan Li, Dehua Huang, Qianwu Wang, and Qiangbin Wang. Recent advances in tracking the transplanted stem cells using near-infrared fluorescent nanoprobes: Turning from the first to the second near-infrared window. *Advanced Healthcare Materials*, 7(20), July 2018.

[283] Yue Yuan, Jia Zhang, Linna An, Qinjingwen Cao, Yun Deng, and Gaolin Liang. Oligomeric nanoparticles functionalized with nir-emitting cdte/cds

qds and folate for tumor-targeted imaging. *Biomaterials*, 35(27):7881–7886, September 2014.

[284] Cristian Matea, Teodora Mocan, Flaviu Tabaran, Teodora Pop, Ofelia Mosteanu, Cosmin Puia, Cornel Iancu, and Lucian Mocan. Quantum dots in imaging, drug delivery and sensor applications. *International Journal of Nanomedicine*, Volume 12:5421–5431, July 2017.

[285] Zhenfeng Yu, Christina Eich, and Luis J. Cruz. Recent advances in rare-earth-doped nanoparticles for nir-ii imaging and cancer theranostics. *Frontiers in Chemistry*, 8, June 2020.

[286] Nitzan Dar and Rinat Ankari. Theoretical models, preparation, characterization and applications of cyanine j-aggregates: A minireview. *ChemistryOpen*, 11(11), November 2022.

[287] Tarita Biver, Angela De Biasi, Fernando Secco, Marcella Venturini, and Sergiy Yarmoluk. Cyanine dyes as intercalating agents: Kinetic and thermodynamic studies on the dna/cyan40 and dna/ccyan2 systems. *Biophysical Journal*, 89(1):374–383, July 2005.

[288] Surendra B. Anantharaman, Sergii Yakunin, Chuyao Peng, Marcus Vinícius Gonçalves Vismara, Carlos F. O. Graeff, Frank A. Nüesch, Sandra Jenatsch, Roland Hany, Maksym V. Kovalenko, and Jakob Heier. Strongly red-shifted photoluminescence band induced by molecular twist-

ing in cyanine (cy3) dye films. *The Journal of Physical Chemistry C*, 121(17):9587–9593, April 2017.

[289] Yutaka Kawabe and Sho Kato. Spectroscopic study of cyanine dyes interacting with the biopolymer, dna. *Dyes and Pigments*, 95(3):614–618, December 2012.

[290] Chen-Ming Lin, Syed Usama, and Kevin Burgess. Site-specific labeling of proteins with near-ir heptamethine cyanine dyes. *Molecules*, 23(11):2900, November 2018.

[291] Marena Manley and Vincent Baeten. *Spectroscopic Technique: Near Infrared (NIR) Spectroscopy*, page 51–102. Elsevier, 2018.

[292] Natalia G. Zhegalova, Shawn He, Haiying Zhou, David M. Kim, and Mikhail Y. Berezin. Minimization of self-quenching fluorescence on dyes conjugated to biomolecules with multiple labeling sites via asymmetrically charged nir fluorophores. *Contrast Media & Molecular Imaging*, 9(5):355–362, April 2014.

[293] Haicheng Lu, Yuqian Wang, Sophie K. Hill, Hanqiu Jiang, Yubin Ke, Shaohui Huang, Dunjin Zheng, Sébastien Perrier, and Qiao Song. Supra-cyanines: Ultrabright cyanine-based fluorescent supramolecular materials in solution and in the solid state. *Angewandte Chemie International Edition*, 62(48), October 2023.

[294] Qinsi Zheng, Steffen Jockusch, Zhou Zhou, and Scott C. Blanchard. The contribution of reactive oxygen species to the photobleaching of organic fluorophores. *Photochemistry and Photobiology*, 90(2):448–454, December 2013.

[295] Hajnal Klelemen, Gabriel Hancu, Edina Kacsó, and Lajos-Attila Papp. Photosensitivity reactions induced by photochemical degradation of drugs. *Advanced Pharmaceutical Bulletin*, May 2021.

[296] Eric A. Owens, Maged Henary, Georges El Fakhri, and Hak Soo Choi. Tissue-specific near-infrared fluorescence imaging. *Accounts of Chemical Research*, 49(9):1731–1740, August 2016.

[297] Wei-Liang Chen, Julie Wagner, Nicholas Heugel, Jeffrey Sugar, Yu-Wen Lee, Lisa Conant, Marsha Malloy, Joseph Heffernan, Brendan Quirk, Anthony Zinos, Scott A. Beardsley, Robert Prost, and Harry T. Whelan. Functional near-infrared spectroscopy and its clinical application in the field of neuroscience: Advances and future directions. *Frontiers in Neuroscience*, 14, July 2020.

[298] F. Chua and G.J. Laurent. *FIBROBLASTS*, page 213–219. Elsevier, 2006.

[299] Shupeng She, Chunxiu Xu, Xuefeng Yin, Weijun Tong, and Changyou Gao. Shape deformation and recovery of multilayer microcapsules after being squeezed through a microchannel. *Langmuir*, 28(11):5010–5016, March 2012.

[300] Adam Nowakowski, Katarzyna Drela, Justyna Rozycka, Miroslaw Janowski, and Barbara Lukomska. Engineered mesenchymal stem cells as an anti-

cancer trojan horse. *Stem Cells and Development*, 25(20):1513–1531, October 2016.

[301] Chen Zong, Hangjie Zhang, Xue Yang, Lu Gao, Jing Hou, Fei Ye, Jinghua Jiang, Yang Yang, Rong Li, Zhipeng Han, and Lixin Wei. The distinct roles of mesenchymal stem cells in the initial and progressive stage of hepatocarcinoma. *Cell Death & Disease*, 9(3), March 2018.

[302] J. Konen, E. Summerbell, B. Dwivedi, K. Galior, Y. Hou, L. Rusnak, A. Chen, J. Saltz, W. Zhou, L. H. Boise, P. Vertino, L. Cooper, K. Salaita, J. Kowalski, and A. I. Marcus. Image-guided genomics of phenotypically heterogeneous populations reveals vascular signalling during symbiotic collective cancer invasion. *Nature Communications*, 8(1), May 2017.

[303] I.I. Shemiakina, G.V. Ermakova, P.J. Cranfill, M.A. Baird, R.A. Evans, E.A. Souslova, D.B. Staroverov, A.Y. Gorokhovatsky, E.V. Putintseva, T.V. Gorodnicheva, T.V. Chepurnykh, L. Strukova, S. Lukyanov, A.G. Zaraisky, M.W. Davidson, D.M. Chudakov, and D. Shcherbo. A monomeric red fluorescent protein with low cytotoxicity. *Nature Communications*, 3(1), November 2012.

[304] Atsushi Miyawaki. Proteins on the move: insights gained from fluorescent protein technologies. *Nature Reviews Molecular Cell Biology*, 12(10):656–668, September 2011.

[305] Pilar Baldominos, Olga Barreiro, Ulrich von Andrian, Rafael Sirera, Paula Montero-Llopis, and Judith Agudo. Protocol to isolate live single cells while retaining spatial information by combining cell photolabeling and facs. *STAR Protocols*, 3(4):101795, December 2022.

[306] Elena Ivanova and Anton Khmelinskii. (photo)convert to pooled visual screening. *Molecular Systems Biology*, 16(6), June 2020.

[307] D. Axelrod, D.E. Koppel, J. Schlessinger, E. Elson, and W.W. Webb. Mobility measurement by analysis of fluorescence photobleaching recovery kinetics. *Biophysical Journal*, 16(9):1055–1069, September 1976.

[308] Francois Lassailly, Emmanuel Griessinger, and Dominique Bonnet. "microenvironmental contaminations" induced by fluorescent lipophilic dyes used for noninvasive in vitro and in vivo cell tracking. *Blood*, 115(26):5347–5354, July 2010.

[309] Maysaloun Merhi, Christophe Youta Dombu, Alizée Brient, Jiang Chang, Anne Platel, Frank Le Curieux, Daniel Marzin, Fabrice Nesslany, and Didier Betbeder. Study of serum interaction with a cationic nanoparticle: Implications for in vitro endocytosis, cytotoxicity and genotoxicity. *International Journal of Pharmaceutics*, 423(1):37–44, February 2012.

[310] Kai Xiao, Yuanpei Li, Juntao Luo, Joyce S. Lee, Wenwu Xiao, Abby M. Gonik, Rinki G. Agarwal, and Kit S. Lam. The effect of surface charge on

in vivo biodistribution of peg-oligocholic acid based micellar nanoparticles. *Biomaterials*, 32(13):3435–3446, May 2011.

[311] Jinwei Di, Xiang Gao, Yimeng Du, Hui Zhang, Jing Gao, and Aiping Zheng. Size, shape, charge and "stealthy" surface: Carrier properties affect the drug circulation time in vivo. *Asian Journal of Pharmaceutical Sciences*, 16(4):444–458, July 2021.

[312] Malini Visweswaran, Sebastian Pohl, Frank Arfuso, Philip Newsholme, Rodney Dilley, Shazib Pervaiz, and Arun Dharmarajan. Multi-lineage differentiation of mesenchymal stem cells – to wnt, or not wnt. *The International Journal of Biochemistry & Cell Biology*, 68:139–147, November 2015.

[313] Amelia Hurley-Novatny, Navein Arumugasaamy, Megan Kimicata, Hannah Baker, Antonios G Mikos, and John P Fisher. Concurrent multi-lineage differentiation of mesenchymal stem cells through spatial presentation of growth factors. *Biomedical Materials*, 15(5):055035, August 2020.

[314] M. Dominici, K. Le Blanc, I. Mueller, I. Slaper-Cortenbach, F.C Marini, D.S. Krause, R.J. Deans, A. Keating, D.J. Prockop, and E.M. Horwitz. Minimal criteria for defining multipotent mesenchymal stromal cells. the international society for cellular therapy position statement. *Cytotherapy*, 8(4):315–317, 2006.

[315] Rahul Sarugaser, Lorraine Hanoun, Armand Keating, William L. Stanford, and John E. Davies. Human mesenchymal stem cells self-renew and differen-

tiate according to a deterministic hierarchy. *PLoS ONE*, 4(8):e6498, August 2009.

[316] Stefan Fickert, Ute Schröter-Bobsin, Anna-Friederike Groß, Ute Hempel, Claudia Wojciechowski, Claudia Rentsch, Denis Corbeil, and Klaus Peter Günther. Human mesenchymal stem cell proliferation and osteogenic differentiation during long-term ex vivo cultivation is not age dependent. *Journal of Bone and Mineral Metabolism*, 29(2):224–235, September 2010.

[317] Panagiotis Mallis, Efstathios Michalopoulos, Theofanis Chatzistamatiou, and Catherine Stavropoulos Giokas. Interplay between mesenchymal stromal cells and immune system: clinical applications in immune-related diseases. *Exploration of Immunology*, June 2021.

[318] Fu, Liu, Halim, Ju, Luo, and Song. Mesenchymal stem cell migration and tissue repair. *Cells*, 8(8):784, July 2019.

[319] Kristine C. Rustad and Geoffrey C. Gurtner. Mesenchymal stem cells home to sites of injury and inflammation. *Advances in Wound Care*, 1(4):147–152, August 2012.

[320] Andreas Robert Rudolf Weiss and Marc Hendrik Dahlke. Immunomodulation by mesenchymal stem cells (mscs): Mechanisms of action of living, apoptotic, and dead mscs. *Frontiers in Immunology*, 10, June 2019.

[321] Dobroslav Kyurkchiev. Secretion of immunoregulatory cytokines by mesenchymal stem cells. *World Journal of Stem Cells*, 6(5):552, 2014.

[322] Vineet Kumar Mishra, Hui-Hsuan Shih, Farzana Parveen, David Lenzen, Etsuro Ito, Te-Fu Chan, and Liang-Yin Ke. Identifying the therapeutic significance of mesenchymal stem cells. *Cells*, 9(5):1145, May 2020.

[323] Senthilkumar Kalimuthu, Liya Zhu, Ji Min Oh, Prakash Gangadaran, Ho Won Lee, Se hwan Baek, Ramya Lakshmi Rajendran, Arunnehru Gopal, Shin Young Jeong, Sang-Woo Lee, Jaetae Lee, and Byeong-Cheol Ahn. Migration of mesenchymal stem cells to tumor xenograft models and in vitro drug delivery by doxorubicin. *International Journal of Medical Sciences*, 15(10):1051–1061, 2018.

[324] Christina Schug, Aayush Gupta, Sarah Urnauer, Katja Steiger, Phyllis Fung-Yi Cheung, Christian Neander, Konstantinos Savvatakis, Kathrin A. Schmohl, Marija Trajkovic-Arsic, Nathalie Schwenk, Markus Schwaiger, Peter J. Nelson, Jens T. Siveke, and Christine Spitzweg. A novel approach for image-guided 131i therapy of pancreatic ductal adenocarcinoma using mesenchymal stem cell-mediated nis gene delivery. *Molecular Cancer Research*, 17(1):310–320, January 2019.

[325] Jayavardini Vasanthan, Narasimman Gurusamy, Sheeja Rajasingh, Vinoth Sigamani, Shivaani Kirankumar, Edwin L. Thomas, and Johnson Rajasingh. Role of human mesenchymal stem cells in regenerative therapy. *Cells*, 10(1):54, December 2020.

[326] Ria Margiana, Alexander Markov, Angelina O. Zekiy, Mohammed Ubaid

Hamza, Khalid A. Al-Dabbagh, Sura Hasan Al-Zubaidi, Noora M. Hameed, Irshad Ahmad, R. Sivaraman, Hamzah H. Kzar, Moaed E. Al-Gazally, Yasser Fakri Mustafa, and Homayoon Siahmansouri. Clinical application of mesenchymal stem cell in regenerative medicine: a narrative review. *Stem Cell Research & Therapy*, 13(1), July 2022.

[327] S. Cruet-Hennequart, A.M. Prendergast, F.P. Barry, and M.P. Carty. Human mesenchymal stem cells (hmscs) as targets of dna damaging agents in cancer therapy. *Current Cancer Drug Targets*, 10(4):411–421, June 2010.

[328] Francesco P. Russo, Malcolm R. Alison, Brian W. Bigger, Eunice Amofah, Aikaterini Florou, Farhana Amin, George Bou–Gharios, Rosemary Jeffery, John P. Iredale, and Stuart J. Forbes. The bone marrow functionally contributes to liver fibrosis. *Gastroenterology*, 130(6):1807–1821, May 2006.

[329] Yukiya Takayama, Kosuke Kusamori, and Makiya Nishikawa. Mesenchymal stem/stromal cells as next-generation drug delivery vehicles for cancer therapeutics. *Expert Opinion on Drug Delivery*, 18(11):1627–1642, August 2021.

[330] Stefaan De Koker, Liesbeth J. De Cock, Pilar Rivera-Gil, Wolfgang J. Parak, Rachel Auzély Velty, Chris Vervaet, Jean Paul Remon, Johan Grooten, and Bruno G. De Geest. Polymeric multilayer capsules delivering biotherapeutics. *Advanced Drug Delivery Reviews*, 63(9):748–761, August 2011.

[331] Raghava S. Velagaleti, Michael J. Pencina, Joanne M. Murabito, Thomas J. Wang, Nisha I. Parikh, Ralph B. D'Agostino, Daniel Levy, William B. Kannel, and Ramachandran S. Vasan. Long-term trends in the incidence of heart failure after myocardial infarction. *Circulation*, 118(20):2057–2062, November 2008.

[332] Andrew S. Riching and Kunhua Song. Cardiac regeneration: New insights into the frontier of ischemic heart failure therapy. *Frontiers in Bioengineering and Biotechnology*, 8, January 2021.

[333] Virpi Talman and Heikki Ruskoaho. Cardiac fibrosis in myocardial infarction—from repair and remodeling to regeneration. *Cell and Tissue Research*, 365(3):563–581, June 2016.

[334] Hisayuki Hashimoto, Eric N. Olson, and Rhonda Bassel-Duby. Therapeutic approaches for cardiac regeneration and repair. *Nature Reviews Cardiology*, 15(10):585–600, June 2018.

[335] Hisayuki Hashimoto, Zhaoning Wang, Glynnis A. Garry, Venkat S. Malladi, Giovanni A. Botten, Wenduo Ye, Huanyu Zhou, Marco Osterwalder, Diane E. Dickel, Axel Visel, Ning Liu, Rhonda Bassel-Duby, and Eric N. Olson. Cardiac reprogramming factors synergistically activate genome-wide cardiogenic stage-specific enhancers. *Cell Stem Cell*, 25(1):69–86.e5, July 2019.

[336] Bo Wang, Likui Zhang, Hao Cao, Junqi Yang, Manya Wu, Yali Ma, Huimin Fan, Zhenzhen Zhan, and Zhongmin Liu. Myoblast transplantation improves cardiac function after myocardial infarction through attenuating inflammatory responses. *Oncotarget*, 8(40):68780–68794, May 2017.

[337] Philippe Menasché, Albert A Hagège, Jean-Thomas Vilquin, Michel Desnos, Eric Abergel, Bruno Pouzet, Alain Bel, Sorin Sarateanu, Marcio Scorsin, Ketty Schwartz, Patrick Bruneval, Marc Benbunan, Jean-Pierre Marolleau, and Denis Duboc. Autologous skeletal myoblast transplantation for severe postinfarction left ventricular dysfunction. *Journal of the American College of Cardiology*, 41(7):1078–1083, April 2003.

[338] J Herreros. Autologous intramyocardial injection of cultured skeletal muscle-derived stem cells in patients with non-acute myocardial infarction. *European Heart Journal*, 24(22):2012–2020, November 2003.

[339] Peter J. Amos, Esra Cagavi Bozkulak, and Yibing Qyang. Methods of cell purification: A critical juncture for laboratory research and translational science. *Cells Tissues Organs*, 195(1–2):26–40, October 2011.